Analysis of the IGS contribution to ITRF2020

Paul Rebischung[1,2*], Zuheir Altamimi[1,2], Laurent Métivier[1,2], Xavier Collilieux[1,2], Kevin Gobron[1], Kristel Chanard[1,2]

[1]Université Paris Cité, Institut de physique du globe de Paris, CNRS, IGN, Paris, F-75005, France.
[2]Univ Gustave Eiffel, ENSG, IGN.

*Corresponding author(s). E-mail(s): paul.rebischung@ign.fr;
Contributing authors: zuheir.altamimi@ign.fr; laurent.metivier@ign.fr; xavier.collilieux@ensg.eu; gobron@ipgp.fr; chanard@ipgp.fr;

Abstract

As its contribution to the latest release of the International Terrestrial Reference Frame, ITRF2020, the International GNSS Service (IGS) provided a 27-year-long series of daily "repro3" terrestrial frame solutions obtained by combining reprocessed solutions from ten Analysis Centers. This contribution represents an improvement over the previous contribution to ITRF2014, not only by the inclusion of more stations with longer and more complete position time series, but also by a general reduction of random and systematic errors. The IGS contribution to ITRF2020 also provided, for the first time, an independent estimate of the terrestrial scale based on the calibration of the Galileo satellite antennas. Despite the various observed improvements, the repro3 station position time series remain affected by a variety of random and systematic errors. This includes spurious periodic variations in several frequency bands, originating mostly from orbit and tide modeling errors, on top of a combination of white and flicker noise, whose origins remain to be precisely understood. These various components should carefully be accounted for when modeling GNSS station position time series and interpreting them in terms of Earth's surface deformation. The Galileo-based scale of the repro3 solutions is found to be significantly offset (by +4.3 mm at epoch 2015.0) and drifting (by +0.11 mm/yr) from the SLR/VLBI-based scale of ITRF2020. The reasons for this offset and drift remain to be uncovered.

Keywords: IGS, GNSS, Reprocessing, repro3, ITRF, Terrestrial reference frame

1 Introduction

Global Navigation Satellite Systems (GNSS) play a crucial role in the determination and dissemination of the International Terrestrial Reference Frame (ITRF; Altamimi and Collilieux, 2009; Altamimi et al., 2016). The contributions of the GNSS technique to the successive releases of the ITRF are provided by the International GNSS Service (IGS; Johnston et al., 2017). Following the ITRF2020 call for participation[1], the IGS undertook its third reprocessing campaign (repro3). Ten Analysis

[1] https://itrf.ign.fr/docs/solutions/itrf2020/CFP-ITRF2020.pdf

Centers (ACs) re-analyzed the history of GNSS observations acquired by a global tracking network using updated models and methodologies. The contributing ACs provided, among other products, daily terrestrial frame solutions including station position and Earth Rotation Parameter (ERP) estimates. The AC terrestrial frame solutions were then combined on a daily basis, and the daily combined repro3 terrestrial frame solutions form the IGS contribution to ITRF2020 (Altamimi et al., 2023).

Here, we provide a detailed analysis of the IGS contribution to ITRF2020 and assess the improvements (or deteriorations) observed with respect to the previous IGS reprocessing campaign (repro2; Rebischung et al., 2016). A particular focus is given to the analysis of the IGS repro3 station position time series, which is not only relevant to the ITRF2020 construction, but also to a much wider range of GNSS station position time series uses for various geophysical applications (see a review in Bock and Melgar, 2016).

The paper is organized as follows. Section 2 presents the input data, methodology and results of the daily IGS repro3 terrestrial frame combinations. Section 3 provides an analysis of the global geodetic parameters (ERPs, geocenter coordinates and terrestrial scale) in the repro3 combined solutions. Section 4 presents a detailed analysis of the repro3 combined station position time series, including the identification of offsets, the modeling of post-seismic displacements, a confrontation with deformation predicted by geophysical loading models, and a characterization of systematic and random errors. Section 5 presents an inter-comparison between different sets of GNSS station position time series including the IGS combined repro3 and repro2 time series, time series from the different AC contributions to repro3, and time series from two non-IGS providers. Finally, Section 6 summarizes the main findings and lessons learned.

2 Daily repro3 terrestrial frame combinations

This section describes the input data, methodology and results from the daily repro3 terrestrial frame combinations. The different AC contributions to repro3 and modeling updates since repro2 are introduced in Section 2.1. Section 2.2 describes the methodology used for the daily combinations and the provided products. Section 2.3 finally discusses the results of the daily combinations in terms of station network, AC weights and "AC – IGS" residuals.

2.1 Input data and modeling updates

Table 1 lists the AC contributions to the repro3 campaign that could be included in the final daily combined repro3 terrestrial frame solutions provided to the ITRF Combination Centers on April 10, 2021. The contributing ACs provided, among other products (satellite orbits and clocks, tropospheric

Table 1 AC contributions included in the final daily combined repro3 terrestrial frame solutions

AC	Institution	GNSS	from	till	References
COD	Center for Orbit Determination in Europe	GPS	1994-01-02	2020-12-31	Selmke et al. (2020)
		GLONASS	2002-01-01	2020-12-31	Dach et al. (2021)
		Galileo	2013-01-01	2020-12-31	
ESA	European Space Operations Center	GPS	1995-01-01	2020-12-31	Schoenemann et al. (2021)
		GLONASS	2009-01-01	2020-12-31	
		Galileo	2015-01-01	2020-12-31	
GFZ	GeoForschungsZentrum	GPS	1994-01-02	2020-12-31	Männel et al. (2020)
		GLONASS	2012-01-01	2020-12-31	Männel et al. (2021)
		Galileo	2013-12-21	2020-12-31	
GRG	Groupe de Recherche en Géodésie Spatiale	GPS	2000-05-03	2020-12-31	Perosanz et al. (2021)
		GLONASS	2008-11-04	2020-12-31	
		Galileo	2016-12-31	2020-12-31	
JPL	Jet Propulsion Laboratory	GPS	1994-01-02	2020-12-26	Murphy et al. (2021)
MIT	Massachusetts Institute of Technology	GPS	2000-01-02	2020-12-31	Herring (2022)
		Galileo	2017-01-01	2020-12-31	
NGS	National Geodetic Survey	GPS	1994-01-02	2020-12-31	Damiani et al. (2019)
TUG	Graz University of Technology	GPS	1994-01-02	2020-12-31	Strasser and Mayer-Gürr (2021)
		GLONASS	2009-01-01	2020-12-31	Strasser (2022)
		Galileo	2013-01-01	2020-12-31	
ULR	Université de la Rochelle	GPS	2003-01-01	2020-12-31	Gravelle et al. (2022, 2023)
WHU	Wuhan University	GPS	2008-01-01	2019-12-31	Shi et al. (2023)
		GLONASS	2010-09-28	2019-12-31	

delays and horizontal gradients, code and phase biases), daily terrestrial frame solutions in SINEX[2] format, which include station position and ERP estimates. Note that, since then, certain ACs have extended their repro3 contributions both backward and forward in time, and daily combined repro3 terrestrial frame solutions have been made available for the years 2021 and 2022 (Rebischung, 2023b). All AC contributions to repro3 are publicly available at https://cddis.nasa.gov/archive/gnss/products/wwww/repro3/, where *wwww* stands for the 4-character GPS week number.

As indicated in Table 1, a majority of ACs have provided multi-GNSS repro3 solutions: in addition to GPS observations, six ACs processed GLONASS observations and another six ACs processed Galileo observations, for various periods of time. This is a major evolution compared to the repro2 campaign in which only two ACs had processed GLONASS observations. The impacts of this shift toward multi-GNSS on the repro3 terrestrial frame solutions will be discussed in the next sections.

In addition to the emergence of multi-GNSS solutions, a number of new models and conventions have been adopted in repro3[3] compared to repro2. The main updates are detailed below together with their (expected) impact on terrestrial frame solutions. These updates have also been incorporated in the IGS operational products since GPS week 2238 (27 November 2022), at the same time as the IGS20/igs20.atx framework (Rebischung et al., 2022; Masoumi, 2022).

[2] https://www.iers.org/IERS/EN/Organization/AnalysisCoordinator/SinexFormat/sinex.html
[3] https://igs.org/acc/reprocessing/#repro3

Secular pole

The new secular pole model, recommended by the IERS 2010 Conventions (v1.2.0 and higher; Petit and Luzum, 2010), was used in repro3, replacing the previous mean pole model from the original IERS 2010 Conventions used in repro2. The original IERS 2010 mean pole model was a cubic fit to polar motion observations over the 1976.0–2010.0 period, linearly extrapolated afterwards. Pole tide corrections based on this model were missing non-linear, long-period components over the 1976.0–2010.0 period, and were subject to linear extrapolation errors afterwards, thus inducing artificial degree-2, order-1 spherical harmonic deformation pattern in geodetic station position time series (King and Watson, 2014). The new IERS secular pole model, based on a long-term linear fit to polar motion observations over the 1900–2017 period, is now recommended to solve both these issues. As a result of this change, the repro3 terrestrial frame solutions show a time-varying degree-2, order-1 spherical harmonic deformation pattern with respect to the IGS repro2 solutions, but also to the ITRF2014 (Altamimi et al., 2016) and IGS14 (Rebischung et al., 2017) reference frames. The amplitude of this pattern is relatively small until 2010, but then increases linearly, reaching about 3 mm in vertical and 1 mm in horizontal in 2020 (King and Watson, 2014).

Satellite radial phase center offsets (z-PCOs)

The GPS and GLONASS satellite z-PCOs conventionally used in the IGS operational products up to GPS week 2237 and compiled in the igs14.atx[4] ANTEX file had been estimated based on the ITRF2014 terrestrial scale (Rebischung et al., 2017; Schmid, 2017). On the other hand, the GPS and GLONASS satellite z-PCOs used in repro3 and compiled in igsR3.atx[5] have been shifted by constellation-wise corrections of −16.0 cm and −15.7 cm, respectively, to become consistent with the calibrated Galileo satellite z-PCOs published by the European GNSS Service Center (GSC, 2023; Rebischung, 2020; Villiger, 2020). As a consequence, the terrestrial scale of the IGS repro3 solutions is independent of the ITRF scale, but is instead based on the Galileo satellite antenna calibrations. The resulting scale is discussed and compared with the ITRF2020 scale in Section 3.3.

Ground antenna calibrations

In order to enable the processing of Galileo data in repro3, the L1/L2-only calibrations of several ground antenna types in igs14.atx were replaced by new multi-GNSS calibrations in igsR3.atx (Villiger, 2020). As usual, such ground antenna calibration updates induce antenna type- and station-dependent position offsets of a few mm in horizontal and up to about 1 cm in vertical.

[4] https://files.igs.org/pub/station/general/igs14.atx
[5] http://ftp.aiub.unibe.ch/awg/igsR3_2233.atx

IGSR3 reference frame

Because of the updates mentioned above, the daily repro3 solutions could not have been aligned to the IGS14 reference frame without systematic errors. A particular reference frame called IGSR3[6], consistent with the new IERS secular pole model, the igsR3.atx satellite PCOs and the igsR3.atx ground antenna calibrations, was thus used in repro3. While IGSR3 has its scale based on the igsR3.atx satellite z-PCOs, it is aligned in origin and orientation to ITRF2014. Details about its computation can be found in Rebischung (2020). Note that the daily and weekly repro3 solutions are aligned in orientation and origin to IGSR3, but not in scale. Their scale is a weighted average of those of the contributing AC solutions, and is thus based on the igsR3.atx satellite z-PCOs.

Rotation of phase center corrections for antennas not oriented North

While some ground GNSS antennas are not oriented North, the IGS practice until repro3 had been to overlook these mis-orientations and use the phase center corrections from the IGS ANTEX files as if all antennas were oriented North. In repro3, however, the phase center corrections from igsR3.atx have been rotated when necessary to align with the actual antenna orientations reported in the site logs. These rotations of phase center corrections have impacts of up to a few cm in horizontal and a few mm in vertical on the estimated positions of the affected stations. Antenna orientations, extracted from the site logs, are reported in an extra column in the SITE/ANTENNA blocks of the repro3 SINEX files.

Sub-daily ERP tides

The sub-daily ERP tide model from Desai and Sibois (2016) was adopted in repro3 in replacement of the current IERS model. This was shown to have practically no impact on station position estimates, but to reduce spurious aliased tidal signals in GNSS-derived ERP time series to some extent (Sibois, 2019, see also Section 3.1).

Ocean tidal loading

ACs have used recent ocean tidal loading models in repro3: either EOT11A (Savcenko and Bosch, 2012, ESA, WHU), GOT4.8 (Ray, 2013, JPL) or FES2014b (Lyard et al., 2021, all other ACs). This can be expected to reduce spurious aliased tidal signals in the repro3 station position time series to some extent (Penna and Stewart, 2003).

Solar radiation pressure

ACs have refined their solar radiation pressure models since repro2: more ACs used a priori solar radiation pressure models in repro3 (ESA, GRG, JPL, MIT, TUG for all the constellations they

[6] ftp://igs-rf.ign.fr/pub/IGSR3/IGSR3_2077.snx

processed; COD for Galileo) than in repro2 (EMR, ESA, JPL). As for the empirical parametrization of solar radiation pressure, all ACs which used variants of the Empirical CODE Orbit Model (ECOM) (Beutler et al., 1994) in repro2 switched to variants of the extended ECOM2 model (Arnold et al., 2015) in repro3. These improvements can be expected to reduce spurious draconitic signals (Ray et al., 2008) in the repro3 station position and geocenter coordinate time series. More details on the orbit modeling strategies of the individual repro3 ACs can be found in Zajdel et al. (2023).

Time-variable gravity field

Contrary to repro2, all ACs have used time-variable gravity field models in repro3. The expected impact on terrestrial frame solutions is sub-millimetric (Amiri et al., 2016).

2.2 Combination methodology and products

The daily combinations of the AC repro3 terrestrial frame solutions follow essentially the same strategy as the one used in repro2, detailed in Rebischung et al. (2016) and summarized below, with only a few changes marked in italic below. One notable change is that the variance component estimator used to weigh the AC solutions in the combinations is applied iteratively until convergence rather than just once. Another change is that the terrestrial scale is handled in a similar way as the apparent geocenter coordinates: the scale information contained in the AC solutions is made explicit in scale parameters, which represent the difference between the observed (Galileo-based) scale and the scale of the IGSR3 reference frame, and that are then combined into an explicit scale parameter. However, unlike for the combined geocenter coordinates that are kept as separate parameters in the final combined solutions, this combined scale information is eventually brought back into the combined station positions. Station positions in the daily repro3 combined solutions are thus aligned in origin (and orientation) to the IGSR3 reference frame, but have their scale based on the igsR3.atx satellite z-PCOs.

Each daily combination starts with a preprocessing of the daily AC solutions, which consists of:

- removing the constraints applied by the ACs to their solutions;
- re-parameterizing the unconstrained AC normal equations to make apparent geocenter coordinates *as well as scale factors* with respect to the IGSR3 reference frame explicit;
- eliminating from the unconstrained AC normal equations stations with incorrect metadata reported in the AC SINEX files. *The policy adopted in repro3 was to confront metadata reported in the AC SINEX files with site logs collected from different sources and systematically reject stations with either an incorrect antenna type, an eccentricity error larger than 1 mm in either East, North or Up, or an antenna orientation error larger than* 10°. *This led in particular to reject all stations with*

antenna mis-orientations larger than 10° *from the solutions of COD, NGS and WHU, as these ACs did not rotate phase center corrections and reported* 0° *or no mis-orientations in their SINEX files;*

- inverting the re-parameterized AC normal equations under no-net-rotation, translation *nor scale* (NNR+NNT+*NNS*) constraints with respect to IGSR3. These constraints are needed to define the frame of the re-parameterized station positions, but they do not overwrite the original origin *and scale* information of the AC solutions, which is kept in the separate geocenter coordinates *and scale* parameters;
- assigning a priori variance factors to the preprocessed AC solutions in the same way as in repro2.

Then, the preprocessed AC solutions are iteratively combined in a least-squares adjustment in which combined station positions, combined ERPs, combined geocenter coordinates *and a combined scale parameter – representing the difference between the combined observed (Galileo-based) scale and the scale of the IGSR3 reference frame –* are estimated together with 7-parameter Helmert transformations between each AC solution and the combined solution. At each iteration, the AC solutions are screened for possible outliers, i.e., stations with largely different positions than in the combined solution. *Namely, any AC station position estimate with a normalized residual larger than 5 in either East, North or Up is considered as an outlier and rejected from the corresponding AC solution. At each iteration, the weights of the AC solutions in the combination are also updated.* The same unbiased variance component estimator is used as in repro2, *but it is applied iteratively instead of only once at the last iteration.* Iterations are performed until no more outliers are detected *and the AC weights have converged to better than* 10^{-3} *in a relative sense.*

The daily combined solution is at this step obtained using NNR+NNT+*NNS* constraints with respect to IGSR3, via the well-distributed sub-network of IGSR3 core stations[7], and includes combined geocenter coordinates *and a combined scale factor with respect to IGSR3. In a last post-processing step, the combined normal equation is re-inverted with NNR+NNT constraints only while fixing the combined scale parameter to 0. By doing so, the scale of the combined station positions is enforced to match the combined observed scale. In other words, the combined scale information (based on the igsR3.atx satellite z-PCOs) is brought back into the combined station positions.*

In addition to the daily combined solutions, weekly combined repro3 solutions are also provided. The weekly combined repro3 solutions are obtained by iteratively stacking the seven daily combined solutions of the week. The daily solutions are given a uniform a priori variance factor of 1, and a single common corrective variance factor is estimated. After each iteration, station position estimates with

[7] ftp://igs-rf.ign.fr/pub/IGSR3/IGSR3_core.txt

normalized residuals larger than 5 are removed from the corresponding daily solutions. Iterations are performed until no such outlier remains.

Table 2 lists the products available from the repro3 terrestrial frame combinations, whose names follow the new IGS long product file name convention[8]. At present, those products are publicly available at the following URLs, where *wwww* stands for the 4-character GPS week number:

- https://cddis.nasa.gov/archive/gnss/products/wwww/repro3
- ftp://igs.ign.fr/pub/igs/products/wwww/repro3
- ftp://igs-rf.ign.fr/pub/repro3/wwww

Note that the opportunity of repro3 was taken to change the style of the traditional SINEX combination residual and summary files and to make them additionally available in machine-readable YAML[9] format.

Table 2 Products from the repro3 terrestrial frame combinations. *yyyy* stands for the 4-character year and *doy* for the 3-character day-of-year (first day of the week in the case of weekly files).

File name	Description
IGS1R03SNX_*yyyydoy*0000_01D_01D_SOL.SNX	Daily combined SINEX solution
IGS1R03SNX_*yyyydoy*0000_01D_01D_CRD.SNX	Daily combined SINEX solution without covariance matrix
IGS1R03SNX_*yyyydoy*0000_01D_01D_RES.RES	Daily combination residuals
IGS1R03SNX_*yyyydoy*0000_01D_01D_RES.YML	Daily combination residuals in YAML format
IGS1R03SNX_*yyyydoy*0000_07D_07D_SOL.SNX	Weekly combined SINEX solution
IGS1R03SNX_*yyyydoy*0000_07D_07D_CRD.SNX	Weekly combined SINEX solution without covariance matrix
IGS1R03SNX_*yyyydoy*0000_07D_01D_ERP.ERP	Weekly ERP file
IGS1R03SNX_*yyyydoy*0000_07D_07D_SUM.SUM	Weekly combination summary
IGS1R03SNX_*yyyydoy*0000_07D_07D_SUM.YML	Weekly combination summary in YAML format

2.3 Combination results

2.3.1 Station network

The complete network of stations present in the repro3 combined solutions is shown in Figure 1. It includes 1905 stations in total, among which 1201 are out of the 1212 stations that had been proposed to ACs for inclusion in their reprocessing. This list of 1212 stations[10] includes all current and former IGS stations, selected GNSS stations co-located with other space geodetic techniques, as well as stations proposed by regional and national network representatives. Among the 704 other stations present in repro3, about 220 were selected and systematically processed by ULR for being co-located with tide gauges and having long, stable position time series. Most of the remaining stations were only processed occasionally by some single AC and therefore have short and/or sparse time series.

[8] https://files.igs.org/pub/resource/guidelines/Guidelines_For_Long_Product_Filenames_in_the_IGS_v2.0.pdf
[9] https://yaml.org/
[10] http://acc.igs.org/repro3/repro3_station_priority_list_060819.pdf

Compared to repro2, a larger number (1397) and fraction (73 %) of stations have time series with more than 1000 daily points in repro3. It should also be noted that the repro3 station position time series are generally more complete than in repro2. This is thanks to the effort made by most ACs to process the stations they selected as exhaustively as possible, i.e., whenever they had observations available.

Figure 2 shows the time evolution of the number of stations in the daily AC and combined repro3 solutions (note that stations excluded from AC solutions because of metadata errors or outlying residuals are not included in the counts). It clearly appears that ACs have processed daily station networks of significantly varying sizes, ranging from 80 stations for JPL to over 800 stations for TUG. This implies that many repro3 combined station position time series are actually based on position estimates from only one or two ACs.

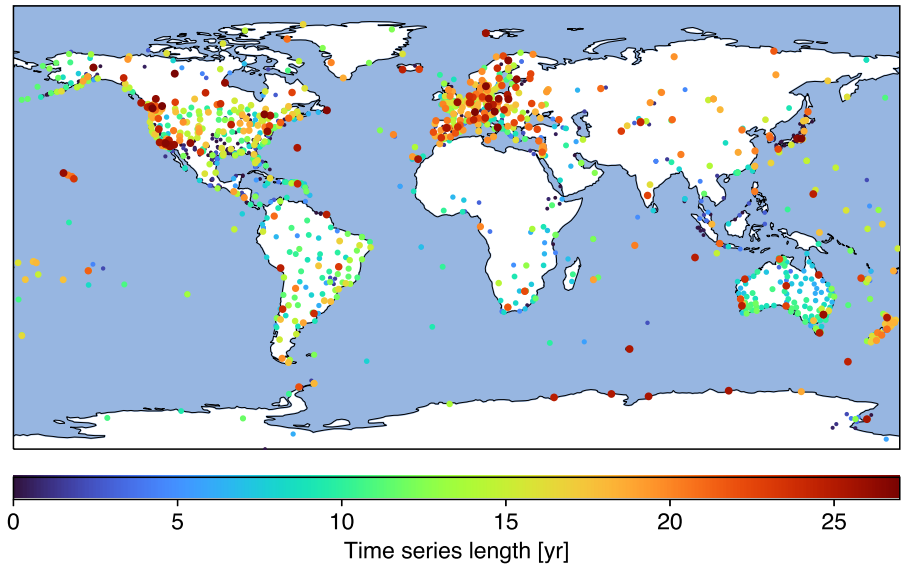

Fig. 1 repro3 station network. The sizes and colors of the dots indicate the lengths of the repro3 combined position time series.

2.3.2 AC weights

To assess the weights of the different ACs in the daily repro3 combinations, we extracted the formal errors of station position estimates from the AC solutions after they had been preprocessed and reweighted for the daily combinations. We then computed daily median formal errors for each AC and each East, North, Up component. Figure 3 shows smoothed time series of these median formal errors. They can be considered both as a measure of the level of agreement between the daily AC solutions and as a proxy for the AC weights in the daily combinations.

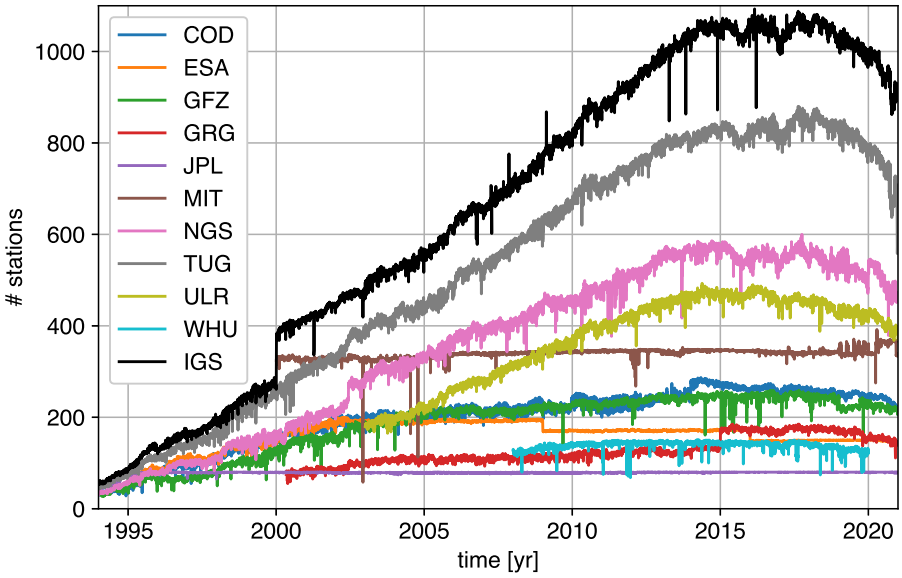

Fig. 2 Numbers of stations in daily AC and IGS combined repro3 solutions

Like in repro2, the overall level of agreement between AC solutions significantly improves with time until about 2005, along with the modernization of both the GPS constellation and the ground tracking network. After 2005, the overall level of agreement between ACs remains at a stable level. With only one exception (TUG), the adjusted median station position formal errors are then close to 1 mm in East and North and between 3 and 4 mm in Up for all ACs, which are similar levels as observed in repro2. A notable difference with repro2 is that, apart from TUG, all AC contributions to repro3 appear to be of very homogeneous quality. Consequently, while some AC contributions had been excluded from the repro2 combinations, no such exclusion was necessary in repro3.

In Figure 3, TUG clearly stands out from all other ACs. After 2005, the median station position formal errors in the re-weighted TUG solutions are about 1.4 – 1.5 times less than for the next "best" ACs, meaning that TUG gets about twice their weight in the daily combinations. It should be noted that the TUG orbits for the GPS and Galileo satellites were also observed to get the heaviest weights (lowest RMS) among the ACs in the repro3 orbit combinations (Zajdel et al., 2023). This naturally raises questions about the justification for this heavier weight.

Before delving into these questions, we would first like to recall some properties of the variance component estimator that was used to weigh the AC solutions in the daily repro3 combinations. Under the hypotheses that errors in the AC solutions are independent from one AC to the next, are normally distributed, have zero expectation and have their (co)variances well described by the covariance matrices provided in the AC SINEX files, up to unknown variance factors, then the variance component estimator we used is the best (i.e., minimum variance) unbiased quadratic estimator of

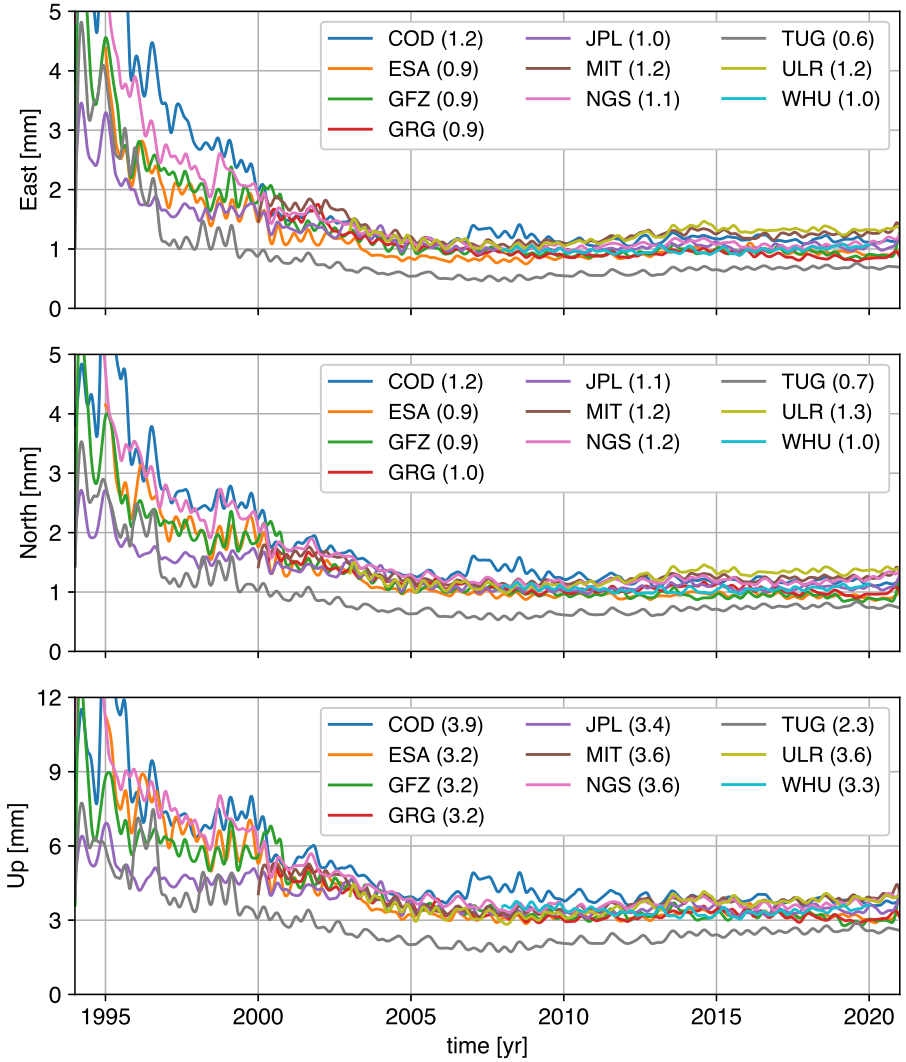

Fig. 3 Median formal errors of station positions in daily re-weighted AC solutions. All time series were smoothed by a Vondrák filter (Vondrák, 1969, 1977) with a cutoff frequency of 2.5 cpy. The numbers in the legends are the medians of the time series of daily median formal errors for the period after 2005.0, in mm.

these variance factors (Amiri-Simkooei, 2007). The unbiasedness property is the most important to the present discussion. It implies that the estimator accounts for the level of redundancy between AC solutions. The estimator is, in particular, not biased by the various numbers of stations in the AC solutions or by the fact that some stations are processed by a single AC. Stations processed by a single AC can actually be shown not to contribute to the variance factor estimates. It is very likely, however, that the hypotheses cited above do not perfectly hold in practice, so that the unbiasedness property may not hold either. Yet, these hypotheses are most commonly made when combining geodetic solutions, so that the variance component estimator we used can nevertheless be considered as the best available under the most common working hypotheses.

TUG performance

To investigate whether the heavier weight of TUG in the daily repro3 combinations is justified, we compared station position time series extracted from the different AC repro3 solutions. These comparisons, fully described in Section 5, reveal that the TUG station position time series are indeed less scattered (i.e., more precise) than those of any other AC. Besides, if AC variance factors are estimated on a station and component basis using a generalized three-cornered hat approach, rather than on a daily basis in the daily combinations, then the AC weights in the daily combinations are largely confirmed, and the predominance of TUG appears justified (Section S1).

The next logical question is: what analysis-specific factors can explain the higher precision of the TUG station position estimates? It should first be noted that the TUG solutions were obtained with the latest-generation geodetic analysis software package GROOPS (Mayer-Gürr et al., 2021). An important characteristic of the TUG analysis is that it is based on the raw observation approach (Strasser et al., 2019), i.e., no differencing nor linear combinations of the GNSS observables are made. Yet, only L1 and L2 observations were available in the period during which the predominance of TUG is most marked in the repro3 combinations (∼2000–2009; see Figure 3). Since, in the case of only two frequencies, the raw observation approach is equivalent to the use of zero-differenced, ionosphere-free linear combinations (Strasser et al., 2019), this predominance cannot be attributed to the raw observation approach. It must also be mentioned that TUG used similar standards in their repro3 analysis as the other ACs in most aspects of GNSS observation modeling, in particular for satellite orbits, so that the predominance of their solutions is likely not fully attributable to refined models of the GNSS observations. One notable exception is the modeling of tropospheric delays affecting GNSS observations, for which TUG used a priori zenith delays and mapping functions from the refined VMF3 model (Landskron and Böhm, 2017), while other ACs used either the previous VMF1 model (Böhm et al., 2006b), or models that only reflect seasonal fits to the ECMWF (European Centre for Medium-Range Weather Forecasts) weather data, namely GPT2 (Lagler et al., 2013) and/or GMF (Böhm et al., 2006a). As will be shown in Section 5, the use of VMF3 by TUG contributes to the lower scatter of their station position time series, once corrected for non-tidal atmospheric loading, but mostly in the vertical component, and to an extent that cannot fully explain the predominance of TUG in the repro3 combinations. Another possible complementary explanation to this predominance could be the refined observation weighting scheme used by TUG (iterative station- and signal-specific variance component estimation with outliers automatically downweighted; Strasser et al., 2019; Strasser, 2022), but this hypothesis remains to be tested. At the moment, we are thus unable to provide a definitive explanation for the higher precision of the TUG station position estimates. We can only encourage further research into this question, as

it holds the potential to benefit not only other ACs and the IGS combined products but also users of GNSS station position time series.

2.3.3 Station position residuals

The station position residuals from the daily combinations are the differences between the AC and combined station position estimates, adjusted for 7-parameter Helmert transformations between the AC and combined solutions. As these combination residuals represent differences between daily AC station position estimates and their weighted mean, they do not include any Earth's surface deformation signal, nor the weighted mean of the AC errors. They should in particular not be confused with residuals obtained from the adjustment of trajectory models to station position time series, which will be analyzed in Section 5. The combination residuals analyzed in this section cannot be used to evaluate errors in the AC station position estimates in an absolute sense, but nevertheless provide useful information on the departures of particular AC solutions from the average AC results.

Time series of the weighted root mean squares (WRMS) of the AC station position residuals are shown in Figure S1. Their time evolution is generally similar to that of the median formal errors shown in Figure 3. However, some ACs (mainly TUG and ULR) have WRMS notably lower than their median formal errors. This is because, as discussed in Rebischung et al. (2016), WRMS of station position residuals are a biased measure of the precision of the AC solutions, and are, in particular, biased low by stations processed by a single AC. This is also why we discussed the weights and precisions of the AC solutions in Section 2.3.2 based on median formal errors rather than WRMS.

It is more instructive to examine station position residuals in the spectral domain. For that purpose, we computed average Lomb-Scargle periodograms (Scargle, 1982) of the station position residual time series for each AC and each East, North and Up component. Not all residual time series were considered in these periodograms. First, all data before 2000.0 were discarded due to their clearly larger scatter (see Figures 3 and S1). Then, all residual time series with less than 1000 daily points or more than half missing values were discarded. Finally, for every station, if residual time series from less than 5 ACs were remaining at this stage, then these series were discarded. This last selection criterion ensures that the average periodograms of the different ACs are based on a relatively common set of station position estimates, so that they are more comparable than if all stations (especially those observed by a single AC) had been used. Lomb-Scargle periodograms of the selected residual time series were then computed and averaged for each AC and each East, North and Up component, ensuring that for a given frequency f, only time series longer than $1/f$ contribute to the average power. For each AC, frequencies at which the average power was based on less than half of the available stations were discarded from

the periodograms. The average Lomb-Scargle periodograms thus obtained are shown by the colored lines in Figure 4 for the North component; Figures S2 and S3 for the East and Up components. Note that the power normalization used in these figures ensures that the levels of background noise (i.e., the background continuous parts of the spectra) are comparable amongst ACs, but not the amplitudes of periodic signals (i.e., the heights of the spectral peaks), which will be discussed separately in the following.

To facilitate the comparison of background noise levels amongst ACs, the averaged periodograms were smoothed by adjusting cubic splines (black lines in Figures 4, S2 and S3) by least-squares to the average periodograms. The adjustments were made iteratively in order to mitigate the impact of spectral peaks on the adjusted splines (at each iteration, powers at frequencies larger than 0.8 cpy and with normalized residuals larger than 3 were discarded). The splines adjusted to the average periodograms of the different ACs are shown on top of each other in Figure 5 for the North component; Figures S4 and S5 for the East and Up components.

Background noise

It appears from Figures 4–5 and S2–S5 that the average background noise in the AC residual station position time series is generally dominated by white noise (i.e., has flat power spectra) at high ($>\approx 100$ cpy) frequencies. An exception is JPL, whose residual spectra do not show such a flattening at high frequencies, a behavior explained by the fact that JPL provides overlapping 30 h solutions instead of strictly daily solutions, which has the effect of smoothing out the high-frequency white noise in JPL's station position time series (see Section 5.3). Another exception is COD, whose residual spectra start flattening at lower frequencies than the other ACs, and then rise moderately at the highest frequencies in North and Up, reaching higher power than all other ACs. Such a behavior was not observed with COD's repro2 residuals (Rebischung et al., 2016). It should be noted that, unlike in repro2, COD provided overlapping 3-day solutions for repro3, from which we recovered and used strictly daily station position estimates, but those were still based on 3-day orbital arcs. This specificity might influence the behavior of COD's residual spectra at high frequencies to an extent that remains to be understood.

After a progressive transition, the background noise in the AC station position residual time series is then dominated by colored noise at lower frequencies ($\approx 0.4-8$ cpy). The slopes of the spectra (i.e., the spectral indices of the noise) are relatively constant over this frequency range. Interestingly, these slopes are smaller (in absolute) than -1, the slope of flicker noise, which best describes the average colored noise in the loading-corrected repro3 combined station position time series (Section 4.5). The actual slopes of the spline fits in the $0.4-8$ cpy range are rather scattered around an average of about -0.8. This suggests that the flicker noise observed in GNSS station position time series may arise from

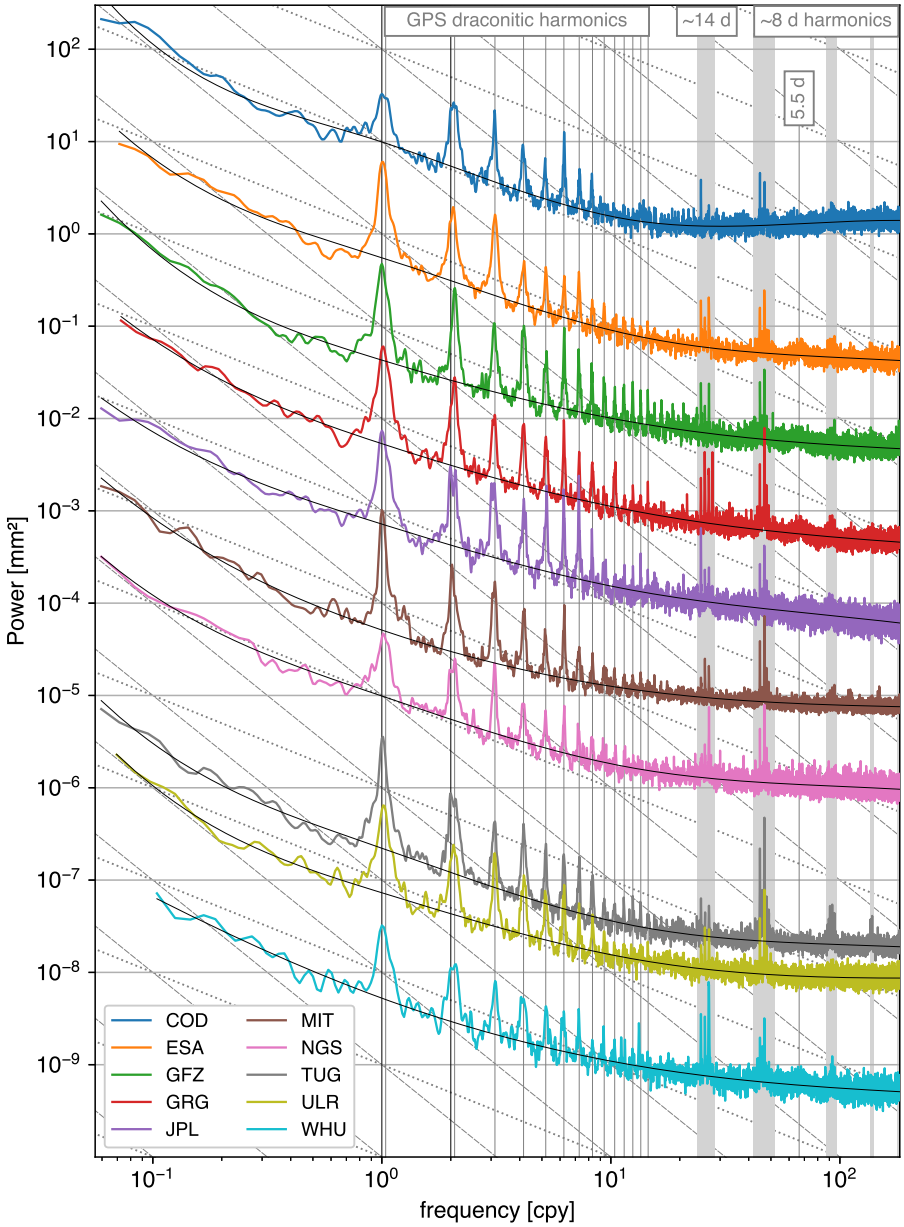

Fig. 4 *Colored lines:* average Lomb-Scargle periodograms of selected AC station position residual time series – North component – offset by powers of 10. *Black lines:* cubic spline fits to the average periodograms. The *black vertical lines* indicate the annual and semi-annual periods. The *gray vertical lines* indicate the first 14 harmonics of the GPS draconitic year and the 5.5 d period. The *gray vertical patches* span periods around 14 d and harmonics of 8 d. The *gray dotted lines* indicate the slope of flicker noise ($\propto 1/f$). The *gray dashed lines* indicate the slope of random walk ($\propto 1/f^2$).

somewhat different processes than the colored noise observed in the differences between AC station position estimates.

At even lower frequencies ($<\approx 0.2$ cpy), another transition occurs toward even more colored noise, with the slopes of the AC residual spectra getting closer to that of a random walk, i.e., -2. A possible explanation for this behavior could be the presence of offsets related to equipment changes in the AC residual time series, due to different responses of the AC processings to equipment-related errors (e.g.,

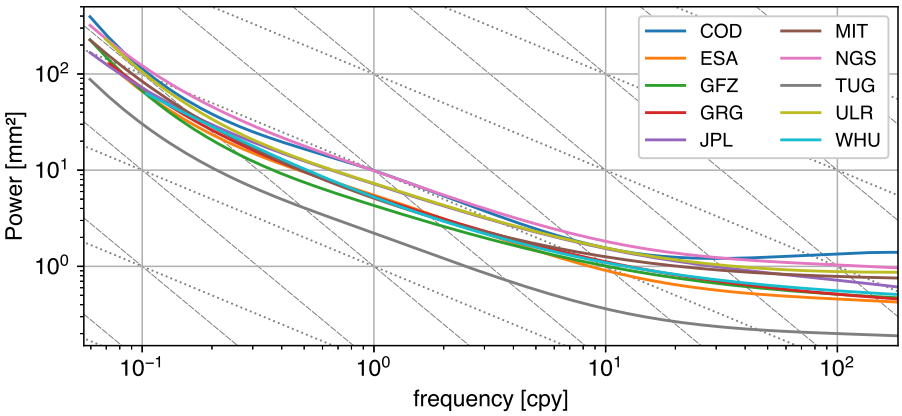

Fig. 5 *Colored lines:* splines adjusted to the average Lomb-Scargle periodograms of selected AC station position residual time series – North component. The *gray dotted lines* indicate the slope of flicker noise ($\propto 1/f$). The *gray dashed lines* indicate the slope of random walk ($\propto 1/f^2$).

errors in antenna phase center corrections, multipath). Such offsets are clearly visible in a few residual time series (see the example of station CAS1, Casey, Antarctica in Figure S6). But smaller offsets may be more generally present in the AC residual time series and mimic random walk (Williams, 2003).

Periodic variations

In addition to this increasingly colored background noise, distinct spectral peaks are clearly visible in Figures 4, S2 and S3. These peaks correspond to periodic signals in the AC station position residual time series. To facilitate the comparison of these spectral peaks amongst ACs, we computed another set of average periodograms, with each individual periodogram normalised by the number of points in the corresponding time series. This re-normalization allows the interpretation of spectral peak heights as squared amplitudes of periodic signals. However, the continuous parts of the spectra cannot be interpreted in terms of background noise levels anymore. Zooms on specific frequency ranges from these re-normalized average periodograms are shown in Figures S7–S9.

Figure S7 is a zoom on the $0.7 - 10$ cpy frequency range. In this band, spectral peaks covering harmonics of the annual and/or GPS draconitic frequencies are visible for all ACs and components, at least up to the eighth harmonic. Generally, these peaks exhibit more power at the annual frequency compared to the fundamental draconitic frequency, but larger power at the higher draconitic harmonics than at the higher annual harmonics. Apart from TUG, with lower spectral peaks as expected from their higher weight in the daily combinations, spectral peaks of other ACs are of comparable heights, with only two notable exceptions. First, the JPL spectral peaks stand out at the odd harmonics in East, and at almost all harmonics (especially the highest) in the North component. Given that draconitic variations in the repro3 combined station position time series are primarily attributed to mismodeling of GPS satellite orbits (Section 4.3), JPL's departure from the AC mean could be related to its unique

approach to solar radiation pressure modeling. While other ACs use either no or simple analytical (box-wing) a priori solar radiation pressure models, JPL uses the empirically derived GSPM models (GPS solar pressure model; Bar-Sever and Russ, 1997; Bar-Sever and Kuang, 2004; Sibois et al., 2014; Sakumura et al., 2017). Additionally, while the other ACs adjust different sets of constant and periodic empirical accelerations in the satellite-Sun DYB frames (Beutler et al., 1994; Arnold et al., 2015), JPL adjusts constant scaling factors to their a priori models, constant Y accelerations, and stochastic accelerations in the satellite XYZ frames. The second notable feature in Figure S7 is the unusually broad spectral peak surrounding the semi-annual and semi-draconitic frequencies in COD's East residuals. At present, we are unable to provide a plausible explanation for this observation.

Figure S8 focuses on fortnightly frequencies, revealing three main categories of spectral peaks. First, peaks centered on the alias period of the M_2 tide via daily sampling (24.74 cpy / 14.76 d) are visible in the horizontal residuals of most ACs as well as in WHU's vertical residuals. Second, peaks centered on the alias period of the O_1 tide via daily sampling (25.74 cpy / 14.19 d) are visible for some ACs, predominantly in the North component. Third, peaks around periods of 13.6 – 13.7 d are visible for all ACs and all three components. These could be due to model errors for the M_f (26.74 cpy / 13.66 d) tide and the tidal wave with Doodson number 075, 565 (26.79 cpy / 13.63 d), as well as aliases of M_2 ($\approx$26.82 cpy / 13.62 d) and O_1 ($\approx$26.78 cpy / 13.64 d) tide model errors via the ground repeat period of the GPS satellites (Penna et al., 2007; Abraha et al., 2018). The spectral resolution achievable with the repro3 residual time series is sufficient to dismiss a dominant contribution of direct M_f errors except in the case of WHU's North residuals and GRG's horizontal residuals. On the other hand, it is not possible, based on Figure S8, to know which of direct 075, 565 errors or aliased O_1 or M_2 errors contribute more to the other $\approx$13.6 d peaks. Note finally the outstanding power of NGS's $\approx$13.6 d peaks in horizontal and of WHU's $\approx$13.6 d peaks in all three components, suggesting potential issues in the implementation of some tide models by these two ACs. In addition to these three main categories of peaks, GRG's horizontal residuals show two more spectral peaks at frequencies of 25.69 cpy (14.22 d) and 27.78 cpy (13.15 d), for which we could not identify any corresponding tidal frequency.

A zoom on $\approx$8 d periods of the average periodograms (Figure S9) reveals two main spectral peaks at frequencies of $\approx$44.76 cpy (8.16 d) and $\approx$46.82 cpy (7.80 d). Smaller peaks, regularly spaced in frequency with an interval corresponding to the GLONASS draconitic frequency, are also visible, mostly in the East component. Spectral peaks at the same periods are observed in the repro3 combined station position time series and likely explained by GLONASS orbit modeling errors (Section 4.3). It is therefore plausible that the $\approx$8 d peaks observed here in the AC residual time series result from (a) only a subset of ACs having processed GLONASS observations and (b) different GLONASS orbit

modeling errors among those ACs. Note that these ≈8 d peaks are generally larger for ACs that either did not process or downweighted GLONASS observations (i.e., GRG, JPL, MIT, NGS, ULR), as these ACs form a weighted minority in the repro3 combinations.

Clusters of spectral peaks around periods of ≈4, ≈2.7 and ≈2 d are also visible in the averaged periodograms of the AC residual time series. We do not provide zooms for these frequency bands, as they present similar characteristics to the ≈8 d band, i.e., clusters of regularly spaced peaks separated by the GLONASS draconitic frequency, likely explained by GLONASS orbit modeling errors and more prominent for ACs that did not process or downweighted GLONASS observations.

Another feature visible in Figures 4 and S3 is the presence of bumps in the power spectra of the North and Up residuals of some ACs (ESA, GFZ, GRG and maybe WHU) centered on a ≈5.5 d period. Such broad ≈5.5 d bumps were first observed by Amiri-Simkooei (2013) and Ray et al. (2013) in the PPP station position time series provided by JPL (Heflin et al., 2020). They were also identified in the Up repro2 combination residuals of several ACs (EMR, ESA, GFZ, GRG – but not JPL; Rebischung et al., 2016). ≈5.5 d signals in GPS station position time series were investigated by Selle et al. (2014) and Fernandes et al. (2019) and found to be both station- and analysis-settings-dependent, but a precise explanatory mechanism yet remains to be discovered.

Let us finally mention some spectral peaks in the AC station position residual time series that do not fall in any of the previously mentioned frequency bands. Specifically, the Up residuals of MIT and ULR (both ACs using the GAMIT software[11]) show sharp spectral peaks at 39.99 cpy (9.13 d), which were previously observed in their repro2 residuals (Rebischung et al., 2016), but for which no explanation is known. A nearby (40.07 cpy / 9.12 d) but less pronounced peak is also visible in the Up residuals of WHU. Still within the ≈9 d band, another spectral peak is observed in the North and Up residuals of NGS at 37.99 cpy (9.61 d), which corresponds to the aliasing period of the N_2 tide via daily sampling, suggesting a potential tide model implementation error at NGS.

2.3.4 ERP residuals

Statistics of the AC ERP residuals from the daily repro3 combinations are provided in the first part of Table 3. The corresponding time series are shown in Figures S10–S14 and their amplitude spectra in Figures S15–S19. Note that, similar to the IGS repro2 and operational SINEX combinations, the AC LOD estimates have been corrected by 10-day moving averages with respect to the IERS Bulletin A[12] before the repro3 combinations. Figures S14 and S19 actually show the sums of these moving averages and of the LOD combination residuals. Table 3 contains statistics for both parts separately.

[11] http://geoweb.mit.edu/gg/
[12] https://maia.usno.navy.mil/products/bulletin-a

A consequence of this calibration of the AC LOD estimates with respect to Bulletin A is that the low-frequency component (< 0.1 cpd) of the IGS combined LOD estimates are conventionally copied from Bulletin A, hence should not be considered as "observed" in subsequent uses of the IGS products.

Biases and dispersion

The WRMS values of the AC ERP residuals provided in Table 3 measure the overall level of agreement between the AC ERP estimates. With the exceptions of NGS and TUG, the WRMS of the pole coordinate residuals fall in the range $15 - 30$ µas. There is thus a clear improvement of the level of agreement between AC pole coordinates compared to repro2, where the WRMS of the AC pole coordinate residuals mostly fell in the range $25-40$ µas (Rebischung et al., 2016). A similar improvement can be observed for pole rate residuals, with typical WRMS of $100 - 150$ µas/d in repro3 compared to $150 - 200$ µas/d in repro2, as well as for LOD residuals, with typical WRMS of $5 - 10$ µs in repro3 compared to $8 - 20$ µs in repro2. TUG clearly dominates the repro3 combined ERPs, as explained by both the heavier weight of TUG in the daily repro3 combinations (Section 2.3.2) and the larger station network processed by TUG (Figure 2; see explanation in Rebischung et al. (2016)). Finally, Table 3 highlights a large average bias of the GFZ LOD estimates with respect to Bulletin A (≈ 70 µs) and the other ACs (≈ 80 µs). This bias arises from GFZ inadvertently accounting twice for the permanent tide in their repro3 analysis, by adding the time-independent contribution of solid Earth tides to the "zero tide" geopotential model GOCO06s model (Kvas et al., 2021), which already accounts for it. This constant bias has, however, no impact on the repro3 combinations, as it was fully corrected in the preceding calibration of the GFZ LOD estimates with respect to Bulletin A.

Periodic variations

The amplitude spectra of the AC ERP residuals shown in Figures S15–S19 exhibit a variety of spectral peaks, either common to most ACs, or specific to some of them. Spectral peaks at the annual and semi-annual frequencies and at harmonics of the GPS draconitic year, often up to the fifteenth or even higher, are ubiquitous. Although their amplitudes vary amongst ACs, none of these peaks clearly stands out, except maybe the annual peak in the GRG Y-pole rate residuals and the semi-annual peaks in the ESA and JPL LOD residuals.

Spectral peaks at the alias frequencies of the M_2 (24.74 cpy / 14.76 d) and O_1 (25.74 cpy / 14.19 d) tides via daily sampling are also visible for most ACs and ERPs. Note that for pole coordinates and pole rates, the 14.76 and 14.19 d peaks of GFZ and NGS clearly stand out. Furthermore, the NGS pole coordinate and pole rate residuals exhibit several other unique fortnightly spectral lines. Still in the fortnightly band, the LOD residuals of all ACs show clear peaks at precisely the M_f tide frequency

Table 3 Statistics of AC ERP, geocenter and terrestrial scale residuals from the repro3 combinations. The geocenter and scale offsets are given at epoch 2010.0.

	COD	ESA	GFZ	GRG	JPL	MIT	NGS	TUG	ULR	WHU
X-pole WRMS [µas]	26	18	28	24	24	21	45	10	27	16
Y-pole WRMS [µas]	28	19	26	13	24	18	39	8	22	17
X-pole rate WRMS [µas/d]	109	125	149	78	129	131	176	47	170	78
Y-pole rate WRMS [µas/d]	112	108	214	165	120	114	184	61	132	92
LOD average bias [µs]	−3	−13	69	−7	−15	−13	−4	−7	−14	−19
LOD 10 d bias WRMS [µs]	5	13	10	5	19	7	8	5	8	8
LOD residual WRMS [µs]	7	8	10	5	13	4	6	3	5	9
X-geocenter offset [mm]	1.7	−0.3	0.5	3.1	−0.1	−1.2	−0.4	−0.4	2.0	0.3
Y-geocenter offset [mm]	1.8	0.5	0.1	−0.9	0.4	0.3	−0.9	−0.4	0.4	0.3
Z-geocenter offset [mm]	−1.9	0.3	−2.1	−0.9	1.2	1.5	2.3	−0.2	0.9	1.7
X-geocenter rate [mm/yr]	0.02	−0.18	−0.03	−0.09	0.13	0.12	−0.11	−0.01	0.12	−0.11
Y-geocenter rate [mm/yr]	−0.30	0.05	0.03	0.00	−0.16	−0.00	0.19	0.04	−0.05	−0.30
Z-geocenter rate [mm/yr]	−0.11	0.34	−0.10	−0.58	−0.25	−0.02	−0.23	0.01	0.03	0.08
X-geocenter WRMS [mm]	3.1	2.6	2.9	3.0	3.9	2.0	3.2	1.2	2.8	2.2
Y-geocenter WRMS [mm]	3.0	2.5	2.9	3.4	4.0	2.1	3.5	1.2	2.9	2.7
Z-geocenter WRMS [mm]	6.1	6.1	11.1	8.8	6.8	5.4	9.8	4.5	7.1	9.6
scale offset [mm]	0.8	0.9	−0.5	0.4	0.1	−0.2	−0.3	−0.3	0.2	0.2
scale rate [mm/yr]	0.03	0.02	0.00	−0.03	−0.02	−0.05	−0.00	0.03	−0.09	0.02
scale WRMS [mm]	0.7	0.5	0.6	0.5	0.5	0.5	0.6	0.4	0.6	0.5

(26.74 cpy / 13.66 d), as well as smaller peaks at the alias frequency of the O_{O_1} tide via daily sampling (27.74 cpy / 13.17 d). Small 13.17 d peaks are also discernible in the Y-pole residuals of GRG and the X-pole rate residuals of COD and JPL.

Another series of spectral peaks emerges at periods around 9 d. In this frequency band, the GFZ and NGS pole coordinate and pole rate residuals exhibit unique clusters of spectral peaks. Apart from this characteristic, small spectral peaks at the alias frequency of the N_2 tide via daily sampling (37.99 cpy / 9.61 d) can be seen in the pole rate residuals of several ACs. The LOD residuals of most ACs show a clear peak at 39.99 cpy (9.13 d), for which we do not have an explanation. The LOD residuals of NGS finally show another clear peak at the alias frequency of the Q_1 tide via daily sampling (38.99 cpy / 9.37 d).

In the weekly band, besides other unique clusters of spectral peaks in the pole coordinates and pole rate residuals of GFZ and NGS, two more tidal aliases via daily sampling can be observed in the pole rate residuals of most ACs and in the pole coordinate residuals of some ACs: μ_2 (49.47 cpy / 7.38 d) and $2N_2$ (51.29 cpy / 7.13 d). The MIT X-pole residuals show an additional unique spectral peak at 52.18 cpy (7.00 d), as well as peaks at the next two weekly harmonics, which are likely explained by constraints applied by MIT on a weekly basis to their empirical orbit parameters.

Two last frequency bands are marked in Figures S15–S19, around periods of 5.7 and 4.7 d. In these bands, unique clusters of spectral peaks are observed in the pole coordinate and pole rate residuals of GFZ and NGS, like in the ≈14, ≈9 and ≈7 d bands. Such clusters were absent from the GFZ ERP residuals in repro2. A possible explanation for these unique clusters could therefore be errors in the

implementation of the new sub-daily ERP tide model from Desai and Sibois (2016) by GFZ and NGS. Such errors may also explain the outstanding 14.76 and 14.19 d peaks in the GFZ and NGS pole coordinate and pole rate residuals, as well as the generally larger semi-annual peaks compared to other ACs.

2.3.5 Geocenter residuals

The AC geocenter residuals discussed in this section provide insights into the *differences* between the coordinates of the Earth's center of mass in the IGSR3 frame, as determined by the different ACs. Time series of *absolute* geocenter coordinates derived from the different AC contributions to repro3 will later be analyzed in Section 3.2.

The second part of Table 3 presents results from linear fits to the time series of AC geocenter residuals from the daily repro3 combinations. The reported offsets and rates provide an evaluation of the agreement between the origins and origin rates of the long-term frames realized by the solutions of each AC. Similar to repro2, they mostly fall in the ranges ±3 mm and ±0.3 mm/yr for all three components. The only notable exception is for the Z component of GRG's apparent geocenter, which shows a clear −0.6 mm/yr drift with respect to the AC mean (see Figure S22). The WRMS reported in Table 3 measure the inter-AC level of agreement on non-linear geocenter motion. Except for TUG, they are scattered in the range $2-4$ mm for the X and Y components and in the range $6-11$ mm for the Z component, similar to the ranges observed in repro2. For the same reasons as with ERPs, TUG dominates the repro3 combined geocenter coordinates.

The full time series of AC geocenter residuals are shown in Figures S20–S22 and their amplitude spectra in Figures S23–S25. Spectral peaks are observed at the annual and semi-annual frequencies and at harmonics of the GPS draconitic year, particularly pronounced in the Z component. The amplitudes of those peaks vary amongst ACs, but none clearly stands out, except the annual peak in the GRG Y-geocenter residuals. In the fortnightly band, 14.76 d lines (M_2 alias via daily sampling) are visible for most ACs in the Z component, 13.62 d lines (M_2 alias via ground repeat period of the GPS satellites) are visible for some ACs in the X and Y components. The GRG geocenter residuals also show unique 13.66 d peaks (M_f tide) in all three components. Finally, like for station positions, several GLONASS-related ≈8 d lines are visible in the geocenter residuals of most ACs, mostly in X and Y.

2.3.6 Terrestrial scale residuals

The last part of Table 3 provides results from linear fits to the time series of AC terrestrial scale residuals from the daily repro3 combinations. These time series are illustrated in Figure 6, where they are smoothed and superimposed in order to better emphasize the long-term (dis)agreement between

the terrestrial scales realized by the solutions of the different ACs. The full time series of AC terrestrial scale residuals are shown in Figure S26, and their amplitude spectra in Figure S27, where spectral peaks can be observed at the annual and semi-annual frequencies and at harmonics of the GPS draconitic year. None of these peaks particularly stands out, and no other peaks are clearly visible.

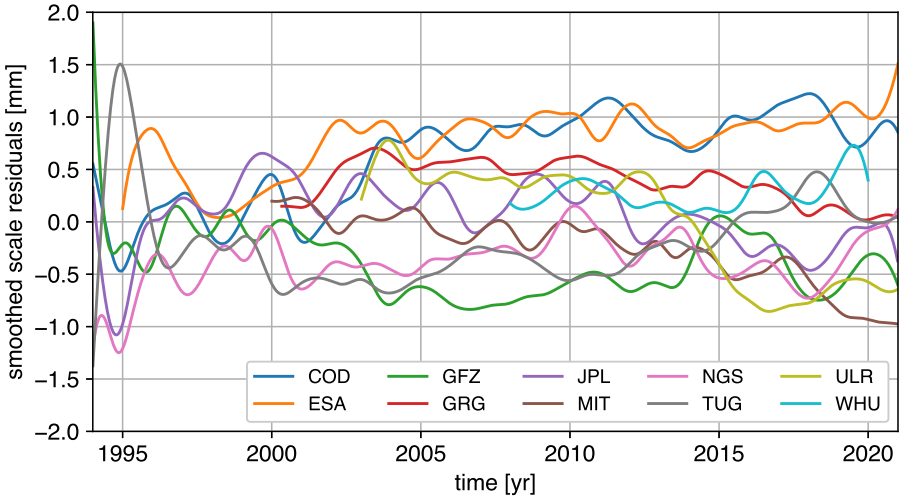

Fig. 6 AC terrestrial scale residual time series, smoothed by a Vondrák filter with a cutoff frequency of 0.5 cpy

As illustrated in Figure 6 and supported by the offsets reported in Table 3, the terrestrial scales realized by the different AC solutions agree within ±1 mm on the long term. With the exception of ULR, the estimated inter-AC scale rates are within ±0.05 mm/yr. The WRMS of the non-linear parts of the inter-AC scale differences are all about 0.5 mm. These values are comparable to the ones obtained in repro2 and indicate an excellent agreement between the terrestrial scales realized by the different AC solutions. Another observation from Figures 6 and S26 is that the progressive inclusion of additional GNSS (i.e., GLONASS and/or Galileo) by some ACs has generally no visible impact on the inter-AC scale offsets. The only notable exceptions are the inclusion of Galileo by GFZ on 2013-12-21 and by MIT on 2017-01-01, which may be responsible for small offsets in their scale residual time series of about +0.5 mm and −0.5 mm, respectively. Overall, the scales implied by the three GNSS included in repro3 appear quite consistent with each other. In other words, the GPS and GLONASS satellite z-PCOs in igsR3.atx have successfully been made consistent with the calibrated Galileo satellite z-PCOs published by GSC.

3 Analysis of repro3 combined polar motion, geocenter and scale

This section provides a brief analysis and evaluation of the global geodetic parameters in the daily repro3 combined solutions, namely polar motion (Section 3.1), geocenter coordinates (Section 3.2) and terrestrial scale (Section 3.3).

3.1 Combined polar motion

External evaluation of GNSS polar motion estimates is difficult given their higher precision compared to any other polar motion measurements. An error budget for the long-term accuracy of the IGS polar motion estimates was nevertheless drawn up by Ray et al. (2017), concluding to a probable $25-30$ µas overall accuracy. We will not repeat this assessment here, but only focus on a particular aspect of the repro3 polar motion estimates: the impact of adopting the new sub-daily ERP tide model from Desai and Sibois (2016) in place of the current IERS model.

The evaluation of this impact does not require any external reference, but relies on a simple internal metric: midnight polar motion discontinuities. Every day, we propagate the pole coordinates estimated at noon to the epoch 24h00 of the day using the estimated pole rates. Similarly, we propagate the pole coordinates estimated at noon on the next day to the epoch 00h00 of the next day. We finally form the difference between both pole coordinate sets propagated at the day boundary, namely, midnight polar motion discontinuities. The long-period polar motion signals cancel in such differences, leaving only the aliased signatures of sub-daily effects and model errors (as well as long-period errors in the pole rate estimates). This makes polar motion discontinuities particularly well suited to investigate sub-daily ERP tide models, as demonstrated by Kouba (2003).

Figure 7 shows the amplitude spectra of time series of midnight polar motion discontinuities derived from the IGS repro2 solutions, complemented with the IGS operational solutions since February 2015 on one hand, and the IGS repro3 solutions on the other hand. The corresponding time series are shown in Figure S28. The vertical plain lines in Figure 7 indicate the tidal aliasing frequencies at which a clear spectral peak is seen in either set of polar motion discontinuities. At all these frequencies, the spectral amplitude is reduced from repro2 to repro3, pointing to smaller errors in the new sub-daily ERP tide model from Desai and Sibois (2016) compared to the current IERS model. The improvement is remarkable at the annual frequency (the aliasing frequency of both the K_1 and P_1 tides) as well as at the aliasing frequencies of the M_2 (24.74 cpy / 14.76 d), O_1 (25.74 cpy / 14.19 d) and Q_1 (38.99 cpy / 9.37 d) tides. Smaller peaks at the aliasing frequency of the O_{O_1} tide (27.74 cpy / 13.17 d) are also clearly reduced with the new model. It is worth noting that no clear M_2, Q_1 or O_{O_1} peaks persist

with the new model, while O_1 peaks persist in both X- and Y-pole discontinuities and an annual peak remains in the Y-pole discontinuities. Overall, the new sub-daily ERP tide model from Desai and Sibois (2016) appears superior to the current IERS model for all tides of which we can see trace in the IGS polar motion discontinuities. The only possible exception would be for the μ_2 tide, with an aliasing frequency of 49.47 cpy (7.38 d) at which a small peak might appear in the repro3 X-pole discontinuities, although it hardly stands out of the surrounding background noise.

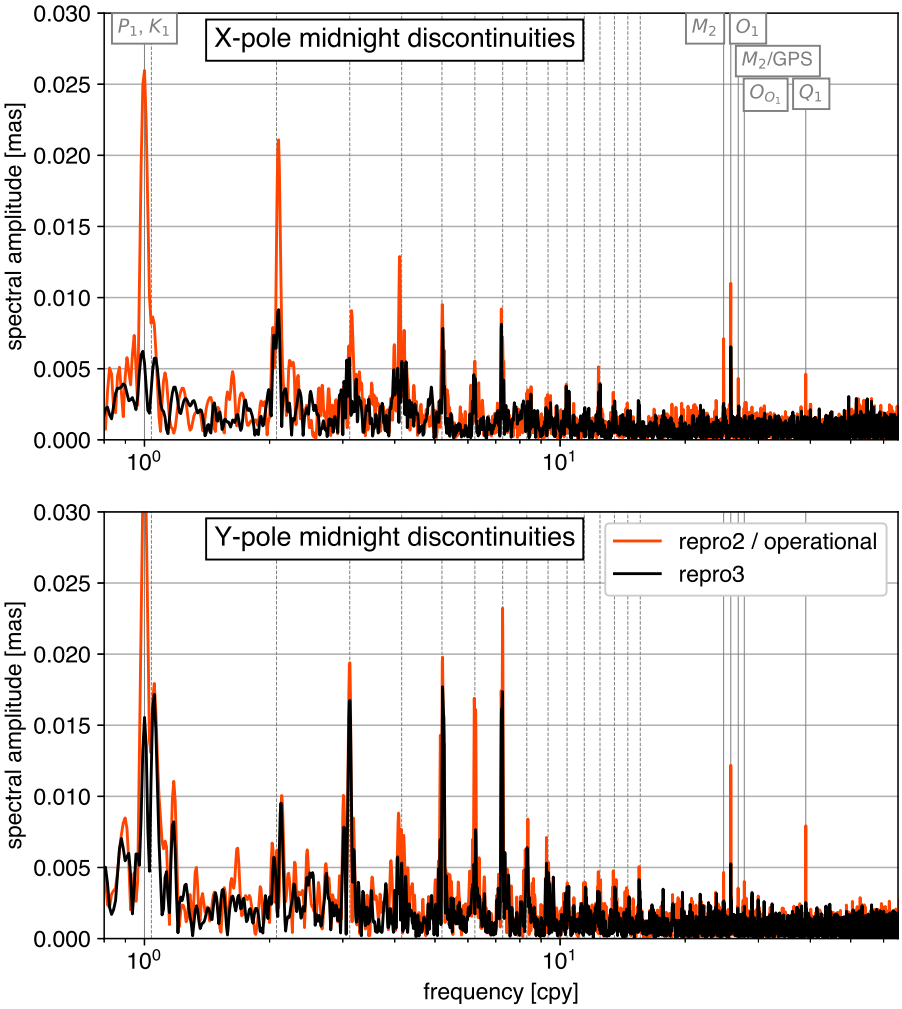

Fig. 7 Amplitude spectra of polar motion discontinuities from the IGS repro2 and operational combined solutions (*orange*) and from the IGS repro3 combined solutions (*black*). The *vertical dashed lines* indicate harmonics of the GPS draconitic year. The *vertical plain lines* indicate the aliasing frequencies of different tides via daily sampling and the aliasing frequency of the M_2 tide via the ground repeat period of the GPS constellation.

Other than tidal aliases, both sets of polar motion discontinuities show marked spectral peaks up to the fifteenth harmonic of the GPS draconitic year. These peaks could be explained by either long-period errors in the IGS pole rate estimates directly at the GPS draconitic harmonic frequencies, or by the aliasing of sub-daily orbit errors into polar motion discontinuities in a similar way as described

for station positions in Section 4.3. The amplitude spectra of the IGS pole rate estimates suggesta probable combination of both origins. Regardless, it is worthwhile noting that the draconitic peaks in polar motion discontinuities have been systematically reduced, some of them drastically, from repro2 to repro3, suggesting some improvement in the modeling of GPS satellite orbits.

3.2 Combined geocenter coordinates

Figure 8 shows the time series of repro3 combined geocenter coordinates, i.e., daily estimates of the coordinates of the Earth's center of mass in the IGSR3 reference frame, which inherits its origin from ITRF2014. The red lines, obtained with a low-pass filter, emphasize their ≈annual and inter-annual frequencies. The ITRF2020 annual geocenter motion model[13] is shown in cyan for comparison. This model was obtained from a weighted average of the ITRF2020 annual station motions, which are referred to the Earth's center of mass as sensed in the ITRF2020 Satellite Laser Ranging (SLR) input data (Altamimi et al., 2023). Figure S29 shows the amplitude spectra of the repro3 combined geocenter coordinate time series. Clear spectral peaks can be seen at the annual (and semi-annual in the X and Z components) frequencies, as expected from seasonal mass redistribution within the Earth's fluid envelopes. However, peaks around the GPS draconitic harmonics are also visible and especially marked in the Z component. The Z component additionally shows a strong spectral line at 24.74 cpy (14.76 d; alias of the M_2 tide via daily sampling), while the X component shows a smaller peak at 26.82 cpy (13.62 d; alias of the M_2 tide via the ground repeat period of the GPS satellites). Small peaks at GLONASS-related ≈8 d periods are discernible in all three components.

To extract the long-term trends and seasonal signals from the repro3 combined geocenter time series, we fit them with models composed of linear trends, annual and semi-annual sine waves, plus other sine waves at the first thirteen GPS draconitic harmonics, as well as at periods of 14.76 d, 13.62 d, 8.16 d and 7.80 d. Visual inspection of their power spectra suggests that the background noise of the repro3 combined geocenter time series could be well described by a white + power-law noise model in the X and Y components, and by a white + first-order autoregressive noise model in the Z component, as found by Ma et al. (2020) for the repro2 geocenter time series. However, adjusting such noise models to the repro3 geocenter time series is challenging due to the presence of particularly broad peaks in their spectra (see, e.g., the ≈annual peak in the Z component), which cannot be captured by simple steady sine waves (see a discussion of the same matter for station position time series in Section 4.4). Therefore, we do not attempt to adjust realistic noise models to the repro3 geocenter time series here, but instead use a simple variable white noise model. The adjusted linear trends and seasonal signals are reported in Table 4 with no uncertainties provided due to the lack of realistic noise models.

[13] https://itrf.ign.fr/ftp/pub/itrf/itrf2020/ITRF2020-geocenter-motion.dat

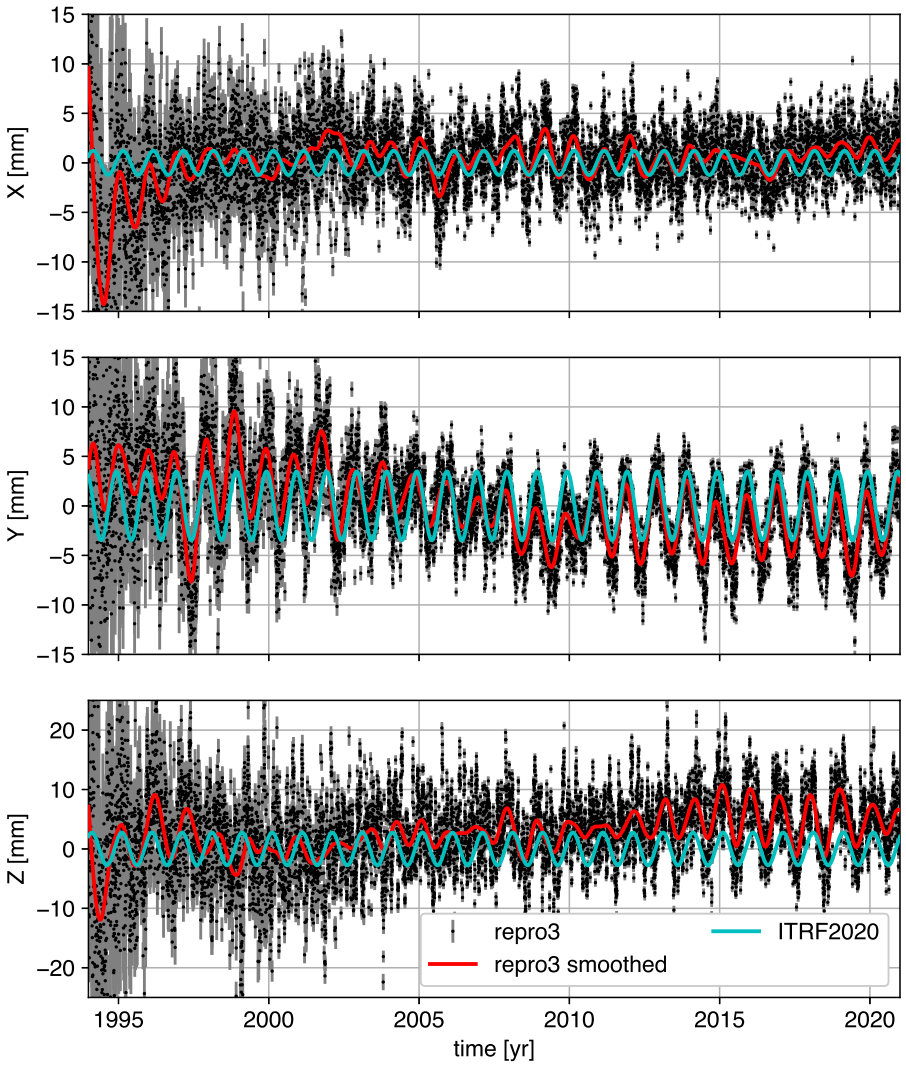

Fig. 8 repro3 combined geocenter coordinates (*black dots*) smoothed using a Vondrák filter with a cutoff frequency of 1.25 cpy (*red line*). The *cyan line* is the ITRF2020 annual geocenter motion model.

Long-term trends

The repro3 combined geocenter coordinates represent the coordinates of the Earth's center of mass (CM), as sensed by the average of the contributing ACs, with respect to the IGSR3 reference frame, which inherits its origin from ITRF2014. The linear trends adjusted to the repro3 combined geocenter time series and given in the first two lines of Table 4 thus represent the long-term drift between CM as sensed by the IGS ACs and the ITRF2014 origin, which linearly follows CM as sensed in the ITRF2014 SLR input data (Altamimi et al., 2016). The next two lines in Table 4 were obtained by adding the translation and translation rate estimated by Altamimi et al. (2023) between ITRF2014 and ITRF2020, and thus represent the long-term drift between CM as sensed by the IGS ACs and the ITRF2020 origin, which follows CM as sensed in the ITRF2020 SLR input data.

Table 4 Linear trends and seasonal signals adjusted to the repro3 combined geocenter time series. The linear trends are given with respect to both the IGSR3/ITRF2014 and the ITRF2020 origin. The ITRF2020 seasonal geocenter motion model is given for comparison. For seasonal signals, the same sign and phase conventions are used as for the ITRF2020 seasonal geocenter motion model.

	repro3			ITRF2020 seasonal geocenter motion model		
	X	Y	Z	X	Y	Z
Offset at 2010.0 wrt ITRF2014 [mm]	0.5	−0.9	3.2	–	–	–
Rate wrt ITRF2014 [mm/yr]	0.02	−0.19	0.21	–	–	–
Offset at 2010.0 wrt ITRF2020 [mm]	1.9	0.0	1.8	–	–	–
Rate wrt ITRF2020 [mm/yr]	0.02	−0.09	0.01	–	–	–
Annual amplitude [mm]	1.0	3.5	2.9	1.2 ± 0.2	3.5 ± 0.2	2.8 ± 0.3
Annual phase [deg]	−133	132	−168	-123 ± 7	153 ± 3	-140 ± 7
Semi-annual amplitude [mm]	0.6	0.3	1.3	0.5 ± 0.2	0.2 ± 0.2	1.2 ± 0.3
Semi-annual phase [deg]	83	23	32	107 ± 18	2 ± 39	31 ± 16

The drifts in Table 4 are smaller or commensurate to the 1-sigma uncertainties derived by Riddell et al. (2017) for the ITRF2014 origin rate. The offsets in Table 4 are similarly smaller or commensurate to the long-term precision of the ITRF2014 origin assessed by Altamimi et al. (2023) based on the transformation parameters to previous ITRF versions. Therefore, it can be concluded that the long-term CM sensed by the average of the repro3 ACs agrees with the long-term CM sensed by SLR, within the statistical uncertainty of the latter.

Seasonal variations

The seasonal amplitudes and phases in Table 4 constitute an estimate of seasonal geocenter motion based on the "network shift" approach (as opposed to the "degree-1" and "CM" approaches described by Lavallée et al. (2006)). Note that the estimate in Table 4 is based on the well-distributed sub-network of IGSR3 core stations used to align the daily repro3 combined solutions to the origin of the IGSR3 reference frame. GNSS geocenter motion estimates based on the network shift approach have been considered unreliable, especially in the Z direction, due to strong correlation with other parameters and contamination by orbit modeling errors (Rebischung et al., 2014; Meindl et al., 2013; Männel and Rothacher, 2017). The annual signals adjusted to the repro2 combined geocenter coordinates showed reasonable agreement with SLR estimates in the X and Y directions, but were out of phase with SLR in the Z direction, likely due to unsuccessful separation from draconitic errors (Rebischung et al., 2016; Ma et al., 2020). In Table 4, however, a remarkable agreement can be observed between the repro3 seasonal geocenter motion estimates and the SLR-based ITRF2020 seasonal geocenter motion model, not only at the annual, but also at the semi-annual frequency. All amplitude differences are less than 0.2 mm and within the formal errors of the ITRF2020 geocenter motion model. All phase differences are also rather small (less than 30 degrees, i.e., one month for the annual signals), although some are

significant compared to the formal errors of the ITRF2020 geocenter motion model, especially for the Y and Z annual components.

Although small but significant phase differences remain, the agreement with SLR on seasonal geocenter motion has remarkably improved from repro2 to repro3, particularly for the annual Z component. This improvement may be attributed to two complementary factors. First, the longer span of the repro3 geocenter motion time series may facilitate separation between real annual geocenter motion and draconitic errors. Second, the draconitic errors have been reduced from the repro2 to the repro3 geocenter motion time series, especially in the Z component and at the first draconitic harmonic (Figure S29). This might, in turn, be explained by improvements in the modeling of GPS satellite orbits from repro2 to repro3.

AC-specific seasonal variations

To investigate whether different solar radiation pressure modeling strategies could be related to different performances in retrieving seasonal geocenter motion, we examined geocenter motion time series derived from the individual AC contributions to repro3. The time series, obtained by summing the repro3 combined geocenter coordinates with the AC geocenter residuals, are shown in Figures S30–S32. In the X and Y components, the apparent annual variations in the AC geocenter motion time series are generally roughly in phase with the ITRF2020 model, like observed with repro2 data by Ma et al. (2020). In the Z component, some ACs appear alternately in phase and out of phase with the ITRF2020 model, which is consistent with the general behavior observed in repro2. Others (e.g., ESA, GFZ, MIT) appear to stay roughly in phase with the ITRF2020 model for the whole period after ≈2000, a behavior not observed in repro2, except possibly for ESA.

We modeled the AC geocenter time series in the same way as the repro3 combined geocenter time series. The estimated annual and semi-annual signals are displayed in Figures S33 and S34. In the X and Y components, the scatter of the estimated annual amplitudes and phases is of the same order as in repro2 (Ma et al., 2020). In the Z component, the estimated annual amplitudes are also similarly scattered as in repro2 (from ≈1 mm for COD and GRG up to 4.5 mm for ESA and MIT). However, the Z annual phases show much less scatter in repro3, with values within $-165 \pm 30°$ for all ACs , except GRG. In repro2, two groups of ACs with quasi-opposite Z annual phases could clearly be identified: those who used a priori solar radiation pressure models and those who did not (Ma et al., 2020). In repro3, there is no such clear distinction anymore, although several ACs still did not use a priori solar radiation pressure models. The more consistent Z annual phases in repro3 should therefore be attributed to other factors. One possibility is that all ACs not using a priori solar radiation pressure

models switched from variants of the Empirical CODE Orbit Model (ECOM) (Beutler et al., 1994) in repro2 to variants of ECOM2 (Arnold et al., 2015) in repro3.

Except for GRG, whose Y and Z annual signals stand out for some unknown reason, the seasonal signals extracted from the AC repro3 geocenter time series cannot be grouped into clear categories. It is thus difficult to draw any other conclusion than the fact that the switch to ECOM2 seems to have benefited the Z component of geocenter motion.

Note finally that, even if the agreement between the seasonal signals in the repro3 combined geocenter coordinates and the ITRF2020 seasonal geocenter motion model is remarkable (Table 4), the scatter of the AC-specific seasonal signals remains quite large (Figures S33–S34), especially for the X and Z annual components. Combining different subsets of AC solutions could, for instance, have led to combined seasonal geocenter motions much further away from the ITRF2020 model. Hence, although some improvement in the repro3 geocenter coordinates compared to repro2 is indisputable, it seems that the good agreement observed in Table 4 is actually partly due to chance. It would therefore be premature to conclude that the network shift approach finally yields reliable results with GNSS. On the contrary, the scatter in Figures S33–S34 and the persistence of prominent draconitic errors in the repro3 AC and combined geocenter time series are signs that progress is still needed.

3.3 Combined terrestrial scale

Figure 9 shows the time series of scale factors with respect to the IGSR3 reference frame, extracted from the daily repro3 combined solutions before the combined scale information was brought back into station coordinates (see Section 2.2). Its power spectrum is shown in Figure S35. There, annual and semi-annual peaks stand out, which are expected from the aliasing of the Earth's seasonal deformation into the scale parameters (Collilieux et al., 2012). Spectral peaks at the second and fourth GPS draconitic harmonics are also distinguishable.

Long-term trend

To extract the long-term trend from the time series of repro3 scale factors with respect to IGSR3, we fit it with a model composed of a linear trend, annual and semi-annual sine waves, plus other sine waves at the first four GPS draconitic harmonics. We simultaneously estimate the parameters of a variable white + power-law noise model using restricted maximum likelihood, an unbiased alternative to classical maximum likelihood (Harville, 1977; Gobron et al., 2022). The power spectrum of the adjusted noise model is shown by the red line in Figure S35. The estimated scale offset at epoch 2015.0 is -0.3 ± 0.2 mm. The estimated scale rate is $+0.01 \pm 0.02$ mm/yr. Since the scales of the repro3

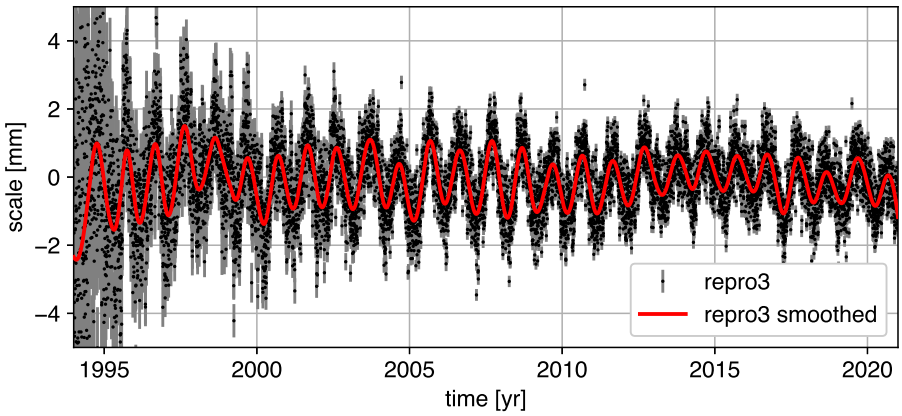

Fig. 9 Scale factors between repro3 combined solutions and IGSR3 (*black dots*) smoothed by a Vondrák filter with a cutoff frequency of 1.25 cpy (*red line*)

combined solutions and the IGSR3 reference frame both derive from the igsR3.atx satellite z-PCOs, these values are of little interest except as a consistency check.

It is more instructive to compare the scale of the repro3 combined solutions with that of ITRF2020, which is based on an average of selected contributions from the SLR and VLBI techniques. Taking the values estimated by Altamimi et al. (2023), but keeping the uncertainties obtained above with a variable white + power-law noise model, the scale offset at epoch 2015.0 and the scale rate between the repro3 combined solutions and ITRF2020 are respectively $+4.3 \pm 0.2$ mm and $+0.11 \pm 0.02$ mm/yr. From Altamimi et al. (2023)'s Figure 9, it is indeed clear that the scale of the repro3 combined solutions shows a significant bias and drift with respect to the (post-1997.75) SLR input solutions to ITRF2020. Given the scatter and non-linearity of the VLBI scale factor time series, it is less evident to conclude, from the same figure, to a significant scale bias and drift between repro3 and the VLBI contribution to ITRF2020. Note that the DTRF2020 analysis (Seitz et al., 2023) concludes to a good agreement (0.25 mm offset at epoch 2010.0; 0.025 mm/yr drift) between the repro3 scale and that of the VLBI contribution to ITRF2020. However, it confirms the existence of an offset and a drift between the repro3 scale and that of the SLR contribution to ITRF2020, although the offset is found to be smaller than in the ITRF2020 analysis (2.2 mm at epoch 2010.0 between the GNSS/VLBI average and SLR). As for the JTRF2020 analysis (Gross et al., 2023; Abbondanza et al., 2023), it concludes to a 4.9 mm offset at epoch 2010.0 and a 0.03 mm/yr drift between the repro3 scale and that of the SLR contribution to ITRF2020; 1.8 mm and -0.04 mm/yr with respect to VLBI. It therefore appears worth investigating possible reasons for systematic bias and drift that could affect the scale of the repro3 combined solutions.

Possible origins for the scale bias with respect to ITRF2020

The mean scale of the repro3 combined solutions is based on the average of the satellite z-PCOs in igsR3.atx, which are themselves based on the calibrated Galileo satellite z-PCOs published by GSC (Rebischung, 2020; Villiger, 2020). A first possible reason for a mean scale bias of the repro3 combined solutions could thus be a systematic error in the alignment of the GPS and GLONASS satellite z-PCOs to the calibrated Galileo satellite z-PCOs in igsR3.atx. This possibility was investigated by Glaser et al. (2021), who re-estimated the GPS and GLONASS satellite z-PCOs based on the calibrated Galileo satellite z-PCOs in a more rigorous way than was done in igsR3.atx, using the repro3 contributions from four ACs, and evaluated the terrestrial scale implied by their own satellite z-PCO estimates. The mean offsets between their AC-specific scale estimates and the repro3 combined solutions lie within only ± 1 mm, suggesting that the preliminary re-evaluation of the GPS and GLONASS satellite z-PCOs in igsR3.atx was quite accurate, and that the reason for the $+4.3$ mm scale bias between repro3 and ITRF2020 must be sought elsewhere. Another possible reason for a mean scale bias of the repro3 combined solutions would be that the actual in-orbit z-PCOs of the Galileo satellites differ from the pre-launch calibrated values by some mean amount. This possibility was investigated by different authors. For instance, Rebischung (2020) investigated the relative consistency of the calibrated Galileo satellite z-PCOs by estimating satellite-specific in-orbit z-PCOs while fixing their average to that of the calibrated z-PCOs. This exercise could obviously not evidence a mean bias in the calibrated Galileo satellite z-PCOs. Yet, the fact that the calibrated Galileo satellite z-PCOs were found to be consistent, relative to each other, with estimates of the actual in-orbit z-PCOs to within ± 3 cm for most satellites (i.e., ± 1.2 mm in terms of terrestrial scale, using the conversion ratio from Montenbruck et al. (2022)) suggests a certain reliability of the calibrated z-PCOs. More recently, Steigenberger and Montenbruck (2023) investigated the consistency of the calibrated Galileo satellite z-PCOs across different ionosphere-free linear combinations of the Galileo signals, and found inconsistencies that translate into terrestrial scale differences of up to 1.6 mm. While not negligible, these inconsistencies are not large enough to explain the whole $+4.3$ mm scale bias between repro3 and ITRF2020. Villiger et al. (2022) investigated the consistency of the calibrated Galileo satellite z-PCOs with the calibrated z-PCOs of the GPS Block III satellites provided by Lockheed Martin (2021), and found an excellent agreement, at better than 1 mm in terms of terrestrial scale. Finally, Huang et al. (2020) estimated the Galileo (and GPS) satellite z-PCOs in a joint GPS + Galileo + Swarm processing, based on the orbital dynamics of the three Swarm satellites. They found an average difference of -21 mm with the calibrated Galileo satellite z-PCOs – about 1 mm in terms of terrestrial scale. These different consistency checks suggest a certain confidence in the calibrated Galileo satellite z-PCOs, hence in

the repro3 scale, at a better level than the +4.3 mm scale bias between repro3 and ITRF2020. It is however not impossible that these internal consistency checks miss an overall bias of the GNSS-derived terrestrial scale. In any case, the reason(s) for the +4.3 mm scale bias between repro3 and ITRF2020 remain(s) to be uncovered.

Possible origins for the scale drift with respect to ITRF2020

Regarding the scale rate of the repro3 combined solutions, it relies on the assumption, made in igsR3.atx and any of the other IGS ANTEX files, that GNSS satellite z-PCOs are (on average) constant with time. Different physical factors, such as fuel consumption during maneuvers or antenna aging, could induce drifts of the GNSS satellite z-PCOs, consequently biasing the repro3 scale rate. Quantification of such possible drifts is, however, hardly available in the literature, except for the estimate by Degnan and Pavlis (1994) that the centers of mass of the GPS Block IIA satellites were expected to move by about 4.6 mm in the Z direction over their lifetimes, thus having a negligible impact on the GNSS-derived terrestrial scale rate. A more empirical approach to assessing the long-term stability of the GPS satellite z-PCOs was followed by Collilieux and Schmid (2013), who estimated satellite-specific z-PCO trends while relying on the ITRF2008 scale rate. They found a scatter of about 5 mm/yr across GPS satellites, i.e., of about 0.25 mm/yr in terms of terrestrial scale rate. A similar exercise was recently repeated by Rebischung (2023a), who reached a slightly lower scatter (about 3.5 mm/yr across GNSS satellites; 0.18 mm/yr in terms of terrestrial scale rate). This scatter remains larger than the +0.11 mm/yr scale rate difference between repro3 and ITRF2020, but it represents the scatter of the scale rate estimates that would be obtained by assuming each individual satellite z-PCO constant with time separately. This assumption is likely more accurate when considering the average of the GNSS satellite z-PCOs. However, we do not know how to quantify this accuracy, except by comparing the GNSS-based scale rate with estimates from other space geodetic techniques, bearing in mind that the latter might also be biased. Like for the scale bias, the reason(s) for the +0.11 mm/yr scale rate difference between repro3 and ITRF2020 remain(s) to be uncovered.

4 Analysis of repro3 combined station position time series

After the publication of the daily repro3 combined solutions, we conducted a detailed analysis of the repro3 station position time series as part of the ITRF2020 preparation. As usual with GNSS station position time series, the first step, described in Section 4.1, was the identification of offsets in the time series. During this process, we also developed models for the post-seismic displacements recorded by certain stations. We then confronted the repro3 station position time series corrected for offsets and

post-seismic deformation with two different non-tidal loading models (Section 4.2), before analyzing their spectral content (Section 4.3), modeling the various periodic variations they contain (Section 4.4), and finally analyzing their noise content (Section 4.5).

4.1 Offset identification and post-seismic deformation modeling

To identify the offsets and model the post-seismic displacements contained in the repro3 station position time series, we followed a two-step procedure. A manual iterative approach was used at first to specify post-seismic deformation models and identify a list of potential offsets. Comprehensive trajectory and stochastic models were then adjusted to the time series, so that the statistical significance of the potential offsets could be assessed. The potential offsets found to be insignificant were eventually discarded.

In the initial manual step, we started by fitting to each of the 1460 repro3 time series with more than 700 daily station position estimates a trajectory model consisting of a linear trend, an annual sine wave and a semi-annual sine wave. Upon visual inspection of the adjustment residuals, the trajectory model was then iteratively improved, when needed, by adding position offsets, velocity changes and exponential and/or logarithmic functions describing post-seismic deformation. To help identify offsets and relate them to known events, we used as ancillary data the equipment changes recorded in the station log files, as well as a list of co-seismic displacements predicted using the approach of Métivier et al. (2014). Note that velocity changes were not added with every position offset, but only when judged visually necessary. In the case of visible post-seismic deformation, we systematically tried to model it using either an exponential or a logarithmic function, and selected the function that yielded residuals with the lowest WRMS. In cases where a single exponential or logarithmic function was not enough to capture the post-seismic deformation consecutive to a given earthquake, a second exponential or logarithmic function was added to the trajectory model, selected with the same criterion as the first function. Note that position offsets and velocity changes were always added simultaneously to the three East, North and Up components of the trajectory model. On the other hand, functions describing post-seismic deformation were selected and added separately for each component. Also note that during this first step, the trajectory models were adjusted assuming variable white noise only in the series, and that daily position estimates with normalized residuals larger than 5 along any East, North or Up component were iteratively rejected.

Figure 10 shows an example of a trajectory model obtained at this stage of the repro3 time series analysis, namely for the East component of station ASPA (Pago Pago, American Samoa). In addition to a mean linear trend, an annual sine wave and a semi-annual sine wave, the trajectory model

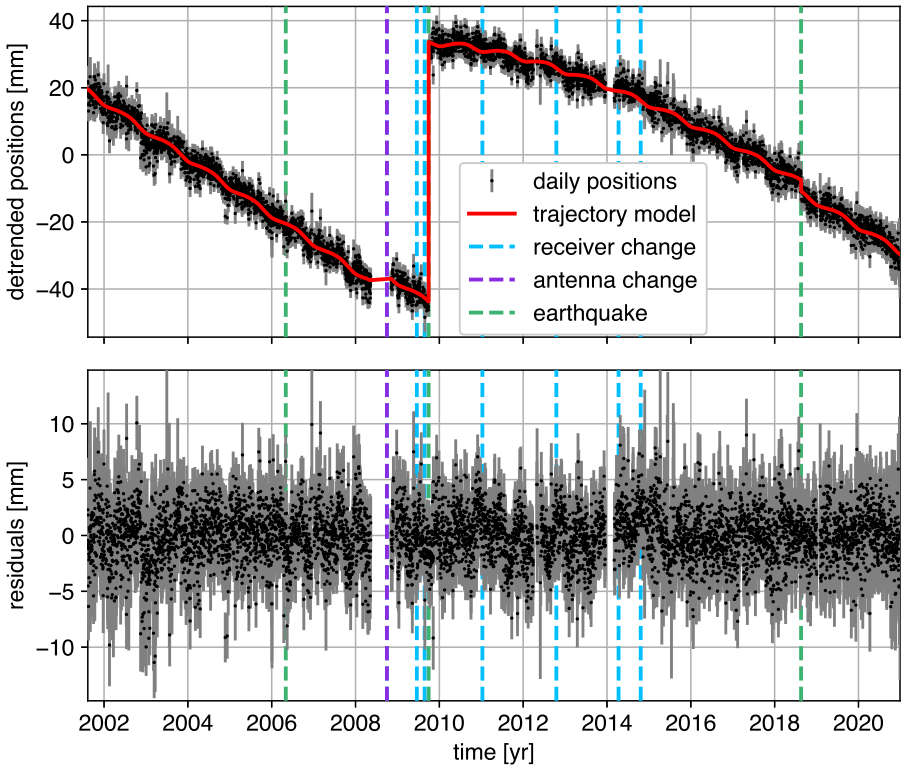

Fig. 10 *Top*: East component of the detrended repro3 position time series of station ASPA, Pago Pago, American Samoa (*black dots*) and adjusted trajectory model (*red line*). *Bottom*: residuals from the trajectory model (*black dots*). The *vertical light blue, violet and green dashed lines* respectively indicate receiver changes at the station, antenna changes at the station, and earthquakes predicted to have caused co-seismic displacements larger than 1 mm at the station based on Métivier et al. (2014)'s approach.

includes, in this case, three position offsets coinciding with the 2008 antenna change, the 2009 M_w 8.1 Samoa earthquake and the 2018 M_w 8.2 Fiji earthquake, one velocity change coinciding with the 2009 earthquake, and one exponential function describing post-seismic deformation consecutive to the same earthquake.

As mentioned above, the trajectory models were adjusted assuming variable white noise only during this first step. Consequently, the statistical significance of the offsets and velocity changes could not be realistically assessed. The following subsections describe how the trajectory and stochastic models of the series were refined to account for the presence of time-correlated noise in the series, as well as the presence of non-seasonal (e.g., draconitic) periodic variations. Based on those enhanced models, realistic formal errors could be computed for the manually detected position offsets and velocity changes. Some of them were found to be statistically insignificant (i.e., with magnitudes smaller than their formal errors) and were removed from the trajectory models. The time series analysis described in the rest of Section 4 was then repeated based on this final, cleaned set of position offsets and velocity changes. All the following results are those from this final analysis.

A total of 3054 position offsets were identified in the 1460 analyzed repro3 station position time series, corresponding to an average recurrence rate of one offset every 6.3 years. About half (1526) of these offsets were related to equipment changes, among which mostly antenna changes (1361) and more rarely receiver changes (159) or other changes (6). Nearly one quarter of the offsets resulted from earthquakes (699) or other geophysical events (7). The remaining 822 position offsets have unknown origins.

The complete list of position offsets and velocity changes identified in this analysis can be found in the IGS discontinuity list available at ftp://igs-rf.ign.fr/pub/discontinuities/soln.snx. This list is identical to the ITRF2020 discontinuity list for the common stations and time span, but it includes repro3 stations that are not part of ITRF2020, has been updated with post-2020 discontinuities and is regularly updated with new discontinuities. The complete set of post-seismic deformation models adjusted during this analysis is available at ftp://igs-rf.ign.fr/pub/PSD/psd_IGS.snx. These models are identical to the ITRF2020 post-seismic deformation models for the common stations, but also cover repro3 stations that are not part of ITRF2020.

4.2 Confrontation with non-tidal loading models

To evaluate the amount of variability in the repro3 station position time series that can be explained and corrected by non-tidal loading models, we used two such models. The first one was provided as the IERS Global Geophysical Fluids Center (GGFC) contribution to ITRF2020 (Boy, 2021). It is based on atmospheric loads from the ERA5 reanalysis (Hersbach et al., 2020), the TUGO-m oceanic response to ERA5 surface pressure and winds (Toulouse Unstructured Grid Ocean model; an update on Carrère and Lyard, 2003), and hydrological loads over the continents (soil moisture and snow) from ERA5. The second model is provided by the Earth System Modeling group at GeoForschungsZentrum (ESMGFZ; Dill and Dobslaw, 2013). It is based on atmospheric loads from the ERA-Interim reanalysis (Dee et al., 2011) and ECMWF (European Centre for Medium-Range Weather Forecasts) operational data since October 2019, oceanic loads from the MPIOM circulation model (Jungclaus et al., 2013) and hydrological loads over the continents from the LSDM model (Dill, 2008). We use the station displacements predicted by both loading models in the Center of Figure (CF) frame, since the repro3 combined solutions were aligned to the origin of the IGSR3 reference frame which, like the ITRF2014 origin, reflects CM on the long-term, but CF at sub-secular time scales (Dong et al., 2003).

Impact on seasonal amplitudes and non-seasonal scatter

We correct the 1460 studied repro3 station position time series for loading displacements predicted by either model, and adjust the trajectory models defined in Section 4.1 to the loading-corrected time

series. We then quantify the impact of the loading corrections at the (semi-)annual frequency with the reductions in the amplitudes of the adjusted (semi-)annual signals, from the uncorrected to the corrected series. We also quantify the impact of the loading corrections at non-seasonal frequencies with the reductions of the WRMS of the residuals from the trajectory model adjustments. To separate the contributions of the atmospheric, oceanic and hydrological loads, we do not only quantify the impact of the total loading corrections, but also of each contribution separately. Mean reductions in annual amplitudes, semi-annual amplitudes and non-seasonal scatter achieved with different loading corrections are provided in Table 5. Maps and histograms of the reductions can be found in Figures S36–S59.

Table 5 Impact of loading corrections on the amplitudes of annual signals, the amplitudes of semi-annual signals, and the scatter of non-seasonal variations (WRMS of residuals from the trajectory models) in the repro3 station position time series. The leftmost data column provides mean amplitudes / WRMS in the uncorrected series. The four other data columns indicate by how much these mean amplitudes / WRMS are reduced with different loading corrections (either atmospheric-only, oceanic-only, hydrological-only or the sum of all three contributions; either from GGFC or ESMGFZ) applied to the series. The percentages in parentheses are the relative reductions of the mean amplitudes and WRMS.

			Mean in uncorrected series [mm]	Reduction in mean achieved with loading corrections [mm]: atmospheric	oceanic	hydrological	total
Annual amplitude	GGFC	E	0.88	0.08 (9.6%)	0.02 (2.0%)	0.07 (8.2%)	0.15 (17.2%)
		N	1.10	0.04 (4.0%)	−0.01 (−1.1%)	0.18 (16.8%)	0.23 (20.7%)
		H	3.51	0.45 (12.9%)	0.08 (2.3%)	1.10 (31.5%)	1.70 (48.4%)
	ESMGFZ	E	0.88	0.09 (10.5%)	0.02 (2.6%)	0.09 (10.4%)	0.20 (23.2%)
		N	1.10	0.05 (4.8%)	0.00 (0.0%)	0.23 (20.7%)	0.31 (27.9%)
		H	3.51	0.43 (12.3%)	0.22 (6.3%)	1.18 (33.6%)	1.98 (56.3%)
Semi-annual amplitude	GGFC	E	0.32	0.01 (3.4%)	−0.00 (−0.3%)	−0.01 (−2.6%)	0.00 (0.3%)
		N	0.36	0.03 (7.9%)	−0.00 (−0.7%)	0.02 (5.8%)	0.04 (11.3%)
		H	0.90	0.08 (9.4%)	0.01 (1.3%)	0.05 (5.4%)	0.14 (15.1%)
	ESMGFZ	E	0.32	0.01 (3.6%)	−0.00 (−0.6%)	−0.01 (−1.6%)	0.01 (1.5%)
		N	0.36	0.03 (8.3%)	−0.01 (−2.3%)	0.02 (6.7%)	0.05 (12.5%)
		H	0.90	0.08 (9.4%)	0.03 (3.3%)	0.05 (5.8%)	0.16 (18.3%)
WRMS of residuals	GGFC	E	1.39	0.04 (3.2%)	0.02 (1.4%)	0.01 (0.4%)	0.07 (4.9%)
		N	1.37	0.05 (3.5%)	0.02 (1.2%)	0.01 (0.4%)	0.07 (5.4%)
		H	4.61	0.67 (14.5%)	0.19 (4.1%)	0.09 (2.0%)	0.93 (20.2%)
	ESMGFZ	E	1.39	0.04 (3.2%)	0.01 (0.9%)	0.00 (0.0%)	0.06 (4.2%)
		N	1.37	0.05 (3.5%)	0.01 (1.0%)	−0.00 (−0.1%)	0.07 (4.8%)
		H	4.61	0.67 (14.5%)	0.12 (2.7%)	0.07 (1.5%)	0.89 (19.4%)

Regarding atmospheric loading corrections, it can first be noted that the reductions in seasonal amplitudes and non-seasonal scatter achieved with either loading model are practically the same. This is unsurprising as both models use atmospheric loads from ECMWF reanalyses. The reductions in seasonal amplitudes achieved with atmospheric loading corrections are positive on average, but modest – less than 0.1 mm (10%) on average, except for the reductions in vertical annual amplitudes, which reach 0.45 mm (12.9%) on average with the GGFC model. The positive reductions in seasonal amplitudes are, in fact, confined to particular geographic regions (Figures S36–S39), which vary with

the annual harmonic and component considered. Atmospheric loading corrections also reduce the scatter of non-seasonal variations in more than 90% of the repro3 station position time series, but to a modest average extent again – by about 0.05 mm (3.5%) in horizontal, 0.67 mm (14.5%) in vertical. As observed by Mémin et al. (2020) and Gobron et al. (2021), these reductions in non-seasonal scatter are largest at high latitudes, where they can locally exceed 2 mm (50%) in vertical (Figures S40–S41).

Oceanic loading corrections have a negligible overall impact on seasonal amplitudes in the repro3 station position time series (Figures S42–S45). The only histogram of reductions noticeably offset toward positive values is that of the reductions of vertical annual amplitudes achieved with the ESMGFZ oceanic loading corrections (Figure S43), which reach 0.22 mm (6.3%) on average. On the other hand, like the atmospheric ones, oceanic loading corrections reduce the scatter of non-seasonal variations in a clear majority of repro3 station position time series – more than 85% in the case of GGFC loading corrections. These reductions in non-seasonal scatter are larger with the GGFC than the ESMGFZ corrections, but very modest on average – only about 0.02 mm (1.3%) in horizontal, 0.19 mm (4.1%) in vertical. As observed by Gobron et al. (2021), these reductions are mostly confined to certain coastal regions, particularly around the North Sea and Baltic Sea, and along the coasts of Alaska and Argentina (Figures S46–S47).

Hydrological loading corrections have the largest impact on annual amplitudes in the repro3 station position time series. The reductions in annual amplitudes are larger on average with the ESMGFZ hydrological loading corrections – possibly because the ESMGFZ hydrological loads include not only soil moisture and snow, like the GGFC ones, but also surface water, rivers and lakes – and reach about 0.1 mm (10%), 0.2 mm (20%) and 1.2 mm (34%) in East, North and Up, respectively. They are largest around the Amazon Basin, where hydrological loading has the largest effect (Dill and Dobslaw, 2013), but positive also over most other continental areas (Figures S48–S49). The impact of hydrological loading corrections on semi-annual amplitudes is much smaller. On average, it is close to zero in East, and reaches only 0.02 mm (6%) in North and 0.05 mm (6%) in Up (Figures S50–S51). Finally, the impact of hydrological loading corrections on the non-seasonal scatter in the repro3 series is practically zero (Figures S52–S53) as expected from the mostly seasonal nature of hydrological loading models. The largest achieved reduction is only 0.09 mm (2%), with the GGFC corrections, in vertical.

In total, non-tidal loading corrections account for around 20% of the horizontal annual signals in the repro3 series and around 50% in vertical. These numbers are of the same order as those obtained in other recent studies such as Chanard et al. (2018), Männel et al. (2019) or Niu et al. (2022). Note that the precise average reductions of annual amplitudes are larger with the ESMGFZ than with the GGFC loading corrections, likely thanks, in part, to additional hydrological loads being

accounted for. Yet, large fractions of the annual signals in the repro3 series remain after loading corrections, particularly in horizontal. These unaccounted annual variations comprise, to some extent, missing contributions in the loading models, thermoelastic deformation of the ground and the GNSS monuments, as well as poroelastic deformation. But a large part also consists of spurious seasonal variations in the repro3 series caused by various systematic errors in GNSS observations and in their analysis, such as annual variations in multipath and antenna phase centers under environmental changes (snow and ice cover, soil moisture, vegetation growth), the aliasing of sub-daily tide model errors at the annual frequency, or tropospheric delay mismodeling. See discussion, quantification and references for these various contributions in Dong et al. (2002), Chanard et al. (2020) or Niu et al. (2022). The fractions of semi-annual signals in the repro3 series accounted for by the loading models are even smaller than for annual signals: practically 0% in East, about 12% in North, and up to 18% in Up with the ESMGFZ model. These numbers are close to those obtained by Niu et al. (2022). Contributors to the gap between the repro3 series and the loading models at the semi-annual frequency can be the same as at the annual frequency, with possibly an even larger contribution of GNSS errors. As for the non-seasonal scatter in the repro3 series, about 5% can be explained by the loading models in horizontal, 20% in vertical. There are to our knowledge no analogous global averages available in the literature, except for a 11.4% reduction in vertical, non-seasonal scatter obtained by Gobron et al. (2021) with atmospheric loading corrections only and the precise point positioning (PPP) time series provided by the Nevada Geodetic Laboratory (Blewitt et al., 2018). The corresponding number in Table 5 is somewhat larger (14.5%), likely due to the lower level of background noise in the repro3 series than in the NGL time series (see Section 5), and to the use of the refined VMF3 troposphere model by TUG, the dominant contributor to the repro3 series (see discussion in Section 5.2). The GGFC loading model leads to slightly larger average reductions of the non-seasonal scatter in all three components of the repro3 series than the ESMGFZ model. Besides, the GGFC loading corrections lead to positive reductions of non-seasonal scatter for practically all repro3 stations (more than 96% in all three components; see Figure S58), while the ESMGFZ loading corrections do actually increase the non-seasonal scatter in a certain number of repro3 series, quite significantly in a few cases (Figure S59). For the rest of the analysis of the repro3 station position time series presented in the following, in which the focus is mainly on non-seasonal variations, we will therefore choose the GGFC loading model, as it performs (slightly) better in correcting part of these variations.

Impact on power spectra

It is also instructive to look at the impact of loading corrections in the frequency domain. For that purpose, Figure 11 presents average Lomb-Scargle periodograms of the repro3 station position time

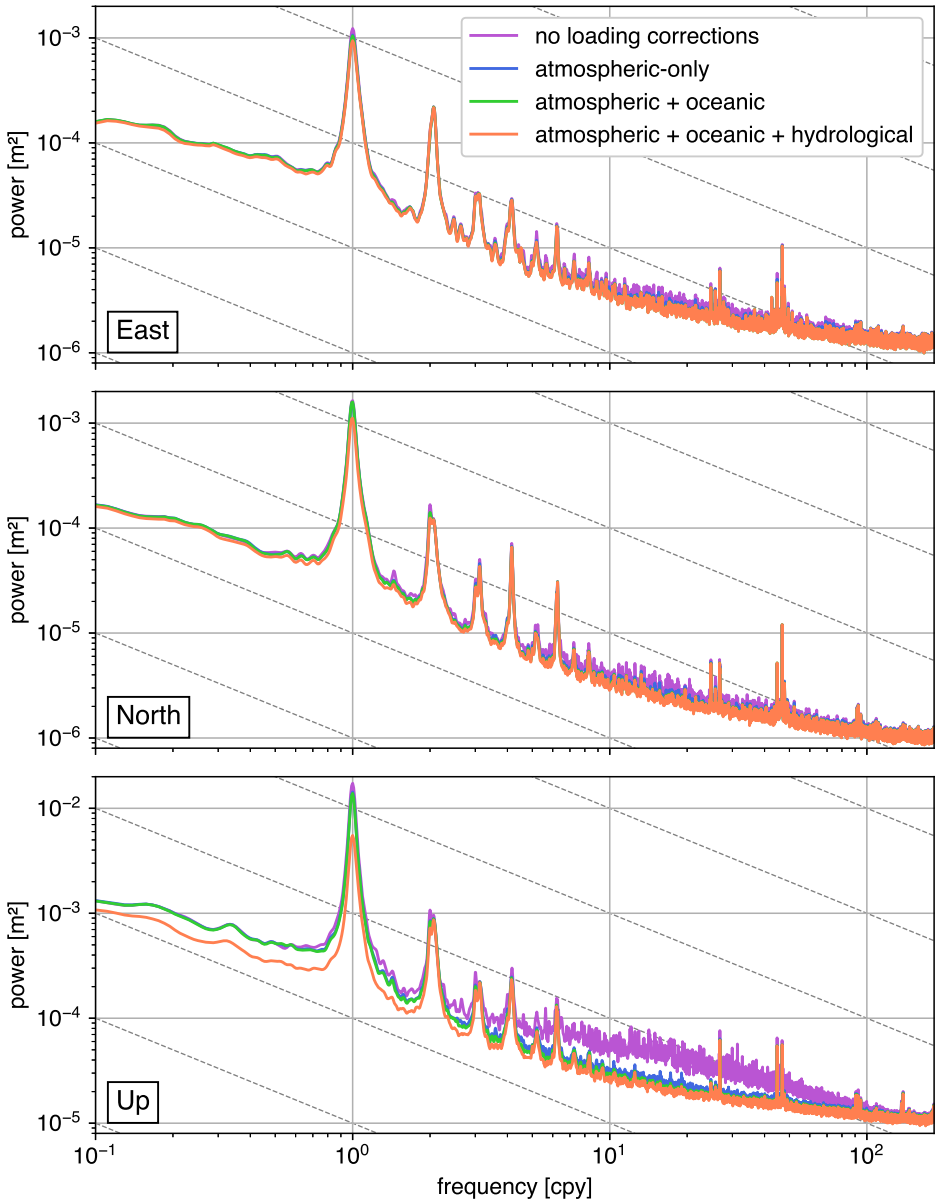

Fig. 11 Average Lomb-Scargle periodograms of residuals from trajectory models adjusted to the repro3 station position time series corrected for various loading effects. In *purple*: no loading corrections applied. In *blue*: GGFC atmospheric loading corrections applied. In *cyan*: GGFC atmospheric and oceanic loading corrections applied. In *green*: GGFC atmospheric, oceanic and hydrological loading corrections applied. The *gray dotted lines* indicate the slope of flicker noise ($\propto 1/f$).

series with various loading corrections applied. These average periodograms are actually those of the residuals from the trajectory models described above into which the estimated annual and semi-annual variations were restored, i.e., of the repro3 station position time series corrected for trends, offsets, post-seismic displacements, outliers – and various loading contributions. Not all of the 1460 analyzed station position time series were used in the average periodograms, but only the 1361 stations with at least 1000 daily data points and less than half missing values over their observation span. Besides, only time series spanning longer than $1/f$ contribute to the average periodograms at a given frequency f.

In Figure 11, the impact of loading corrections is most visible in the vertical component. Atmospheric loading corrections noticeably reduce the average power in the repro3 station height time series over a wide range of frequencies, roughly from 1 to 100 cpy, with the largest impact found around monthly periods. Still in the vertical component, oceanic loading corrections contribute to a further slight reduction of the average power from about 2 to 50 cpy. Hydrological loading corrections finally contribute to another very slight power reduction from about fortnightly to ter-annual periods, but have a much clearer impact at longer periods, from ter-annual up to decadal. As observed by Gobron et al. (2021), the overall shape (spectral peaks excluded) of the average periodogram of the repro3 station height time series uncorrected for loading displacements does not match the shape of the power spectrum of a white + flicker noise process, commonly employed to describe the noise in GNSS station position time series. Hence, as discussed by Gobron et al. (2021), adjusting white + flicker noise models to the repro3 station height time series uncorrected for loading displacements would yield biased noise parameter estimates. In both horizontal components, the impact of loading corrections on the average periodograms is much less pronounced. Only a slight power reduction attributable to atmospheric loading corrections is visible at frequencies from about 5 to 80 cpy.

4.3 Spectral analysis

This section discusses the different features visible in the average periodograms of the repro3 station position time series corrected for trends, offsets, post-seismic displacements, loading displacements and outliers, i.e., of the green curves in Figure 11. While the focus in Figure 11 was on the impact of loading corrections, Figure 12 presents the same average periodograms again, but with a focus on the different features discussed in the following, namely the overall shapes (spectral peaks excluded) of the average periodograms, and all visible spectral peaks.

Background noise

Regarding the overall shapes of the average periodograms first, they can be well described by functions of the form $a + b/f$ (black curves in Figure 12), i.e., by the power spectra of white + flicker noise processes, at least down to about 0.2 cpy. This is consistent with the outcomes from many previous studies which concluded that the stochastic variations in GNSS station position time series are well described by a combination of white noise and flicker noise (e.g., Zhang et al., 1997; Mao et al., 1999; Williams et al., 2004; Santamaría-Gómez et al., 2011). At frequencies lower than about 0.2 cpy, the average periodograms somewhat flatten and depart from the slope of a flicker noise spectrum. As discussed by Santamaría-Gómez and Ray (2021) and Gobron et al. (2022), this flattening at low frequencies is not an indication that the noise in the repro3 series actually departs from flicker noise at

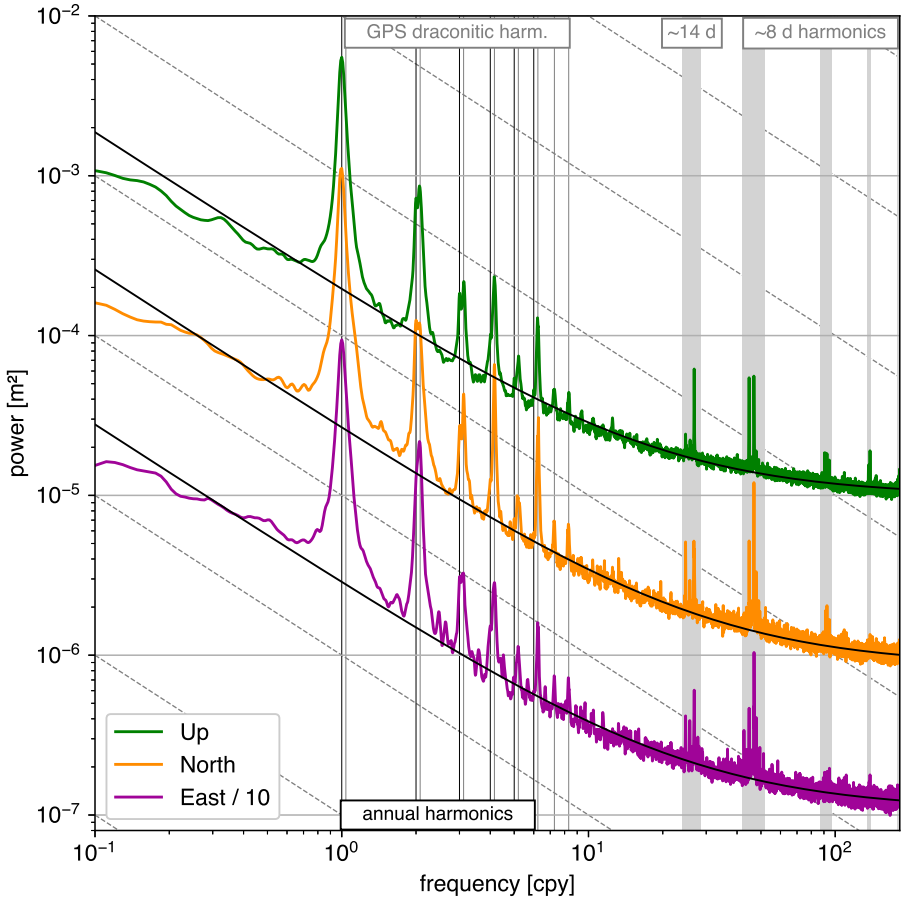

Fig. 12 Average Lomb-Scargle periodograms of residuals from trajectory models adjusted to loading-corrected repro3 station position time series. The average periodogram for the East component is offset by a factor 10 for clarity. The *black curves* represent least-squares fits of white + flicker noise power spectra, i.e., of functions of the form $a + b/f$, to the average periodograms. Note that to mitigate the impact of spectral peaks on the adjusted functions, points with normalized residuals larger than 3 were iteratively discarded from the least-squares fits. The *black vertical lines* indicate the first 6 harmonics of the annual frequency. The *gray vertical lines* indicate the first 8 harmonics of the GPS draconitic year. The *gray vertical patches* span periods around 14 d and harmonics of 8 d. The *gray dotted lines* indicate the slope of flicker noise ($\propto 1/f$).

low frequencies. It is rather due to the fact that part of the low frequencies of the noise is absorbed by the offsets of the trajectory models. In fact, the presence of recurring offsets in GNSS station position time series, with an average frequency of one offset every 6.3 years in the case of the repro3 series (see Section 4.1), makes it an ill-posed problem to characterize the noise content of the series below that offset recurrence frequency.

Periodic variations

On top of their white + flicker background shapes, the average periodograms in Figure 12 exhibit several clusters of spectral peaks which indicate the presence of various periodic variations in the repro3 series. A first cluster of spectral peaks covers the harmonics of both the annual frequency and the GPS draconitic frequency. While the first of these peaks is clearly dominated by annual variations, the next

ones are progressively more and more dominated by variations at the GPS draconitic harmonics. Peaks centered on the GPS draconitic harmonics are clearly visible up to the eighth harmonic, while secondary peaks or bumps are also discernable at the annual harmonics, up to the sixth. Possible contributors to the seasonal variations remaining in the loading-corrected repro3 series were already discussed in Section 4.2. As for the periodic variations at harmonics of the GPS draconitic year, first evidenced in GPS station position time series by Ray et al. (2008), several possible explanations have been proposed in the literature, including orbit mismodeling, the aliasing of tide model errors, or the aliasing of station-specific multipath errors (Ray et al., 2008; Tregoning and Watson, 2009; King and Watson, 2010). Strong, large-scale spatial correlations of the draconitic variations in GPS time series were later observed, suggesting orbit mismodeling as their main driver, without however excluding secondary contributions from station-specific errors (Ray et al., 2011; Amiri-Simkooei, 2013; Santamaría-Gómez et al., 2016). The spatial correlation analysis carried out by Niu et al. (2023) confirmed strong, large-scale correlations of the draconitic variations in the repro3 series, hence orbit mismodeling as their probable main origin.

A second cluster of spectral peaks is visible in Figure 12 around fortnightly periods. Figure S60 provides a zoom on this frequency range of the average periodograms. In this band, spectral peaks are first clearly visible at the alias periods of the M_2 (24.74 cpy / 14.76 d) and O_1 tides (25.74 cpy / 14.19 d) via daily sampling, which are most pronounced in the horizontal components. Such fortnightly variations have been reported in GNSS station position time series by several previous authors (Amiri-Simkooei et al., 2007; Amiri-Simkooei, 2013; Ray et al., 2013; Abraha et al., 2017). Yet, the question of which particular tide model errors are responsible for these mostly horizontal, spurious variations remains open (errors in the IERS model for solid Earth tides? for ocean tides? errors in the modeling of their impact on surface deformation? on geopotential variations? on the Earth's orientation?). In the average periodogram for the East component, adjacent to the O_1 tidal alias via daily sampling, stands a secondary spectral peak centered on a frequency of 25.80 cpy (14.16 d), previously unreported, and potentially attributable to the aliasing of modeling errors of the tidal wave with Doodson number $145,545$ via daily sampling. A last spectral peak corresponding to another tidal alias via daily sampling, also previously unreported, and also visible only in the East component, is that of the Oo_1 tide (27.74 cpy / 13.17 d). It barely stands out from other background oscillations in the average periodogram presented in Figure S60, but it actually becomes much higher and sharper in an average periodogram of only the longest repro3 series (not shown here). The last visible feature in the fortnightly band are broad peaks in all three components at periods around ≈13.6 d. Like the 14.76 and 14.19 d peaks, such ≈13.6 d peaks have long been reported in GNSS station position time series, back to Lambert et al.

(1998). Different possible origins were suggested for these ≈13.6 d peaks: either direct modeling errors of the M_f and 075,565 tides, or the aliasing of M_2 and O_1 tide model errors via the ground repeat period of the GPS satellites and the mechanism described by Penna and Stewart (2003) and Stewart et al. (2005). Abraha et al. (2018) observed a reduction by about half of the ≈13.6 d peak in the average periodogram of PPP-derived station height time series when adding GLONASS observations into their PPP processing, and therefore hypothesized a dominant contribution of aliased M_2 / O_1 errors over direct M_f / 075,565 errors. The spectral resolution achievable with the repro3 station position time series, which span up to 27 years, allows us to shed additional light on the origins of the ≈13.6 d peaks. In the vertical component, the ≈13.6 d spectral peak visible in Figure S60 reaches its maximal power very close to the alias period of the M_2 tide via the GPS ground repeat period. No secondary peaks or bumps are visible on either side, strengthening Abraha et al. (2018)'s hypothesis of a dominant contribution of aliased (M_2) errors. The situation is different in both horizontal components though, where two distinct spectral peaks of comparable magnitudes can be observed in Figure S60, one centered on the alias period of the M_2 tide via the GPS ground repeat period, the other on the M_f tide period. In horizontal, unlike in vertical, aliased (M_2) errors and direct (M_f) errors thus seem to contribute at comparable levels to the ≈13.6 d variations in the repro3 series. However, like for the other fortnightly variations, the particular tide model errors responsible for these spurious ≈13.6 d variations remain to be identified.

The next cluster of spectral peaks visible in Figure 12 lies around periods of ≈8 d. Figure S61 provides a zoom on this frequency range of the average periodograms. Two of the spectral peaks visible in this band, only in the East component, correspond to two more previously unreported tidal aliases via daily sampling: those of the μ_2 tide (49.47 cpy / 7.38 d) and of the $2N_2$ tide (51.25 cpy / 7.13 cpy). The rest of the peaks visible in this band form a comb with teeth regularly spaced in frequency, ranging from 42.69 cpy (8.56 d) to 48.89 cpy (7.47 d), with a spacing of about 1.03 cpy corresponding to the GLONASS draconitic frequency. Similar combs can also be observed in the average periodograms at harmonics of the ≈8 d period, i.e., at periods around 4 d, 2.67 d and 2 d. We do not provide zooms on these frequency ranges of the average periodograms as they present similar features as the main ≈8 d spectral comb. Such spectral combs at harmonics of ≈8 d were unambiguously attributed by Abraha et al. (2017) to GLONASS-related errors. Niu et al. (2023) later evidenced strong, large-scale spatial correlations of the ≈8 d variations in the repro3 station position time series, just like observed for the draconitic variations discussed above. This suggests mismodeling of GLONASS orbits as the main origin of the spectral combs at harmonics of ≈8 d.

Galileo-related spectral peaks are not visible in the average periodograms presented in Figure 12 since those were computed from time series spanning the whole repro3 time span, while Galileo observations contribute significantly to the repro3 station position estimates only in the latest years. However, two spectral combs at periods around ≈3.3 d and ≈2.5 d become visible in the average periodograms presented in Figure S62, which were computed from residual time series restricted to the period after May 2017, i.e., after the number of Galileo satellites reaches 17. Although this remains to be confirmed, the mismodeling of Galileo orbits can be suspected as responsible for these spectral combs.

4.4 Modeling of periodic variations

The spectral analysis presented in Section 4.3 evidenced the presence of various periodic variations in the repro3 station position time series. The objective of this section is now to augment the trajectory models defined in Section 4.1 in order to account for these periodic variations. This is indeed necessary for the purpose of characterizing the background noise in the repro3 time series, which is the objective of Section 4.5.

In a first step, we augmented the trajectory models defined in Section 4.1 with one sine wave at each frequency for which a spectral peak (or secondary bump) was observed in the average periodograms shown in Figure 12. This includes the 41 frequencies listed in Table S2. We noticed however that including these 41 "main" sine waves in the trajectory models was not sufficient to capture all of the quasi-periodic variations in the series. This is illustrated in Figure 13, in which an average periodogram of station height residuals from these trajectory models (medium purple) is compared with an average periodogram of station height residuals from trajectory models without sine waves (dark purple). It can be observed that the adjustment of the 41 main sine waves leads to a reduction of the spectral peaks visible in the periodograms, but does not make them vanish. Peaks clearly standing out of the level of background noise remain visible, especially around GPS draconitic harmonics and the two main GLONASS ≈8 d periods. These remaining peaks appear particularly clearly when only the longest residual time series are considered, which is why the average periodograms in Figure 13 are based only on residual time series that include at least 7000 daily data points. The average periodograms of the East and North residuals exhibit similar remaining peaks as that of the height residuals, hence are not shown in Figure 13.

The presence of these remaining peaks can be explained by the fact that the corresponding initial peaks cover frequency ranges that are broader than the spectral resolution of the longest repro3 series. The broadness of the initial peaks can in turn be explained by the fact that the corresponding periodic

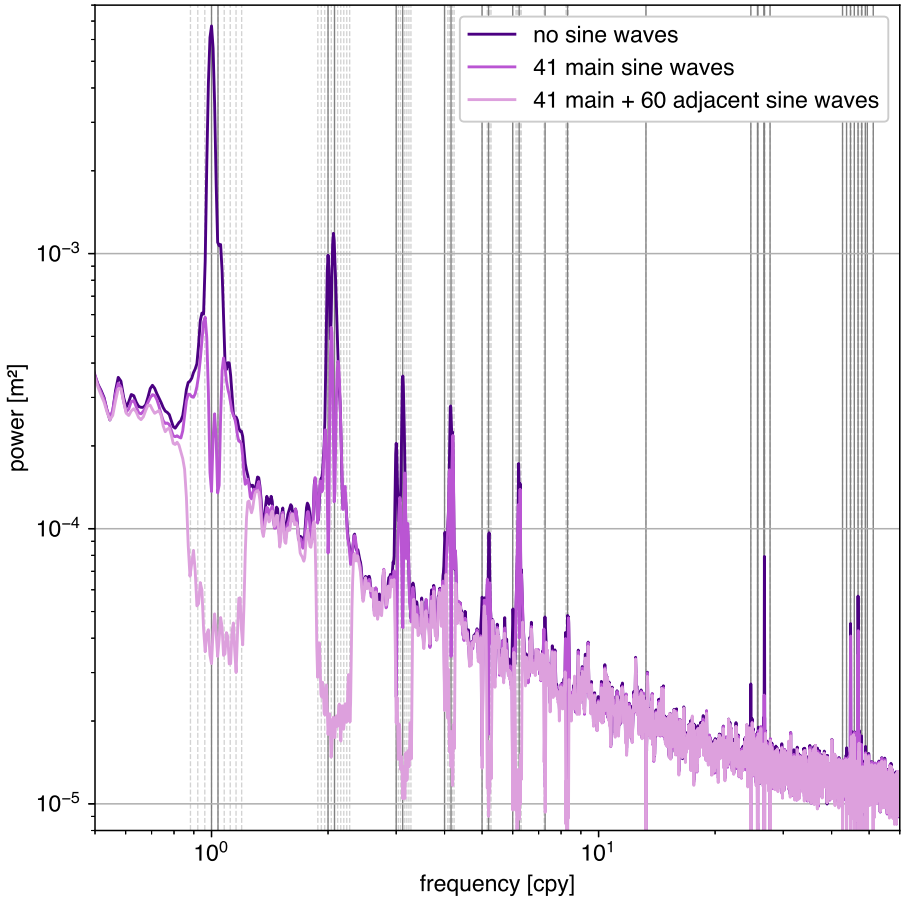

Fig. 13 Average Lomb-Scargle periodograms of residuals from different trajectory models adjusted to loading-corrected repro3 station height time series. In *dark purple*: trajectory models without sine waves. In *medium purple*: trajectory models with 41 main sine waves. In *light purple*: trajectory models with 41 main sine waves and 60 adjacent sine waves. The *gray vertical lines* indicate the frequencies of the 41 main sine waves. The *light gray vertical dashed lines* indicate the frequencies of the 60 adjacent sine waves. Only time series with at least 7000 daily data points were included in the average periodograms.

signals contained in the series are not perfectly time-invariant, but that their amplitudes and phases may vary with time. The broadness of the initial peaks around the annual and semi-annual frequencies may reflect time-variable seasonal surface deformation unaccounted for by the GGFC loading model to some extent, as well as time-variable seasonal GNSS errors. However, the remaining peaks at higher ≈annual harmonics are clearly attributable to time-variable draconitic errors rather than time-variable seasonal variations. It is therefore likely that time-variable draconitic errors also contribute significantly to the broadness of the initial ≈annual and ≈semi-annual peaks. On top of the fact, discussed in Section 4.2, that a large part of annual and semi-annual signals in GNSS time series likely arises from GNSS errors, this makes it even more hazardous to interpret *time-variable* seasonal variations extracted from GNSS series in terms of time-variable seasonal surface deformation.

Different effects may contribute to the time-variability of draconitic errors in the repro3 time series, hence to the remaining draconitic peaks visible in Figure 13. It is first expected that the impact of orbit

mismodeling on station position estimates varies with the long-term evolution of the GPS constellation, but also with the long-term evolution of the GPS satellites' β angles (elevation of the Sun above the satellites' orbital planes), whose main draconitic periodic variations are modulated by 25.5-year orbit precession cycles. (The long-term evolution of the GLONASS constellation and β angles could similarly explain time-variable ≈8 d signals, hence the remaining ≈8 d peaks visible in Figure 13.) Besides, even though they considered a nominal non-evolving GPS constellation, the PPP simulations presented by Rebischung et al. (2021) resulted in broad draconitic spectral peaks, due to the fact that the aliases of the GPS $m \cdot f_u$ frequencies via daily sampling fall coincidentally very close to the m^{th} GPS draconitic harmonic.

Whichever the exact origins of the time-variable periodic signals in the repro3 series, their presence needs to be accounted for when characterizing the background noise in the series. As will be demonstrated in Section 4.5, not accounting for the remaining peaks visible in Figure 13 would indeed bias the noise models adjusted to the series. Several methods have been proposed to handle time-variable periodic signals in GNSS time series and reviewed by Klos et al. (2018), such as the modeling of amplitudes and phases as piecewise polynomials (Davis et al., 2006) or as stochastic processes (Davis et al., 2012), singular spectrum analysis (Chen et al., 2013), or variational Bayesian independent component analysis (Gualandi et al., 2017). We adopt here a new pragmatic approach, namely the incorporation of additional sine waves into the station trajectory models, at frequencies adjacent to those of the 41 main sine waves where remaining peaks are visible in Figure 13. This method indeed offers the two advantages of being easily incorporated into traditional (restricted) maximum likelihood estimation of trajectory and noise models, and of being easily tunable, so that the additional adjacent sine waves account for all quasi-periodic variations in the repro3 series, and not more (see following).

In practice, we choose to separate the frequencies of the additional adjacent sine waves, from each other and from the frequencies of the main sine waves, by multiples of the GPS nodal precession frequency (≈0.04 cpy / 25.47 y). The two reasons driving this choice are that the "main" sine waves at annual and GPS draconitic harmonics are separated by multiples of this frequency, and that this frequency is close to the spectral resolution of the longest repro3 series. If their amplitudes are not constrained, multiple sine waves with such nearby frequencies can however be reliably adjusted only to time series with enough spectral resolution, i.e., with lengths close to or longer than ≈25.47 y. This is why we proceed to the incorporation of the adjacent sine waves into the trajectory models in two steps. In the first one, we use only the longest repro3 time series (those with at least 7000 daily data points), and progressively add more and more (unconstrained) adjacent sine waves into their trajectory models until no spectral peak clearly stands out of the level of background noise in the average periodogram of

their residuals. This procedure leads to the inclusion 60 adjacent sine waves into the trajectory models: 38 around GPS draconitic harmonics, 19 around some of the main GLONASS ≈8 d and ≈4 d periods, and 3 around the ≈13.6 d period. The average periodogram of the station height residuals from these trajectory models is shown in light purple in Figure 13. (Those of the East and North residuals are not shown as they are similar.) The absence of spectral peaks in these average periodograms implies that the residuals from these augmented trajectory models can finally be considered as an image of the background noise in the series, although with some frequency bands filtered out.

In a second step, we compute, for each of the 60 adjacent frequencies f, the standard deviation σ_f of all the corresponding sine and cosine coefficients freely adjusted to the longest repro3 series. We then incorporate each of the 60 adjacent sine waves in the trajectory models of all 1460 repro3 time series with more than 700 daily data points, but constrain its sine and cosine coefficients to $0 \pm \sigma_f$. These constraints turn out to be tight enough to allow for the adjustment of the augmented trajectory models even to short time series, while loose enough to capture all spectral peaks in the average periodograms of the longest residual time series.

4.5 Noise analysis

The residuals from the augmented trajectory models introduced in Section 4.4 are not only corrected for outliers, trends, offsets, post-seismic displacements and loading displacements, but also, as illustrated in Figure 13, for (quasi-)periodic variations. They may therefore be considered as an image of the background noise in the repro3 station position time series, although with certain frequency bands filtered out. As discussed in Section 4.3, this background noise seems to be well described, on average, and after loading corrections, by a combination of white and flicker noise, consistently with the outcomes from many previous studies.

In this section, we adjust realistic noise models to the 1460 analyzed repro3 station position time series simultaneously with the augmented trajectory models introduced in Section 4.4. We choose to adjust variable white + *power-law* noise models (i.e., processes with power spectra of the form $a + b/f^{\alpha}$) rather than variable white + *flicker* noise models in order to allow for possible regional or station-specific departures of the spectral index α from 1. Rather than the classical maximum likelihood estimator (MLE), we use here the restricted maximum likelihood estimator (RMLE) of the noise model parameters, as the former was shown to be affected by non-negligible biases in the case of time series containing offsets (Gobron et al., 2022). The RMLE, on the other hand, is unbiased, as it properly accounts for the estimation of the trajectory model parameters in addition to the noise model parameters. Finally, in order to point out the importance of properly accounting for *all* (quasi-)

periodic variations contained in the series when modeling their noise content, we adjust variable white + power-law noise models not only together with trajectory models including all main and adjacent sine waves introduced in Section 4.4, but also together with trajectory models including only the 41 main sine waves.

The standard deviations of the variable white noise processes adjusted to the loading-corrected repro3 station position time series (together with the full trajectory models) show a clear dependency on latitude, with maximum amplitudes around the equator and minimum amplitudes near the poles (Figure S63). This dependency on latitude was already observed by, e.g., Mao et al. (1999), Williams et al. (2004) and Gobron et al. (2021), and is likely attributable to the mismodeling of tropospheric delays affecting GNSS observations, which is expected to have a stronger impact at low latitudes.

No such dependency on latitude can be observed for the power-law noise parameters (standard deviations and spectral indices), nor any other clear large-scale patterns (Figures S64 and S65). Regional patterns in the power-law noise parameters can nevertheless be noticed, such as increases in amplitude and spectral index around the Amazon basin in the vertical component (likely due to hydrological loading deformation unaccounted for by the GGFC loading model) or in Northern Canada in all three components (likely due to the impact of snow directly covering the antennas and/or increasing local multipath). Apart from these localized deviations, the estimated spectral indices are scattered around 1 (their median values are 0.99, 0.98 and 1.00 in East, North and Up, respectively), confirming that the background noise in the loading-corrected repro3 series is on average well described by a white + flicker noise model.

The spectral indices of power-law noise estimated jointly with trajectory models including either all main and adjacent sine waves, or only the 41 main sine waves, are compared in Figure S66. It clearly appears that incorporating the 60 adjacent sine waves into the trajectory models leads to a systematic reduction of the estimated spectral indices, with their median values decreasing from 1.05 to about 1.00 in all three components. This decrease in the estimated spectral indices is most pronounced for the longest repro3 series: for the repro3 series longer than 15 years, it reaches on average 0.10 in both horizontal components and 0.07 in vertical. A similar systematic reduction of the estimated power-law noise amplitudes can also be observed (not shown). These systematic reductions are signs that the periodic variations remaining in the residuals from the trajectory models with only 41 main sine waves (i.e., the remaining spectral peaks visible in Figure 13), if not accounted for, tend to bias high the estimated amount of colored noise in the repro3 series.

As illustrated in Figure 14, this over-estimation of colored noise content has a clear systematic impact on the estimated uncertainties of the long-term repro3 station velocities. Compared to the case

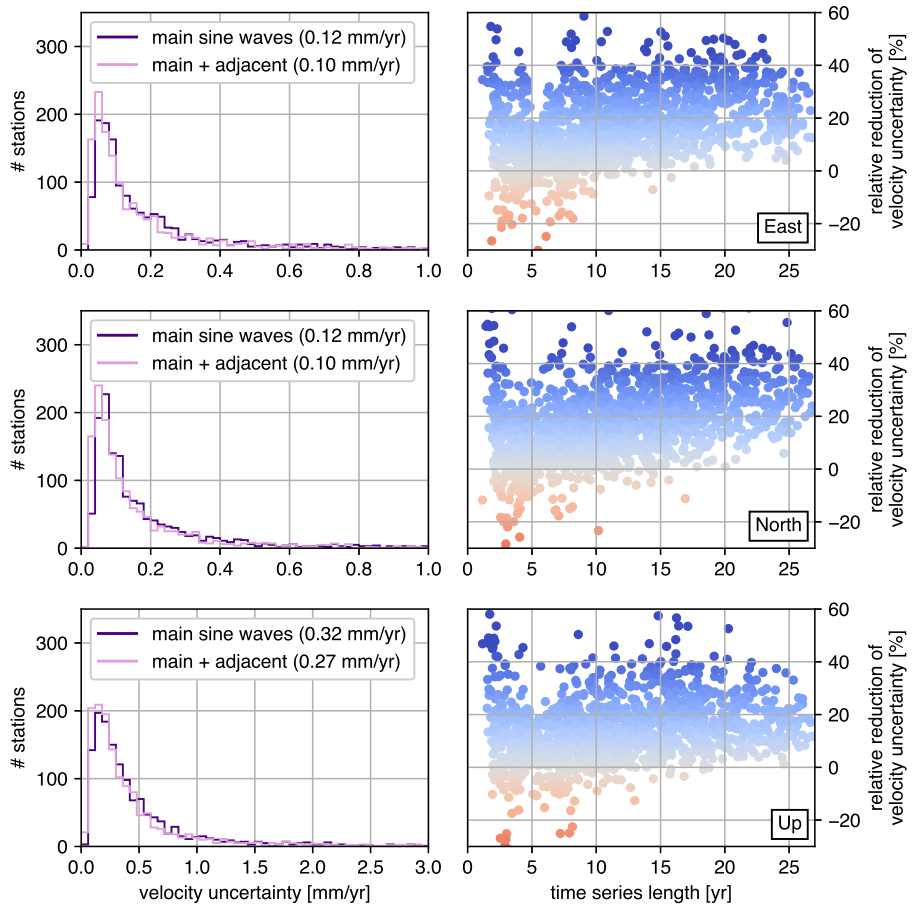

Fig. 14 Comparison of long-term repro3 station velocity uncertainties based on variable white + power-law noise models adjusted together with trajectory models including (a) 41 main sine waves and (b) 41 main sine waves and 60 adjacent sine waves. *Left*: histograms of the velocity uncertainties obtained in both cases. The numbers in parentheses are median velocity uncertainties. *Right*: relative reductions of velocity uncertainties (from case (a) to case (b)), represented as a function of the lengths of the station position time series.

where only 41 main sine waves are included in the trajectory models, the estimated repro3 station velocity uncertainties are indeed reduced on average by 17% in horizontal and 12% in vertical when the 60 adjacent sine waves are incorporated into the trajectory models. Like for the estimated spectral indices and amplitudes of power-law noise, this reduction of the estimated velocity uncertainties is most pronounced for the longest repro3 series: it reaches on average 24% in horizontal and 18% in vertical for the repro3 series longer than 15 years.

These results demonstrate the importance of accounting for the time-variability of the periodic variations contained in GNSS station position time series when characterizing their background noise and assessing the uncertainties of parameters of interest such as station velocities. As mentioned in Section 4.4, other approaches than the one used here (namely, the adjustment of adjacent sine waves with constrained amplitudes) could equally be used to handle time-variable periodic signals in GNSS

time series. However, failure to do so would result in biased noise parameter estimates and velocity uncertainties, especially for stations with long time series.

5 Inter-comparison of GNSS station position time series

The analysis of the station position residuals from the daily repro3 combinations presented in Section 2.3.3 did not allow evaluating errors in the AC station position estimates in an absolute sense, since those residuals represent differences between the AC solutions and their weighted mean. This last section therefore provides a direct comparison of station position time series extracted from the daily AC repro3 solutions, as well as from the daily combined repro3 solutions. The main goal of this comparison is to verify whether the relative weighting of ACs in the daily repro3 combinations, and in particular the predominance of TUG, can be related to different levels of precision of the "absolute" AC station position time series. A secondary goal is to quantify the gain (or loss) in precision achieved by combining the individual AC repro3 contributions into the IGS combined repro3 solutions.

We additionally include in this comparison station position time series extracted from the daily IGS combined repro2 solutions, complemented with daily IGS combined operational solutions after 2015, in order to evaluate the gain (or loss) in precision from repro2 to repro3. We finally include in this comparison station position time series from two non-IGS providers, namely the precise point positioning time series (PPP) provided by the Nevada Geodetic Laboratory (NGL-IGS14; Blewitt et al., 2018) and the Jet Propulsion Laboratory (JPL-2018a; Heflin et al., 2020). These two non-IGS data sets are widely used for different geophysical applications, and the purpose of including them in the comparison is therefore to assess whether and how these data sets and their various usages could possibly benefit from progress made within the frame of the IGS. Both the NGS-IGS14 and JPL-2018a PPP time series are obtained with the GipsyX software (Bertiger et al., 2020) and a homogeneous reprocessed/operational series of fiducial-free orbit and clock products from JPL. They are aligned to the IGS14 reference frame a posteriori by means of 7-parameter transformations estimated via a core network of reference stations.

Section 5.1 describes in more detail the different sets of station position time series used in this comparison, and their preprocessing. Section 5.2 discusses and compares the scatters of non-linear, non-seasonal variations in the time series from the different data sets, and how non-tidal loading corrections are able to reduce them. Section 5.3 finally compares the spectral content of the non-linear variations in the time series from the different data sets.

5.1 Data and preprocessing

The raw IGS repro3 station position time series used in the comparison presented in this section are the same as analyzed in Section 4 and are directly extracted from the daily IGS repro3 combined solutions. The raw IGS repro2 station position time series used in the comparison are likewise directly extracted from the daily IGS repro2 combined solutions. They are complemented, after the end of the repro2 data set on February 14, 2015, by station positions extracted from the daily IGS operational combined solutions. From February 15, 2015 up to the end of our study period (end of 2020), the IGS operational solutions have remained consistent with the repro2 standards, except for the switch from the IGb08/igs08.atx to the IGS14/igs14.atx framework on January 29, 2017 (Rebischung, 2016), which induced both global and station-specific offsets in the IGS combined station position time series.

The raw AC repro3 station position time series used in the comparison are not directly extracted from the daily repro3 solutions provided by the ACs, but from daily AC solutions that were pre-processed in a similar way as before the daily repro3 combinations. The only difference with the preprocessing applied before the daily repro3 combinations and described in Section 2.2 resides in the handling of the terrestrial scale information, which is here implicitly kept in station coordinates, rather than made explicit. Note that we used here some extended AC contributions to repro3 which could not be included in the daily repro3 combinations, namely the ULR contribution for years 2000-2002 and the WHU contribution for year 2020.

Finally, the raw NGL-IGS14 and JPL-2018a PPP time series used in the comparison are those directly provided at http://geodesy.unr.edu/gps_timeseries/tenv3/IGS14 and https://sideshow.jpl.nasa.gov/pub/JPL_GPS_Timeseries/repro2018a/post/point, respectively.

Not all repro3 stations nor the whole repro3 period were considered in the comparison. We chose to only consider data after 2005 (and up to the end of 2020), i.e., the time frame when the level of agreement between repro3 ACs and the AC weights in the daily repro3 combination remain at stable levels, as illustrated in Figure 3. As for station selection, we started by discarding all AC repro3 station position time series with less than 1000 points or less than 50% complete over the 2005-2020 period. We then retained only stations for which position time series from at least 5 different repro3 ACs were still available. This last selection criterion ensures that the subsequent comparison is based on a set of stations which is relatively common to the different repro3 ACs. A total of 326 stations were thus retained, whose geographical distribution is shown in Figure S67. For most repro3 ACs, position time series of more than 200 of those stations could be used in the comparison, with only two exceptions: WHU and JPL, with only 148 and 62 station position time series used in the comparison, respectively. We used the same time period and the same subset of stations for the non-repro3 data sets as well,

and also discarded time series with less than 1000 points or less than 50% complete, leading to 282 repro2, 321 NGL-IGS14 and 292 JPL-2018a station position time series being used in the comparison.

In order to correct the selected time series for trends, offsets, post-seismic displacements, seasonal displacements and outliers, the same trajectory model as defined in Section 4.1 is adjusted to each series, with outliers iteratively rejected using the same procedure. One difference is that the amplitudes and relaxation times of the post-seismic exponential and logarithmic functions are here fixed to the values adjusted to the repro3 combined station position time series. The other only difference is that, in order to account for the switch from the IGb08/igs08.atx to the IGS14/igs14.atx framework, we add offsets on January 29, 2017 into the trajectory models of all IGS repro2/operational station position time series.

To investigate how non-tidal loading corrections are able to reduce the scatter of the different sets of time series considered in the comparison, we additionally remove from all retained station position time series (already cleaned for outliers) the displacements predicted by the same GGFC loading model as used in Section 4, and adjust trajectory models again to the time series.

5.2 Non-seasonal scatter

The WRMS of the residuals from the trajectory models adjusted to the different station position time series provide a measure of their non-seasonal scatter, i.e., of both the stochastic variations and the spurious periodic (draconitic, fortnightly, ≈8-day, etc.) variations contained in the series. Since part of this scatter arises from non-linear, non-seasonal Earth deformation, especially in the case of time series uncorrected for non-tidal loading deformation, these WRMS cannot be interpreted as an absolute measure of errors in the time series. However, the differences in WRMS between different data sets may be interpreted as differences between their error levels.

Table 6 provides the median WRMS of the trajectory model residuals for each considered data set and each East, North, Up component, in the case of both raw and loading-corrected station position time series. For comparison, Table 6 also contains the median formal errors of the post-2005 AC repro3 station position estimates as derived from the weighting of AC solutions in the daily repro3 combinations (VCE columns; see Section 2.3.2 and Figure 3). Similarities can be observed between those combination-based estimates of AC precisions and the median WRMS of loading-corrected residuals. The latter are generally larger by 0.5–0.6 mm in both horizontal components, and by 0.6–1.1 mm in vertical. Hence, the "ranking" of ACs determined from the repro3 combinations is generally preserved when looking at the non-seasonal, non-loading scatter of their station position time series. In particular, the non-seasonal, non-loading scatter of the TUG time series is lower than that of any other AC in

all three components. ACs with the largest non-seasonal, non-loading scatters are also generally those with the least weight in the repro3 combinations.

Table 6 *VCE*: Median formal errors of post-2005 AC repro3 station position estimates as derived from the weighting of AC solutions in the daily repro3 combinations (see Section 2.3.2 and Figure 3). *TCH*: Median formal errors of post-2005 AC repro3 station position estimates as derived from the generalized three-cornered hat approach described in Section S1. *WRMS*: Median WRMS of residuals from the trajectory models adjusted to selected, either raw or loading-corrected, post-2005 station position time series (see Section 5.1). The percentages in parentheses are the relative reductions of these median WRMS achieved with loading corrections.

	East [mm]				North [mm]				Up [mm]			
			WRMS				WRMS				WRMS	
	VCE	TCH	raw	load corr.	VCE	TCH	raw	load corr.	VCE	TCH	raw	load corr.
COD	1.2	1.3	1.8	1.7 (1.4%)	1.2	1.3	1.8	1.7 (2.9%)	3.9	3.5	5.2	4.5 (13.8%)
ESA	0.9	1.0	1.5	1.5 (3.0%)	0.9	1.0	1.5	1.4 (2.5%)	3.2	3.1	4.7	4.3 (9.2%)
GFZ	0.9	1.1	1.7	1.6 (1.4%)	0.9	0.9	1.5	1.5 (3.2%)	3.2	3.0	4.7	4.3 (8.6%)
GRG	0.9	0.9	1.4	1.3 (3.4%)	1.0	1.1	1.4	1.3 (3.6%)	3.2	3.1	4.2	4.0 (5.6%)
JPL	1.0	1.2	1.6	1.5 (1.8%)	1.1	1.3	1.5	1.5 (1.3%)	3.4	3.1	4.8	4.2 (13.8%)
MIT	1.2	1.2	1.7	1.6 (3.3%)	1.2	1.1	1.6	1.5 (4.3%)	3.6	3.5	5.1	4.2 (18.8%)
NGS	1.1	1.5	1.8	1.8 (1.8%)	1.2	1.3	1.7	1.7 (2.0%)	3.6	3.7	5.3	4.8 (9.5%)
TUG	0.6	0.8	1.3	1.2 (5.7%)	0.7	0.8	1.3	1.2 (6.4%)	2.3	2.3	4.4	3.4 (22.5%)
ULR	1.2	1.4	1.9	1.8 (1.6%)	1.3	1.3	1.7	1.6 (3.4%)	3.6	3.4	5.1	4.5 (11.5%)
WHU	1.0	1.1	1.7	1.6 (3.3%)	1.0	1.1	1.6	1.6 (1.9%)	3.3	3.3	5.3	5.1 (4.3%)
IGS repro3			1.2	1.2 (3.6%)			1.3	1.2 (5.6%)			4.2	3.4 (20.8%)
IGS repro2			1.4	1.4 (2.1%)			1.4	1.4 (3.7%)			4.5	3.7 (17.6%)
NGL-IGS14			1.6	1.6 (2.5%)			1.6	1.6 (2.5%)			5.2	4.3 (16.0%)
JPL-2018a			1.6	1.5 (2.2%)			1.6	1.5 (3.7%)			5.0	4.8 (4.5%)

This comparison of the non-seasonal, non-loading scatters of the AC station position time series does however not allow a full validation of the weights attributed to the different ACs in the repro3 combinations. The predominance of TUG appears, in particular, stronger in the repro3 combinations than in terms of non-seasonal, non-loading scatter. As a further attempt to (dis)confirm the weights attributed to the different ACs in the repro3 combinations, we estimated the precision of the AC station position estimates on a station and component basis using a generalized three-cornered hat approach (Section S1), rather than on a daily basis in the daily repro3 combinations. The median precisions thus estimated are reported in the TCH columns of Table 6. They match the median formal errors of the post-2005 AC station position estimates as derived from the weighting of AC solutions in the daily repro3 combinations (VCE columns of Table 6) within a few tenths of mm. The "ranking" of ACs as determined from the repro3 combinations is largely preserved with this alternative variance component estimation approach. Like in the repro3 combinations, TUG is in particular estimated to provide the most precise station position estimates. The predominance of TUG over the other repro3 ACs is admittedly a bit less pronounced in the generalized three-cornered hat results. Yet, this alternative variance component estimation approach largely confirms the weights applied to the different AC solutions in the daily repro3 combinations, and in particular the predominance of TUG.

It is also interesting to compare in Table 6 the median non-seasonal, non-loading scatters of the station position time series from the individual repro3 ACs with that of the repro3 combined station position time series. It appears from this comparison that the median non-seasonal, non-loading scatter of the repro3 combined series is at the same level as that of the TUG series (actually a bit smaller, but only by a few hundredths of mm). In that respect, the repro3 combinations thus appear to barely improve the station position time series from TUG. It can also be noted that the median non-seasonal, non-loading scatter of the repro3 combined time series is smaller than that of the repro2 combined time series, by a few tenths of mm. However, it seems likely, from the previous observation, that this improvement from repro2 to repro3 is largely due to the contribution of TUG to repro3. Finally, the median non-seasonal, non-loading scatters of the two PPP data sets considered in the comparison are found to be at the same level as "standard" repro3 ACs, with the scatter of the vertical JPL-2018a series however sitting on the high end.

Inspecting how loading corrections are able to reduce the non-seasonal scatter of the different sets of station position time series is also instructive. In vertical, loading corrections reduce the median WRMS of trajectory model residuals from the different data sets by various amounts, from 0.2 mm only (GRG, WHU, JPL-2018a) up to 1.0 mm (TUG). These various levels of reduction can clearly be associated with different approaches used to model the tropospheric delays affecting GNSS observations. Data sets with the lowest reduction levels (GRG, WHU, JPL-2018a, but also ESA with a 0.4 mm scatter reduction) are indeed those which make use of a priori zenith delays and mapping functions from models referred to by Martens et al. (2020) as "blind" models, i.e., models that reflect seasonal fits to the ECMWF weather data, namely GPT2 (Lagler et al., 2013), GPT2w (Böhm et al., 2015) and/or GMF (Böhm et al., 2006a). The GFZ contribution to repro3, which also shows a relatively low reduction of its median non-seasonal vertical scatter with loading corrections (0.4 mm), also makes use of "blind" a priori zenith delays based on GPT2, but uses the higher-resolution VMF1 mapping functions (Böhm et al., 2006b). The (uncombined) data sets which make use of both high-resolution VMF1 a priori zenith delays and mapping functions (COD, JPL, MIT, NGS, ULR, NGL-IGS14) consistently show higher reductions of their median non-seasonal vertical scatters with loading corrections ranging from 0.5 mm (NGS) to 0.9 mm (MIT, NGL-IGS14). Finally, the TUG data set, which is the only one making use of the refined VMF3 a priori zenith delays and mapping functions (Landskron and Böhm, 2017), is also the one with the largest reduction of its median non-seasonal vertical scatter with loading corrections (1.0 mm).

These observations concur with the findings of Tregoning and Herring (2006), Steigenberger et al. (2009) and Martens et al. (2020) that non-tidal atmospheric loading corrections yield larger scatter

reductions of station position time series when high-resolution a priori zenith delays and mapping functions are used in the analysis of GNSS data. On the other hand, when "blind" tropospheric models are used, non-tidal atmospheric loading deformation is erroneously partially absorbed into tropospheric delay estimates. The fact that, among the data sets considered here, TUG shows the largest reduction of non-seasonal scatter with loading corrections, not only in vertical, but also in horizontal, additionally suggests that the refined VMF3 model may allow an even better preservation of atmospheric loading deformation in station position estimates than the widely employed VMF1 model. In light of these observations, we recommend that latest generation, high-resolution tropospheric models are used by all ACs in the next IGS reprocessing campaign.

5.3 Spectral content

Figure 15 shows average Lomb-Scargle periodograms of the residuals from the trajectory models adjusted to the different sets of station height time series, either raw (light colors) or loading-corrected (dark colors). The thin black curves in Figure 15 all correspond to the average periodogram of the loading-corrected IGS repro3 height residuals. Average periodograms of the East and North residuals from the trajectory models are similarly shown in Figures S68 and S69. Note that in every periodogram shown in Figures 15, S68 and S69, only residual time series longer than $1/f$ contribute to the average power at frequency f. Also note that the periodograms are normalized in such a way that the levels of background noise (i.e., the background continuous parts of the spectra) are comparable amongst the different data sets, but the powers of the periodic signals (i.e., the heights of the spectral peaks) are not rigorously comparable.

Like with the WRMS discussed in Section 5.2, it is possible to observe in Figure 15 differences in the ability of non-tidal loading corrections to reduce the level of background noise in station height time series from the different data sets. In the frequency range from ≈3 to ≈60 cpy, where the impact of non-tidal atmospheric loading is expected to be the largest (see Figure 11), non-tidal loading corrections noticeably reduce the level of background noise in station height time series obtained with high-resolution tropospheric models (e.g., COD, MIT, TUG, NGL-IGS14). On the other hand, the level of background noise is barely reduced in station height time series obtained with "blind" tropospheric models (e.g., GRG, WHU, JPL-2018a).

In the case of data sets for which non-tidal atmospheric loading corrections are effective, the overall shapes of the average periodograms of loading-corrected height residuals seem generally consistent with the power spectra of white + flicker noise processes, at least down to about 0.3 cpy. This is also the case for the average periodograms of the East and North residuals of all data sets, with the exceptions

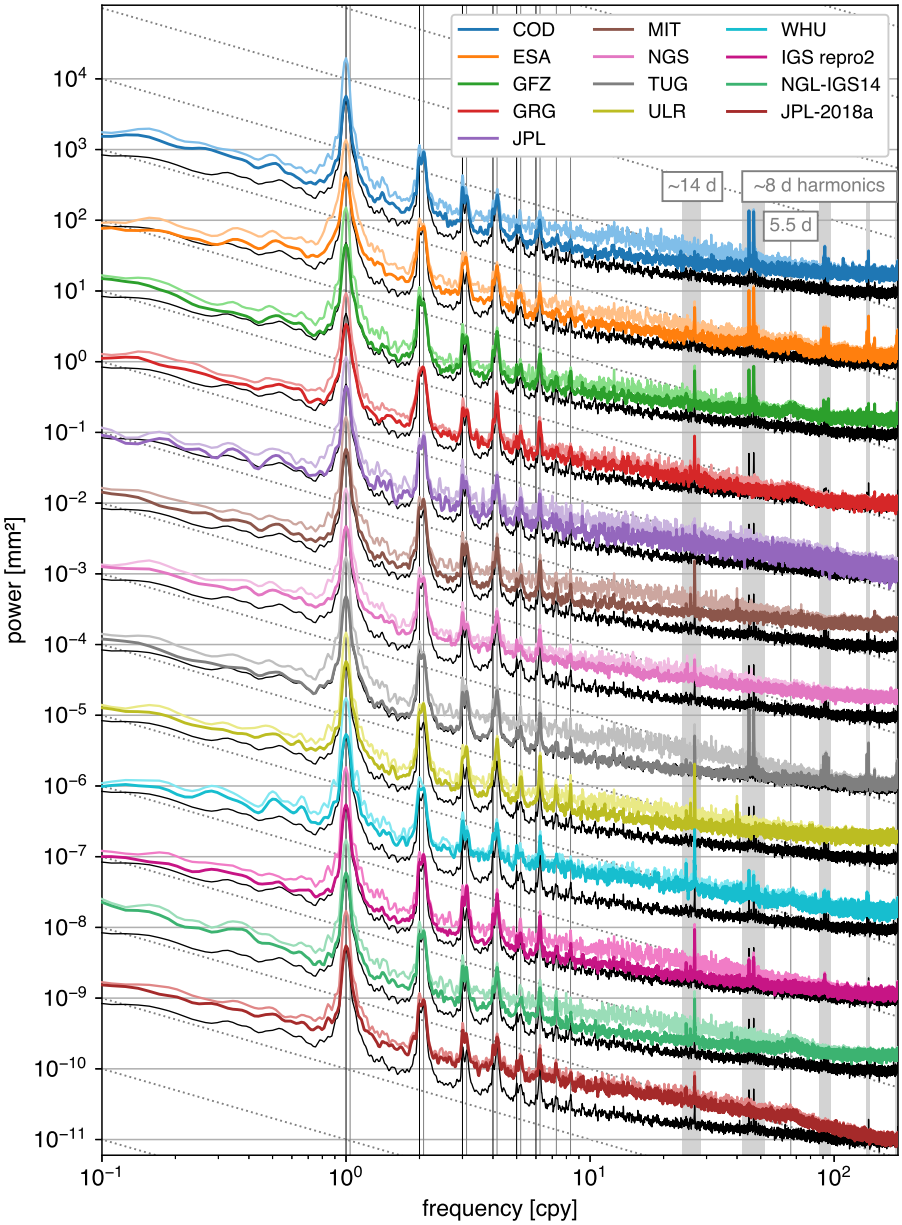

Fig. 15 Average periodograms of residuals from trajectory models adjusted to selected, either raw (*light colors*) or loading-corrected (*dark colors*), post-2005 station height time series, offset by powers of 10. The *thin black curves* all correspond to the average periodogram of the selected loading-corrected post-2005 *IGS repro3* height residuals. The *black vertical lines* indicate the first six harmonics of the annual period. The *gray vertical lines* indicate the first 8 harmonics of the GPS draconitic year and the 5.5 d period. The *gray vertical patches* span periods around 14 d and harmonics of 8 d. The *gray dotted lines* indicate the slope of flicker noise ($\propto 1/f$).

of JPL and JPL-2018a (Figures S68 and S69). At frequencies lower than about 0.3 cpy, all average periodograms somewhat flatten. However, as already discussed in Section 4.3, this flattening is not an indication that the noise in the series actually departs from flicker noise at low frequencies, but is rather due to part of the low frequencies of the noise being absorbed by offsets in the trajectory models. The average periodograms of the loading-corrected height residuals from data sets based on "blind" tropospheric models (e.g., GRG, WHU, JPL-2018a) do not show the progressive transition

from white to flicker noise observed in the other loading-corrected periodograms. In the frequency range where atmospheric loading dominates, they rather keep following the same behavior as uncorrected periodograms, which cannot be adequately described by a white + flicker noise model (Gobron et al., 2021). A last departure from the general white + flicker noise behavior can be observed for the JPL and JPL-2018a average periodograms, which do not flatten at high frequencies. This is because both the JPL AC products and the JPL-2018a PPP series are based on overlapping 30 h data batches, rather than strictly daily data batches, which has the effect of smoothing out the high-frequency white noise seen in the other series.

Regarding the overall levels of background noise in the different data sets, similar remarks can be made based on the loading-corrected average periodograms in Figures 15, S68 and S69 as based on the loading-corrected WRMS in Table 6. The level of background noise in the IGS repro3 combined series appears to be at almost the same level as in the TUG series. It is noticeably smaller than that in the IGS repro2 combined time series, most likely thanks to the contribution of TUG to repro3. As for the levels of background noise in the NGL-IGS14 and JPL-2018a PPP series, they are at similar levels as in the series of "standard" repro3 ACs, with the level of noise in the vertical JPL-2018a series however sitting on the high end, due to the inefficiency of loading corrections to reduce it.

In order to compare the powers of the periodic signals contained in the different sets of station position time series, we computed another set of average periodograms, with each individual periodogram normalized by the number of points in the corresponding time series. With this re-normalization, the heights of the spectral peaks become comparable amongst data sets, but the background continuous parts of the average periodograms cannot be interpreted in terms of background noise levels anymore. If these re-normalized average periodograms of the trajectory model residuals from the different repro3 ACs are compared, similar features can be observed as in the average periodograms of their repro3 combination residuals. We therefore refer the reader to Section 2.3.3 for a detailed discussion of these features, and limit the present discussion to only a subset of the analyzed data sets, namely the IGS repro3, IGS repro2, TUG and NGL-IGS14 data sets. The JPL-2018a average periodograms are not shown as their spectral peaks closely coincide with those of the NGL-IGS14 average periodograms (as expected from the fact that these two data sets are derived from the same JPL orbit and clock products and the same software). Figures S70 and S71 respectively provide zooms on the 0.7 – 10 cpy frequency band and on the fortnightly band of these re-normalized average periodograms.

Draconitic signals are found to be lowest on average in the IGS repro3 data set, with the only exception of the second draconitic harmonic signals in the East component, which are lower on average in the IGS repro2 data set (Figure S70). Like for midnight polar motion discontinuities (Section 3.1)

and geocenter coordinates (Section 3.2), this overall reduction of draconitic errors in station positions from repro2 to repro3 may be explained by improvements in the modeling of GPS satellite orbits. The draconitic peaks in TUG's average periodograms are at similar levels or slightly higher than in the IGS repro3 average periodograms, indicating some benefit from the repro3 combinations. Those in the NGL-IGS14 average periodograms are generally higher, particularly at odd draconitic harmonics in horizontal, as observed in JPL's repro3 combination residuals (Section 2.3.3).

Like for draconitic errors, a clear reduction of the spurious fortnightly signals can be observed from repro2 to repro3 (Figure S71). The IGS repro3 fortnightly peaks are also somewhat smaller than for TUG, indicating some benefit from the repro3 combinations. As for the NGL-IGS14 fortnightly peaks, they are generally higher, but are in fact at similar levels as in the contributions from "standard" ACs to repro3 – except for the peak in East at the alias period of the M_2 tide via daily sampling (24.74 cpy / 14.76 d), which is surprisingly higher than in any AC contribution to repro3, including JPL's.

6 Conclusion

As its contribution to the latest release of the International Terrestrial Reference Frame, ITRF2020, the IGS provided a 27-year-long series of daily "repro3" terrestrial frame solutions obtained by combining reprocessed solutions from ten ACs. This contribution represents an improvement over the previous contribution to ITRF2014 ("repro2"), not only by the inclusion of more stations with longer and more complete position time series, but also by a general reduction of random and systematic errors. As regards station position time series, their median non-seasonal scatter after non-tidal loading corrections was reduced by about 10% from repro2 to repro3 (Table 6), thanks to a reduction of both the level of background noise (Figure 15) and the amplitude of spurious draconitic and fortnightly errors (Figures S70 and S71). Clear reductions of the tidal aliasing errors and draconitic errors could also be evidenced in the repro3 polar motion estimates (Section 3.1), that are respectively attributable to the adoption of the new sub-daily ERP tide model from Desai and Sibois (2016) and to progress in the modeling of GPS satellite orbits. Draconitic errors were also reduced in the repro3 combined geocenter coordinates (Figure S29), so that the agreement of seasonal geocenter motion as determined from the repro3 solutions using the network shift approach with the SLR-based ITRF2020 seasonal geocenter motion model has notably improved (Section 3.2).

An investigation of the residuals from the daily repro3 combinations also reveals some improvements compared to repro2. The overall level of agreement between AC ERP estimates has in particular clearly improved (Section 2.3.4). Regarding geocenter coordinates (Section 2.3.5) and station positions (Section 2.3.3), the overall level of agreement between ACs has remained similar as in repro2. A

notable difference with repro2 though is that the AC contributions to repro3 appear to be of very homogeneous quality, so that, unlike in repro2, all AC contributions could be included in the repro3 combinations. One of the AC contributions to repro3, the one from TUG, actually stands out, but by appearing more precise than any other AC contribution. It thus gets about twice more weight in the daily repro3 combinations than the next "best" ACs (Section 2.3.2). An analysis of the scatter of the AC station position time series (Section 5.2) and the generalized three-cornered hat approach described in Section S1 confirm this higher precision of the TUG station position estimates. However, the precise explanation(s) for this higher precision still need(s) to be uncovered. We encourage research in this direction, as it could eventually benefit other ACs and the IGS combined products, as well as users of GNSS station position time series.

Another major progress of the IGS contribution to ITRF2020 is that it provided, for the first time, an independent estimate of the terrestrial scale based on the calibrations of the Galileo satellite antennas provided by the European GNSS Service Center (GSC, 2023). However, the ITRF2020 analysis subsequently revealed a significant bias (+4.3 mm at epoch 2015.0) and drift (+0.11 mm/yr) between the long-term terrestrial scale realized by the repro3 solutions and the average of the VLBI and SLR solutions used to define the ITRF2020 scale (Altamimi et al., 2023). As discussed in Section 3.3, different consistency checks were recently performed (Huang et al., 2020; Glaser et al., 2021; Villiger et al., 2022; Steigenberger and Montenbruck, 2023), that suggest a certain confidence in the Galileo satellite antenna calibrations, hence in the repro3 scale, at a better level than the +4.3 mm bias with respect to ITRF2020. It is not impossible however that these consistency checks miss an overall bias (and drift) of the GNSS-derived terrestrial scale. In any case, the reason(s) for the scale bias and drift between repro3 and ITRF2020 remain(s) to be uncovered.

Despite the various improvements observed from repro2 to repro3, the repro3 terrestrial frame solutions remain affected by a variety of random and systematic errors. The fraction of seasonal variations in the repro3 station position time series explained by non-tidal loading models remains at similar levels as in previous studies (about 20% in horizontal and 50% in vertical for the annual component; Section 4.2), suggesting that GNSS errors still largely contribute to the observed seasonal variations. Spurious draconitic variations still evidently contaminate the repro3 combined station position time series (Section 4.3), ERPs (Section 3.1) and geocenter coordinates (Section 3.2), indicating that the current models of non-conservative forces acting on GPS satellites still need to be improved. Spurious fortnightly variations at different frequencies also remain pervasive, for which the responsible tide model errors still need to be identified. Besides, the inclusion of GLONASS and Galileo led to the appearance of new spurious periodic errors in the repro3 station position time series at periods around harmonics

of ≈8 d, and at periods around ≈3.3 d and ≈2.5 d, respectively. The large-scale spatial correlations of the GLONASS-related ≈8 d errors (Niu et al., 2023) point to mismodeling of the GLONASS satellite orbits being responsible for these new errors. As for the background noise in the repro3 station position time series, it is still well described, after non-tidal loading corrections, by a combination of white and flicker noise (Section 4.5), whose origins remain to be precisely understood.

The complexity of the periodic errors contained in the repro3 station position time series makes them hard to model properly. The analysis of the longest repro3 series presented in Section 4.4 indeed reveals that some of these errors, in particular the draconitic errors, have amplitudes and phases that unambiguously vary with time. This makes it not only hazardous to interpret time-variable seasonal variations extracted from GNSS series in terms of time-variable seasonal Earth's surface deformation, but also necessary to account for this time-variability of the periodic errors when modeling the background noise in GNSS series. As shown in Section 4.5, failure to do so can significantly bias the adjusted noise models, as well as the uncertainties inferred for parameters of interest like long-term station velocities.

The analysis of different sets of station position time series presented in Section 5 aligns with the conclusion by Tregoning and Herring (2006), Steigenberger et al. (2009) and Martens et al. (2020) that high-resolution tropospheric models are needed in order to preserve non-tidal atmospheric loading deformation in GNSS time series. Non-tidal loading corrections do indeed noticeably reduce the level of background noise in station height time series obtained with high-resolution tropospheric models (e.g., COD, MIT, TUG, NGL-IGS14), but are barely effective for time series obtained with "blind" tropospheric models (e.g., GRG, WHU, JPL-2018a). The largest reductions of non-seasonal scatter with loading corrections are actually obtained for the TUG series, which are the only ones obtained with the refined VMF3 model. We therefore recommend that latest generation, high-resolution tropospheric models are used by all ACs in the next IGS reprocessing campaign.

Finally, the detailed analysis of the residuals from the daily repro3 combinations presented in Section 2.3 reveals a number of AC-specific features that could deserve further investigation. This includes:

- larger draconitic variations in JPL's horizontal station position time series (Figure S7) – but also in the NGL-IGS14 and JPL-2018a PPP time series derived with JPL's orbit and clock products; see Section 5.3 – likely related to JPL's unique approach to solar radiation pressure modeling;
- outstanding fortnightly variations in station position time series from WHU, NGS and GRG (Figure S8), including two spectral peaks specific to GRG, possibly related to some tide model implementation errors;

- other periodic variations in the station position time series from particular ACs: at 39.99 cpy (9.13 d) for MIT and ULR, 40.07 cpy (9.12 d) for WHU, 37.99 cpy (9.61 d) for NGS;
- bumps centered on a ≈5.5 d period in the power spectra of station position time series from certain ACs (ESA, GFZ, GRG, maybe WHU), as well as of the NGL-IGS14 and JPL-2018a PPP time series (Figure 15;
- unique clusters of spectral peaks in GFZ' and NGS' pole coordinate and pole rate residuals within different frequency bands (Figures S15–S18), that might be explained by errors in the implementation of the new sub-daily ERP tide model from Desai and Sibois (2016).

As an end note, let us mention that there are, for the time being, no plans for a next IGS reprocessing campaign. Indeed, the IERS recently agreed on providing annual updates of ITRF2020. The IGS will contribute to these updates with post-2020 daily combined terrestrial frame solutions, namely, extended repro3 solutions from 1 January 2021 to 26 November 2022 (Rebischung, 2023b), and operational solutions after 27 November 2022 and the switch of the IGS operational products to the repro3 standards (Rebischung et al., 2022; Masoumi, 2022). These annual updates of ITRF2020 aim at prolonging its longevity, by providing up-to-date coordinates for new stations and stations affected by offsets since the end of the initial ITRF2020 input data, and by reducing extrapolation errors of the ITRF2020 coordinates, without however revisiting the defining parameters (origin, scale and orientation) of the frame. The annual updates of ITRF2020 may continue until the need for a new reference frame is identified. This would be the case if, for instance, a drift is observed between the origin of recent SLR solutions and that of ITRF2020, or progress is made toward reconciling terrestrial scale estimates from the different space geodetic techniques, or major advances are made in some other aspects of space geodetic data analysis. Meanwhile, however, the need for a new IGS reprocessing campaign may be postponed.

Acknowledgments. We are grateful to all participating Analysis Centers for the huge efforts they invested into the third IGS reprocessing campaign. This study contributes to the IdEx Université de Paris ANR-18-IDEX-0001. KG is grateful to the Centre National d'Étude Spatiales (CNES) for the postdoctoral fellowship that allowed him to contribute to this work.

Declarations

Data Availability

All AC contributions to repro3 are publicly available at https://cddis.nasa.gov/archive/gnss/products/wwww/repro3/, where *wwww* stands for the 4-character GPS week number. The ESMGFZ and

GGFC loading deformation models are respectively available from http://rz-vm115.gfz-potsdam.de:8080/repository and http://loading.u-strasbg.fr/ITRF2020. The NGL-IGS14 and JPL-2018a PPP time series used in Section 5 are respectively available from http://geodesy.unr.edu/gps_timeseries/tenv3/IGS14 and https://sideshow.jpl.nasa.gov/pub/JPL_GPS_Timeseries/repro2018a/post/point.

Author contribution

PR carried out the daily repro3 combinations and the analysis of the results. PR proceeded to the analysis of the repro3 station position time series and to the comparison with other data sets, with inputs from ZA, LM, XC and KG. All authors discussed the results. PR wrote the initial manuscript. All authors contributed to the final manuscript.

Supplementary Material

S1 Generalized three-cornered hat comparison of AC station position time series

A comparison of the non-seasonal, non-loading scatters of station position time series from the different repro3 ACs (Section 5.2) evidences some correlation between the levels of these scatters and the weights attributed to the different ACs in the daily repro3 combinations. In particular, the station position time series from TUG, the AC which dominates the repro3 combinations, are shown to be the least scattered. However, this comparison does not allow a full validation of the weights attributed to the different ACs in the repro3 combinations. The predominance of TUG appears, in particular, stronger in the repro3 combinations than in terms of non-seasonal, non-loading scatter.

In this section, we therefore attempt to (dis)confirm the weights attributed to the different ACs in the repro3 combinations using an alternative variance component estimation approach. Instead of estimating AC variance factors on a daily basis like in the repro3 combinations, we estimate here AC variance factors on a station and component basis using a generalized three-cornered hat approach. We use for that purpose the same subset of post-2005 station position time series with at least 1000 daily points, less than half missing values, and time series from at least 5 different ACs available for a given station, as introduced in Section 5.1. Note that we use here raw station position time series and not residuals from trajectory models, i.e., the time series analyzed here include trends, offsets, post-seismic displacements, seasonal displacements, etc. They were only corrected for outliers using

the procedure described in Section 5.1.

For a given station and a given East, North or Up component, we thus dispose of position time series from $m \geq 5$ repro3 ACs. Each of these time series consists of a vector of dates $\boldsymbol{t}_i = [t_{i,1}, \ldots, t_{i,n_i}]^T$, a vector of positions $\boldsymbol{y}_i = [y_{i,1}, \ldots, y_{i,n_i}]^T$ and a vector of formal errors $\boldsymbol{\sigma}_i = [\sigma_{i,1}, \ldots, \sigma_{i,n_i}]^T$. We introduce the union vector of all dates from the m individual time series:

$$\boldsymbol{t} = \bigcup_{1 \leq i \leq m} \boldsymbol{t}_i = [t_1, \ldots, t_n]^T \tag{1}$$

and model the concatenation of all m position vectors as follows:

$$\begin{bmatrix} \boldsymbol{y}_1 \\ \vdots \\ \boldsymbol{y}_m \end{bmatrix} \sim \mathcal{N} \left(\begin{bmatrix} \boldsymbol{J}_1 \\ \vdots \\ \boldsymbol{J}_m \end{bmatrix} \cdot \boldsymbol{y} \ , \begin{bmatrix} f_1 \mathrm{diag}(\boldsymbol{\sigma}_1^2) & & \\ & \ddots & \\ & & f_m \mathrm{diag}(\boldsymbol{\sigma}_m^2) \end{bmatrix} \right) \tag{2}$$

where:

- $\boldsymbol{J}_i$ is a $n_i \times n$ matrix of ones and zeros that maps dates $\boldsymbol{t}_i$ into the union vector of dates $\boldsymbol{t}$,
- $\boldsymbol{y}$ is a vector of unknown true positions at dates $\boldsymbol{t}$,
- $f_1, \ldots, f_m$ are AC-specific variance factors to be estimated.

We estimate the unknown AC variance factors $f_1, \ldots, f_m$ by restricted maximum likelihood, an unbiased alternative to classical maximum likelihood estimation, which is equivalent, if the observations are assumed to be normally distributed like here, to several other variance component estimation approaches (MINQUE, BIQUE, Helmert, least-squares VCE; Amiri-Simkooei, 2007). Namely, we search numerically for the variance factors $f_1, \ldots, f_m$ which maximize the following restricted log-likelihood function:

$$l_r(f_1, \ldots, f_m) = -\frac{1}{2} \left(\sum_{i=1}^{m} n_i \log(f_i) + \log(\det \boldsymbol{N}) + \sum_{i=1}^{m} (\boldsymbol{y}_i - \boldsymbol{J}_i \hat{\boldsymbol{y}})^T \left(f_i \mathrm{diag}(\boldsymbol{\sigma}_i^2) \right)^{-1} (\boldsymbol{y}_i - \boldsymbol{J}_i \hat{\boldsymbol{y}}) \right) + \mathrm{c} \tag{3}$$

where $\boldsymbol{N} = \sum \boldsymbol{J}_i^T \left(f_i \mathrm{diag}(\boldsymbol{\sigma}_i^2) \right)^{-1} \boldsymbol{J}_i$, $\hat{\boldsymbol{y}} = \boldsymbol{N}^{-1} \sum \boldsymbol{J}_i^T \left(f_i \mathrm{diag}(\boldsymbol{\sigma}_i^2) \right)^{-1} \boldsymbol{y}_i$ and c is a constant term independent from $f_1, \ldots, f_m$. Once the restricted maximum likelihood estimates $\hat{f}_1, \ldots, \hat{f}_m$ are obtained, we compute the "median estimated precision" (mep) of each time series $\boldsymbol{y}_i$ as the median of its formal errors rescaled by its estimated variance factor $\hat{f}_i$, i.e., as $\mathrm{mep}(\boldsymbol{y}_i) = \sqrt{\hat{f}_i} \cdot \mathrm{median}(\boldsymbol{\sigma}_i)$.

This procedure is repeated for all of the selected stations and all three components, and we finally compute, for each AC and component, a median estimated precision across all stations. These numbers are given in the TCH columns of Table 6. They match the median formal errors of the post-2005 AC station position estimates as derived from the weighting of AC solutions in the daily repro3 combinations (VCE columns in Table 6 within a few tenths of mm. The "ranking" of ACs as determined from the repro3 combinations is largely preserved with this alternative variance component estimation approach. Like in the repro3 combinations, TUG is in particular estimated to provide the most precise station position estimates. The predominance of TUG over the other repro3 ACs is admittedly a bit less pronounced in the generalized three-cornered hat results. Yet, this alternative variance component estimation approach largely confirms the weights applied to the different AC solutions in the daily repro3 combinations, and in particular the predominance of TUG.

Table S1 Constants needed for the derivation of the frequencies in Table S2

description	symbol	reference/formula	value
Earth gravitational constant	GM	Petit and Luzum (2010)	$3.986004418 \cdot 10^{14}$ m^3s^{-2}
mean Earth radius	a_E	Moritz (1992)	6371001 m
Earth dynamical flattening	J_2	Petit and Luzum (2010)	$1.0826359 \cdot 10^{-3}$
mean Earth angular speed	ω_E	Petit and Luzum (2010)	1.0027378 cpd
Earth orbital frequency	f_E	$\omega_E - 1$	0.0027378 cpd
nominal GPS semi-major axis	a_G	US Department of Defense (2020)	26559800 m
nominal GPS inclination	i_G	US Department of Defense (2020)	55°
mean GPS orbital frequency	f_G^o	Agnew and Larson (2007)	2.0057014 cpd
GPS nodal precession frequency	f_G^p	$-(3/2)J_2(a_E/a_G)^2 f_G^o \cos(i_G)$	-0.0001075 cpd
GPS ground repeat frequency	f_G^r	$f_G^o + f_G^p - \omega_E$	1.0028561 cpd
nominal GLONASS semi-major axis	a_R	IAC (2023)	25471000 m
nominal GLONASS inclination	i_R	IAC (2023)	64.8°
mean GLONASS orbital frequency	f_R^o	IAC (2023)	2.1310182 cpd
GLONASS nodal precession frequency	f_R^p	$-(3/2)J_2(a_E/a_R)^2 f_R^o \cos(i_R)$	-0.0000922 cpd
GLONASS / Sun arg. lat. frequency	f_R^u	$f_R^o + f_R^p - f_E$	2.1281882 cpd
GLONASS draconitic frequency	f_R^d	$f_E - f_R^p$	0.0028300 cpd
$145,545$ tide frequency	$f_{145,545}$	Petit and Luzum (2010)	0.9293886 cpd
O_{O_1} tide frequency	$f_{O_{O_1}}$	Petit and Luzum (2010)	0.9294198 cpd
O_1 tide frequency	f_{O_1}	Petit and Luzum (2010)	0.9295357 cpd
$2N_2$ tide frequency	f_{2N_2}	Petit and Luzum (2010)	1.8596904 cpd
μ_2 tide frequency	f_{μ_2}	Petit and Luzum (2010)	1.8645473 cpd
M_2 tide frequency	f_{M_2}	Petit and Luzum (2010)	1.9322734 cpd

Table S2 Frequencies and periods of the 41 main sine waves included in the trajectory models of the repro3 station position time series. $[x]$ denotes the integer closest to x.

description	symbol	reference/formula	frequency [cpd]	period [d]
first annual harmonic	f^a	conventional Julian year	0.0027378	365.2500000
second annual harmonic	-	$2f^a$	0.0054757	182.6250000
third annual harmonic	-	$3f^a$	0.0082136	121.7500000
fourth annual harmonic	-	$4f^a$	0.0109514	91.3125000
fifth annual harmonic	-	$5f^a$	0.0136893	73.0500000
sixth annual harmonic	-	$6f^a$	0.0164271	60.8750000
first GPS draconitic harmonic	f_G^d	$f_E - f_G^p$	0.0028453	351.4567884
second GPS draconitic harmonic	-	$2f_G^d$	0.0056906	175.7283942
third GPS draconitic harmonic	-	$3f_G^d$	0.0085359	117.1522628
fourth GPS draconitic harmonic	-	$4f_G^d$	0.0113812	87.8641971
fifth GPS draconitic harmonic	-	$5f_G^d$	0.0142265	70.2913577
sixth GPS draconitic harmonic	-	$6f_G^d$	0.0170718	58.5761313
seventh GPS draconitic harmonic	-	$7f_G^d$	0.0199171	50.2081126
eighth GPS draconitic harmonic	-	$8f_G^d$	0.0227624	43.9320985
M_m tide frequency	f_{M_m}	Petit and Luzum (2010)	0.0362920	27.5542819
M_2 alias via daily sampling	-	$\lvert f_{M_2} - [f_{M_2}]\rvert$	0.0677266	14.7652473
O_1 alias via daily sampling	-	$\lvert f_{O_1} - [f_{O_1}]\rvert$	0.0704643	14.1915835
$145,545$ alias via daily sampling	-	$\lvert f_{145,545} - [f_{145,545}]\rvert$	0.0706114	14.1620165
M_f tide frequency	f_{M_f}	Petit and Luzum (2010)	0.0732027	13.6607045
M_2 alias via GPS ground repeat period	-	$\lvert f_{M_2} - [f_{M_2}/f_G^r] \times f_G^r\rvert$	0.0734388	13.6167802
O_{O_1} alias via daily sampling	-	$\lvert f_{O_{O_1}} - [f_{O_{O_1}}]\rvert$	0.0759401	13.1682795
μ_2 alias via daily sampling	-	$\lvert f_{\mu_2} - [f_{\mu_2}]\rvert$	0.1354527	7.3826535
$2N_2$ alias via daily sampling	-	$\lvert f_{2N_2} - [f_{2N_2}]\rvert$	0.1403096	7.1270985
GLONASS ≈8 d peak	-	$\lvert f_R^u - 4f_R^d - [f_R^u - 4f_R^d]\rvert$	0.1168682	8.5566476
GLONASS ≈8 d peak	-	$\lvert f_R^u - 3f_R^d - [f_R^u - 3f_R^d]\rvert$	0.1196982	8.3543445
GLONASS ≈8 d peak	-	$\lvert f_R^u - 2f_R^d - [f_R^u - 2f_R^d]\rvert$	0.1225282	8.1613865
GLONASS ≈8 d peak	-	$\lvert f_R^u - f_R^d - [f_R^u - f_R^d]\rvert$	0.1253582	7.9771407
GLONASS ≈8 d peak	-	$\lvert f_R^u - [f_R^u]\rvert$	0.1281882	7.8010300
GLONASS ≈8 d peak	-	$\lvert f_R^u + f_R^d - [f_R^u + f_R^d]\rvert$	0.1310182	7.6325274
GLONASS ≈8 d peak	-	$\lvert f_R^u + 2f_R^d - [f_R^u + 2f_R^d]\rvert$	0.1338482	7.4711502
GLONASS ≈4 d peak	-	$\lvert 2f_R^u - 4f_R^d - [2f_R^u - 4f_R^d]\rvert$	0.2450564	4.0806933
GLONASS ≈4 d peak	-	$\lvert 2f_R^u - 3f_R^d - [2f_R^u - 3f_R^d]\rvert$	0.2478864	4.0341059
GLONASS ≈4 d peak	-	$\lvert 2f_R^u - 2f_R^d - [2f_R^u - 2f_R^d]\rvert$	0.2507164	3.9885704
GLONASS ≈4 d peak	-	$\lvert 2f_R^u - f_R^d - [2f_R^u - f_R^d]\rvert$	0.2535464	3.9440513
GLONASS ≈4 d peak	-	$\lvert 2f_R^u - [2f_R^u]\rvert$	0.2563764	3.9005150
GLONASS ≈4 d peak	-	$\lvert 2f_R^u + f_R^d - [2f_R^u + f_R^d]\rvert$	0.2592064	3.8579294
GLONASS ≈2.7 d peak	-	$\lvert 3f_R^u - 4f_R^d - [3f_R^u - 4f_R^d]\rvert$	0.3732446	2.6792082
GLONASS ≈2.7 d peak	-	$\lvert 3f_R^u - 3f_R^d - [3f_R^u - 3f_R^d]\rvert$	0.3760746	2.6590469
GLONASS ≈2.7 d peak	-	$\lvert 3f_R^u - 2f_R^d - [3f_R^u - 2f_R^d]\rvert$	0.3789046	2.6391868
GLONASS ≈2 d peak	-	$\lvert 4f_R^u - 6f_R^d - [4f_R^u - 6f_R^d]\rvert$	0.4957728	2.0170530
GLONASS ≈2 d peak	-	$\lvert 4f_R^u - 5f_R^d - [4f_R^u - 5f_R^d]\rvert$	0.4986028	2.0056045

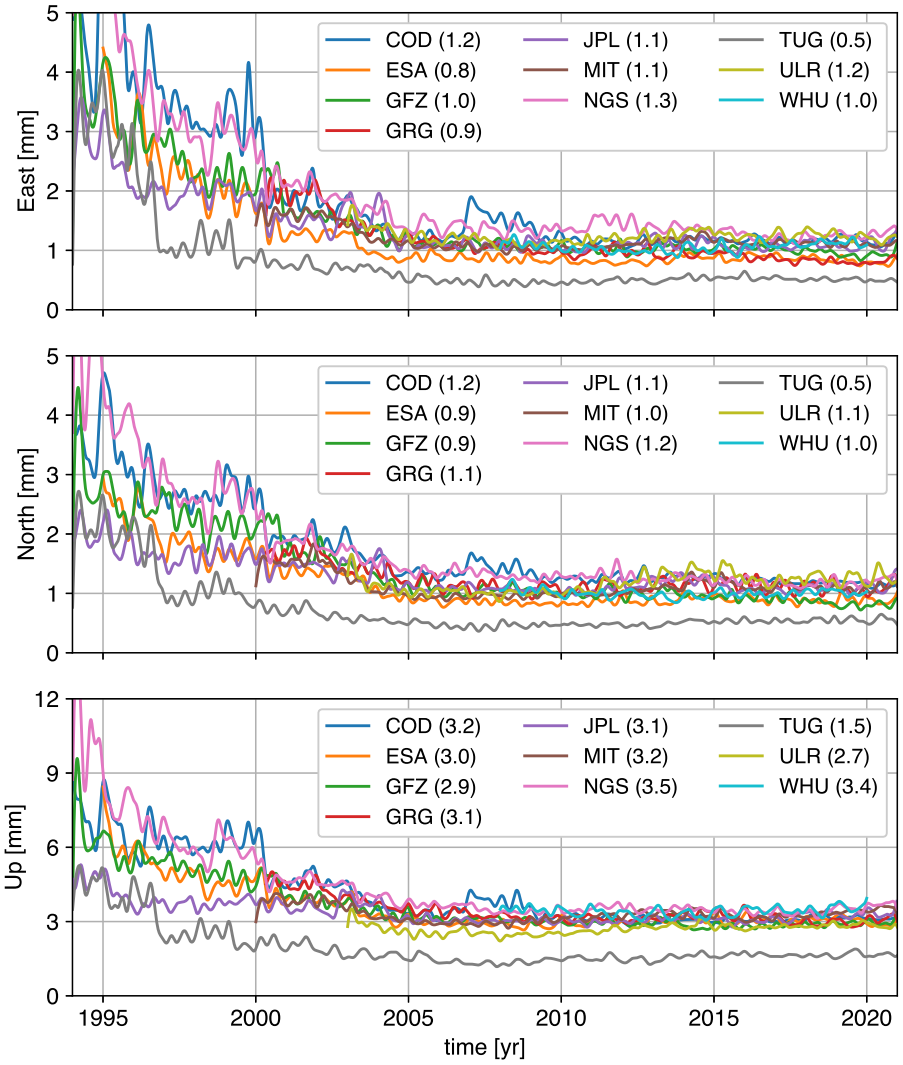

Fig. S1 WRMS of station position residuals from the daily repro3 combinations. All time series were smoothed by a Vondrák filter with a cutoff frequency of 2.5 cpy. The numbers in the legends are the medians of the WRMS time series for the period after 2005.0, in mm.

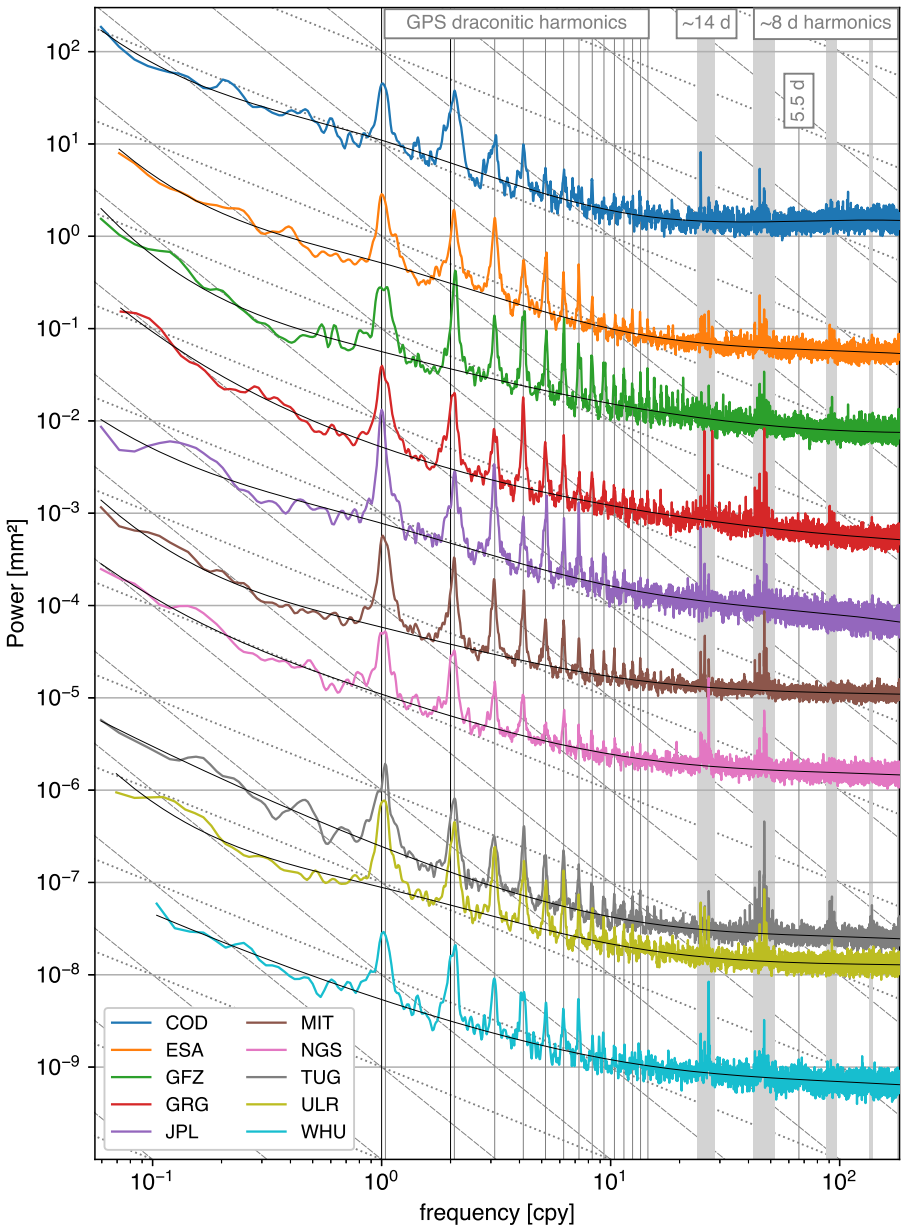

Fig. S2 Same as Figure 4 for the *East* component of the AC station position residual time series

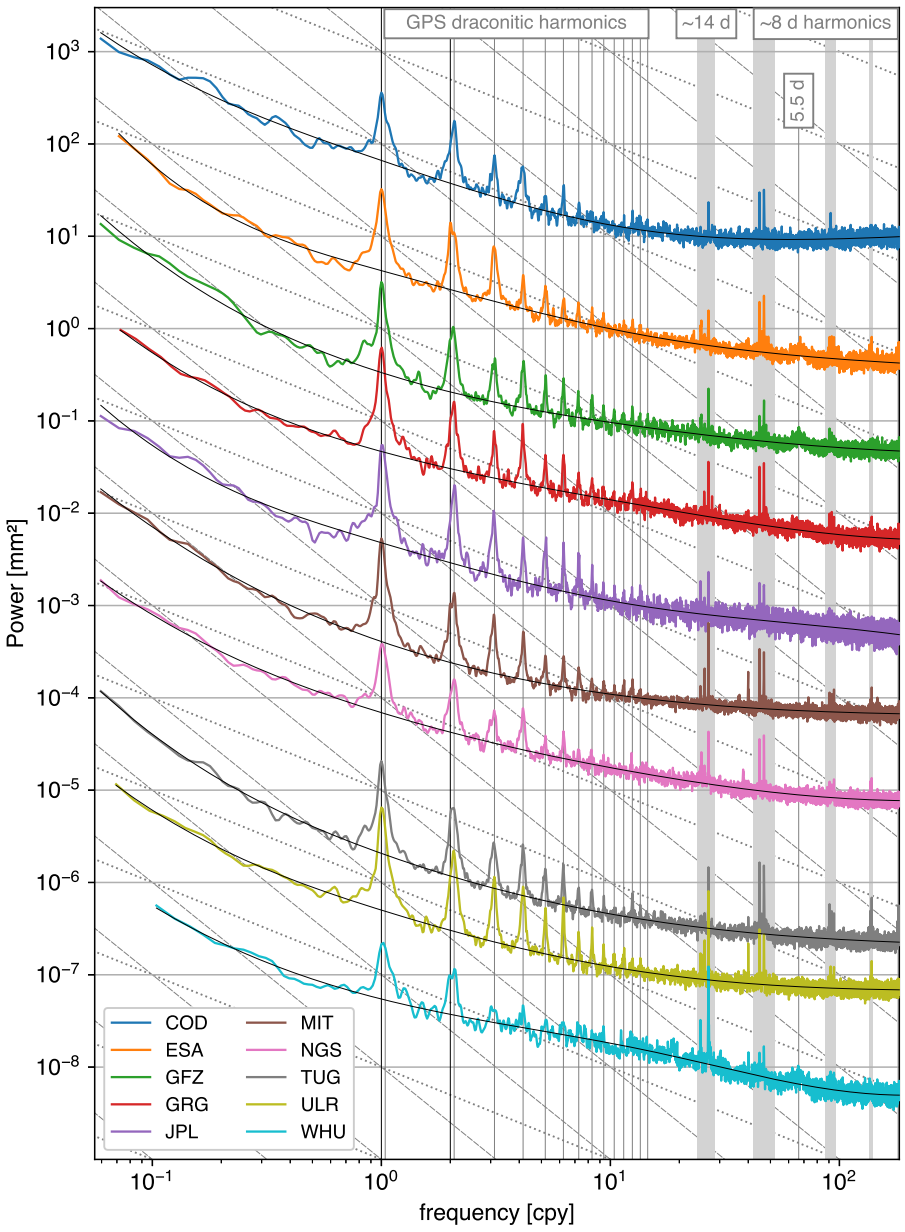

Fig. S3 Same as Figure 4 for the *Up* component of the AC station position residual time series

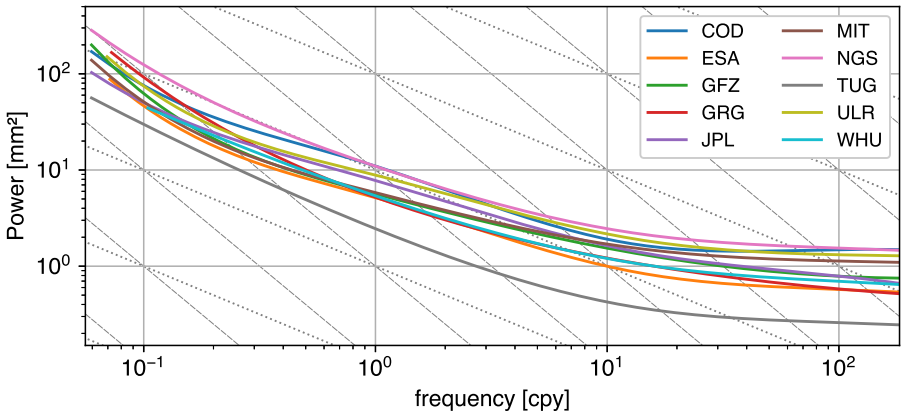

Fig. S4 Same as Figure 5 for the *East* component of the AC station position residual time series

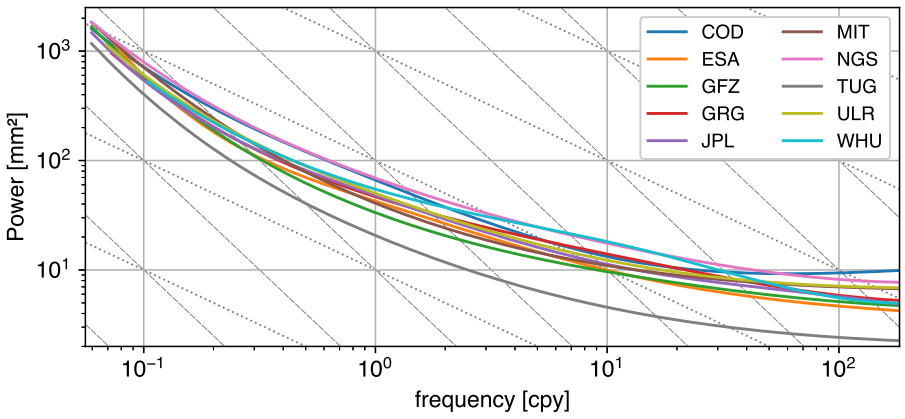

Fig. S5 Same as Figure 5 for the *Up* component of the AC station position residual time series

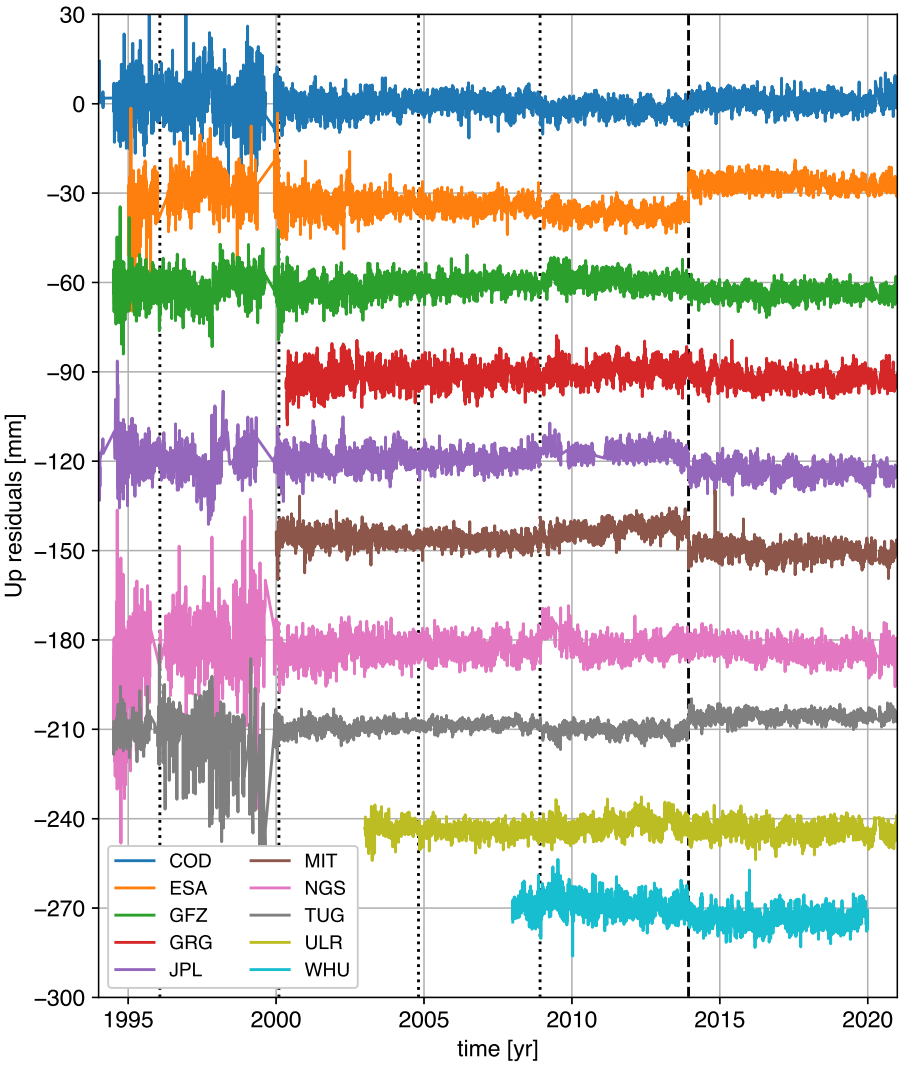

Fig. S6 Daily repro3 combination residuals for the Up component of station CAS1 (Casey, Antarctica). The *vertical dotted and dashed lines* respectively indicate receiver and antenna changes at the station.

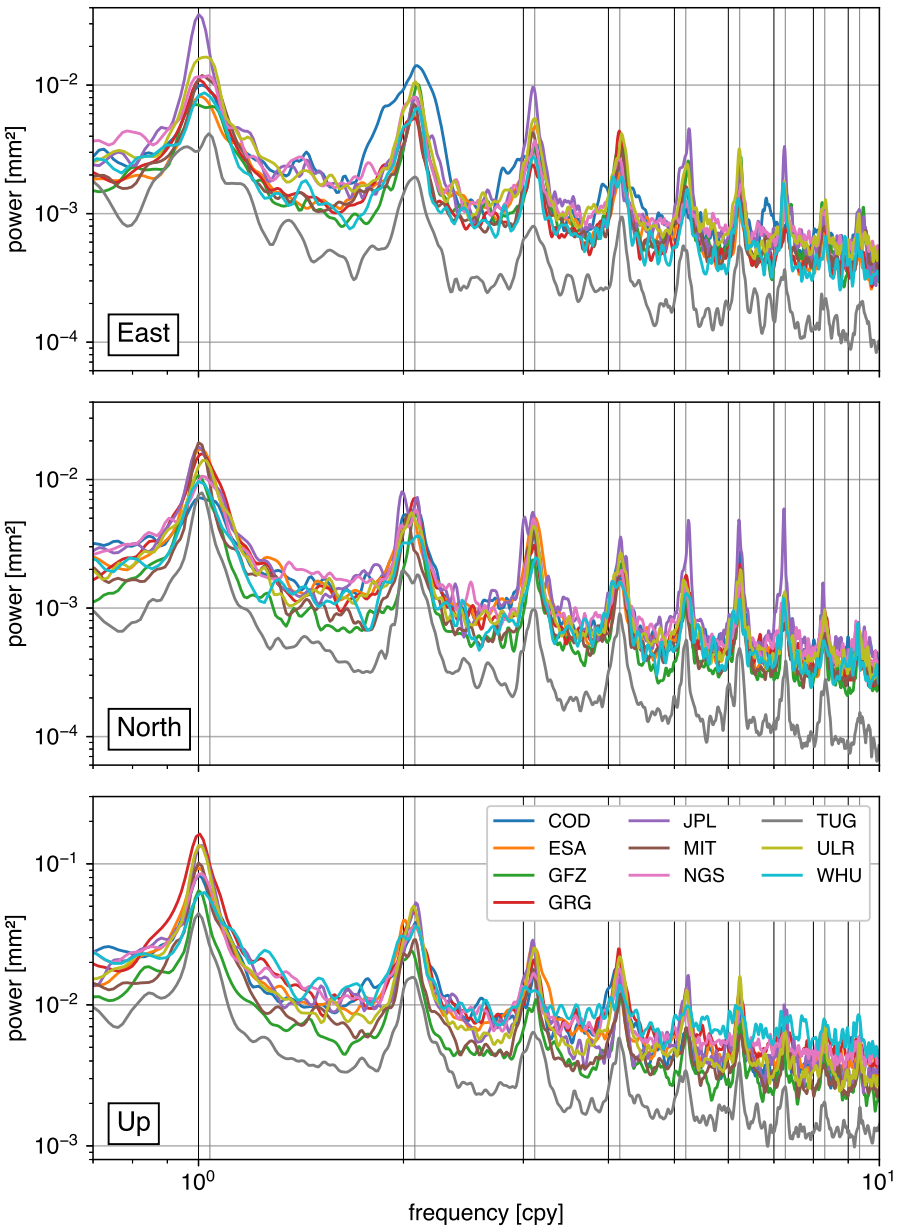

Fig. S7 Average Lomb-Scargle periodograms of selected AC station position residual time series: zoom on the 0.7 – 10 cpy band. The individual periodograms were normalized so that the heights of the spectral peaks are comparable amongst ACs, but the levels of background noise are not. The *black vertical lines* indicate harmonics of the annual frequency. The *gray vertical lines* indicate harmonics of the GPS draconitic frequency.

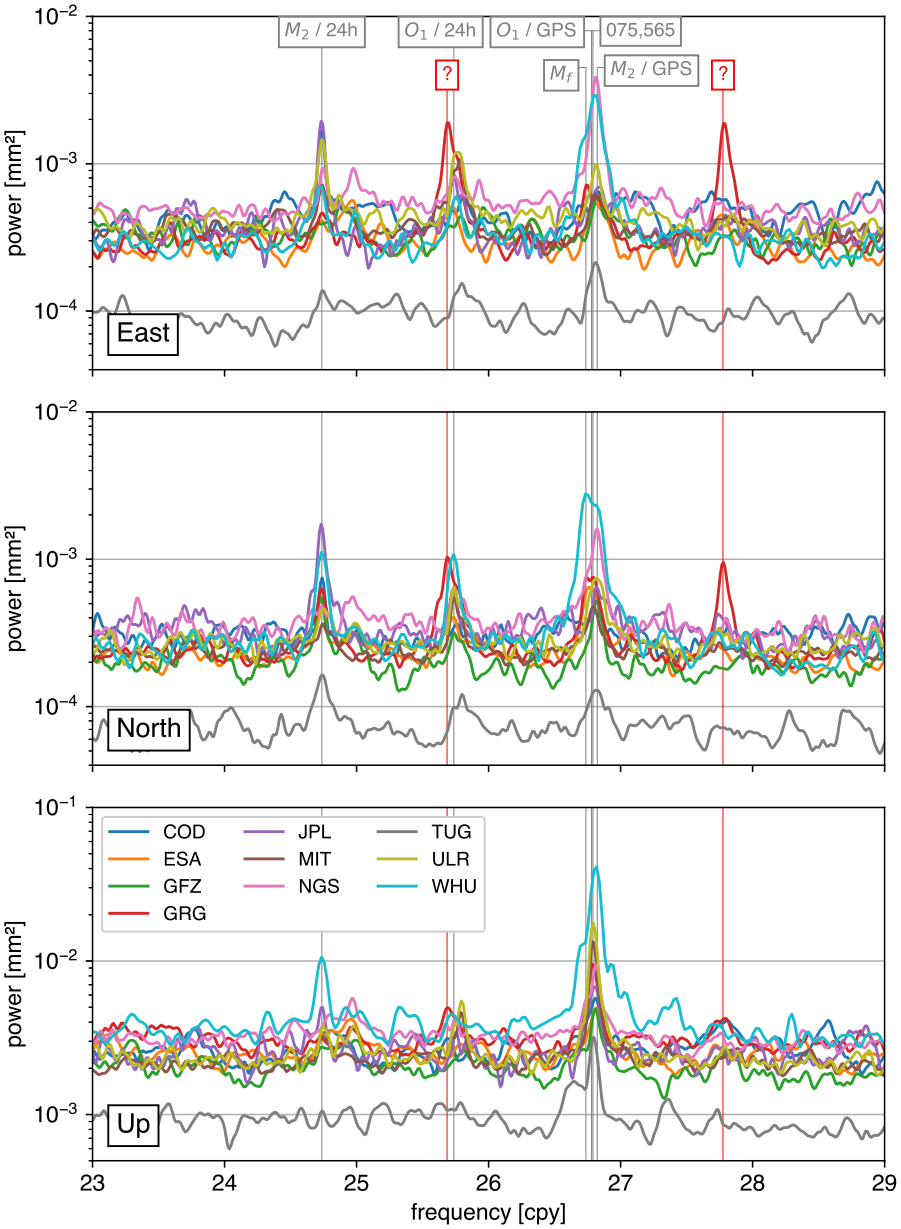

Fig. S8 Average Lomb-Scargle periodograms of selected AC station position residual time series: zoom on the fortnightly band. The individual periodograms were normalized so that the heights of the spectral peaks are comparable amongst ACs, but the levels of background noise are not. The *gray vertical lines* respectively indicate the alias period of the M_2 tide via daily sampling (24.74 cpy / 14.76 d), the alias period of the O_1 tide via daily sampling (25.74 cpy / 14.19 d), the M_f tide period (26.74 cpy / 13.66 d), the alias period of the O_1 tide via the GPS ground repeat period (26.78 cpy / 13.64 d), the 075, 565 tide period (26.79 cpy / 13.63 d) and the alias period of the M_2 tide via the GPS ground repeat period (26.82 cpy / 13.62 d). The *red vertical lines* indicate the frequencies of two spectral peaks of unknown origins found in the GRG residuals (25.69 cpy / 14.22 d and 27.78 cpy / 13.15 d).

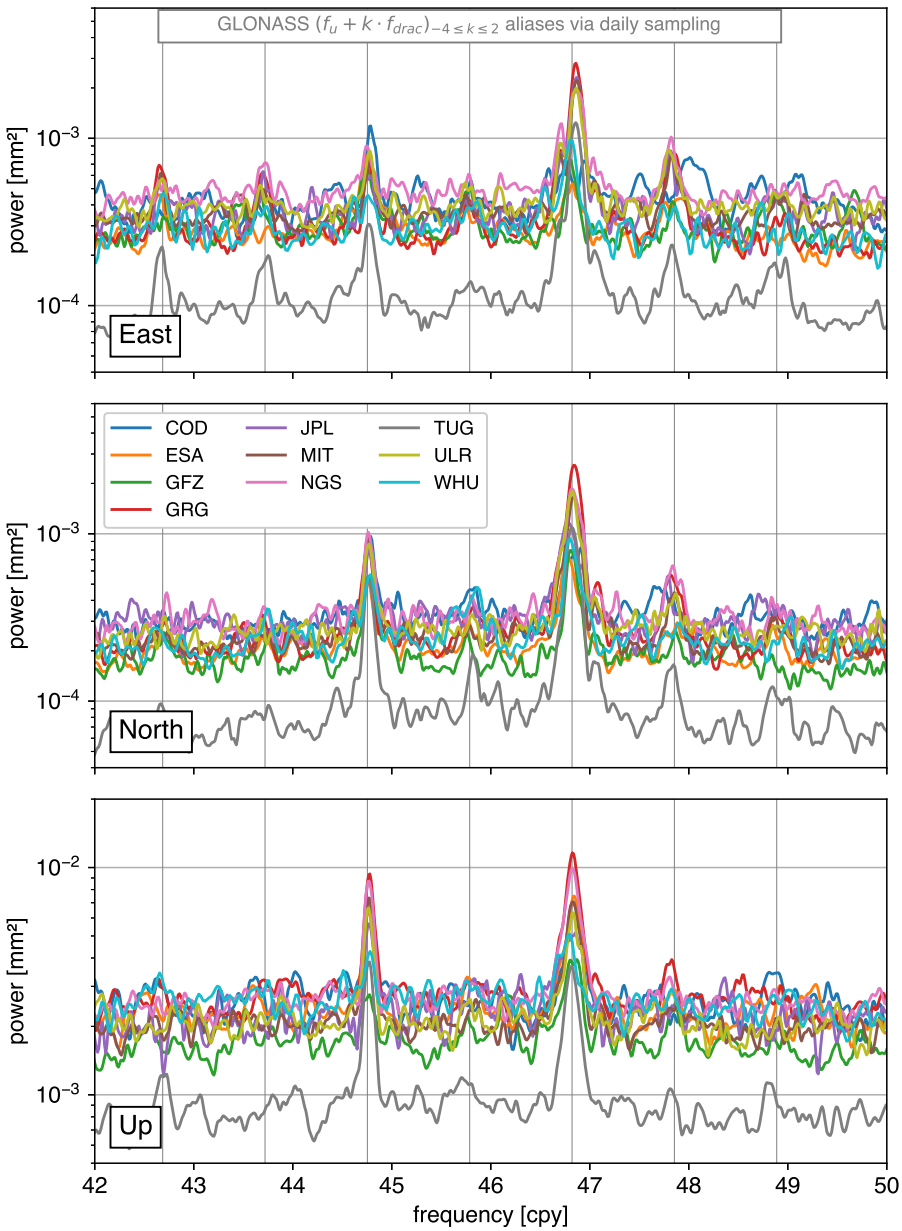

Fig. S9 Average Lomb-Scargle periodograms of selected AC station position residual time series: zoom on the ≈8 d band. The individual periodograms were normalized so that the heights of the spectral peaks are comparable amongst ACs, but the levels of background noise are not. The *gray vertical lines* indicate the alias periods of the $f_u + k \cdot f_{drac}$ frequencies via daily sampling, where f_u is the frequency of the argument of latitude of GLONASS satellites with respect to the Sun, f_{drac} is the draconitic frequency of GLONASS satellites and k is an integer ranging from -4 to 2.

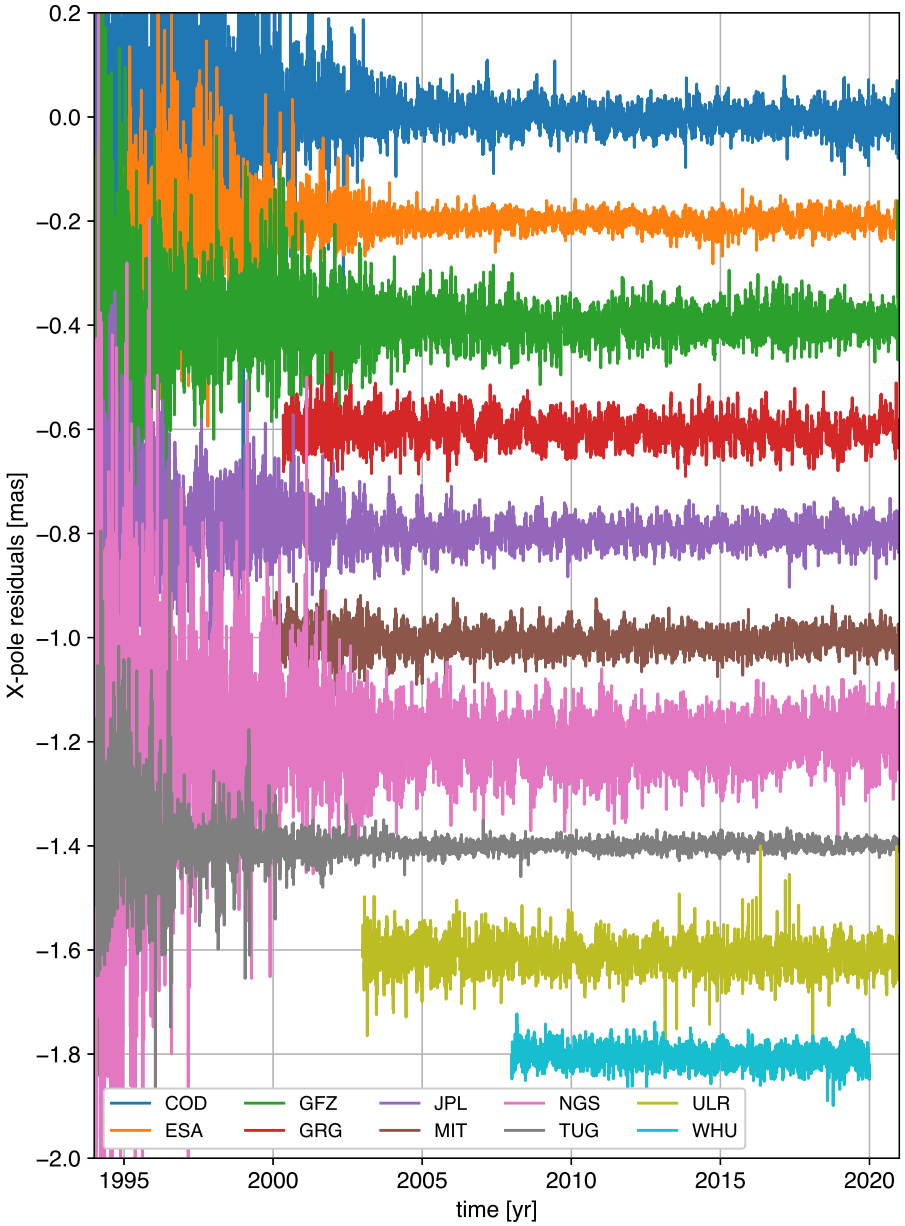

Fig. S10 AC X-pole residuals offset by multiples of 0.2 mas

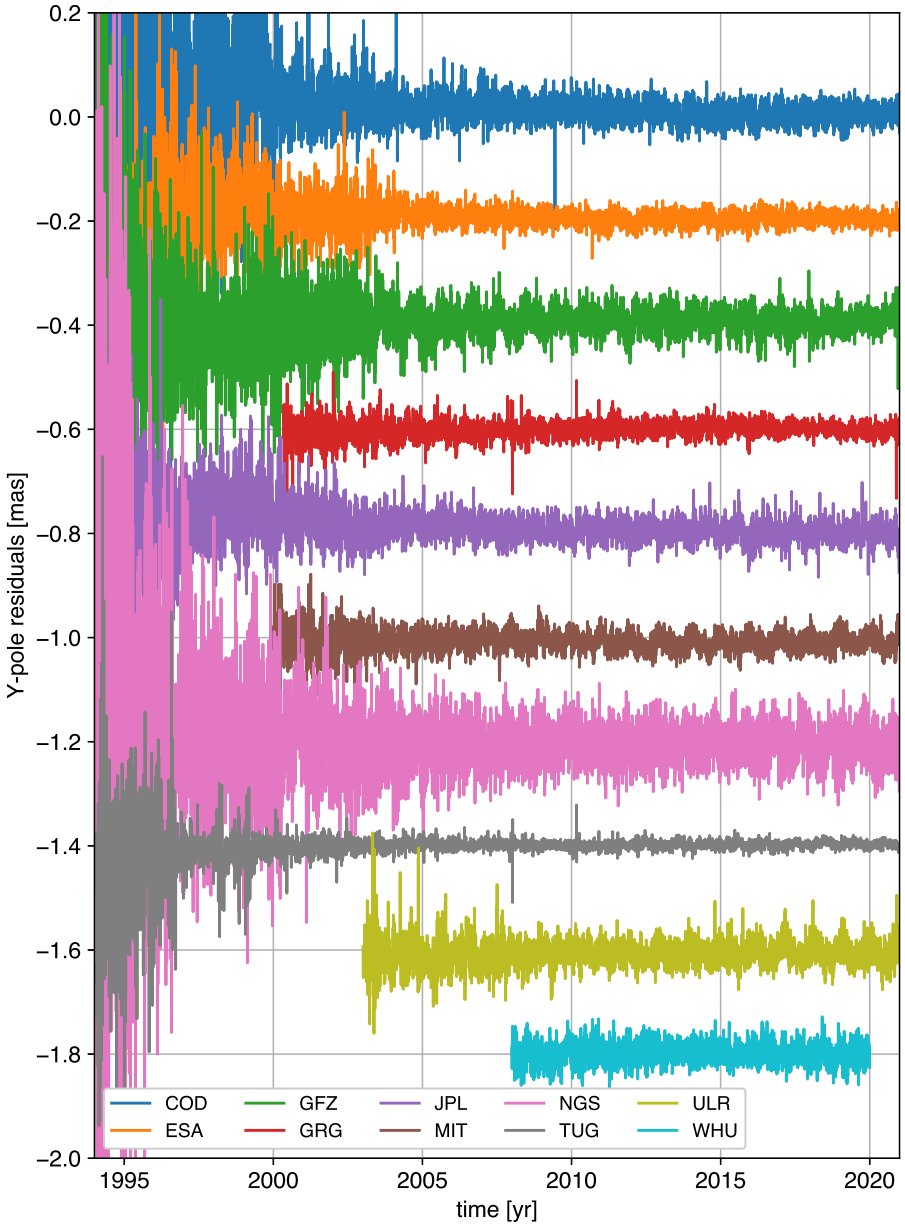

Fig. S11 AC Y-pole residuals offset by multiples of 0.2 mas

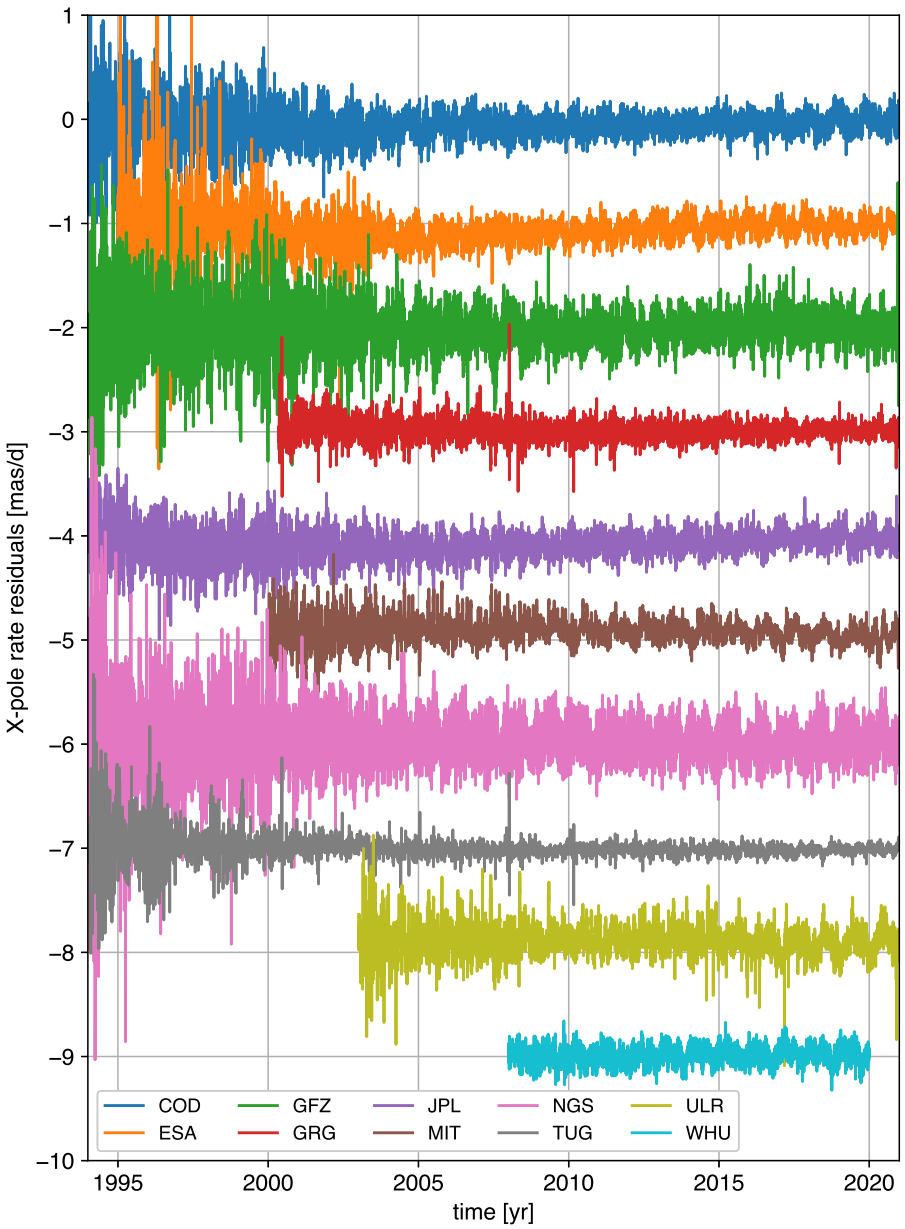

Fig. S12 AC X-pole rate residuals offset by multiples of 1 mas/d

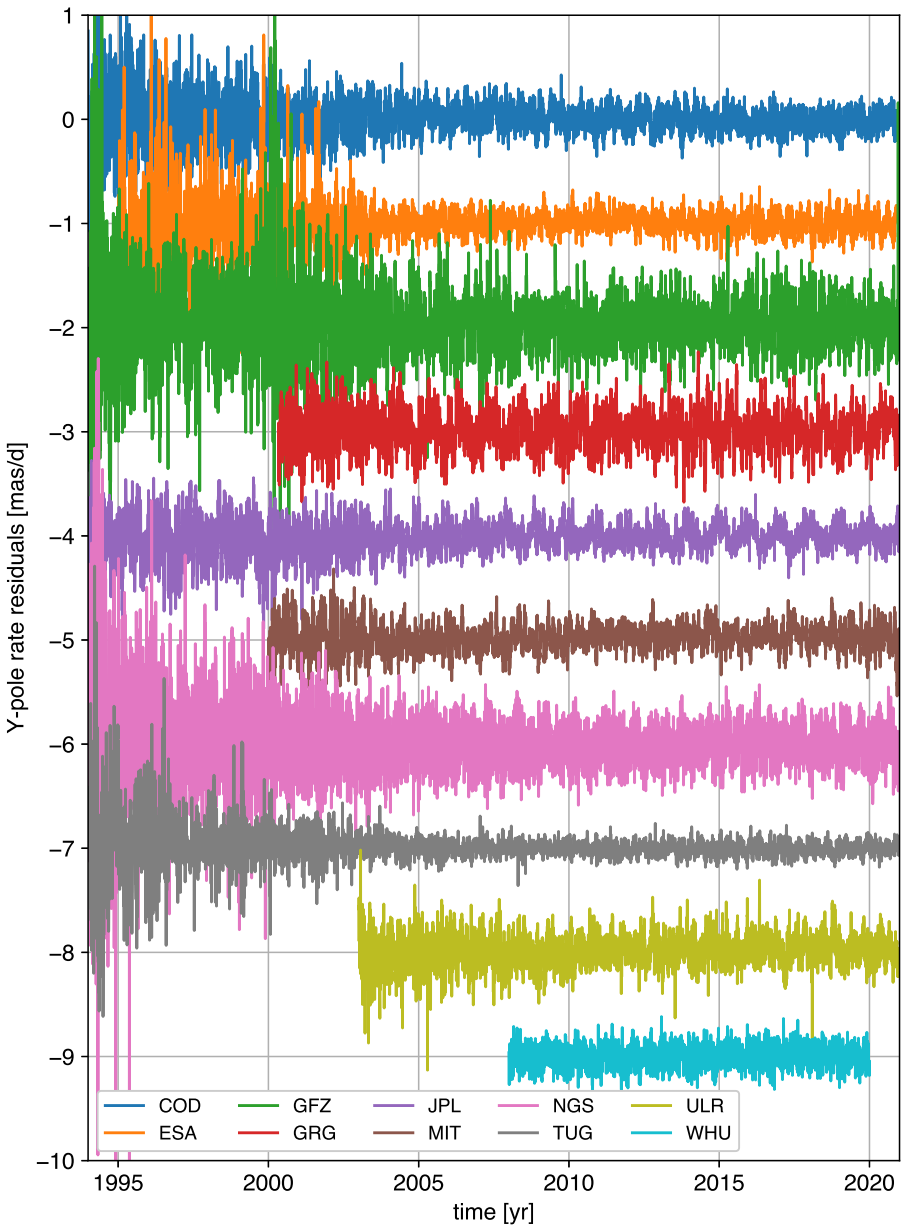

Fig. S13 AC Y-pole rate residuals offset by multiples of 1 mas/d

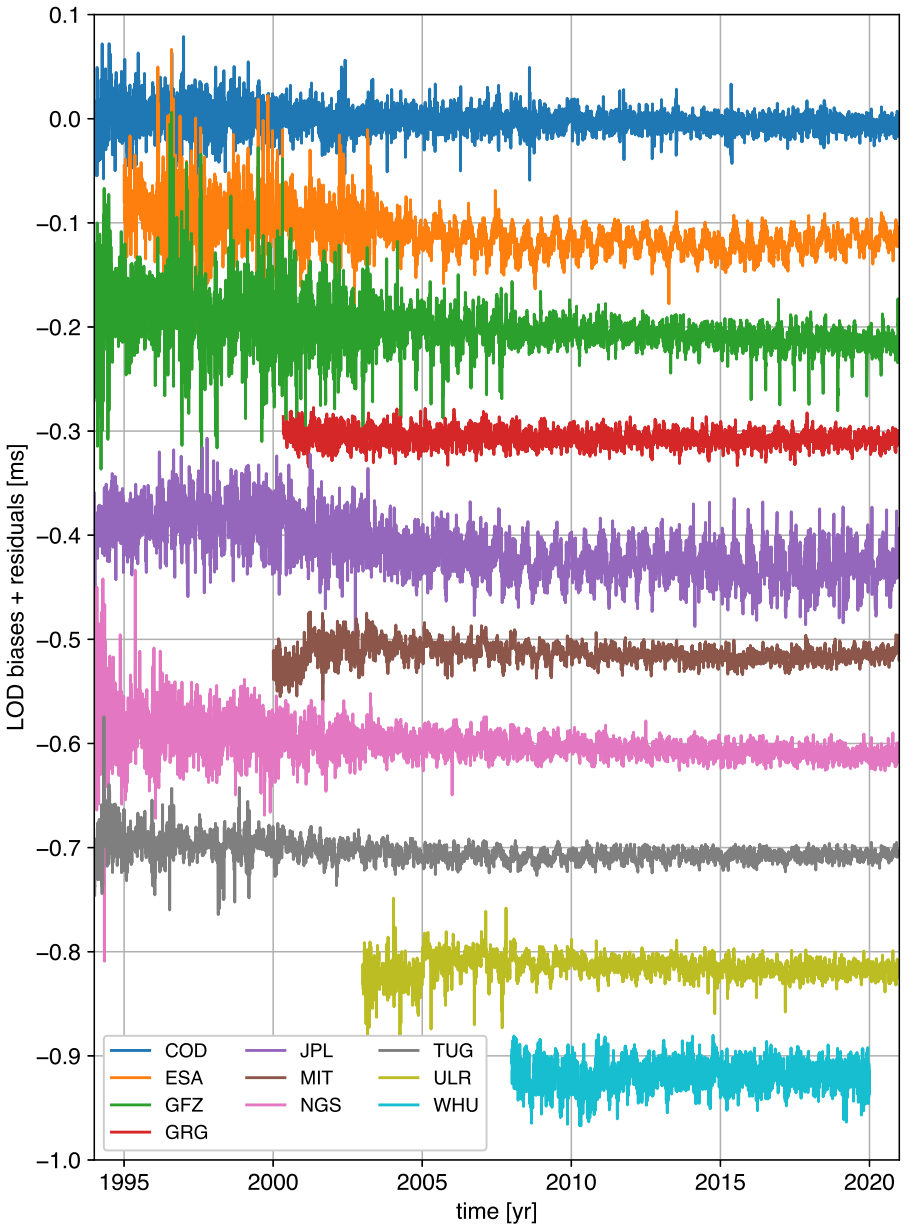

Fig. S14 Sums of the AC running LOD biases with respect to IERS Bulletin A and of the AC LOD residuals, offset by multiples of 0.1 ms. The GFZ LOD estimates actually show an additional offset of +0.075 ms with respect to Bulletin A, which has been removed in the figure so that GFZ does not overlap ESA.

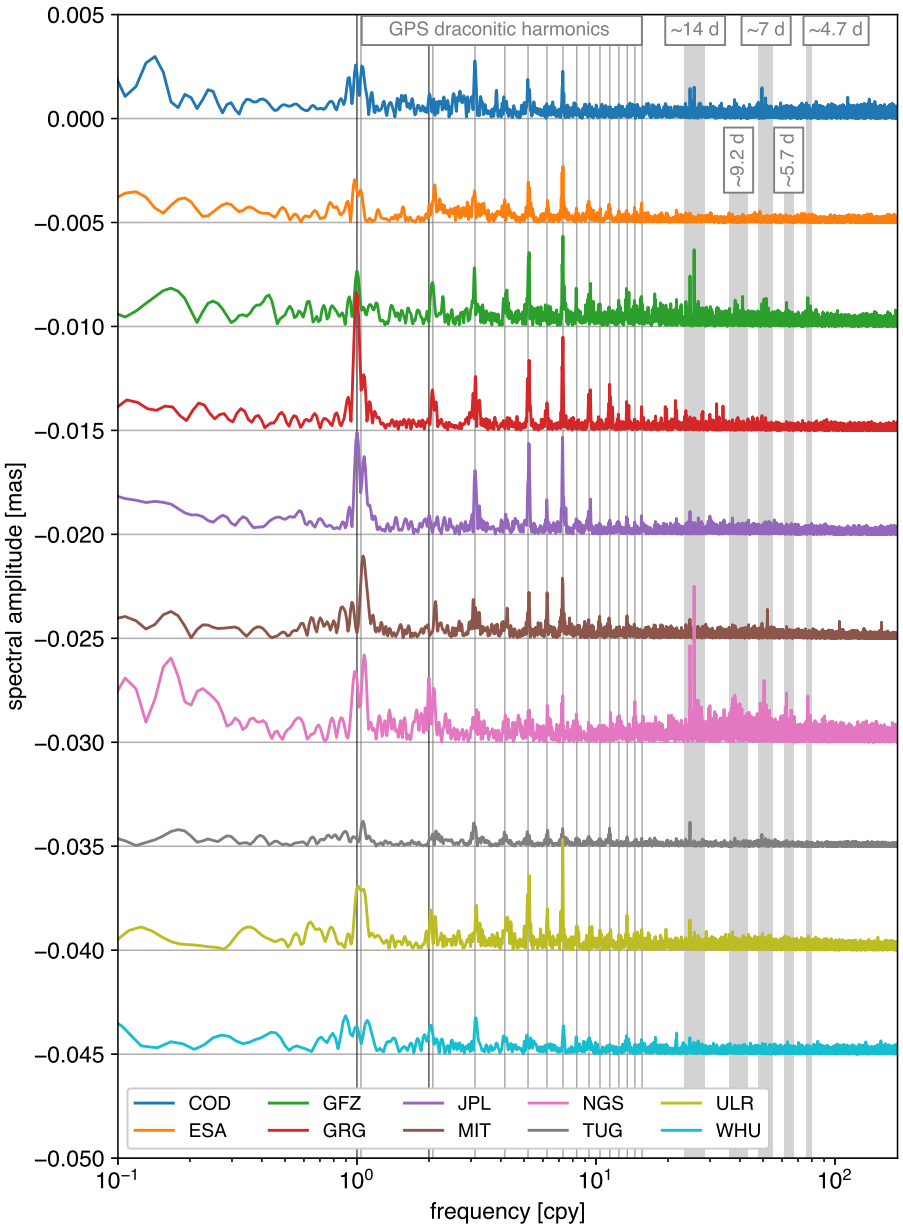

Fig. S15 Amplitude spectra of AC X-pole residuals for the period after 2000.0, offset by multiples of 5 µas. The *black vertical lines* indicate the annual and semi-annual frequencies. The *gray vertical lines* indicate harmonics of the GPS draconitic frequency. The *gray vertical patches* span periods around 14, 9.2, 7, 5.7 and 4.7 d.

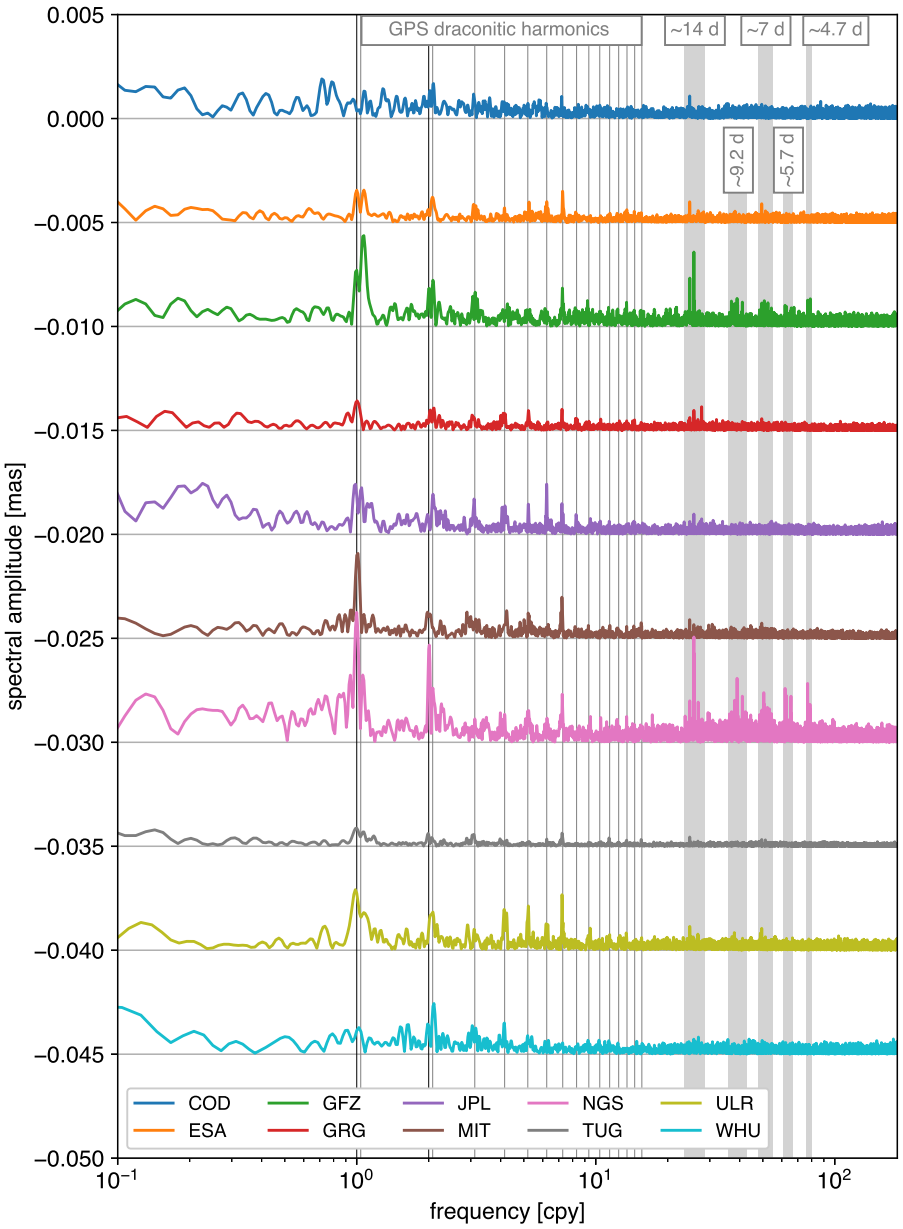

Fig. S16 Amplitude spectra of AC Y-pole residuals for the period after 2000.0, offset by multiples of 5 µas. The *black vertical lines* indicate the annual and semi-annual frequencies. The *gray vertical lines* indicate harmonics of the GPS draconitic frequency. The gray vertical patches span periods around 14, 9.2, 7, 5.7 and 4.7 d.

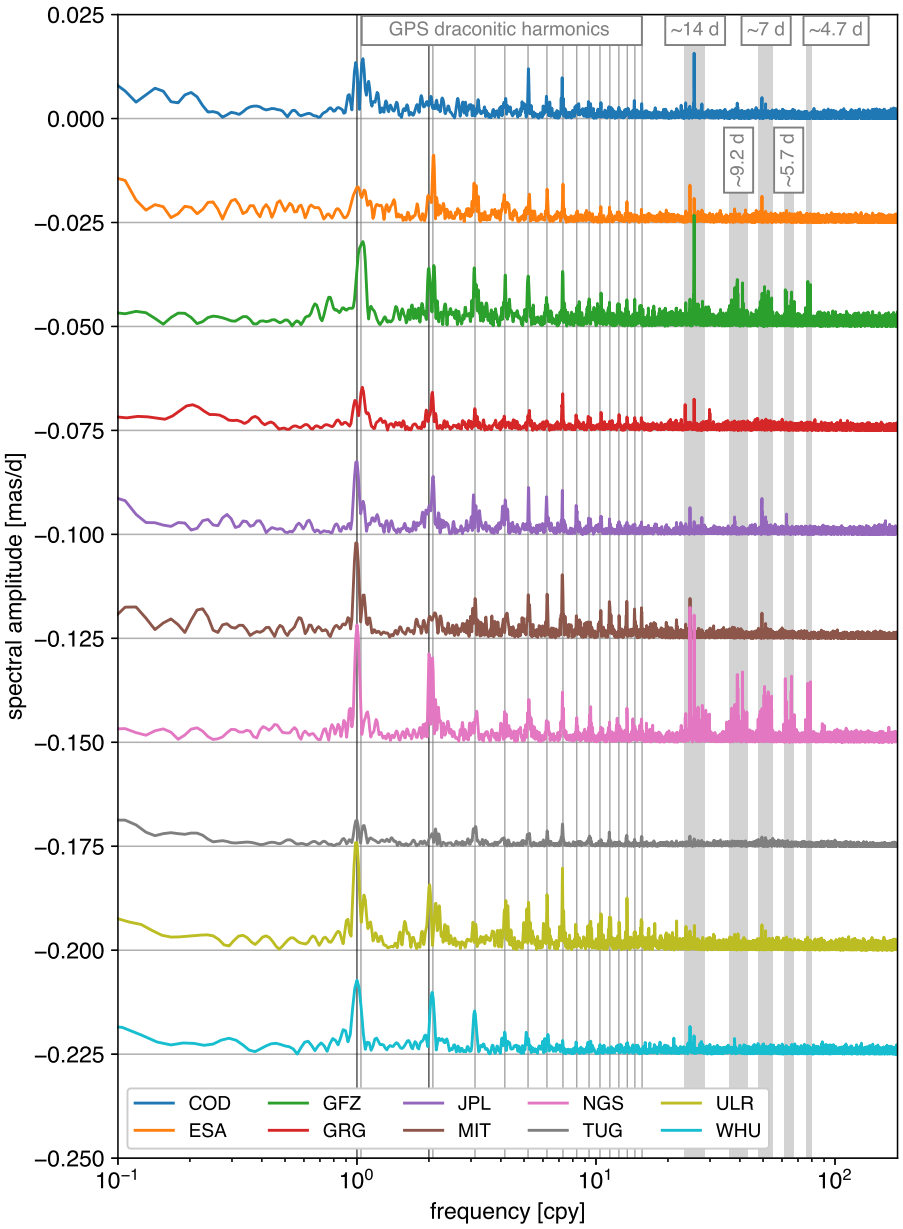

Fig. S17 Amplitude spectra of AC X-pole rate residuals for the period after 2000.0, offset by multiples of 25 µas/d. The *black vertical lines* indicate the annual and semi-annual frequencies. The *gray vertical lines* indicate harmonics of the GPS draconitic frequency. The *gray vertical patches* span periods around 14, 9.2, 7, 5.7 and 4.7 d.

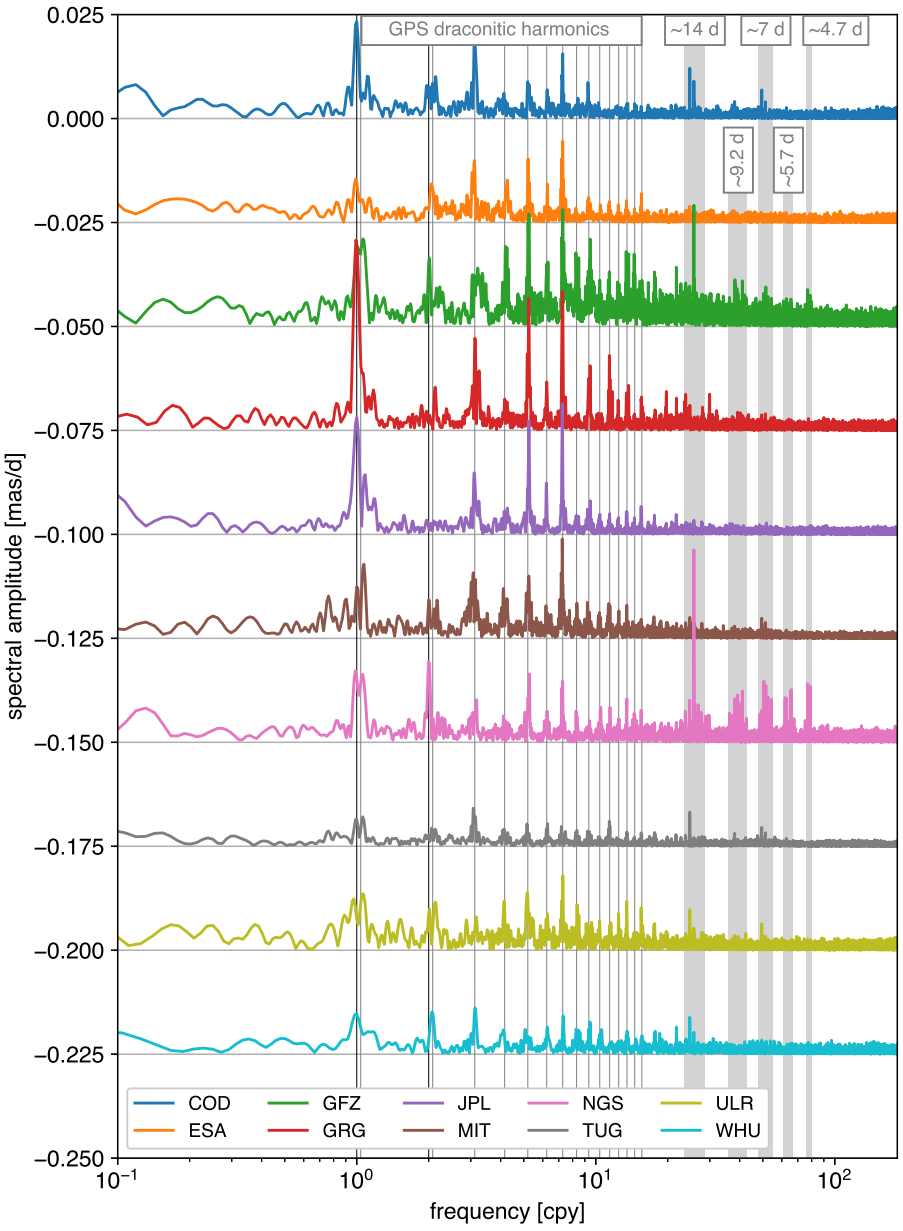

Fig. S18 Amplitude spectra of AC Y-pole rate residuals for the period after 2000.0, offset by multiples of 25 µas/d. The *black vertical lines* indicate the annual and semi-annual frequencies. The *gray vertical lines* indicate harmonics of the GPS draconitic frequency. The *gray vertical patches* span periods around 14, 9.2, 7, 5.7 and 4.7 d.

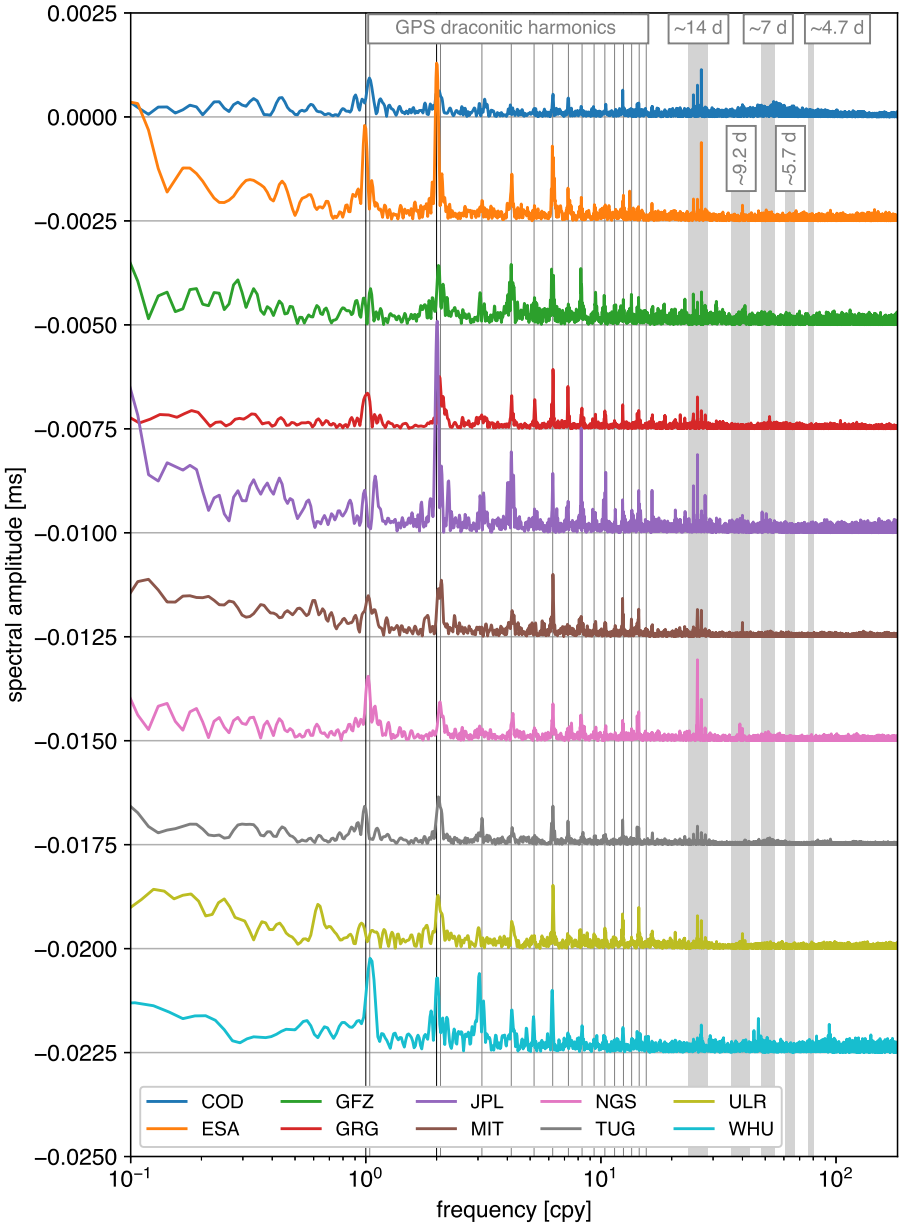

Fig. S19 Amplitude spectra of the sums of the AC running LOD biases with respect to IERS Bulletin A and of the AC LOD residuals, for the period after 2000.0, offset by multiples of 2.5 µs. The *black vertical lines* indicate the annual and semi-annual frequencies. The *gray vertical lines* indicate harmonics of the GPS draconitic frequency. The *gray vertical patches* span periods around 14, 9.2, 7, 5.7 and 4.7 d.

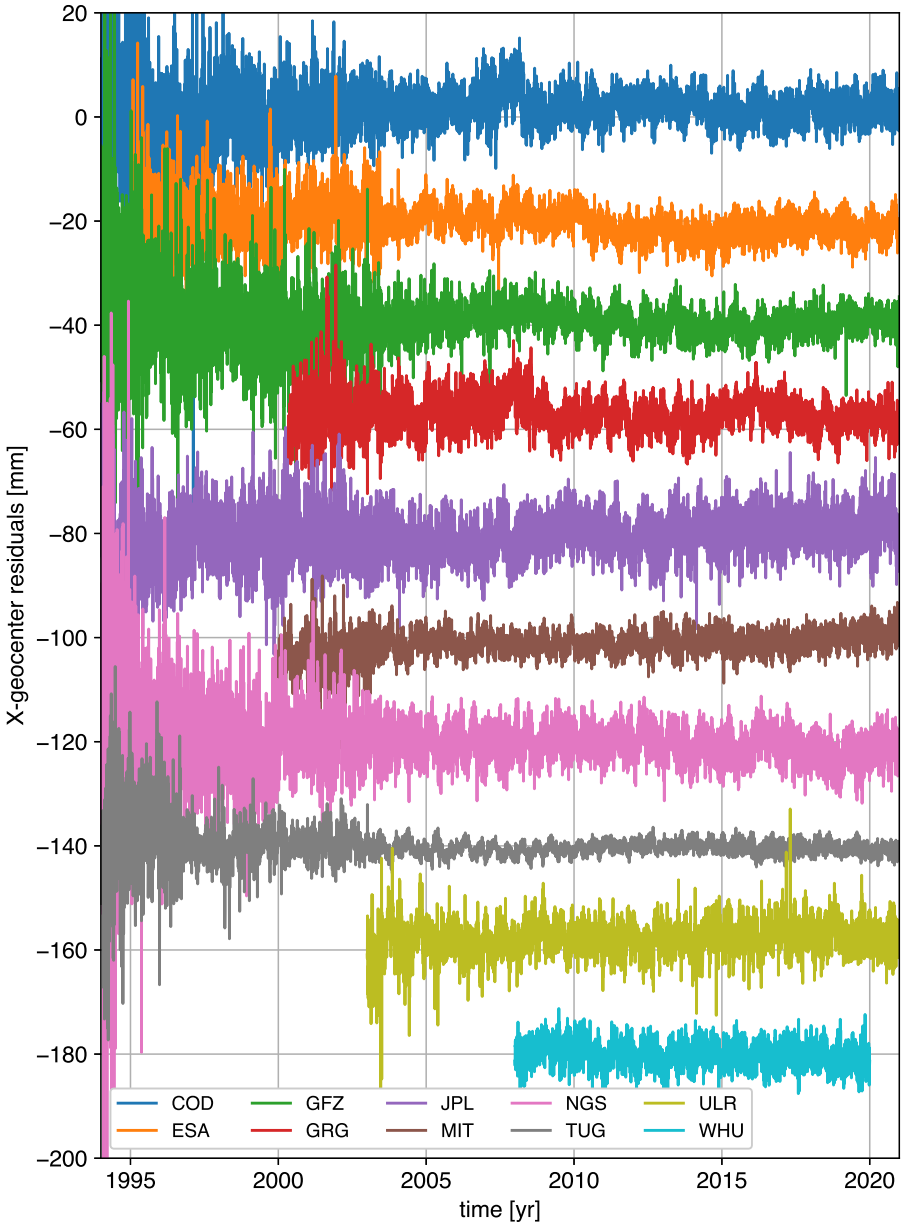

Fig. S20 AC X-geocenter residuals offset by multiples of 20 mm

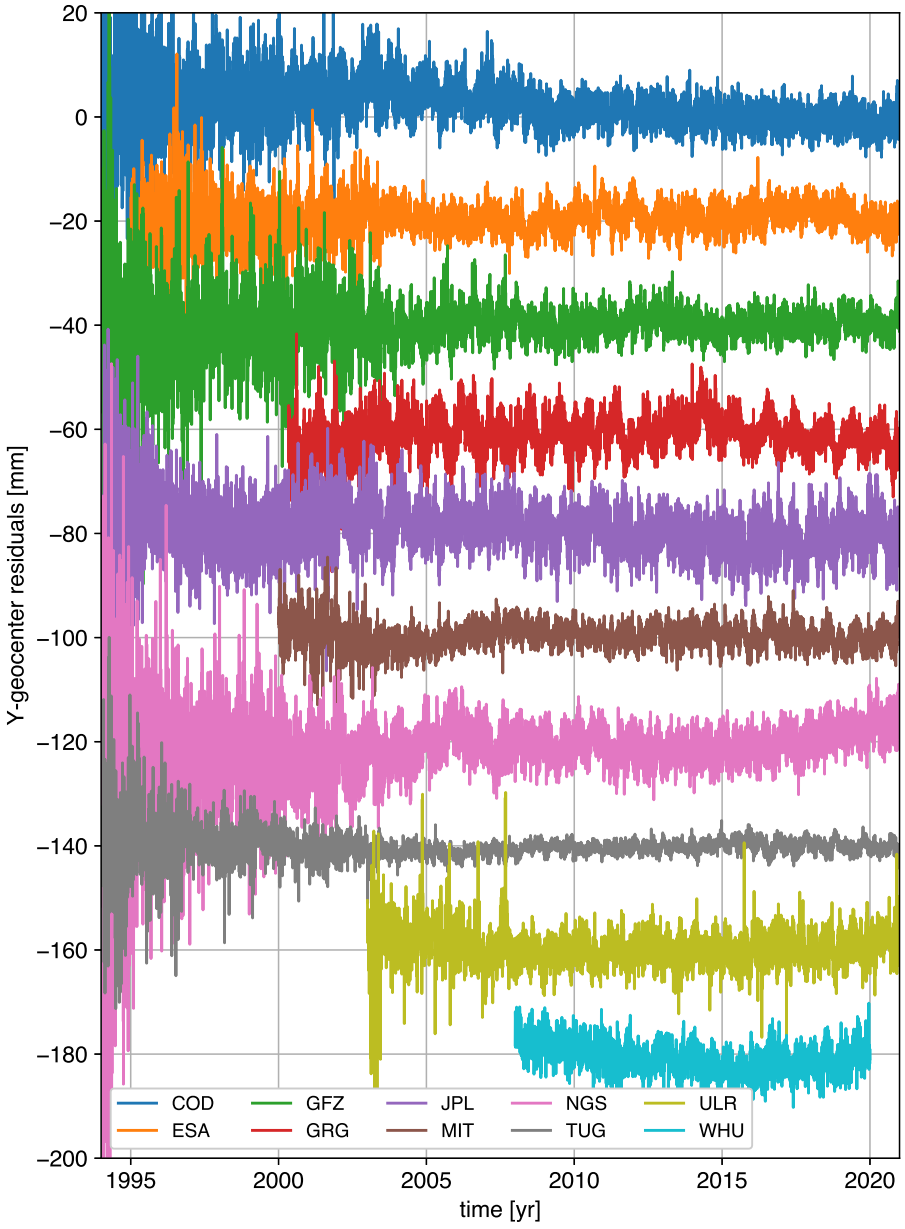

Fig. S21 AC Y-geocenter residuals offset by multiples of 20 mm

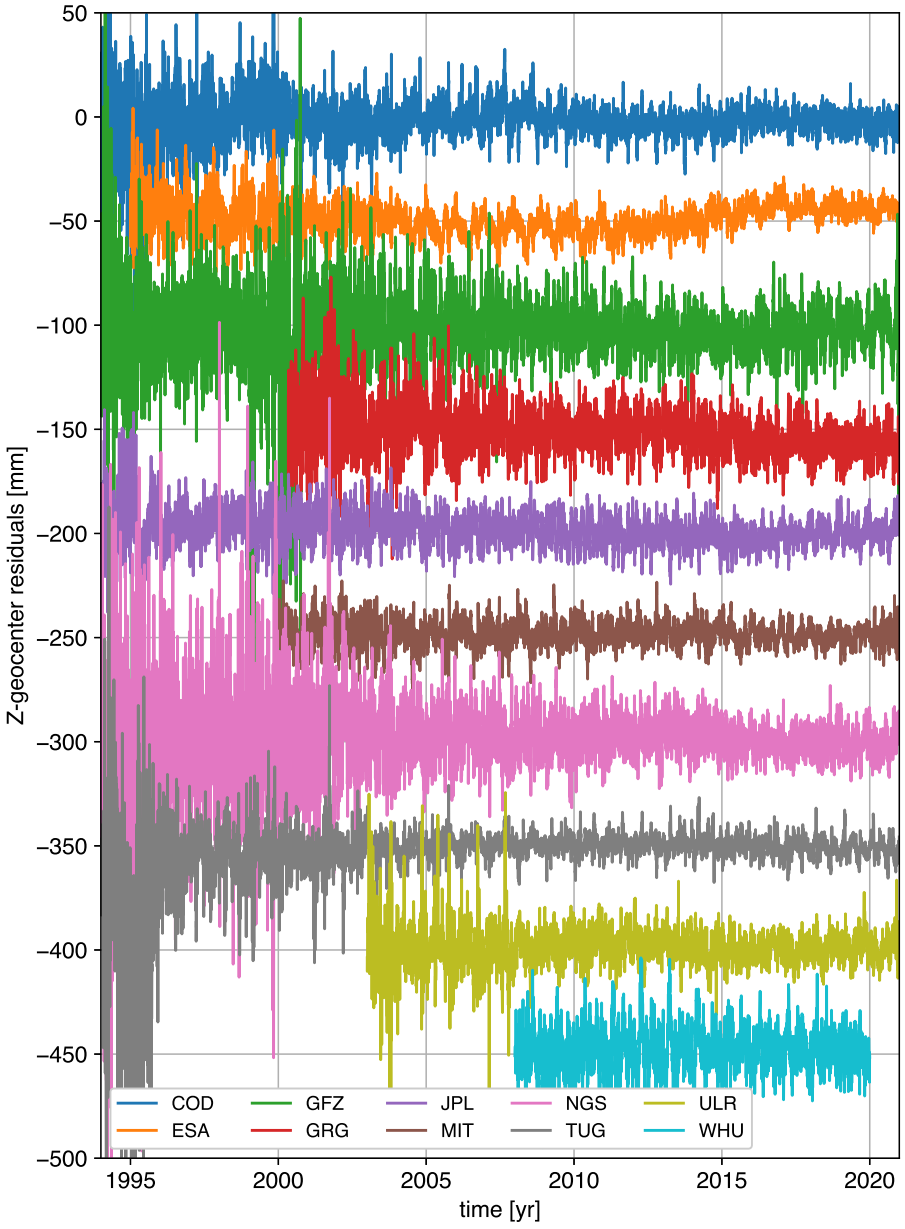

Fig. S22 AC Z-geocenter residuals offset by multiples of 50 mm

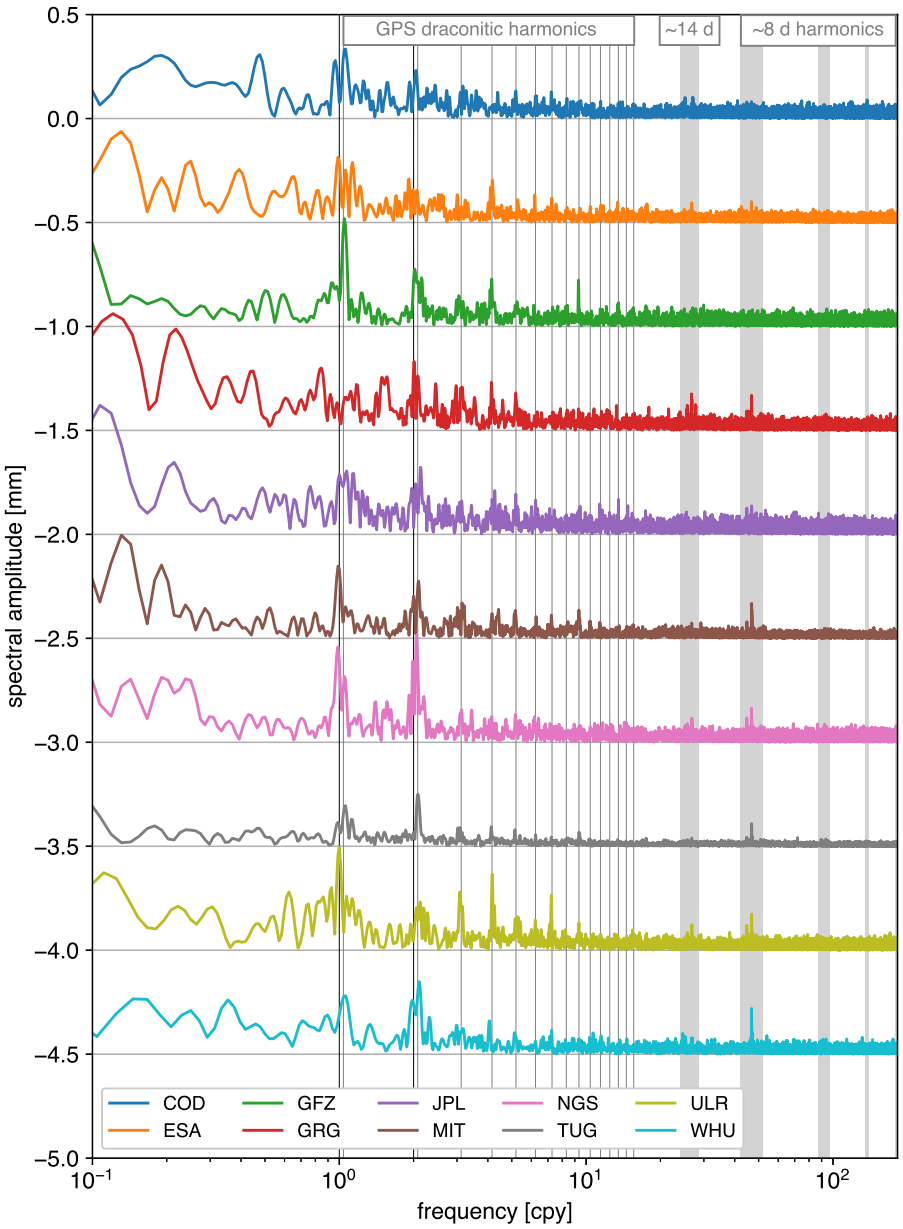

Fig. S23 Amplitude spectra of AC X-geocenter residuals for the period after 2000.0, offset by multiples of 0.5 mm. The *black vertical lines* indicate the annual and semi-annual frequencies. The *gray vertical lines* indicate harmonics of the GPS draconitic frequency. The *gray vertical patches* span periods around 14 d and harmonics of 8 d.

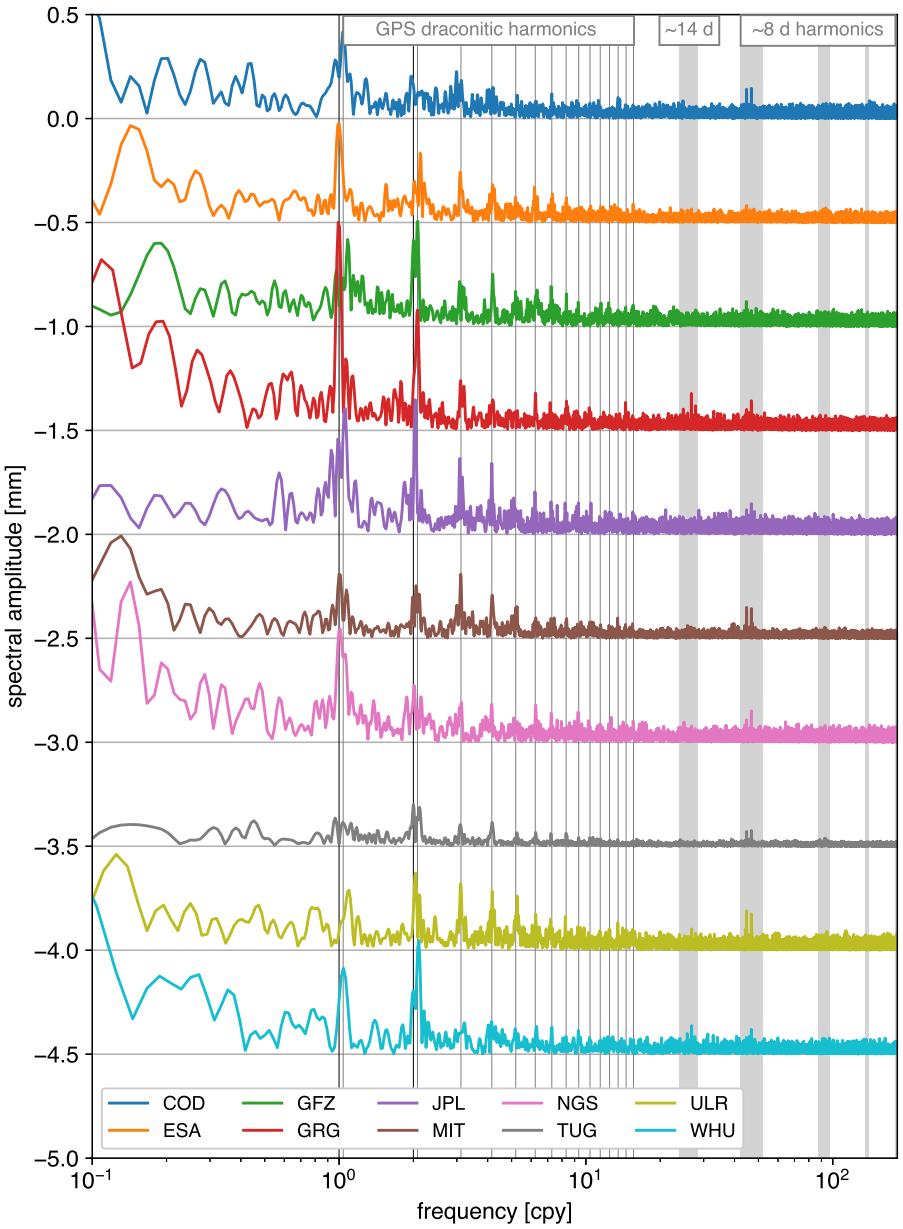

Fig. S24 Amplitude spectra of AC Y-geocenter residuals for the period after 2000.0, offset by multiples of 0.5 mm. The *black vertical lines* indicate the annual and semi-annual frequencies. The *gray vertical lines* indicate harmonics of the GPS draconitic frequency. The *gray vertical patches* span periods around 14 d and harmonics of 8 d.

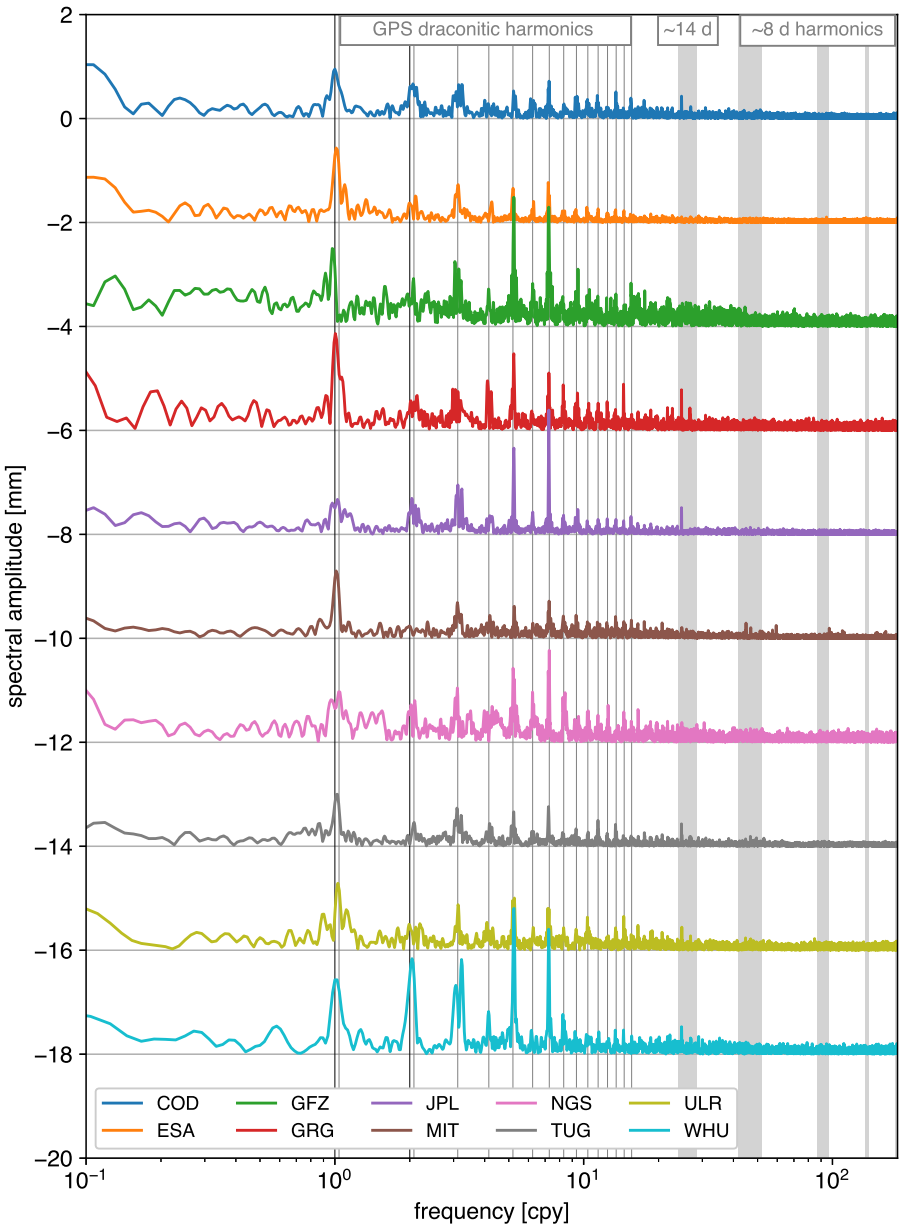

Fig. S25 Amplitude spectra of AC Z-geocenter residuals for the period after 2000.0, offset by multiples of 2 mm. The *black vertical lines* indicate the annual and semi-annual frequencies. The *gray vertical lines* indicate harmonics of the GPS draconitic frequency. The *gray vertical patches* span periods around 14 d and harmonics of 8 d.

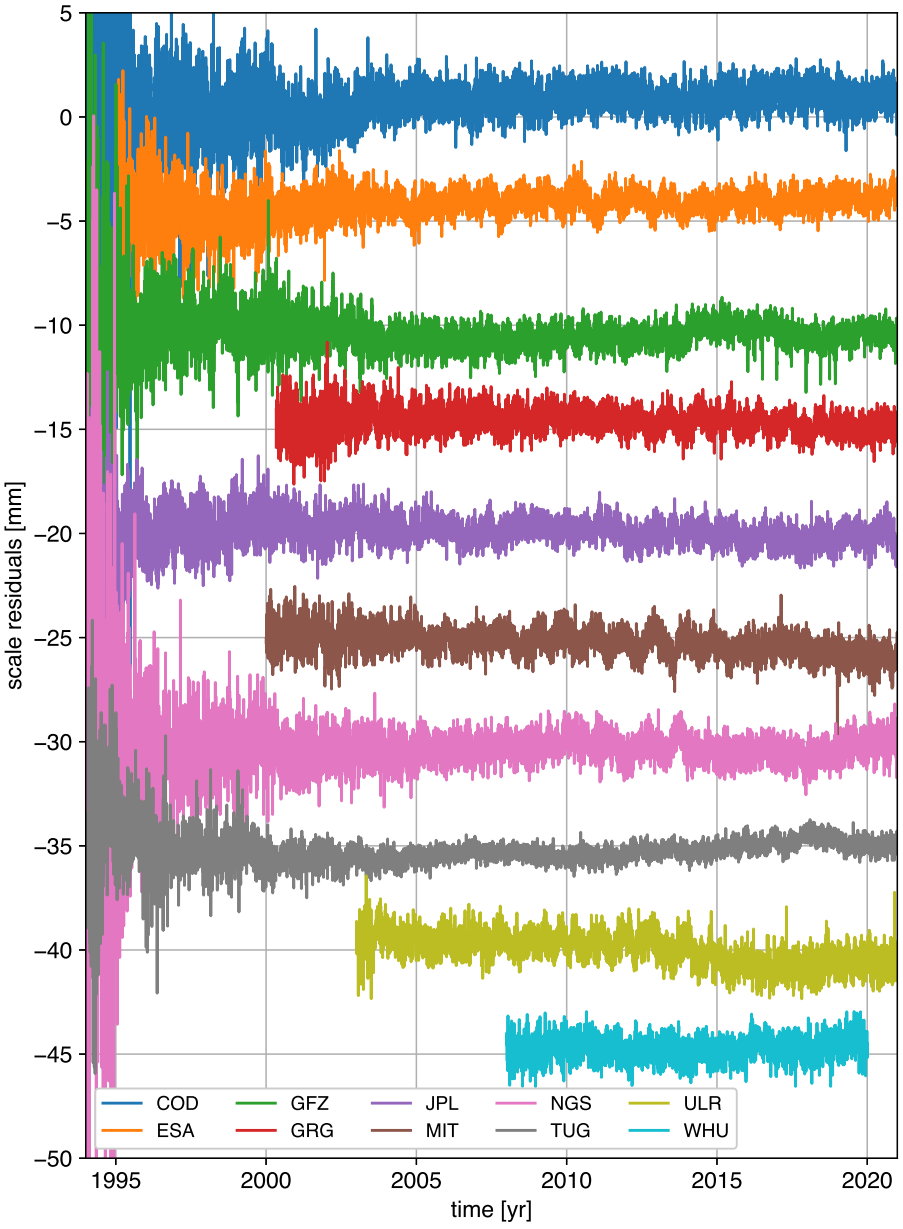

Fig. S26 AC terrestrial scale residuals offset by multiples of 5 mm

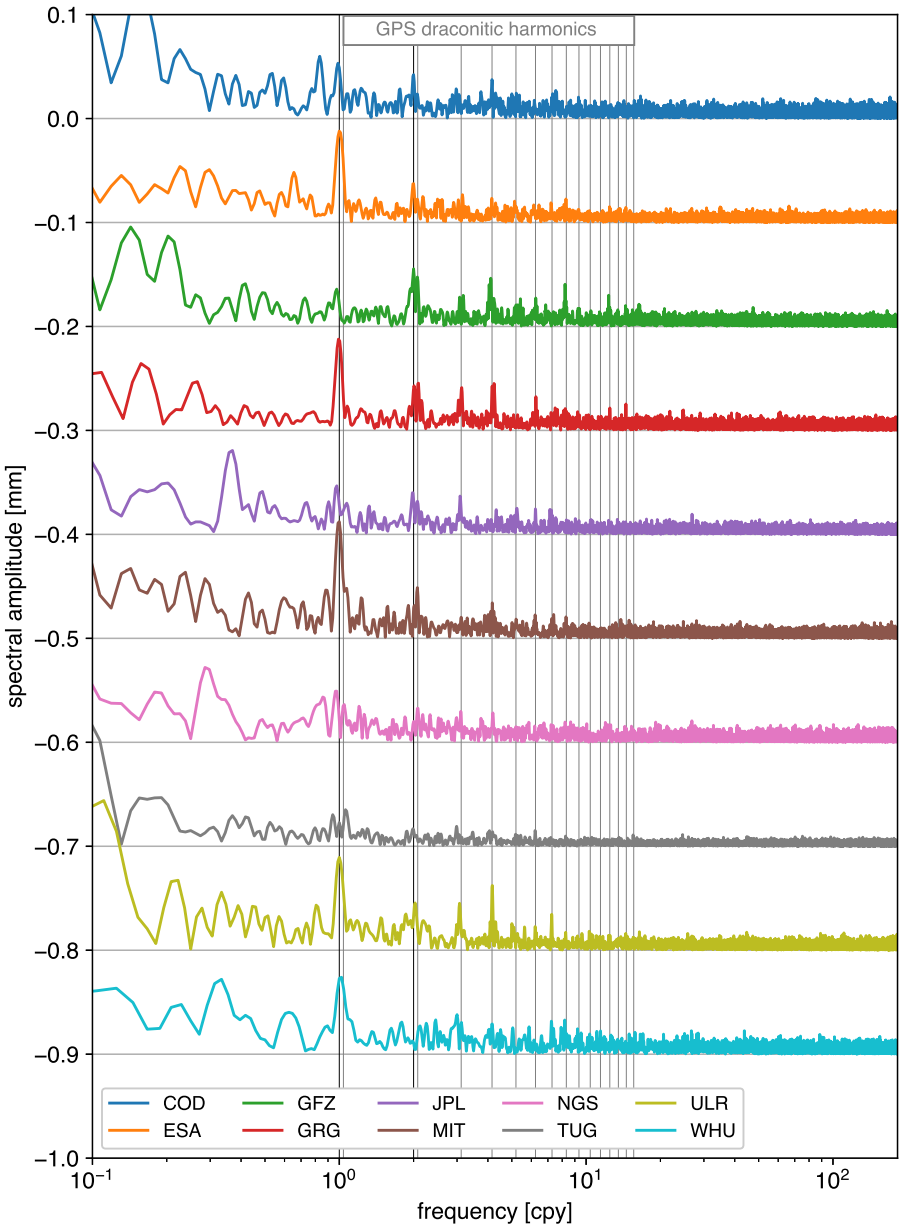

Fig. S27 Amplitude spectra of AC terrestrial scale residuals for the period after 2000.0, offset by multiples of 0.1 mm. The *black vertical lines* indicate the annual and semi-annual frequencies. The *gray vertical lines* indicate harmonics of the GPS draconitic frequency.

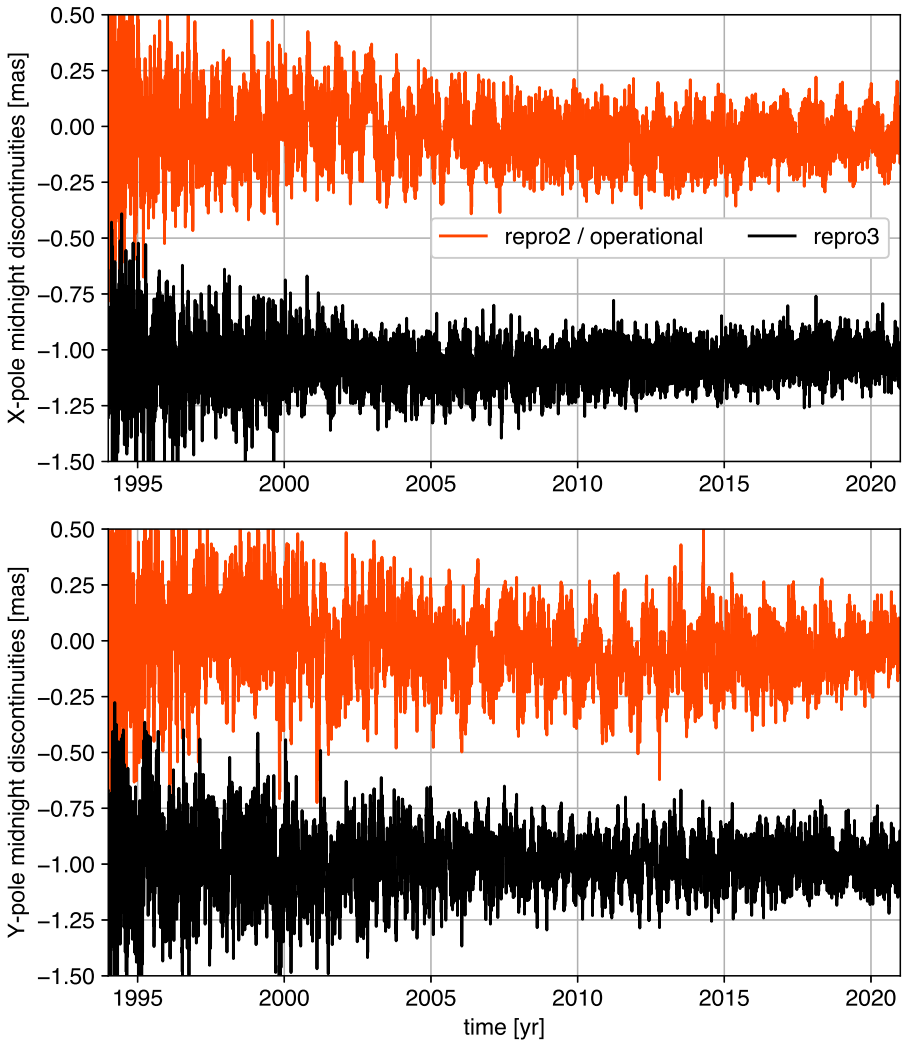

Fig. S28 Midnight polar motion discontinuities from the IGS repro2 and operational combined solutions (orange) and from the IGS repro3 combined solutions (black). The repro3 midnight polar motion discontinuities are offset by 1 mas for clarity.

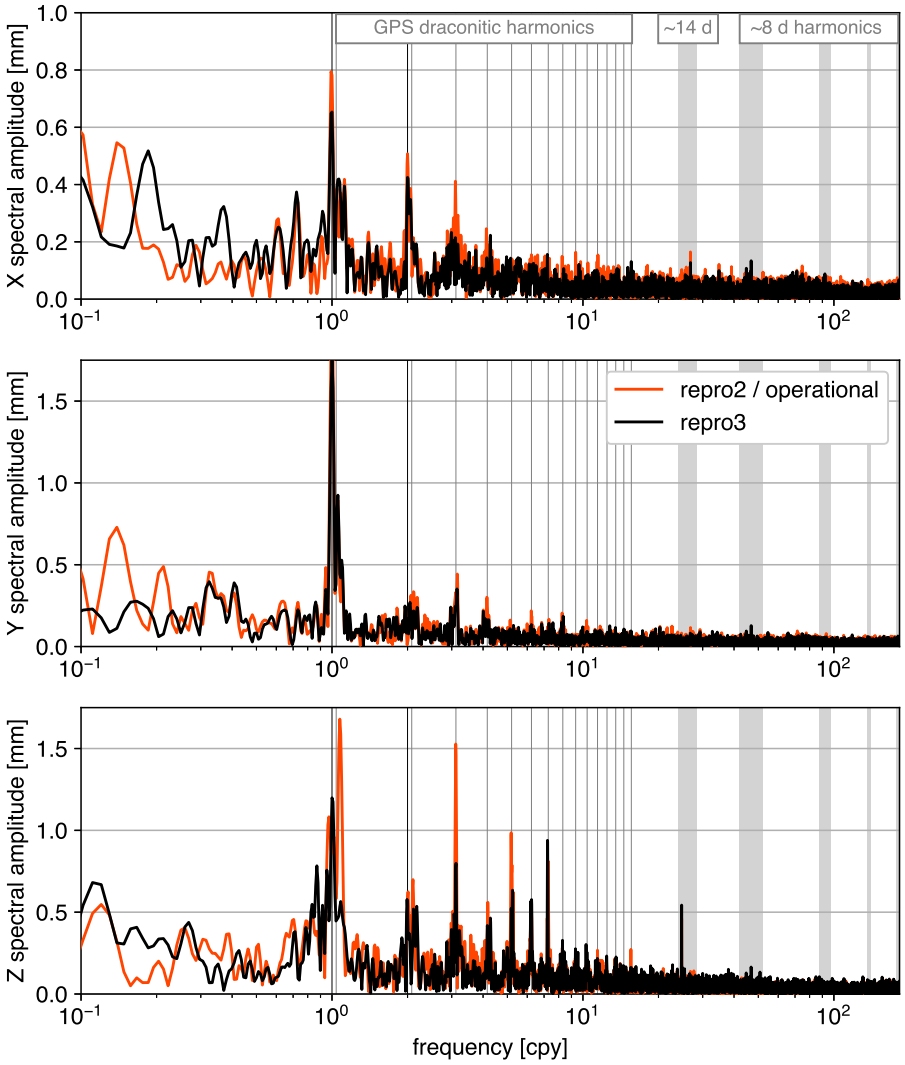

Fig. S29 Amplitude spectra of repro3 combined geocenter coordinate time series. The *black vertical lines* indicate the annual and semi-annual frequencies. The *gray vertical lines* indicate harmonics of the GPS draconitic frequency. The *gray vertical patches* span periods around 14 d and harmonics of 8 d.

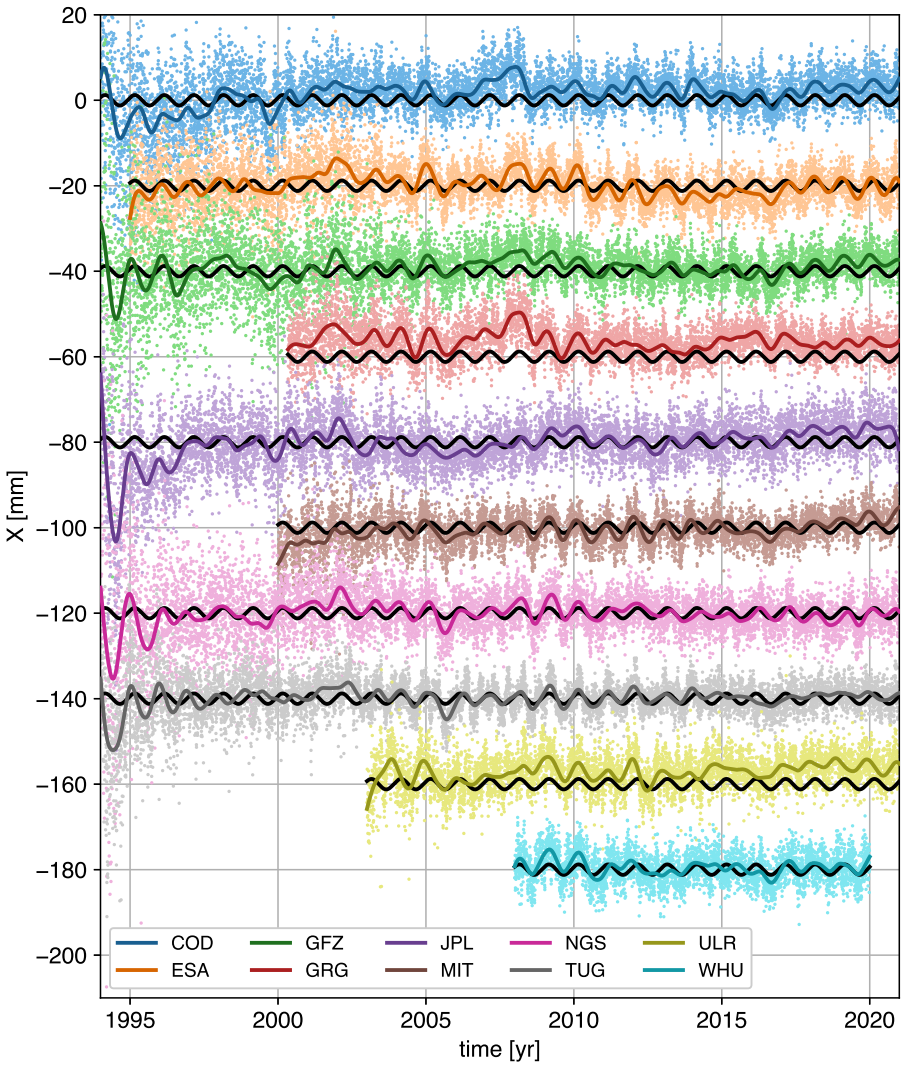

Fig. S30 *Colored dots:* X-geocenter coordinate time series from individual AC contributions to repro3. *Colored lines:* same time series smoothed by a Vondrák filter with a cutoff frequency of 1.25 cpy. *Black lines:* ITRF2020 annual geocenter motion model.

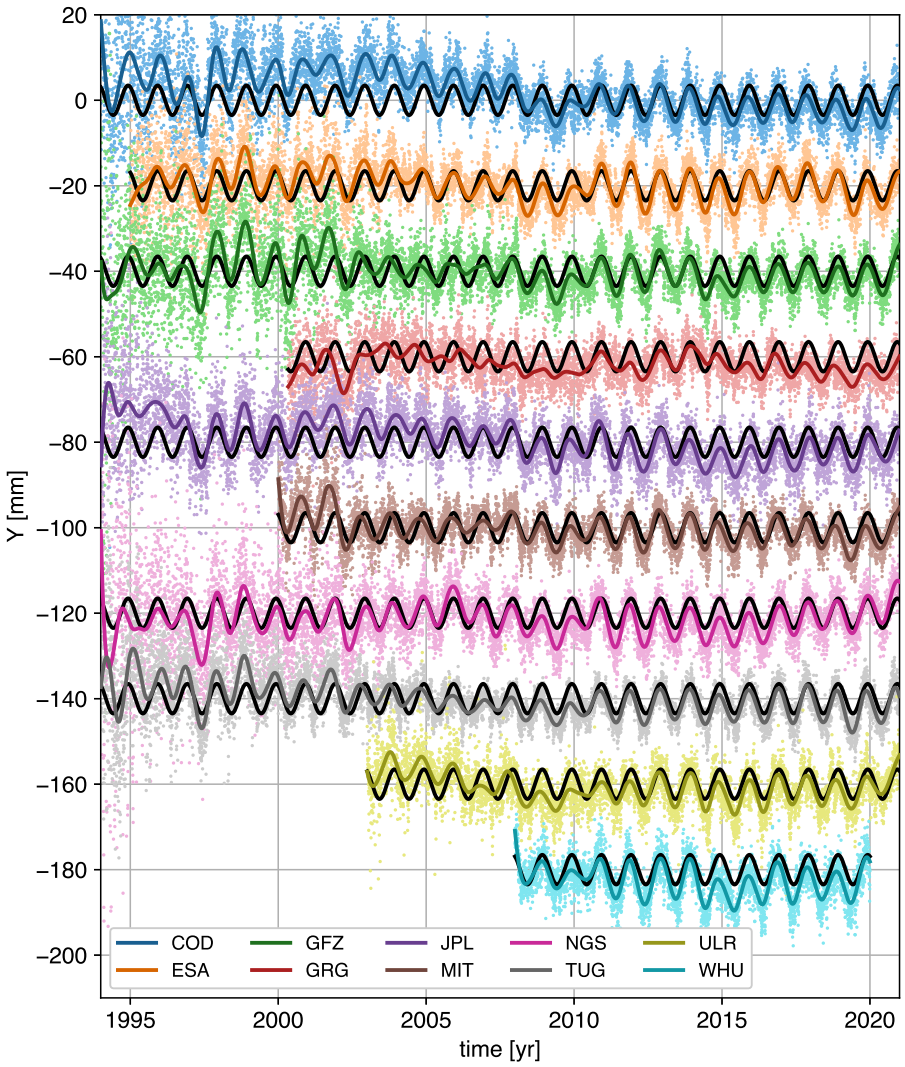

Fig. S31 *Colored dots:* Y-geocenter coordinate time series from individual AC contributions to repro3. *Colored lines:* same time series smoothed by a Vondrák filter with a cutoff frequency of 1.25 cpy. *Black lines:* ITRF2020 annual geocenter motion model.

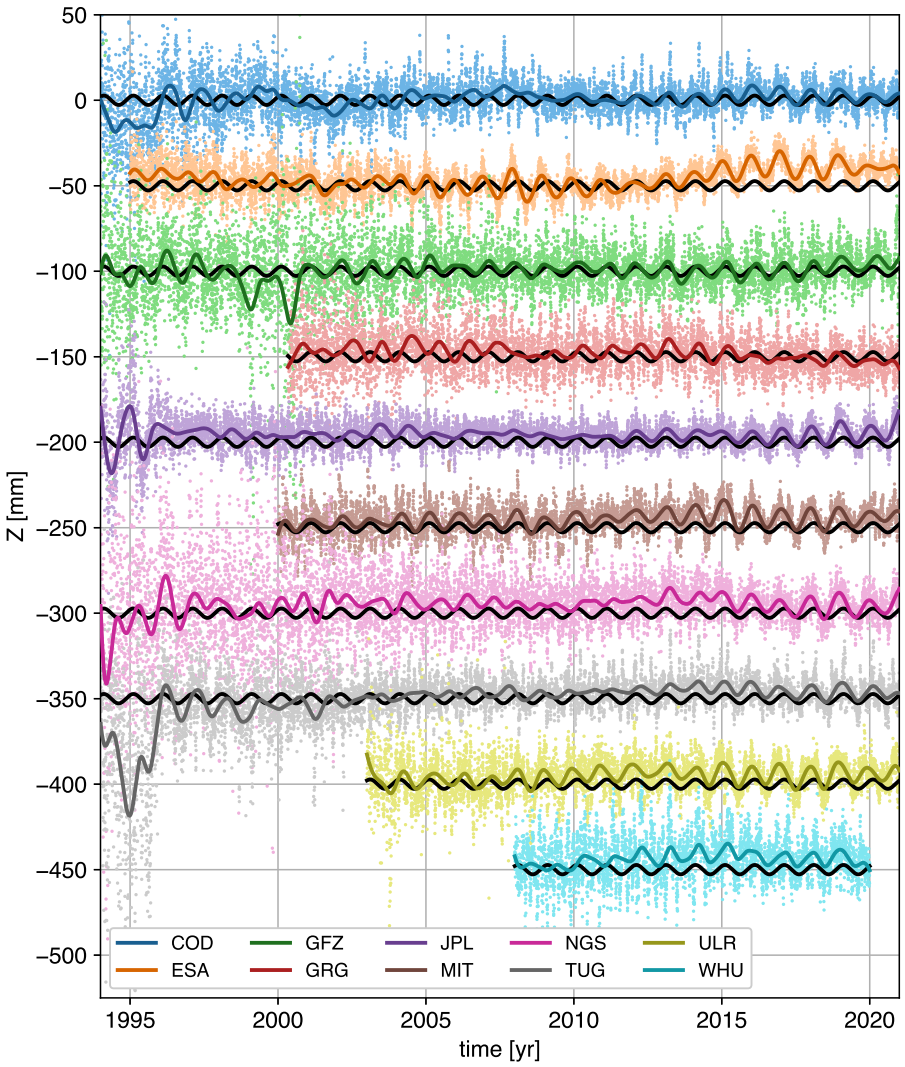

Fig. S32 *Colored dots:* Z-geocenter coordinate time series from individual AC contributions to repro3. *Colored lines:* same time series smoothed by a Vondrák filter with a cutoff frequency of 1.25 cpy. *Black lines:* ITRF2020 annual geocenter motion model.

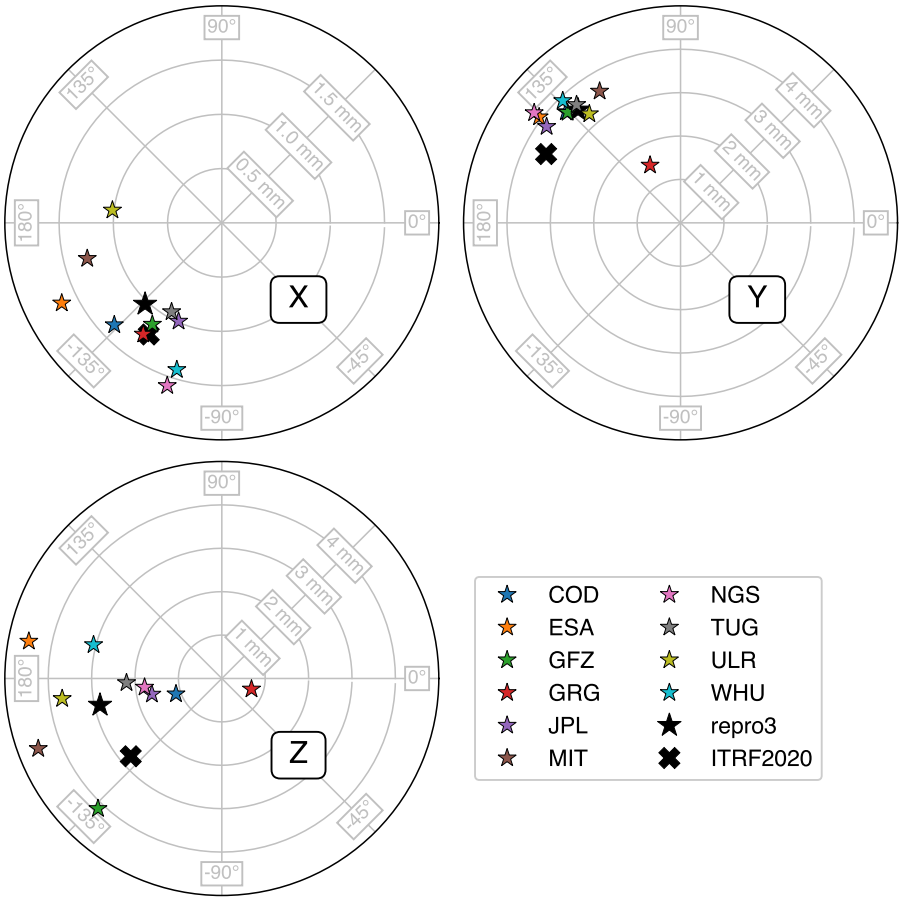

Fig. S33 Annual geocenter motion estimates from the individual AC contributions to repro3, from the repro3 combined solutions, and from ITRF2020

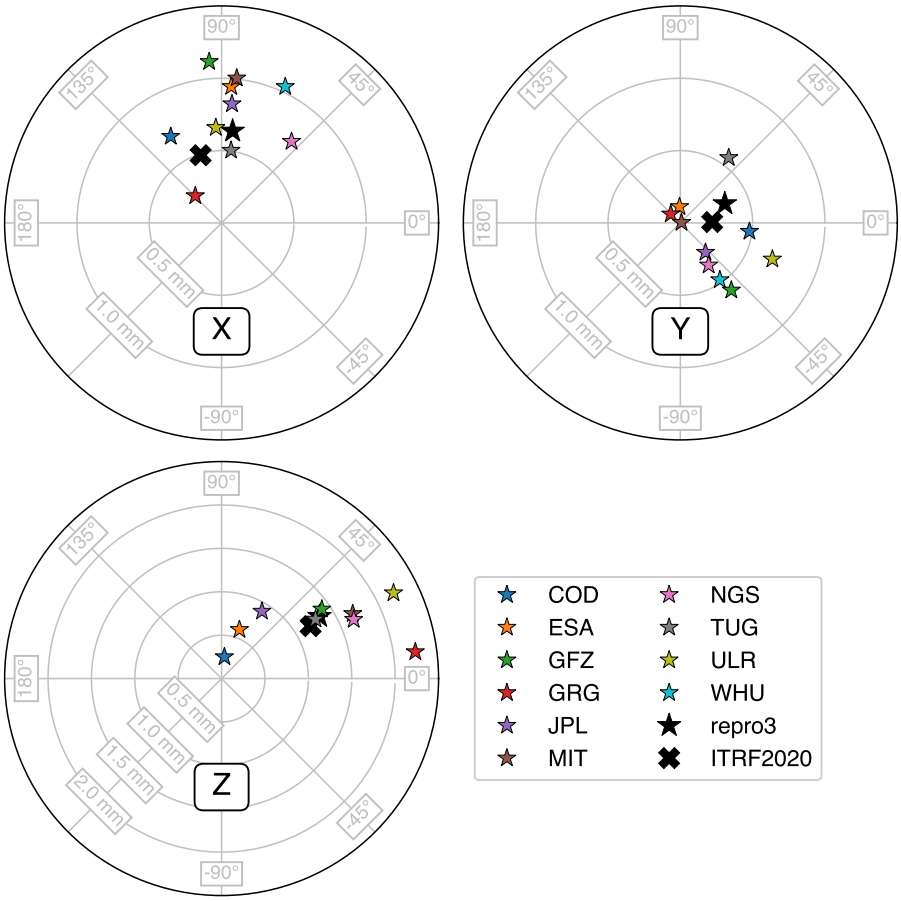

Fig. S34 Semi-annual geocenter motion estimates from the individual AC contributions to repro3, from the repro3 combined solutions, and from ITRF2020

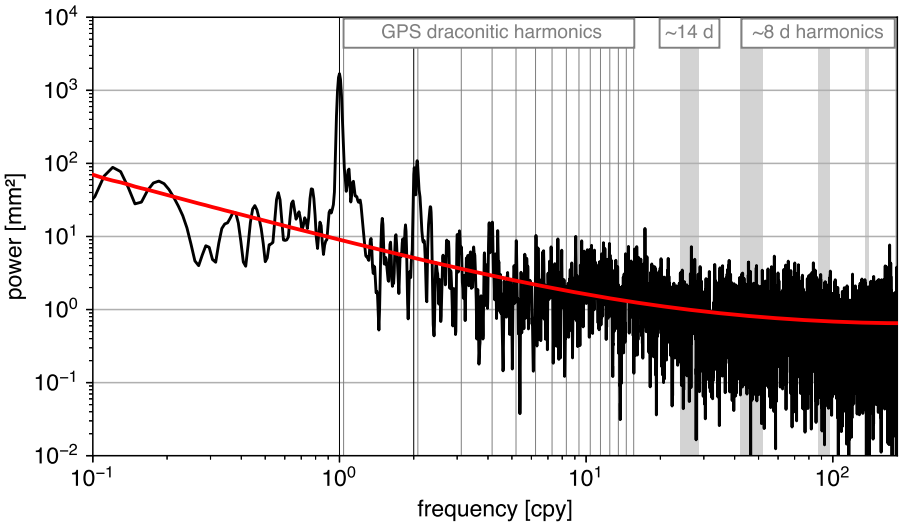

Fig. S35 *Black*: power spectrum of scale factors between repro3 combined solutions and IGSR3. *Red*: power spectrum of adjusted white + power-law noise model

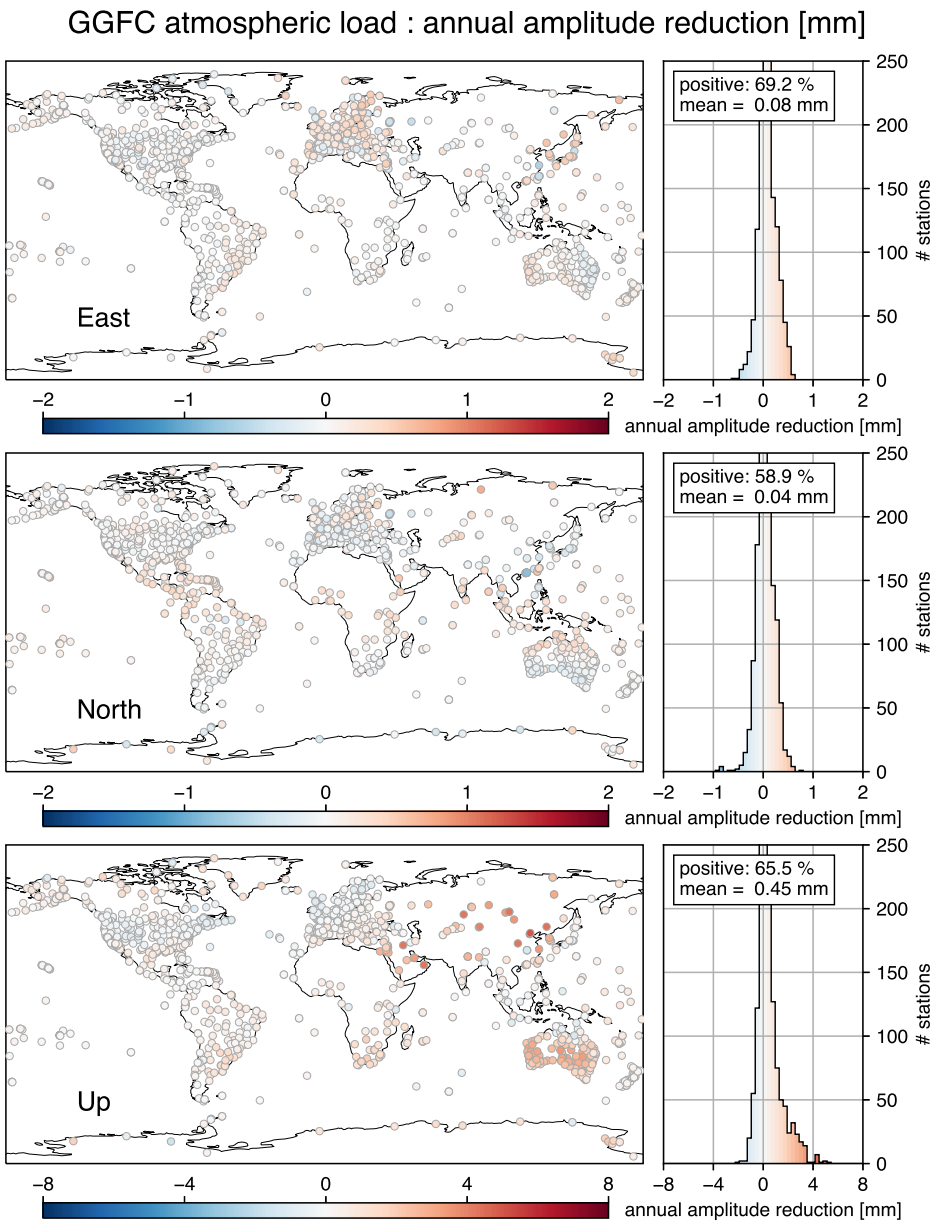

Fig. S36 Reductions of annual amplitudes achieved when correcting repro3 station position time series with GGFC atmospheric loading displacements

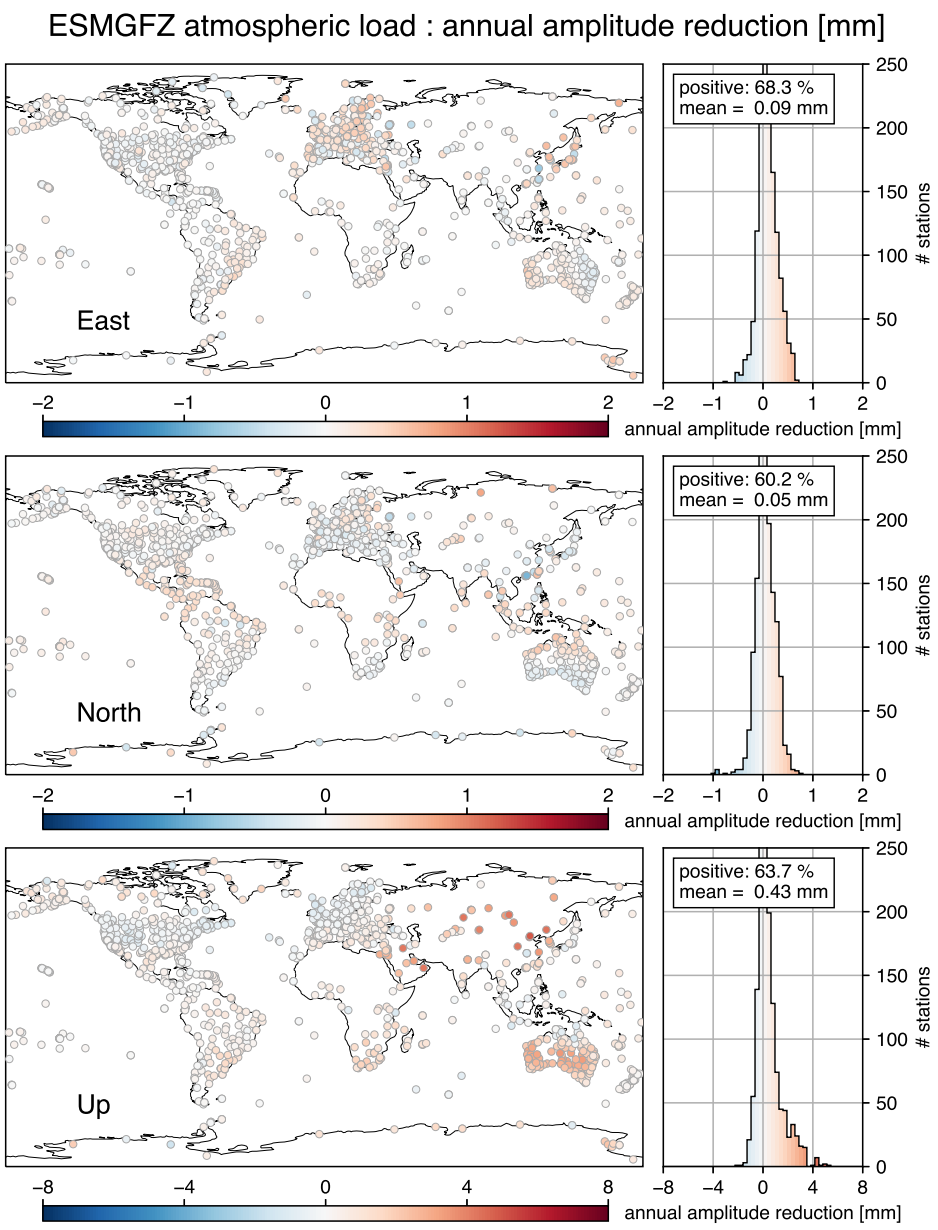

Fig. S37 Reductions of annual amplitudes achieved when correcting repro3 station position time series with ESMGFZ atmospheric loading displacements

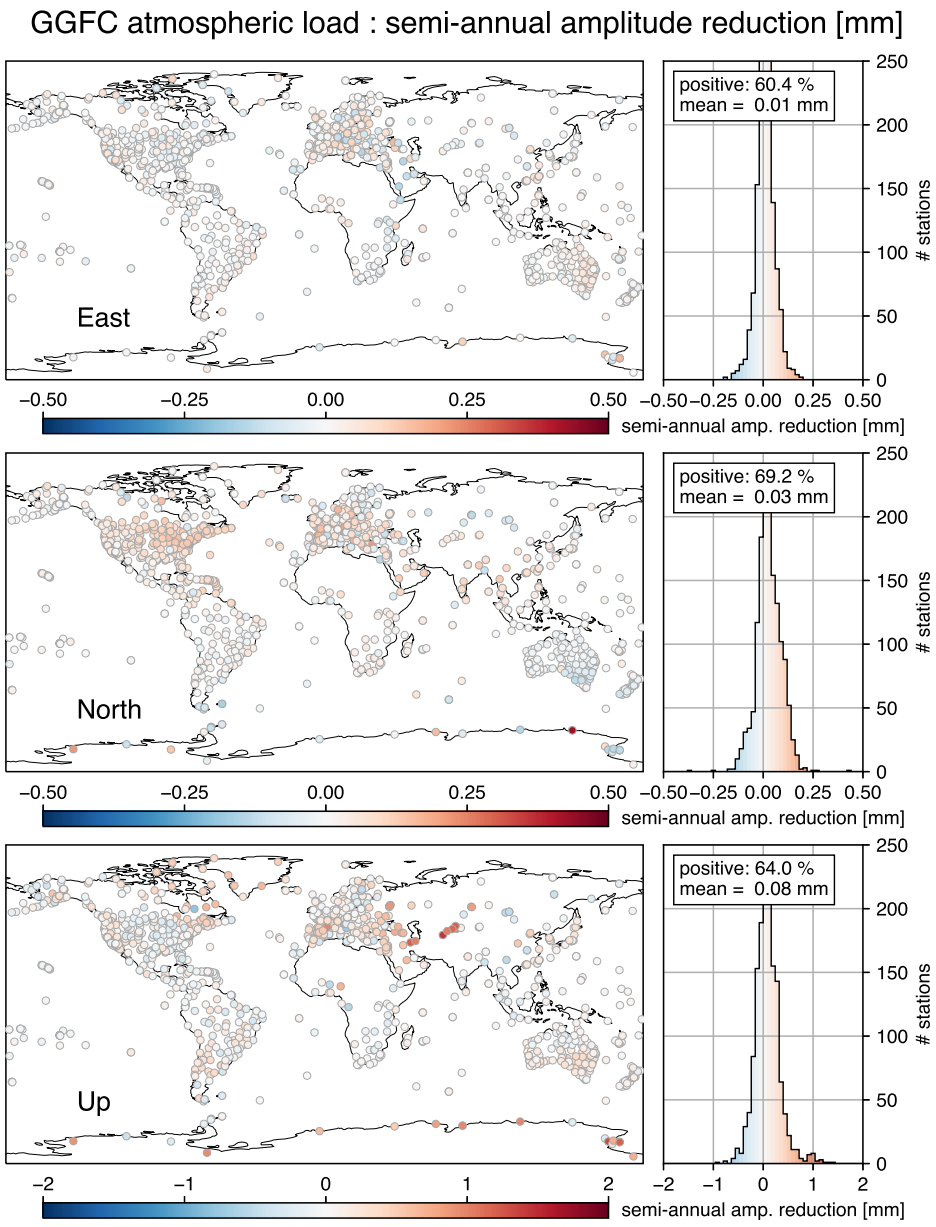

Fig. S38 Reductions of semi-annual amplitudes achieved when correcting repro3 station position time series with GGFC atmospheric loading displacements

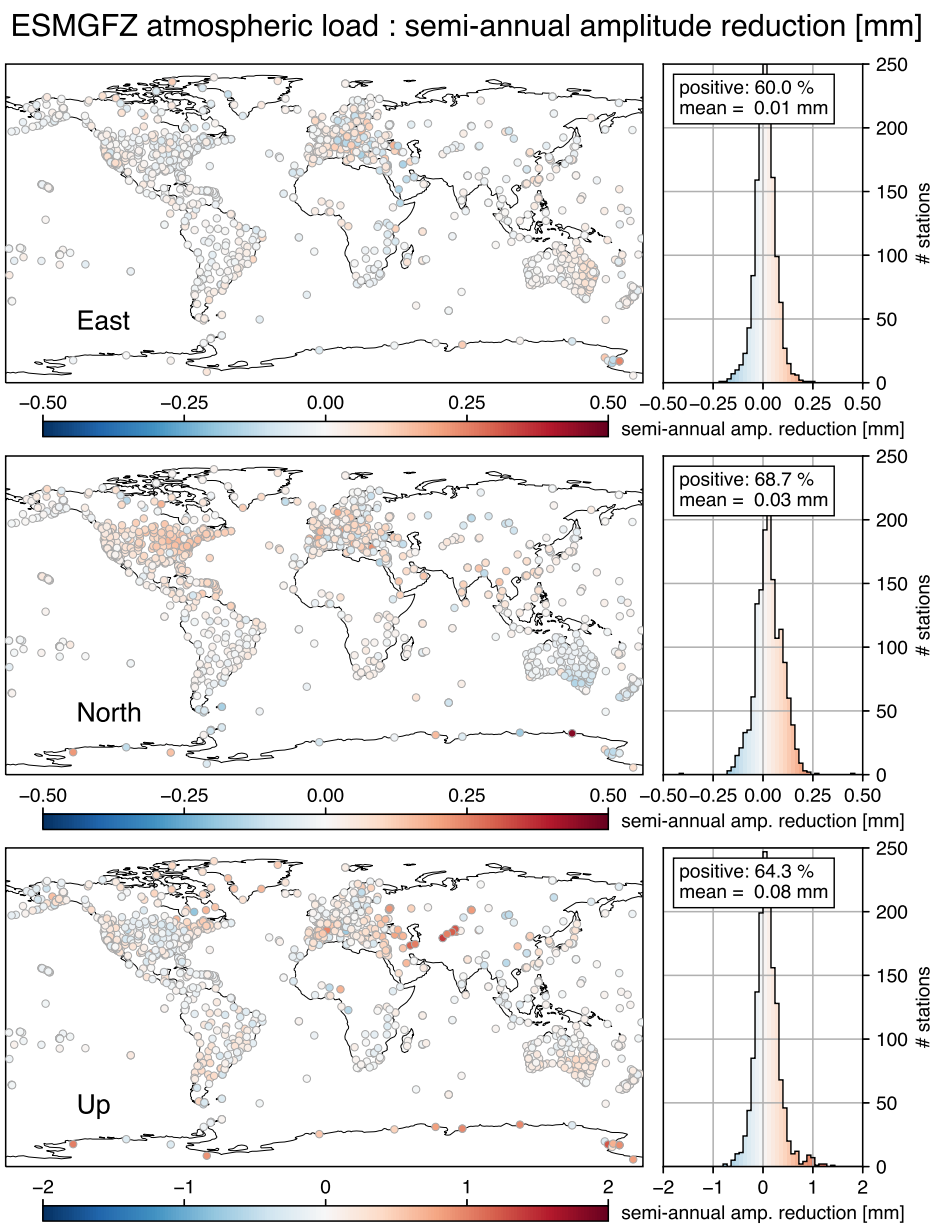

Fig. S39 Reductions of semi-annual amplitudes achieved when correcting repro3 station position time series with ESMGFZ atmospheric loading displacements

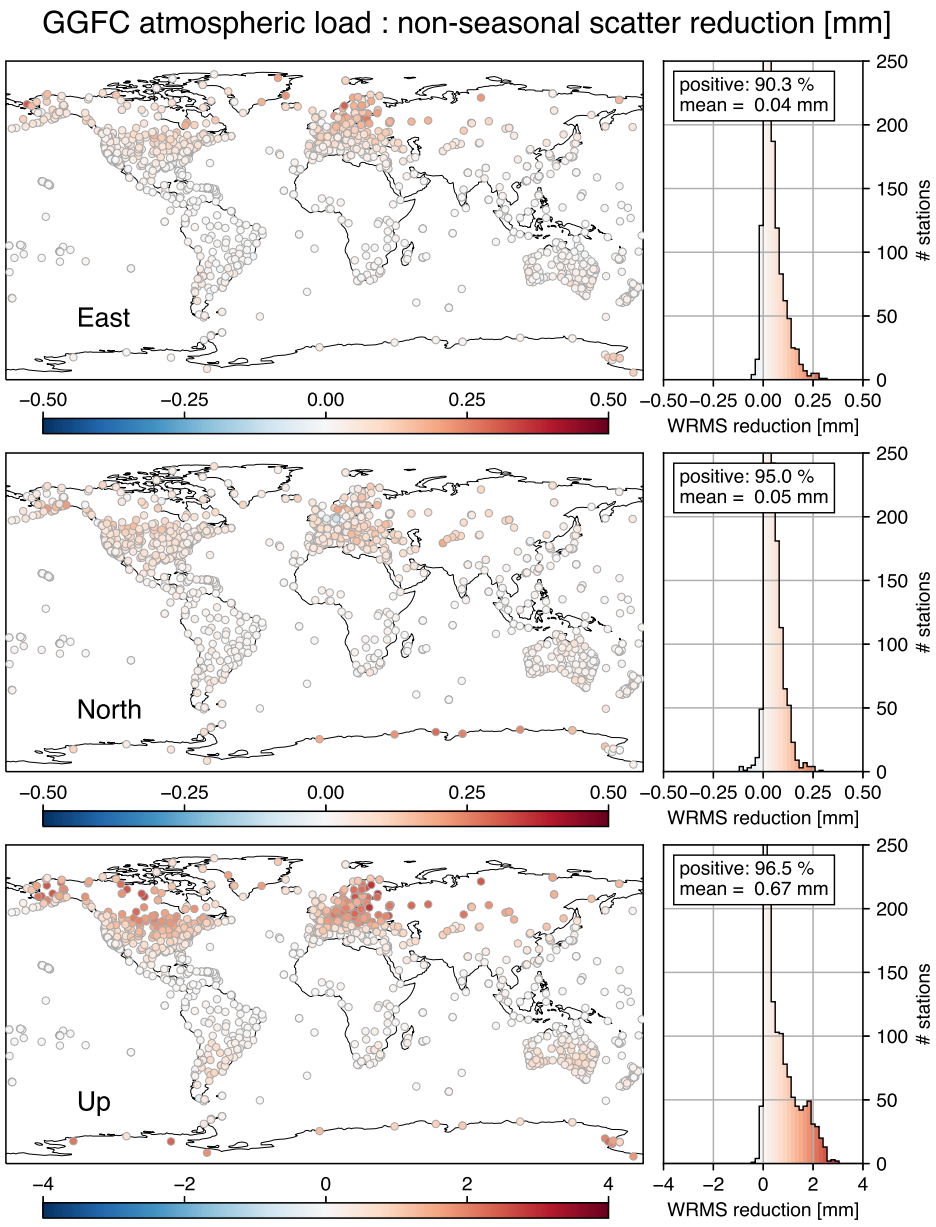

Fig. S40 Reductions of WRMS of trajectory model residuals achieved when correcting repro3 station position time series with GGFC atmospheric loading displacements

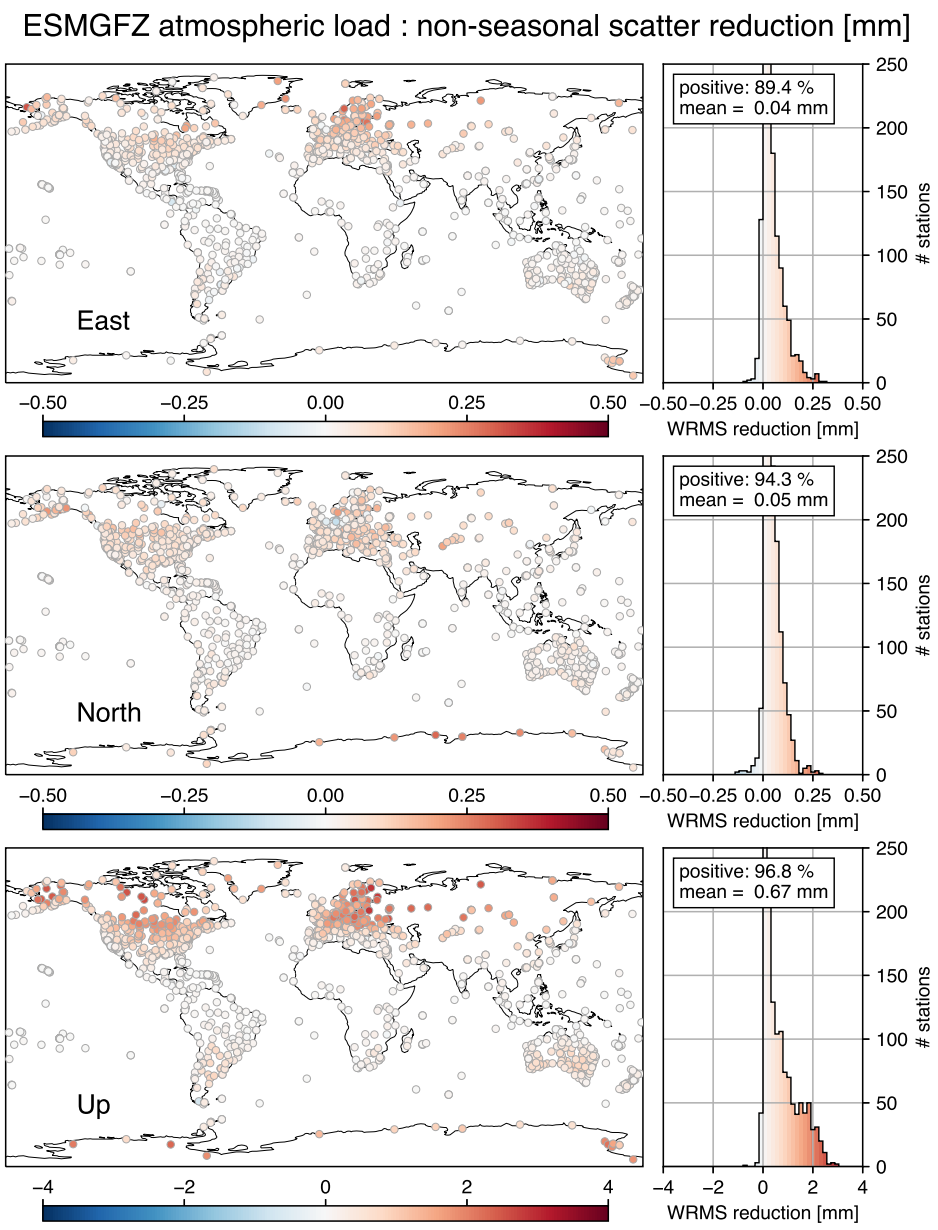

Fig. S41 Reductions of WRMS of trajectory model residuals achieved when correcting repro3 station position time series with ESMGFZ atmospheric loading displacements

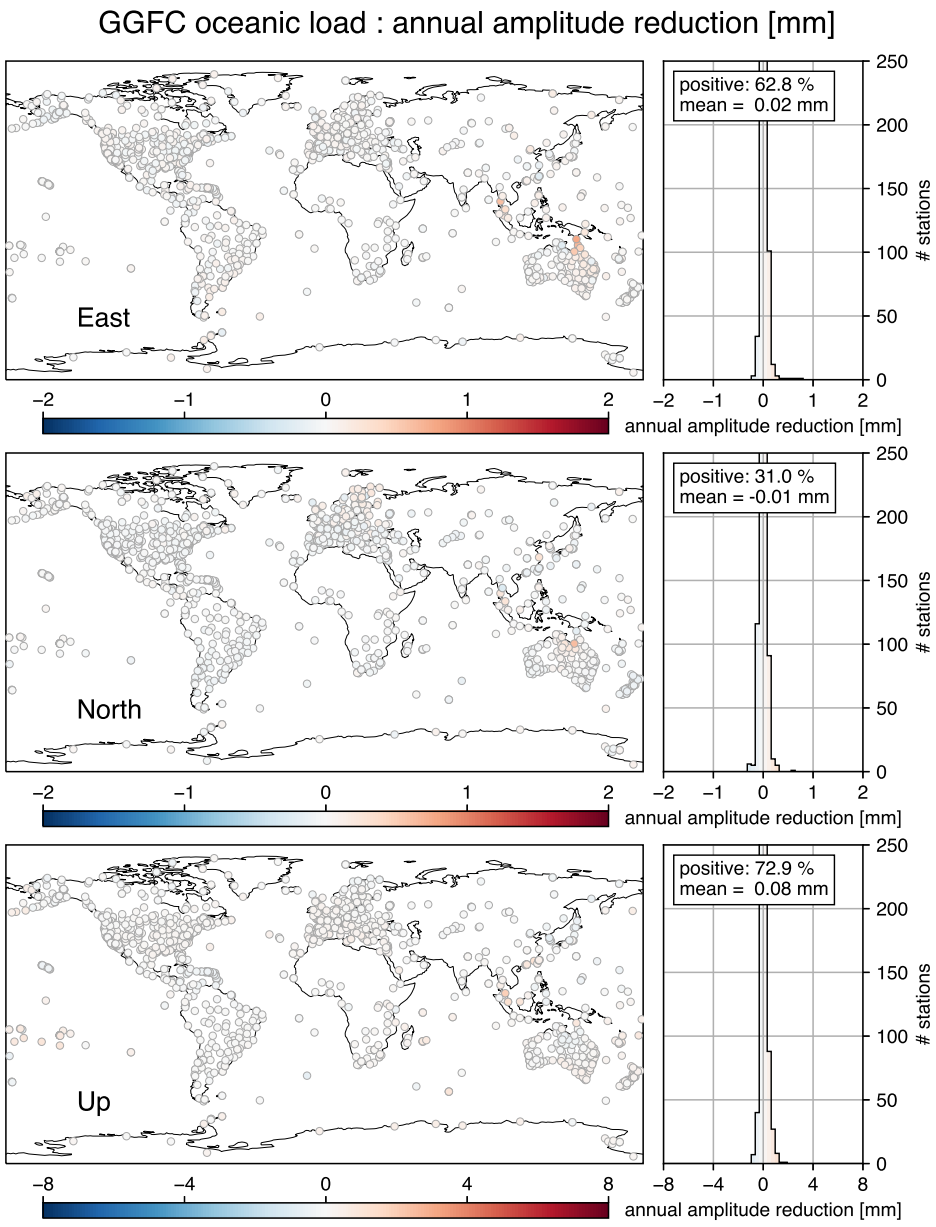

Fig. S42 Reductions of annual amplitudes achieved when correcting repro3 station position time series with GGFC oceanic loading displacements

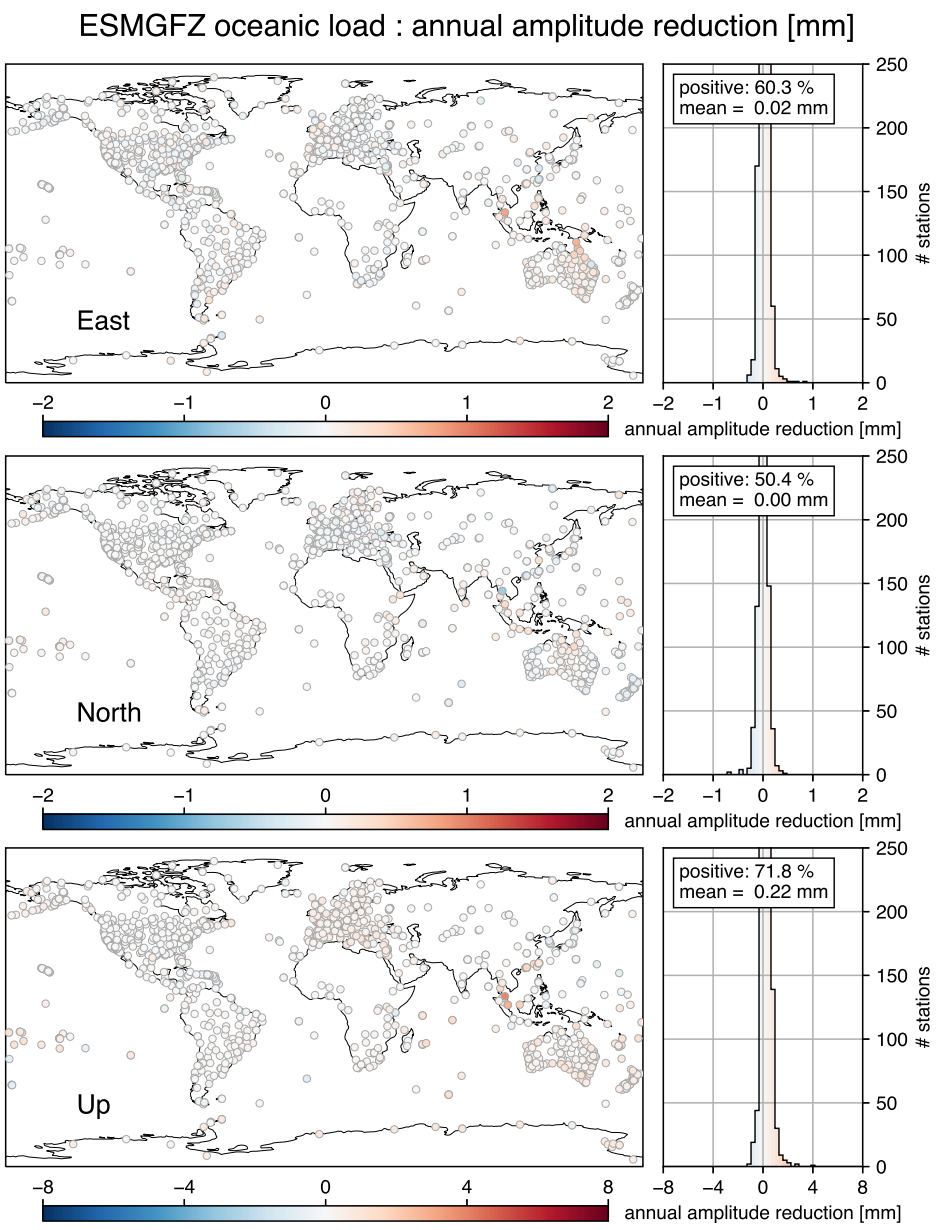

Fig. S43 Reductions of annual amplitudes achieved when correcting repro3 station position time series with ESMGFZ oceanic loading displacements

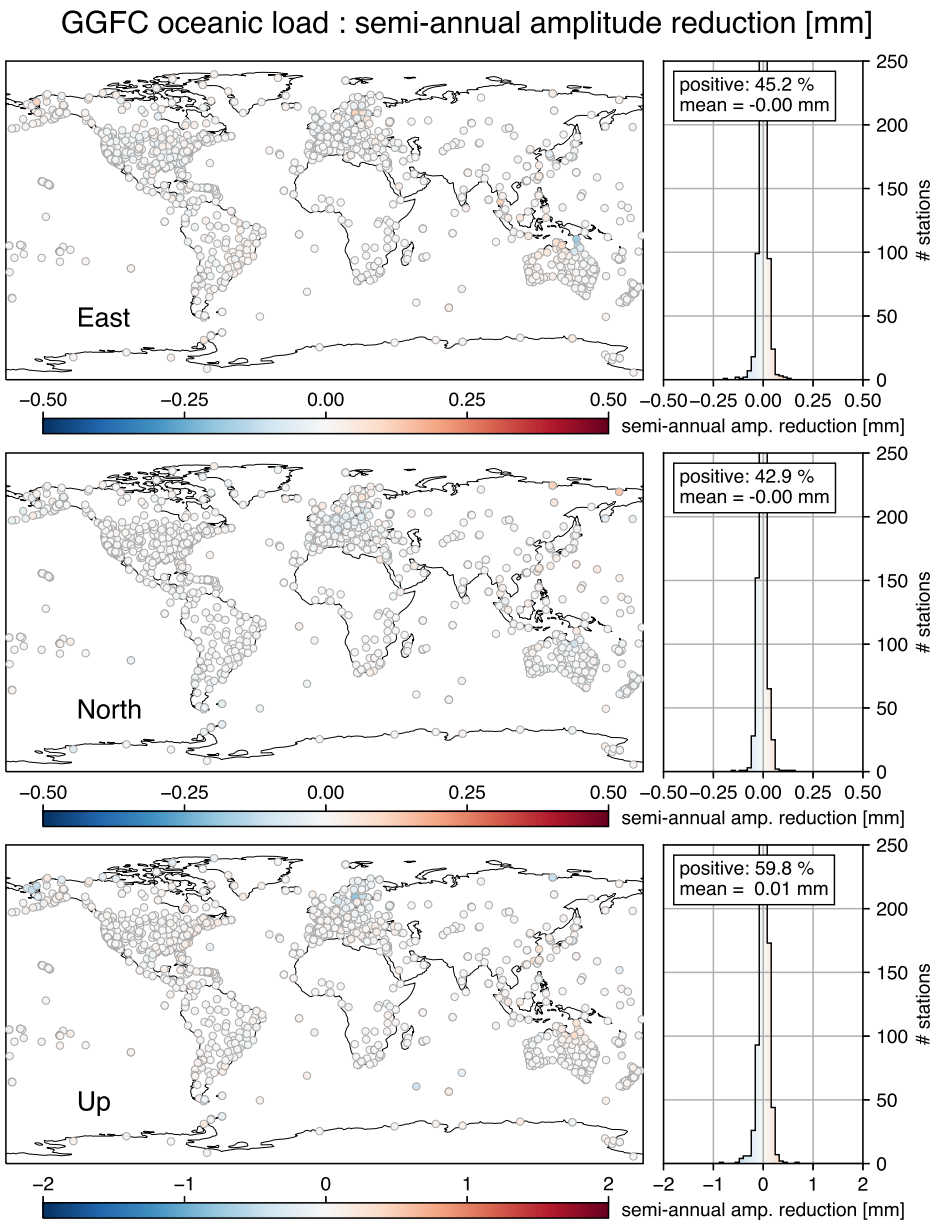

Fig. S44 Reductions of semi-annual amplitudes achieved when correcting repro3 station position time series with GGFC oceanic loading displacements

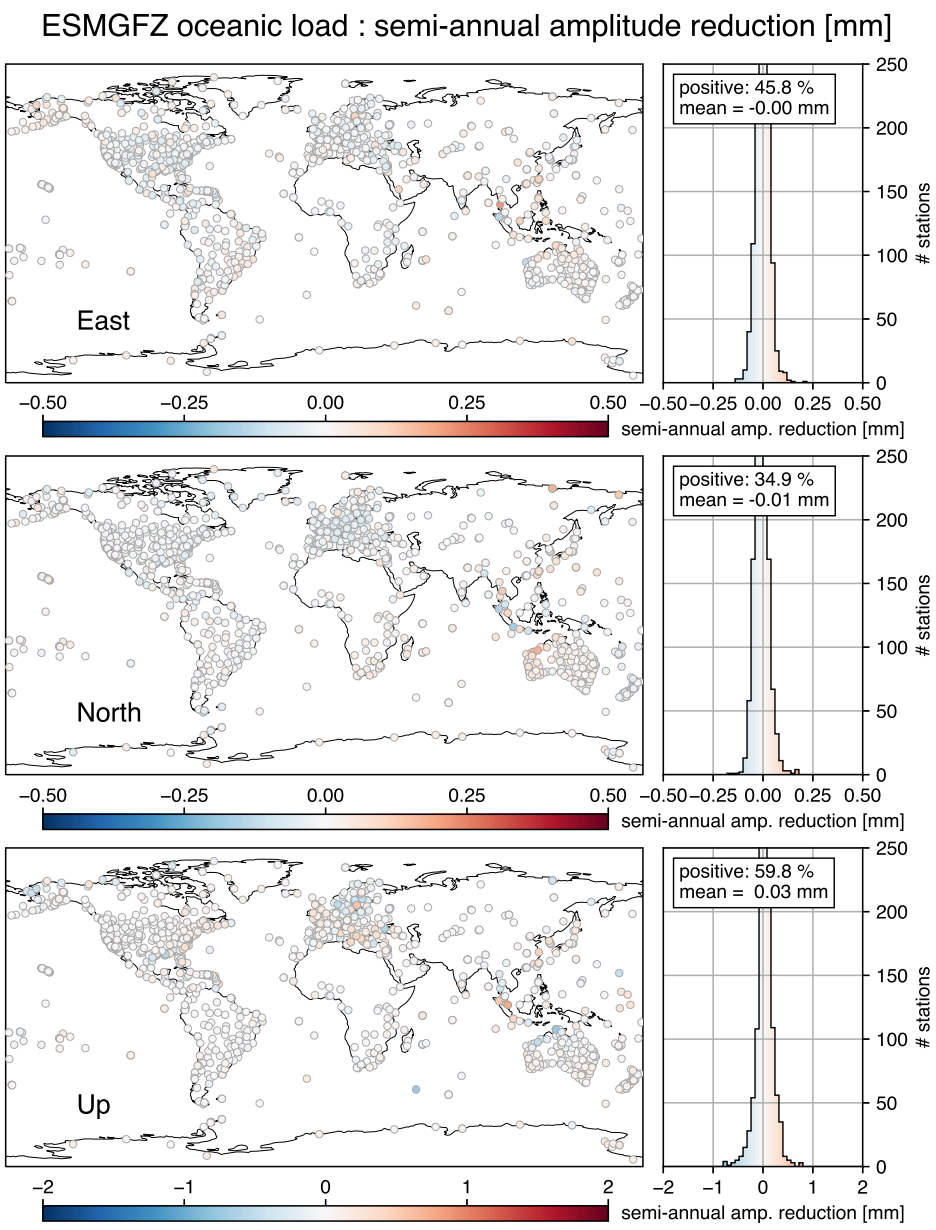

Fig. S45 Reductions of semi-annual amplitudes achieved when correcting repro3 station position time series with ESMGFZ oceanic loading displacements

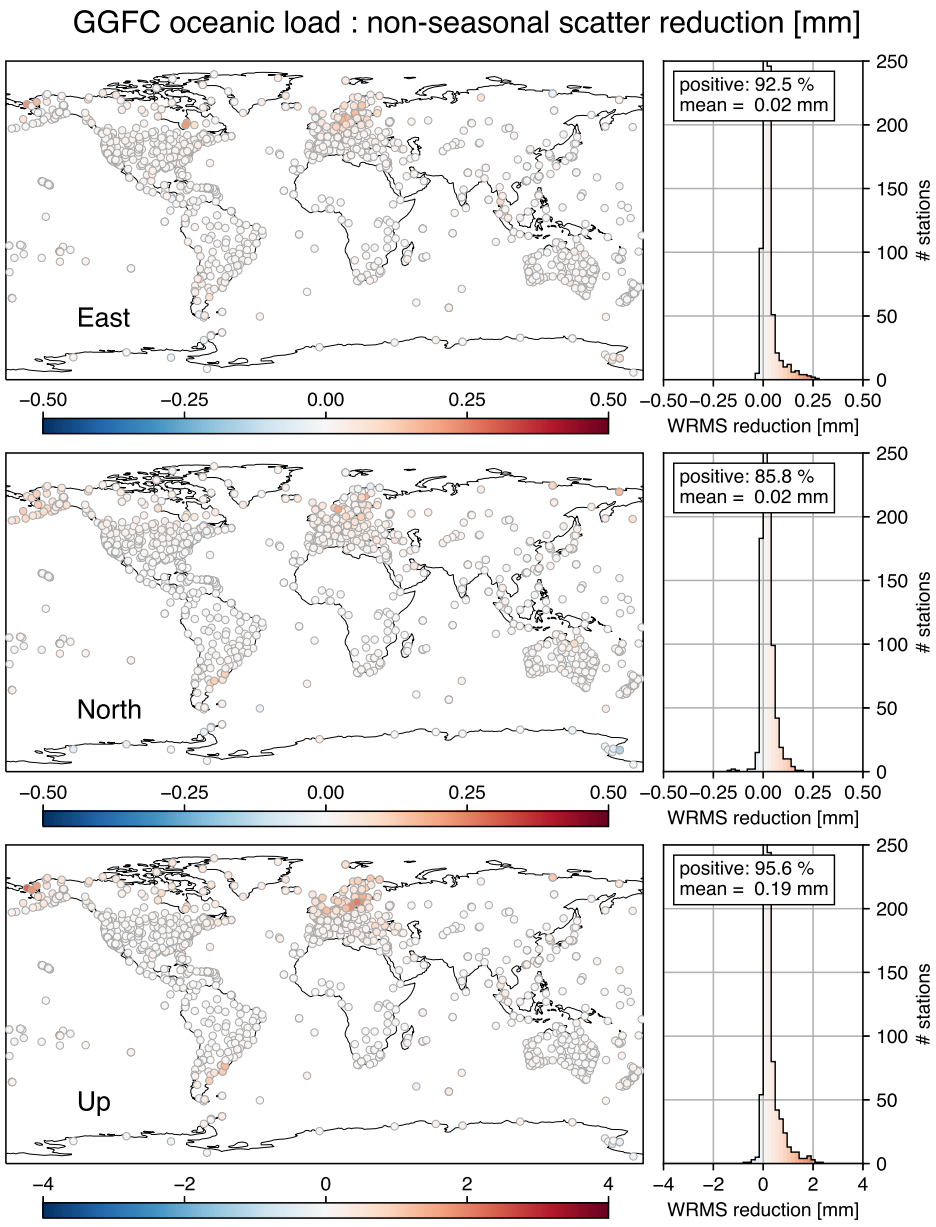

Fig. S46 Reductions of WRMS of trajectory model residuals achieved when correcting repro3 station position time series with GGFC oceanic loading displacements

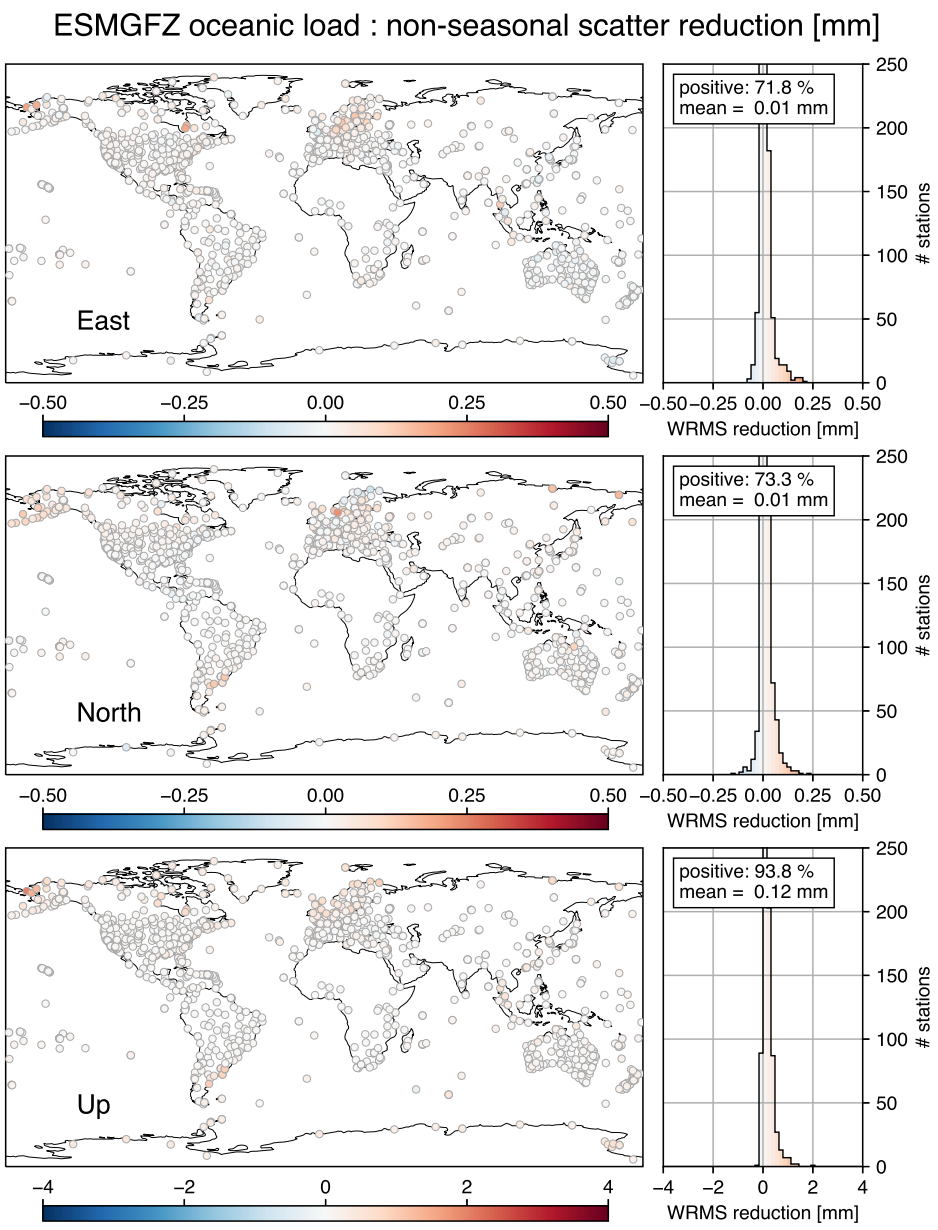

Fig. S47 Reductions of WRMS of trajectory model residuals achieved when correcting repro3 station position time series with ESMGFZ oceanic loading displacements

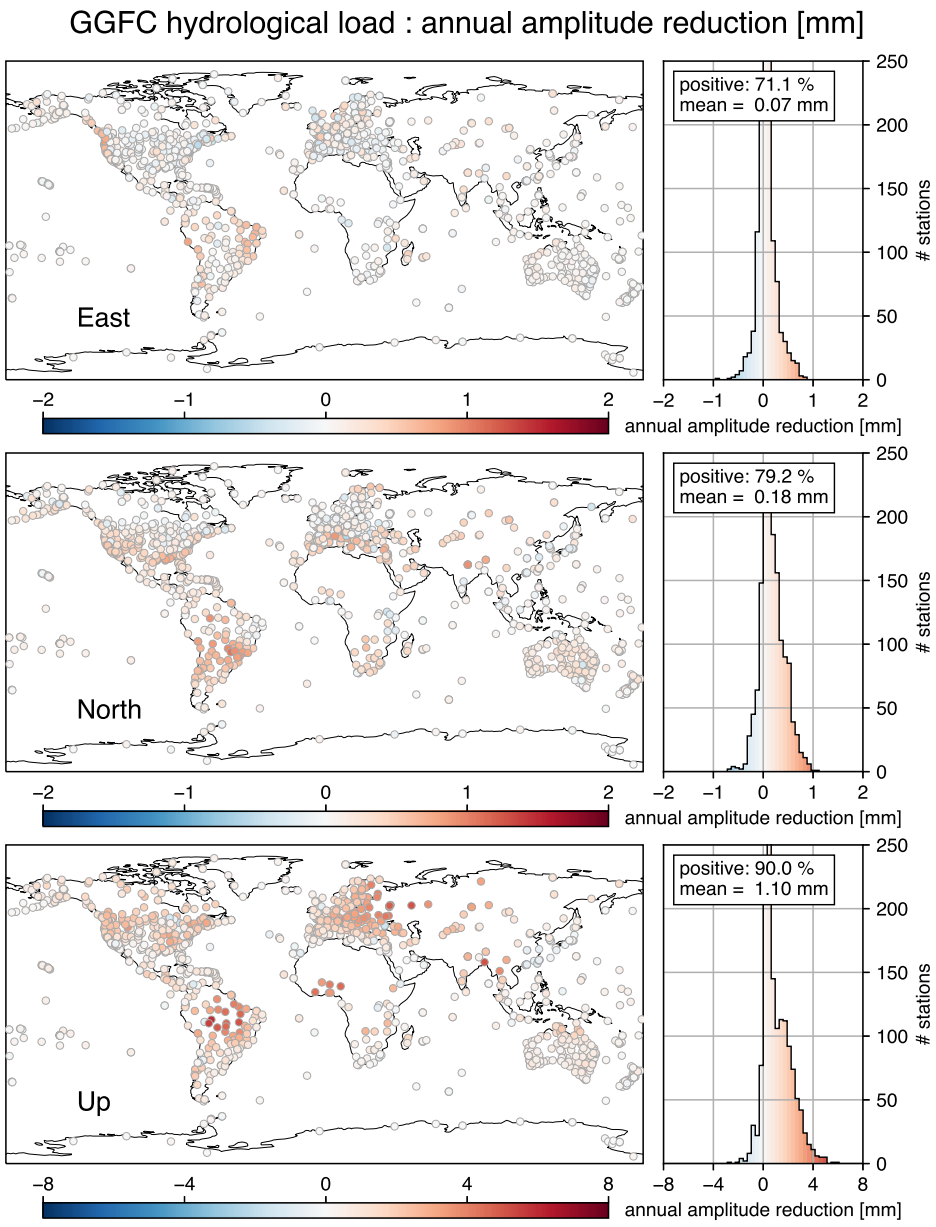

Fig. S48 Reductions of annual amplitudes achieved when correcting repro3 station position time series with GGFC hydrological loading displacements

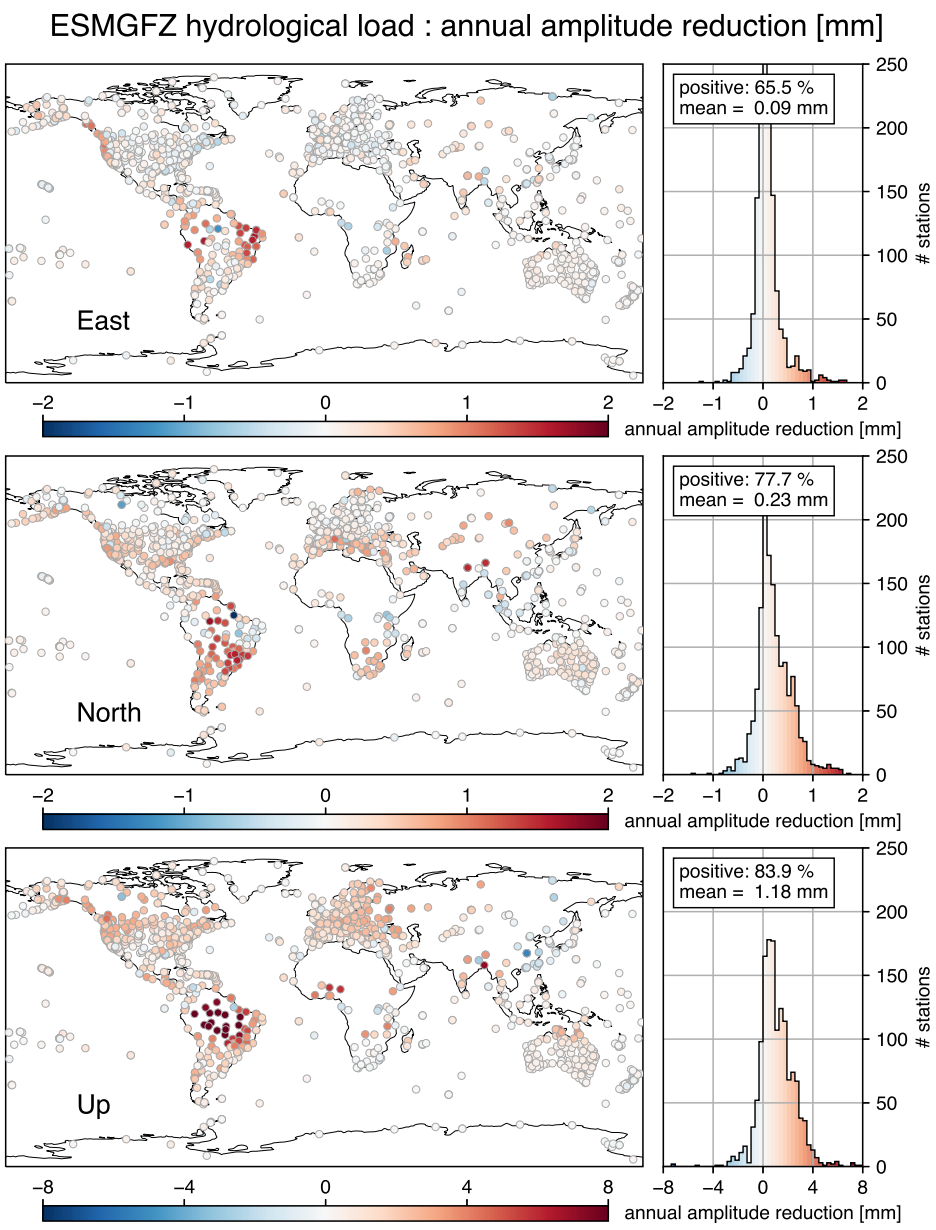

Fig. S49 Reductions of annual amplitudes achieved when correcting repro3 station position time series with ESMGFZ hydrological loading displacements

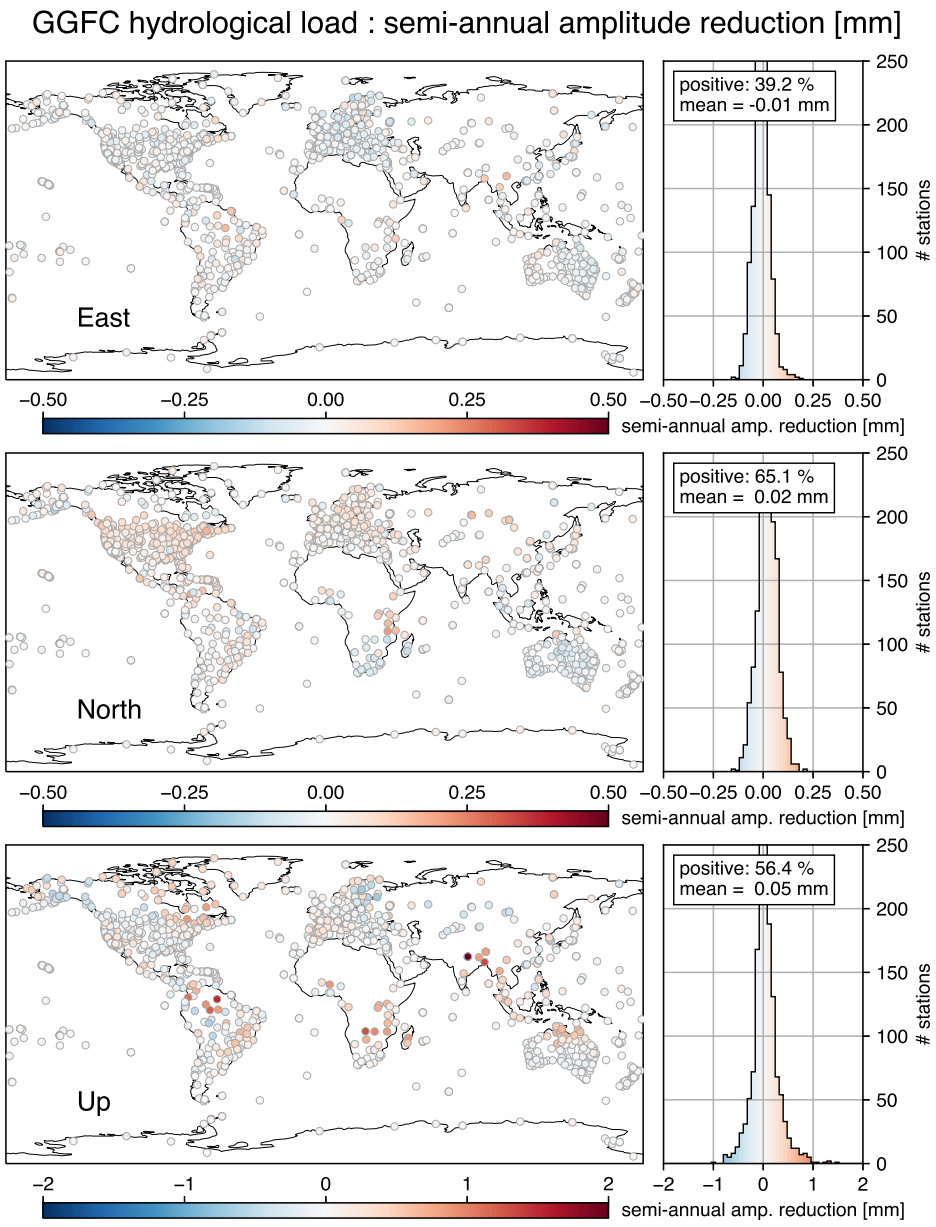

Fig. S50 Reductions of semi-annual amplitudes achieved when correcting repro3 station position time series with GGFC hydrological loading displacements

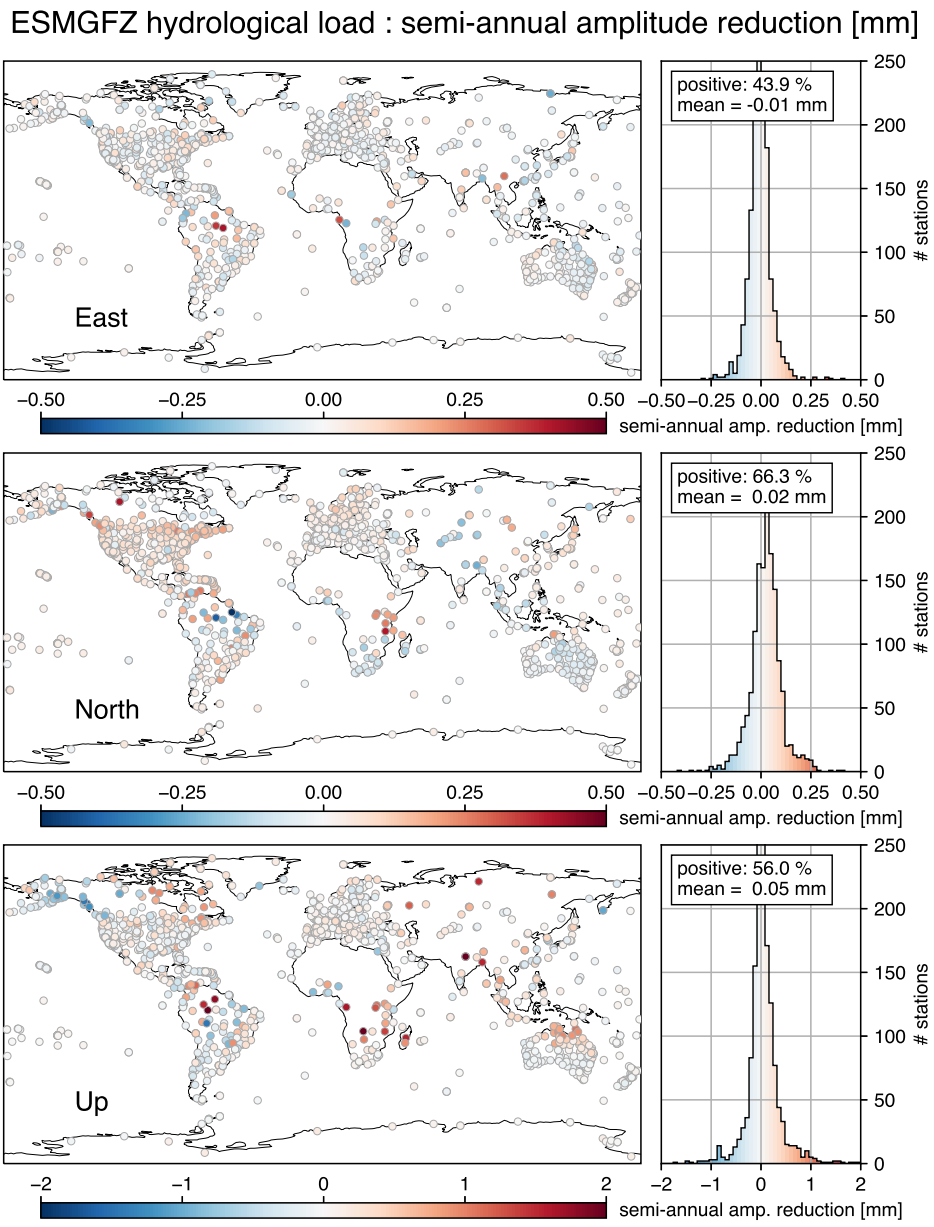

Fig. S51 Reductions of semi-annual amplitudes achieved when correcting repro3 station position time series with ESMGFZ hydrological loading displacements

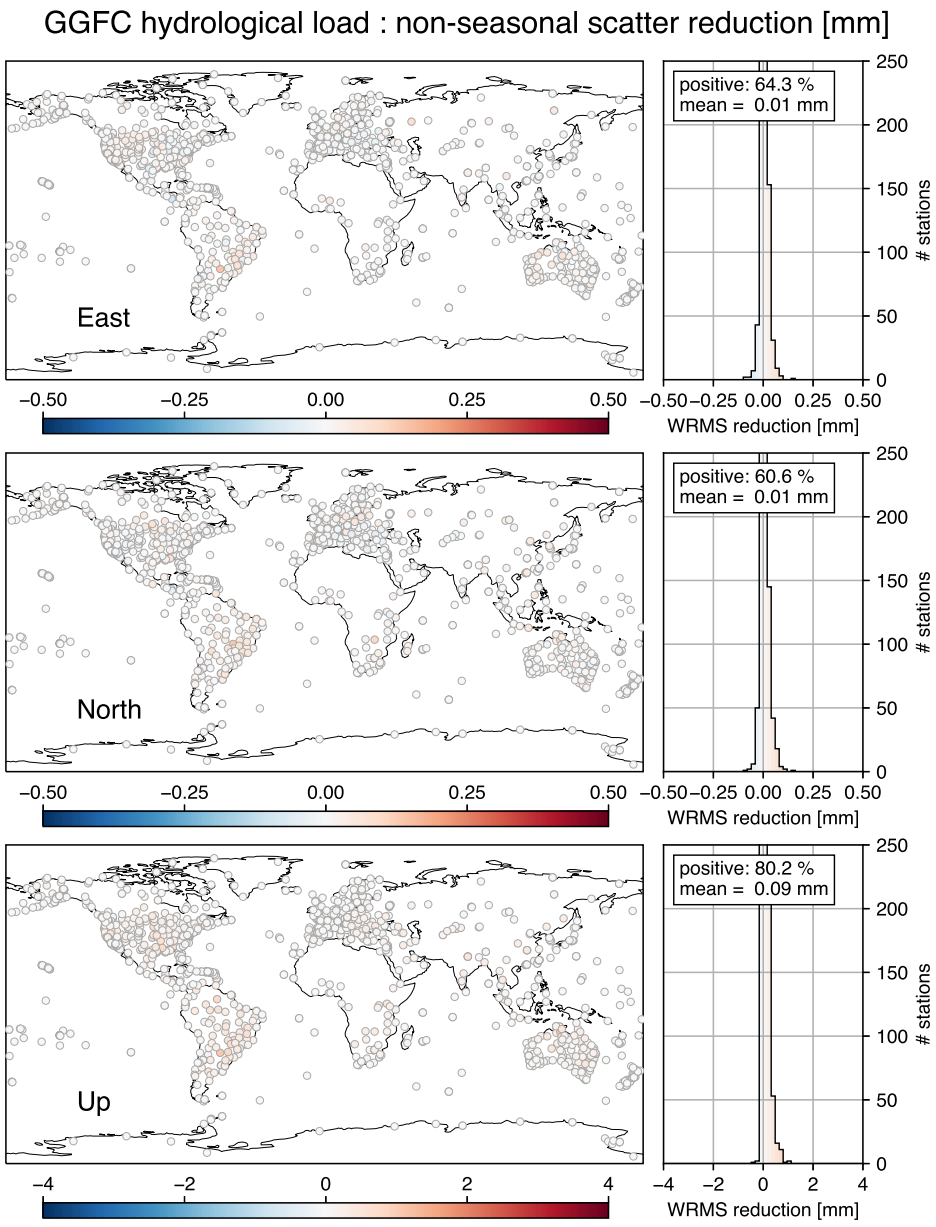

Fig. S52 Reductions of WRMS of trajectory model residuals achieved when correcting repro3 station position time series with GGFC hydrological loading displacements

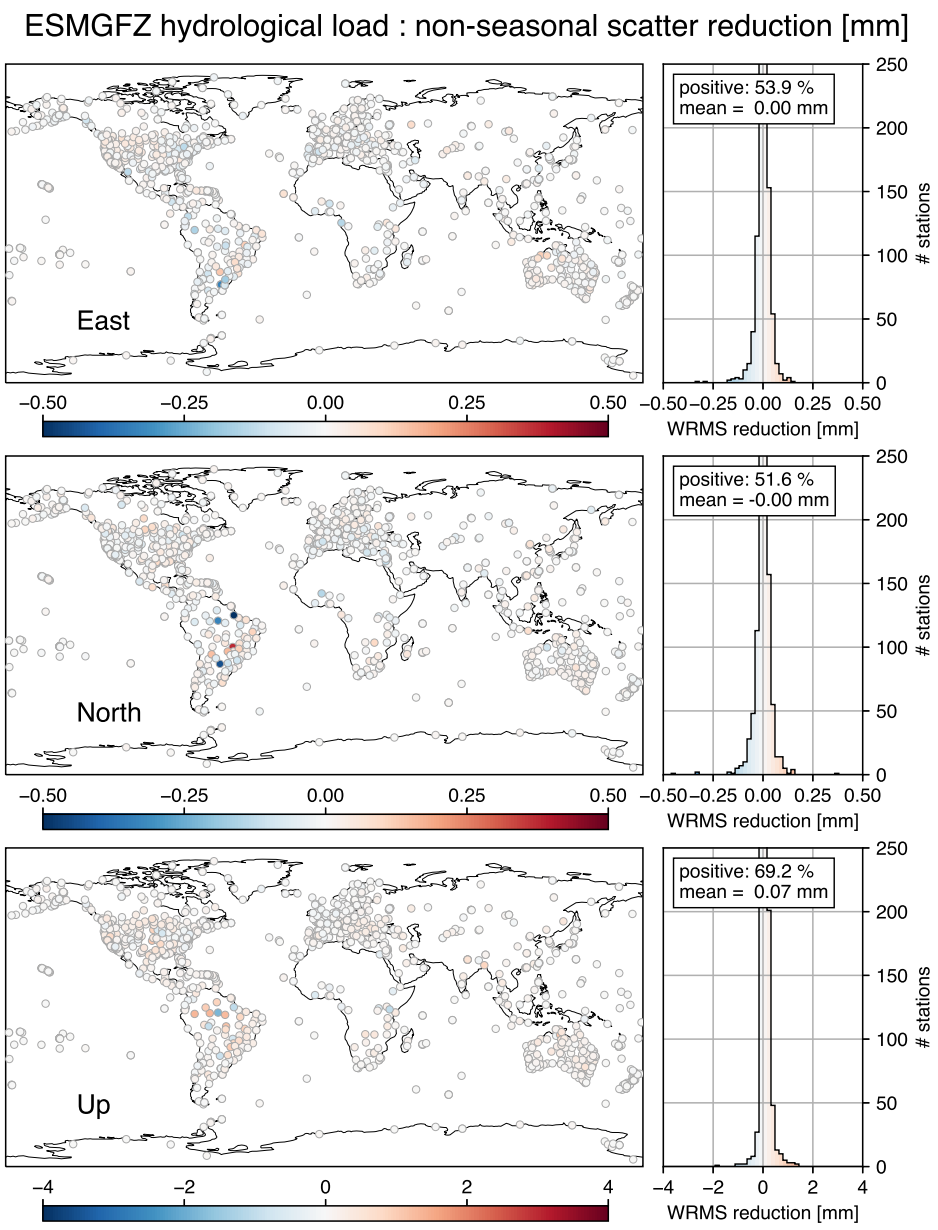

Fig. S53 Reductions of WRMS of trajectory model residuals achieved when correcting repro3 station position time series with ESMGFZ hydrological loading displacements

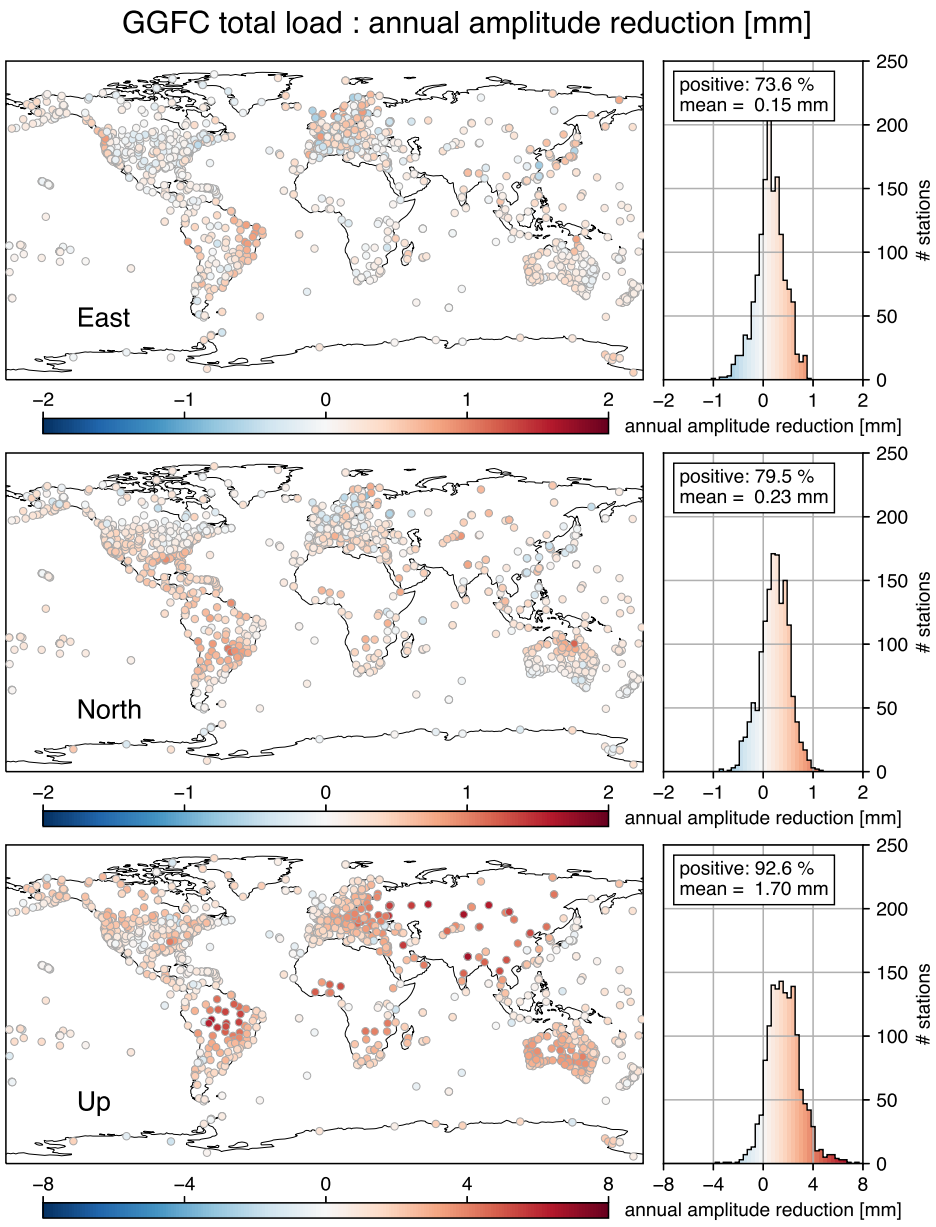

Fig. S54 Reductions of annual amplitudes achieved when correcting repro3 station position time series with GGFC total loading displacements

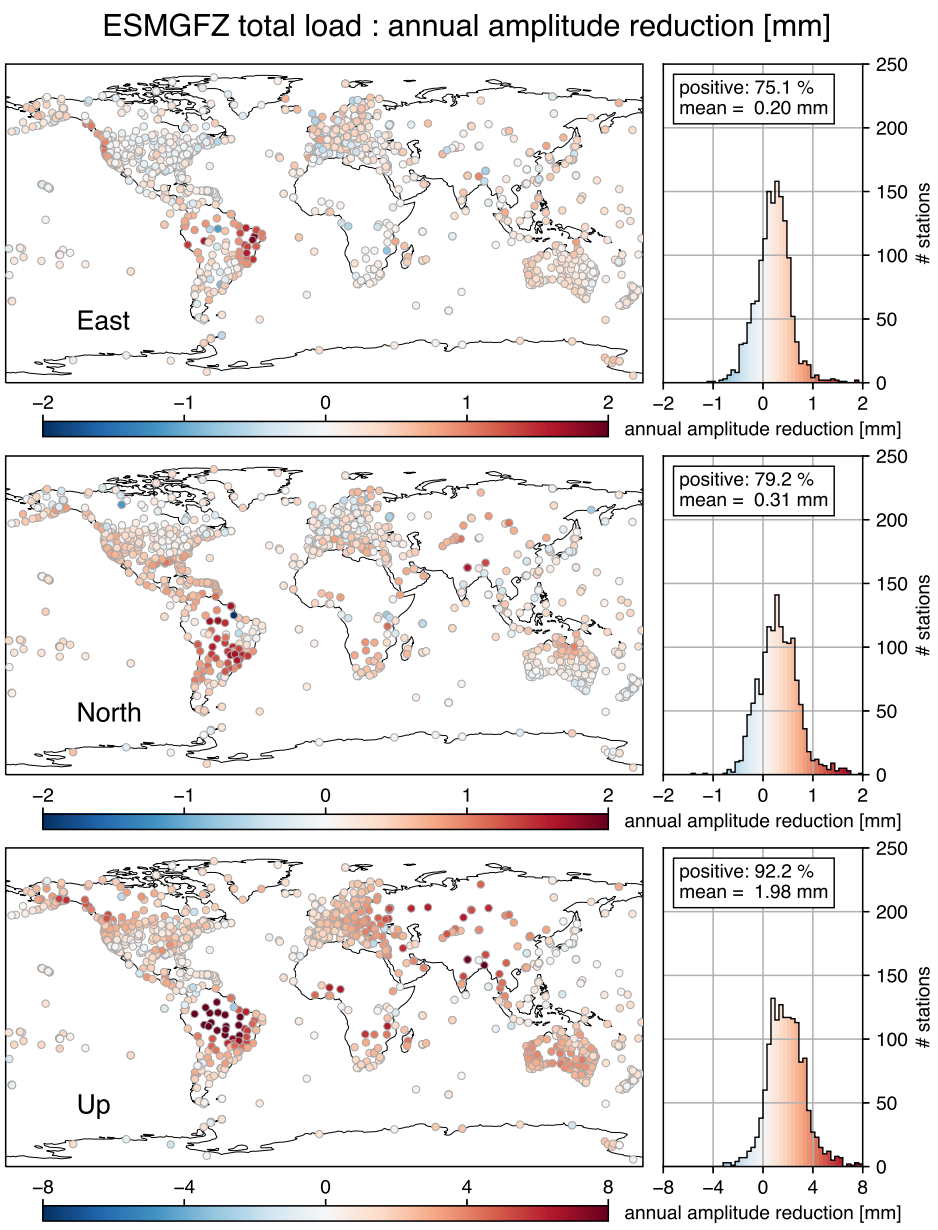

Fig. S55 Reductions of annual amplitudes achieved when correcting repro3 station position time series with ESMGFZ total loading displacements

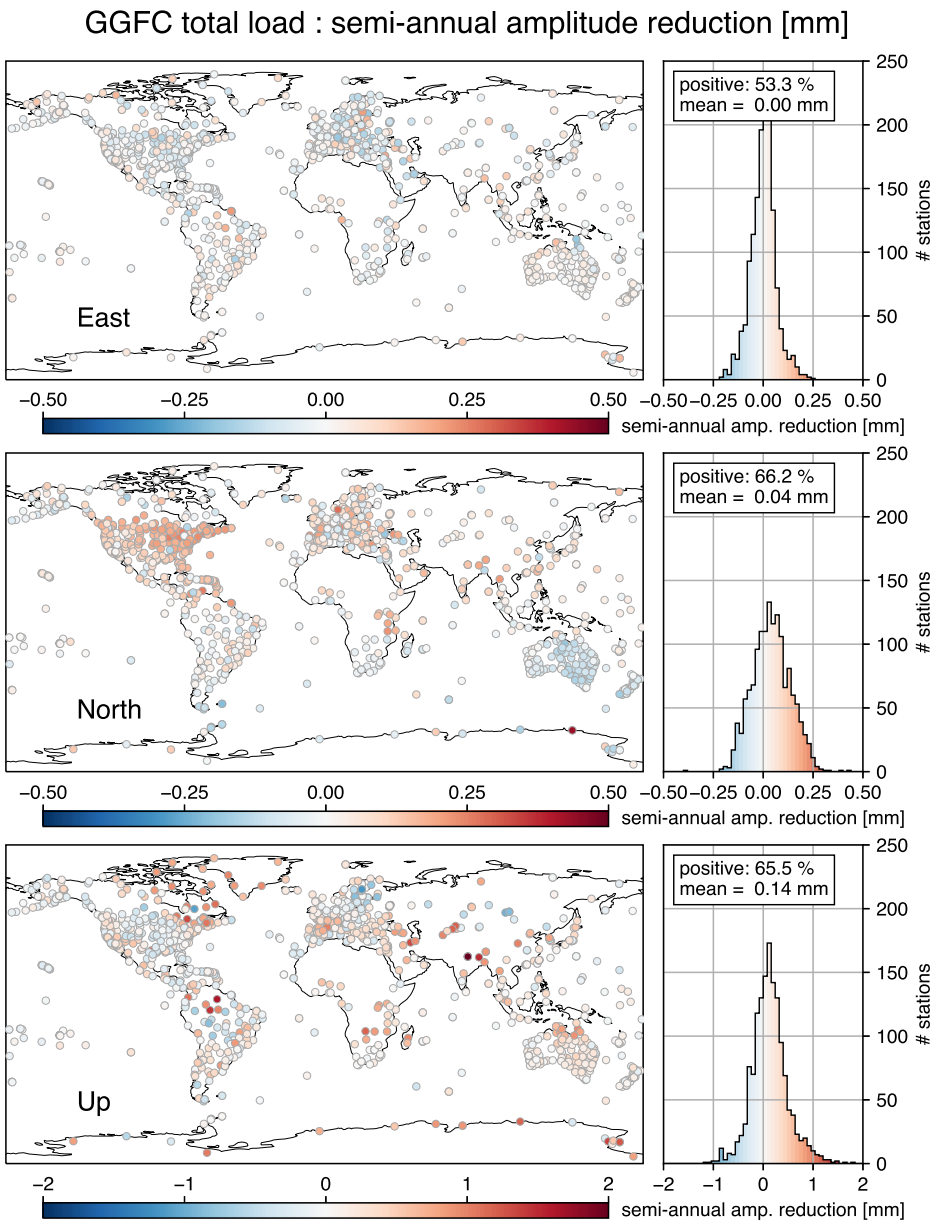

Fig. S56 Reductions of semi-annual amplitudes achieved when correcting repro3 station position time series with GGFC total loading displacements

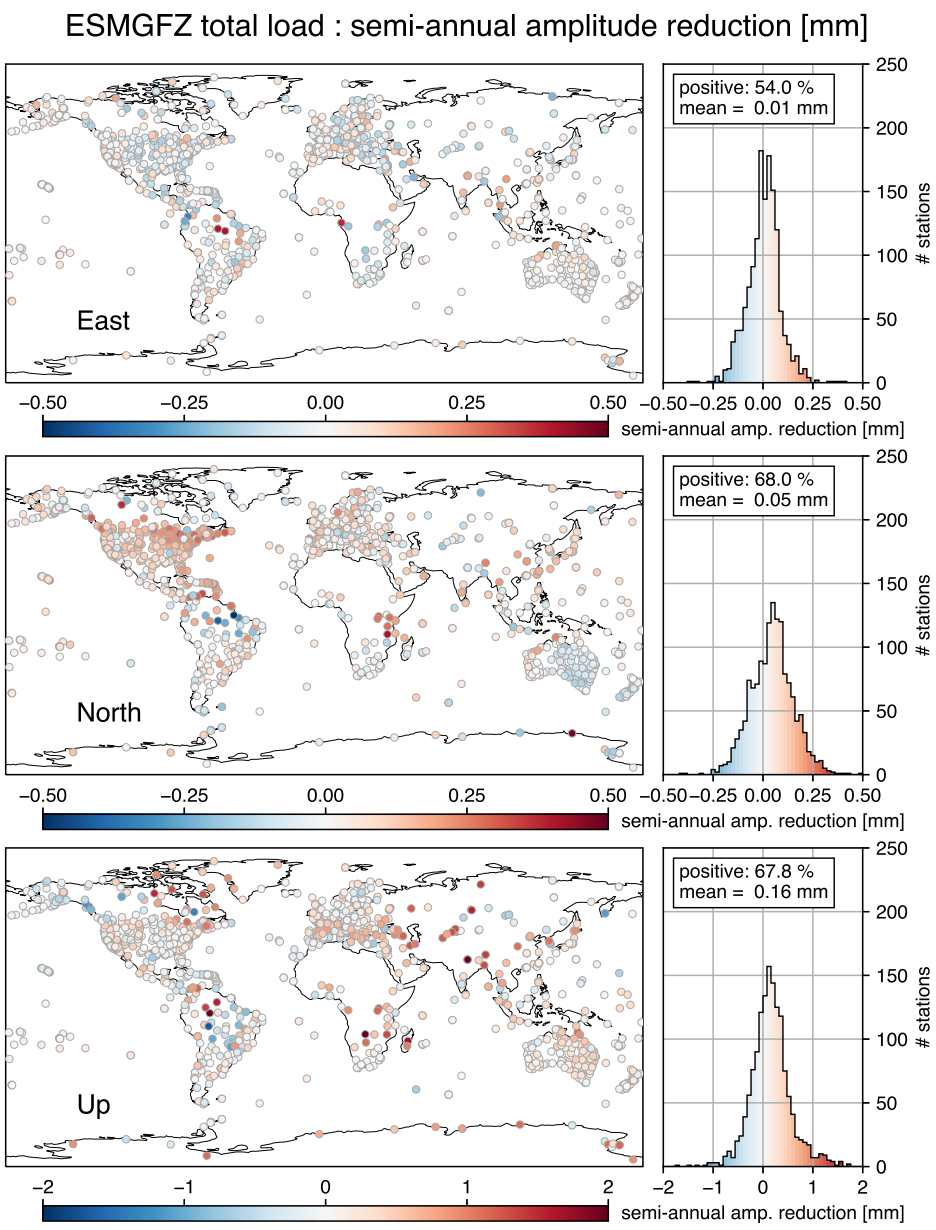

Fig. S57 Reductions of semi-annual amplitudes achieved when correcting repro3 station position time series with ESMGFZ total loading displacements

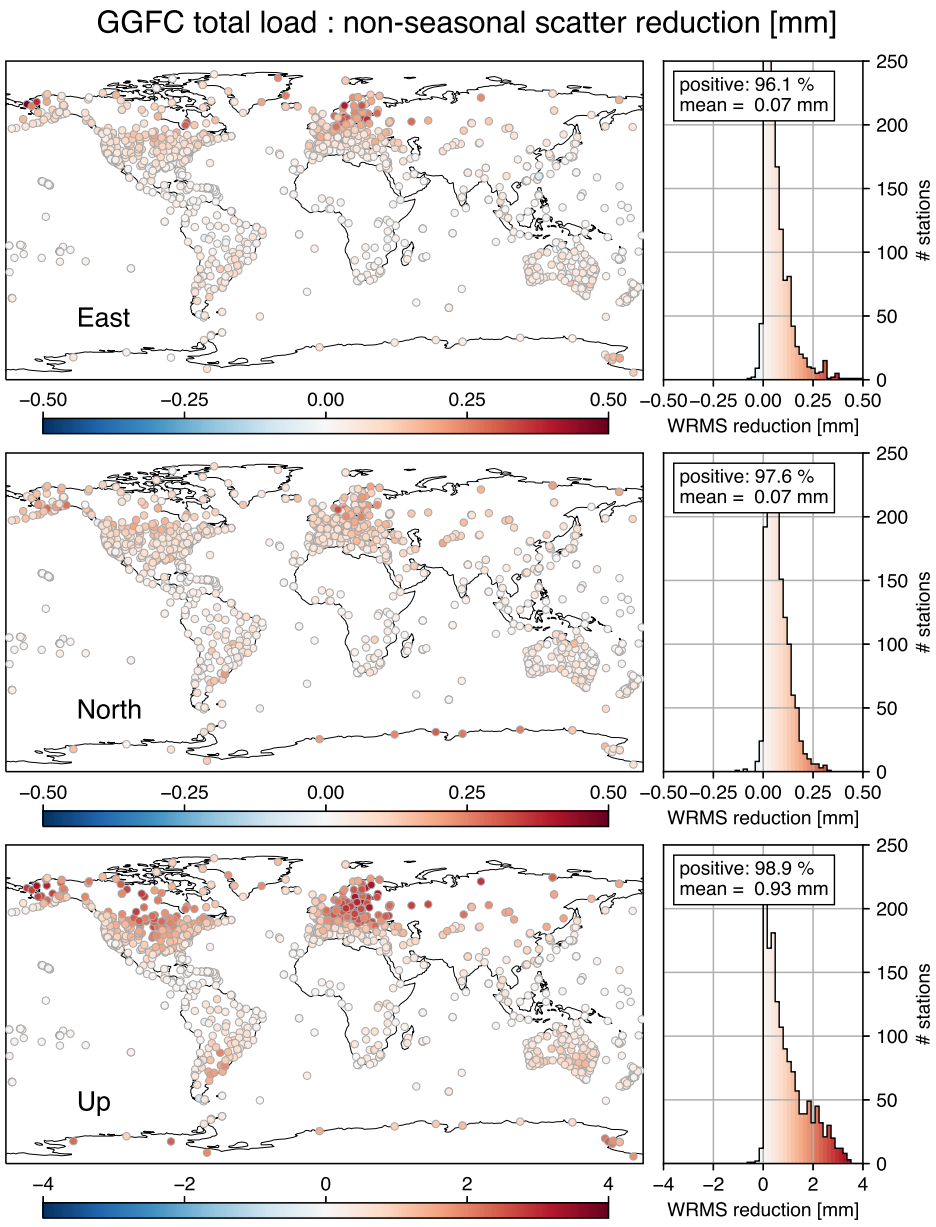

Fig. S58 Reductions of WRMS of trajectory model residuals achieved when correcting repro3 station position time series with GGFC total loading displacements

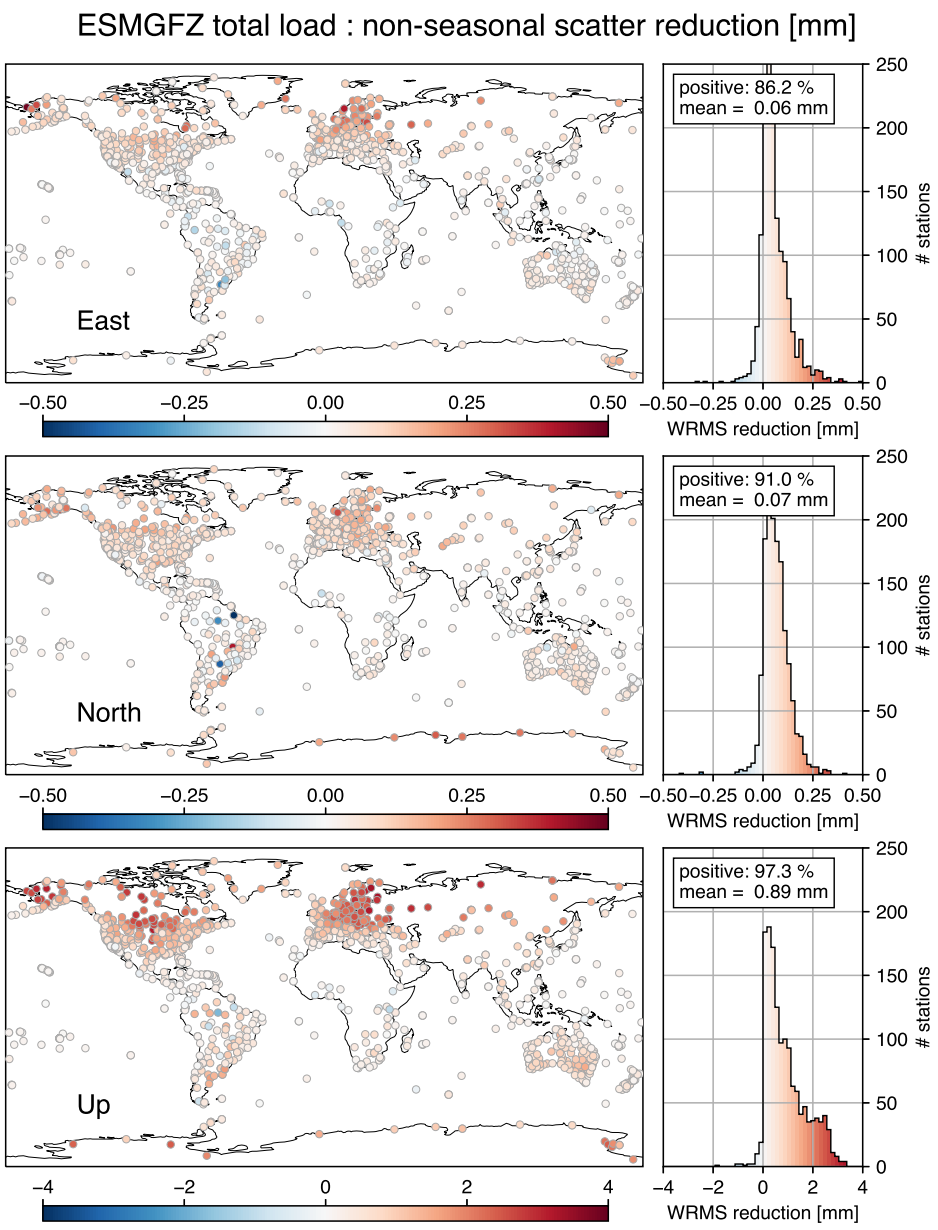

Fig. S59 Reductions of WRMS of trajectory model residuals achieved when correcting repro3 station position time series with ESMGFZ total loading displacements

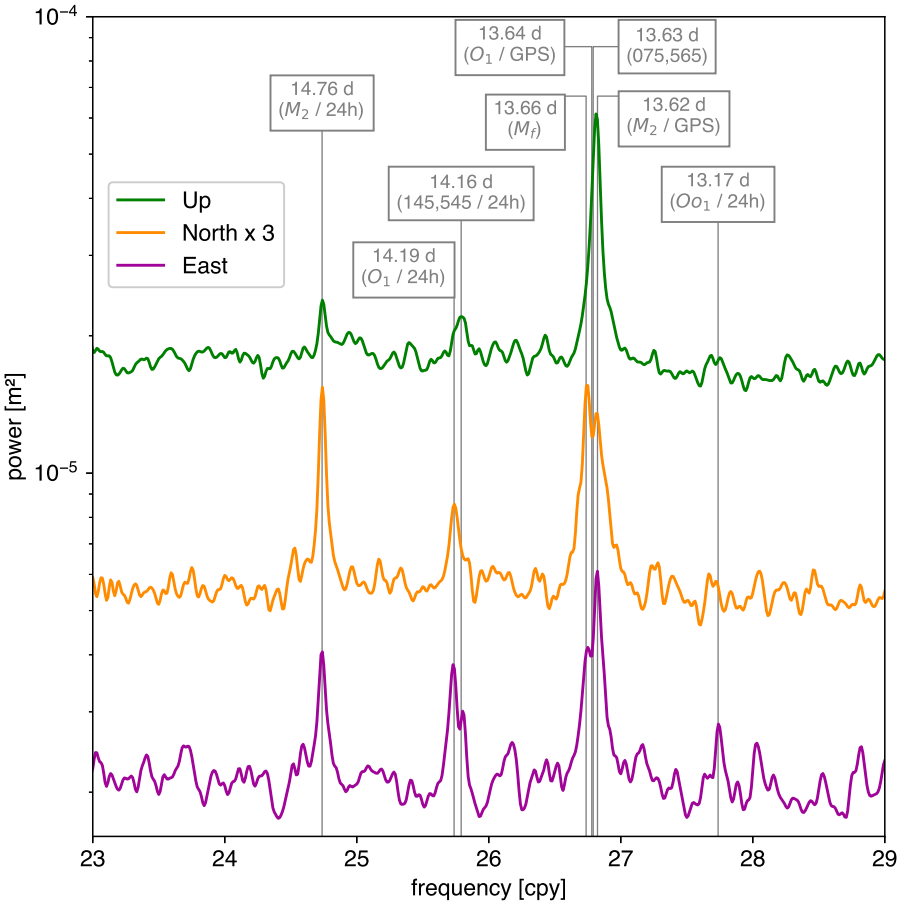

Fig. S60 Average Lomb-Scargle periodograms of residuals from trajectory models adjusted to loading-corrected repro3 station position time series: zoom on the fortnightly band. The average periodogram for the North component is offset by a factor 3 for clarity. The *gray vertical lines* respectively indicate the alias period of the M_2 tide via daily sampling (24.74 cpy / 14.76 d), the alias period of the O_1 tide via daily sampling (25.74 cpy / 14.19 d), the alias period of the 145, 545 tide via daily sampling (25.79 cpy / 14.16 d), the M_f tide period (26.74 cpy / 13.66 d), the alias period of the O_1 tide via the GPS ground repeat period (26.78 cpy / 13.64 d), the 075, 565 tide period (26.79 cpy / 13.63 d), the alias period of the M_2 tide via the GPS ground repeat period (26.82 cpy / 13.62 d) and the alias period of the Oo_1 tide via daily sampling (27.74 cpy / 13.17 d).

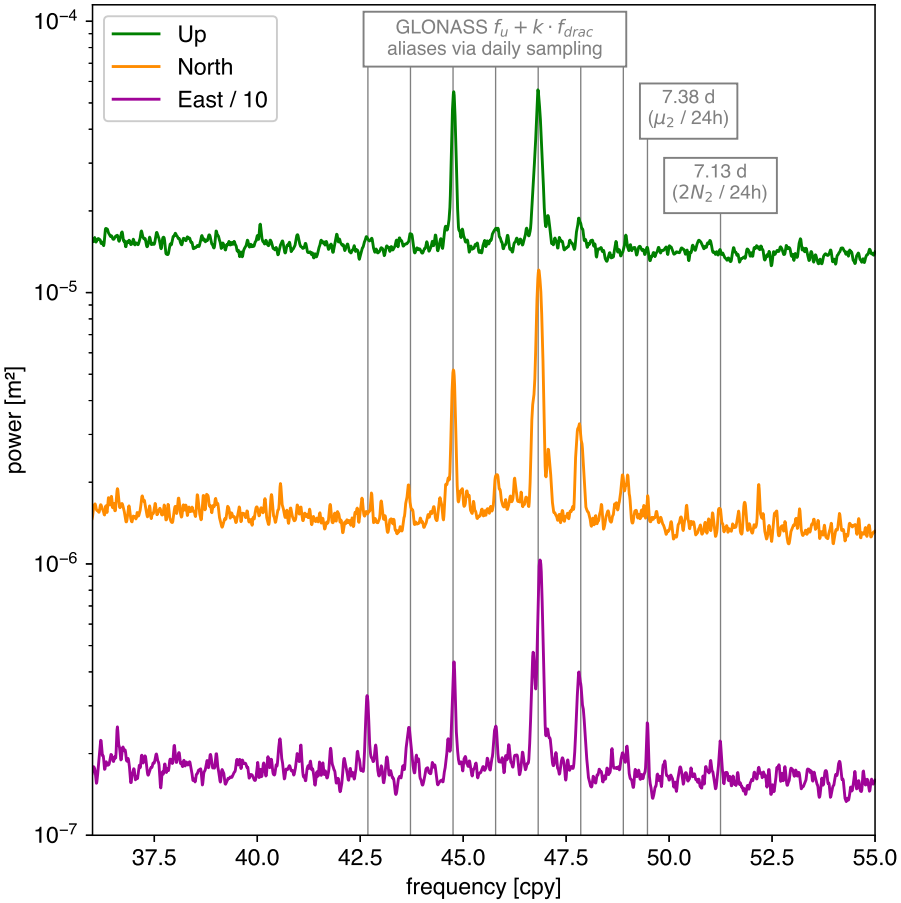

Fig. S61 Average Lomb-Scargle periodograms of residuals from trajectory models adjusted to loading-corrected repro3 station position time series: zoom on the ≈8 d band. The average periodogram for the East component is offset by a factor 10 for clarity. The *gray vertical lines* respectively indicate the alias period of the μ_2 tide via daily sampling (49.47 cpy / 7.38 d), the alias period of the $2N_2$ tide via daily sampling (51.25 cpy / 7.13 d), and the alias periods of the $f_u + k \cdot f_{drac}$ frequencies via daily sampling, where f_u is the frequency of the argument of latitude of GLONASS satellites with respect to the Sun, f_{drac} is the draconitic frequency of GLONASS satellites and k is an integer ranging from -4 to 2.

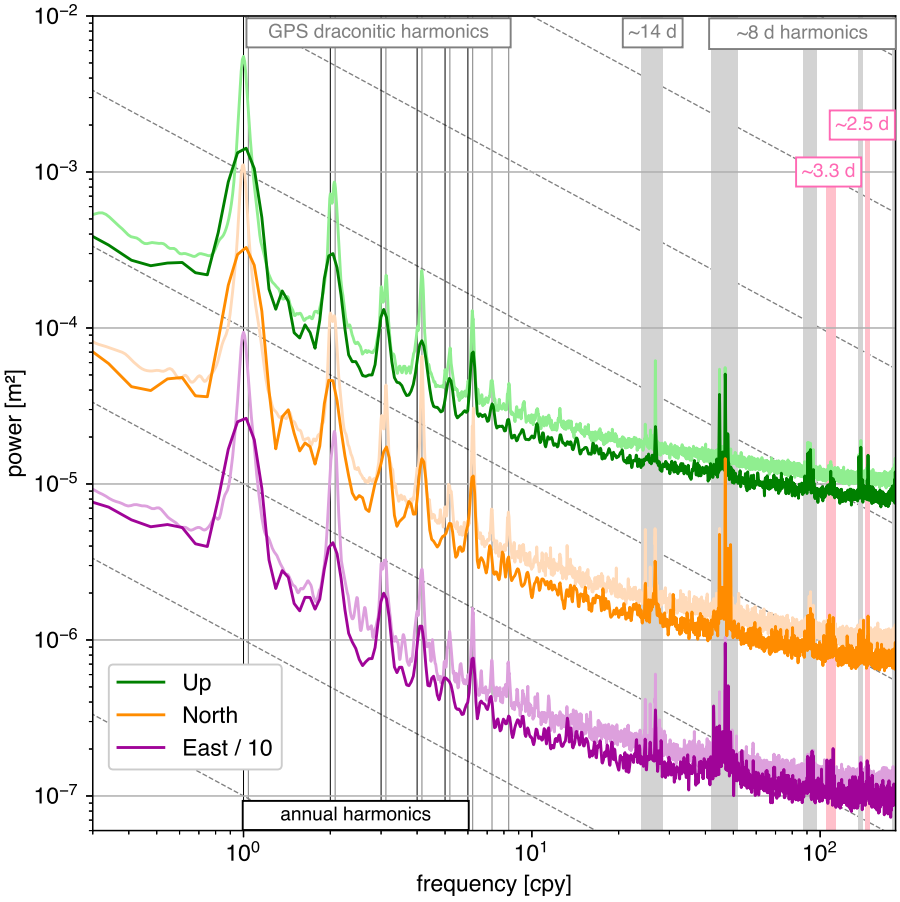

Fig. S62 Average Lomb-Scargle periodograms of residuals from trajectory models adjusted to loading-corrected repro3 station position time series. The curves in *light colors* are the same average periodograms as shown in Figure 12, computed from residual time series spanning the whole repro3 time span. Those in *dark colors* are average periodograms of the same residual time series restricted to the period after May 2017. The *pink vertical patches* span periods around 3.3 d and 2.5 d, where Galileo-related spectral combs become visible in the average periodograms of the late residual time series. The other features (*black and gray lines and patches*) are described in the legend of Figure 12.

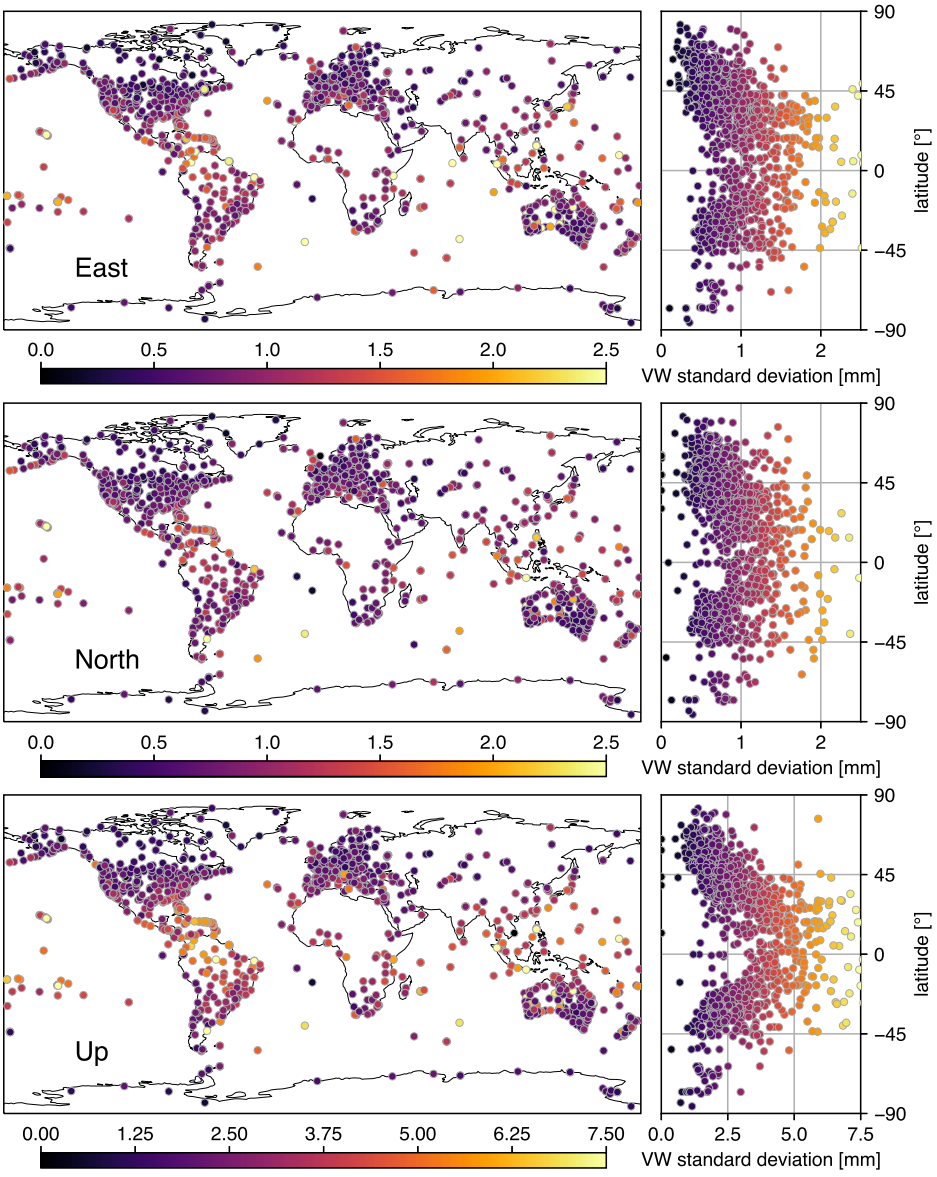

Fig. S63 Standard deviations of variable white noise processes adjusted to loading-corrected repro3 station position time series

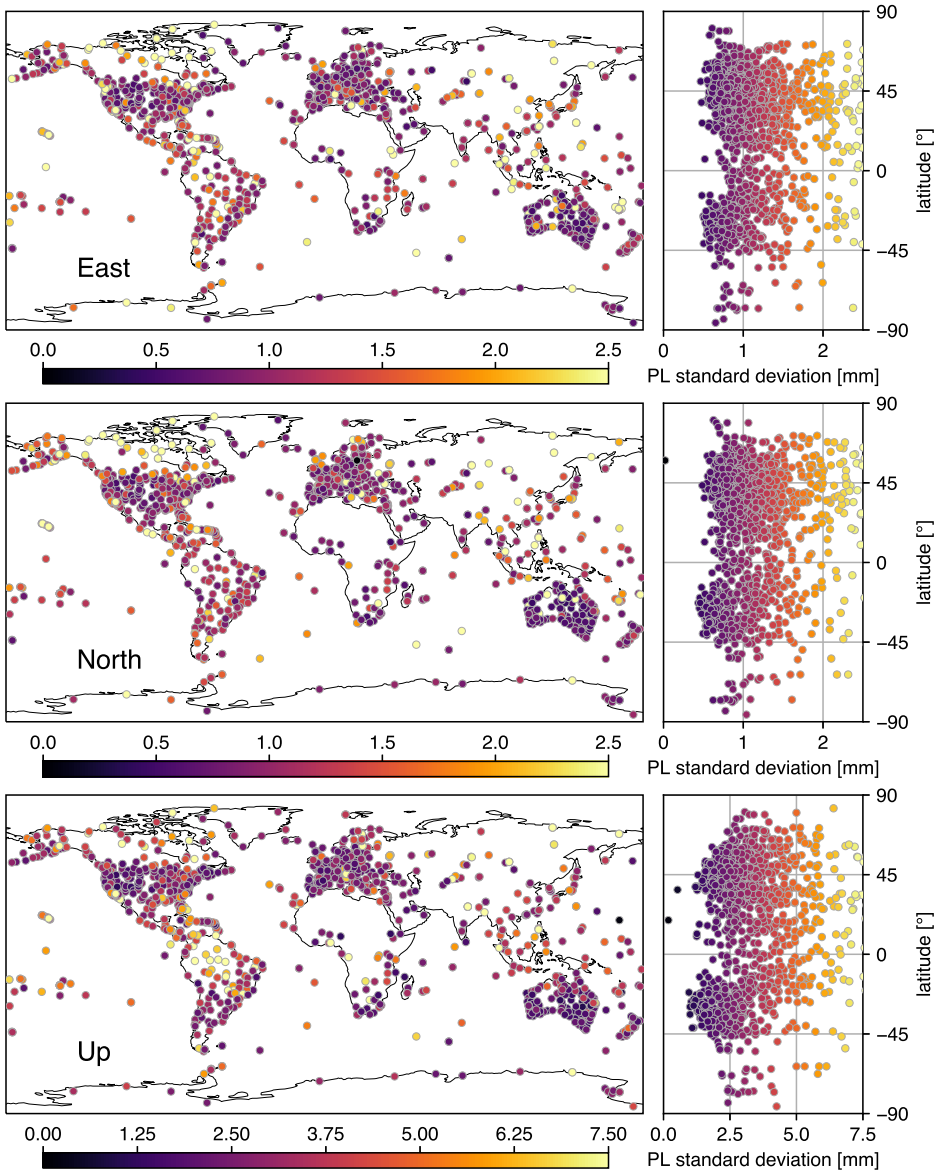

Fig. S64 Standard deviations of power-law noise processes adjusted to loading-corrected repro3 station position time series. For comparability among power-law processes with different spectral indices and stations with different observation spans, the displayed standard deviations are actually the expected standard deviations of 10-year long power-law noise series, computed with Equation 5 of Gobron et al. (2021).

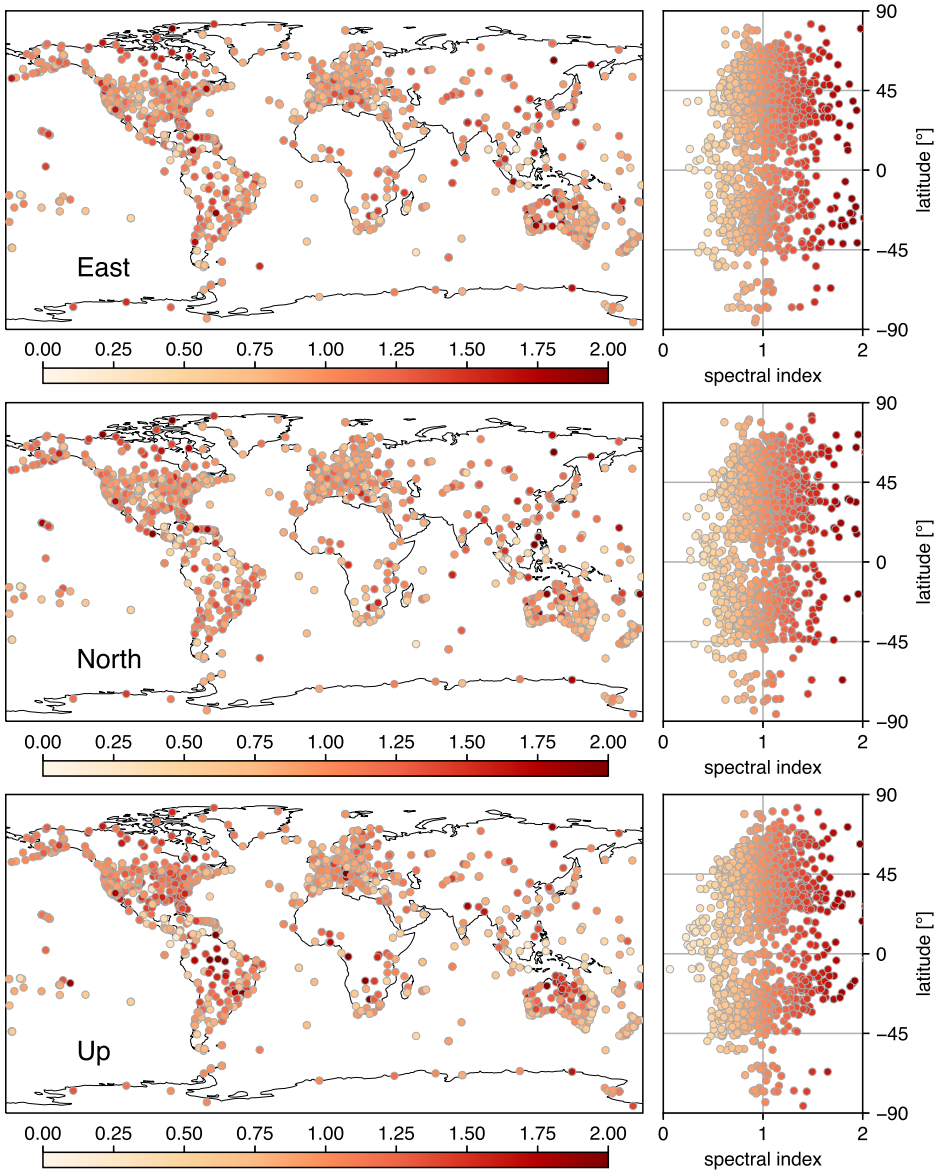

Fig. S65 Spectral indices of power-law noise processes adjusted to loading-corrected repro3 station position time series

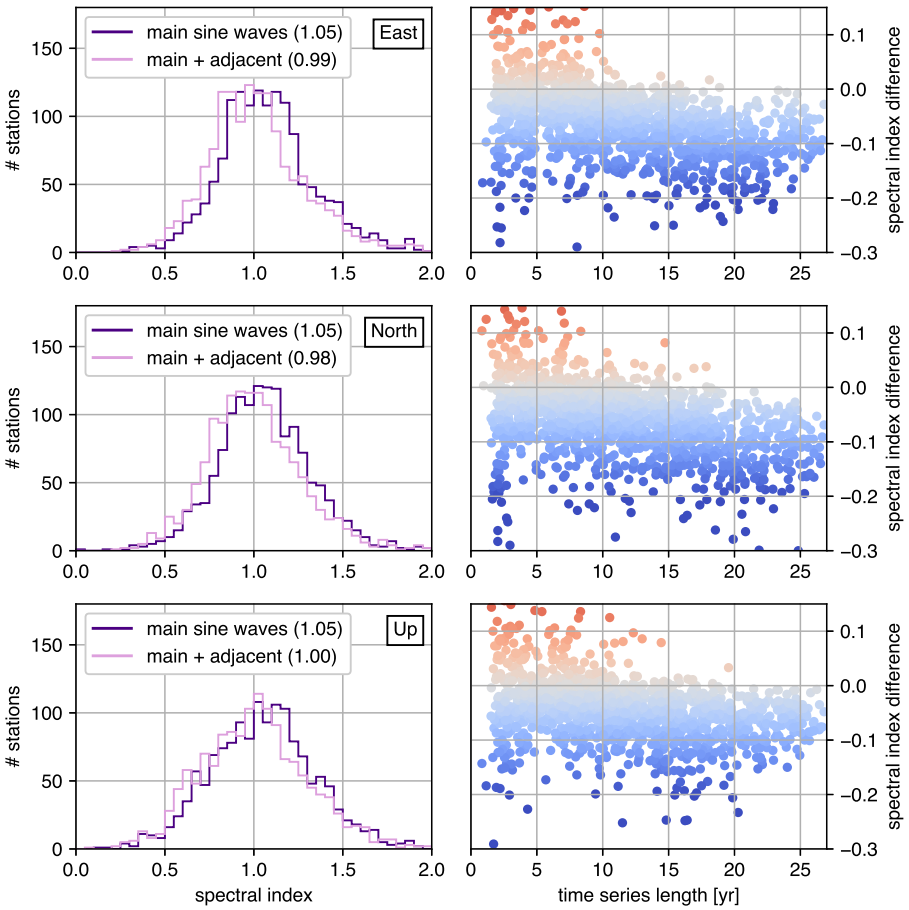

Fig. S66 Comparison of spectral indices of power-law noise processes adjusted to loading-corrected repro3 station position time series together with trajectory models including (a) 41 main sine waves and (b) 41 main sine waves and 60 adjacent sine waves. *Left*: histograms of the spectral indices estimated in both cases. The numbers in parentheses are the medians of the estimated spectral indices. *Right*: differences ((b) - (a)) in the estimated spectral indices, represented as a function of the lengths of the station position time series.

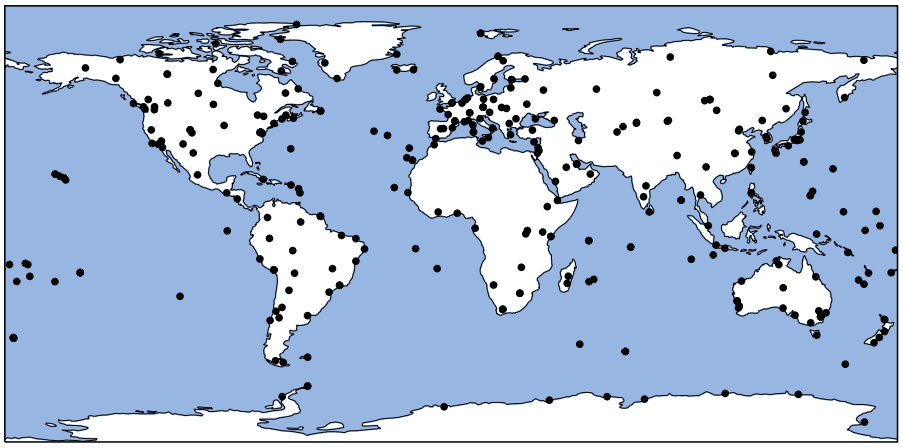

Fig. S67 Distribution of the 326 stations used for the inter-comparison of station position time series presented in Section 5

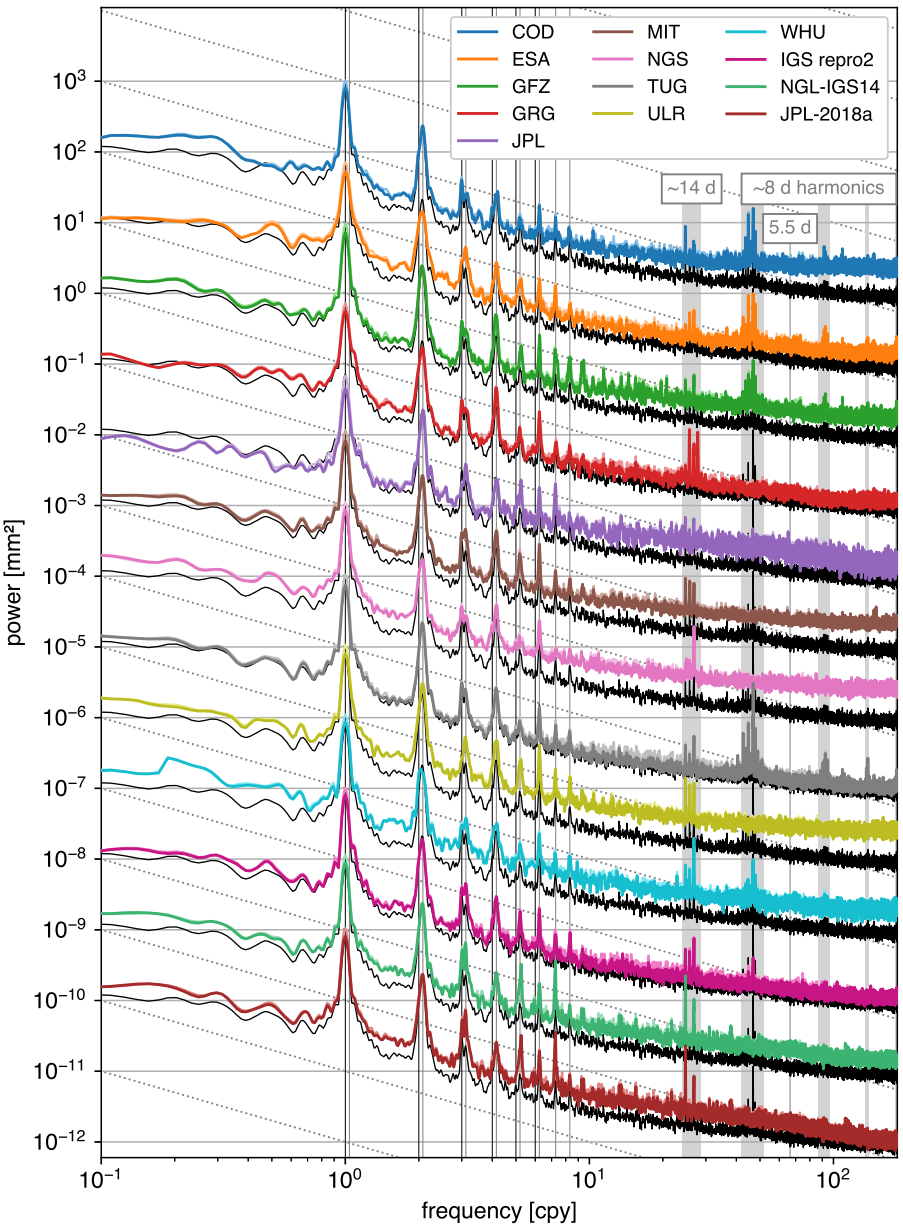

Fig. S68 Same as Figure 15 for the *East* component of trajectory model residuals

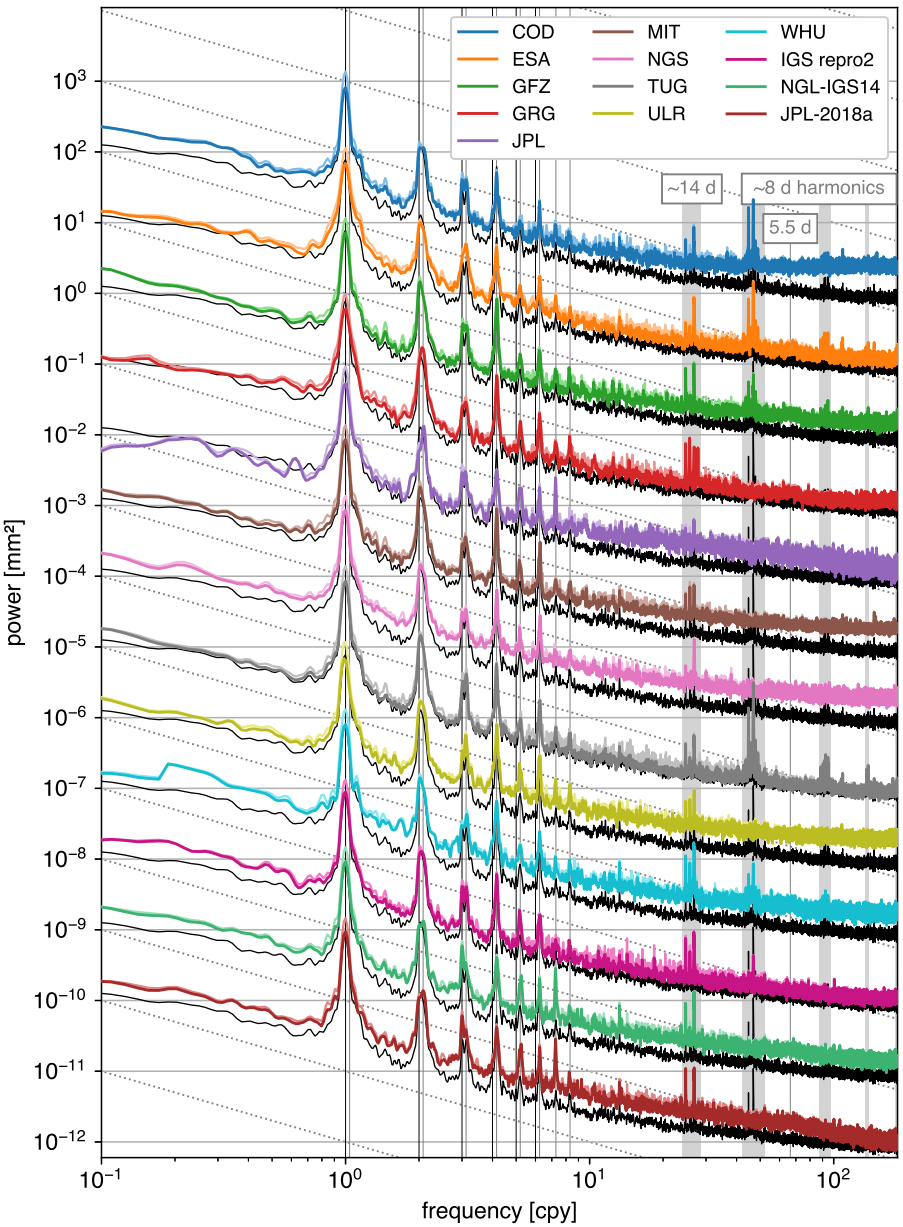

Fig. S69 Same as Figure 15 for the *North* component of trajectory model residuals

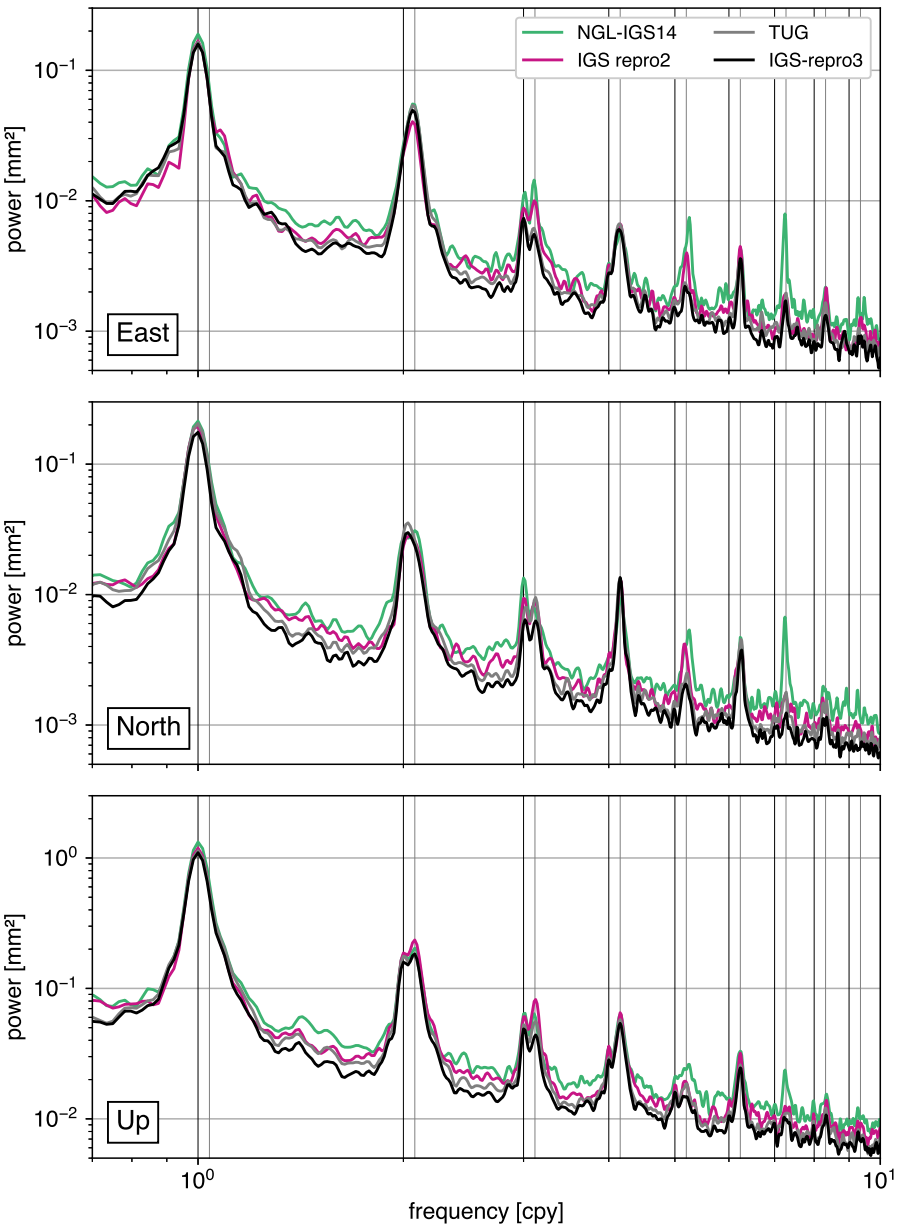

Fig. S70 Average periodograms of residuals from trajectory models adjusted to selected, loading-corrected, post-2005 station position time series: zoom on the 0.7 – 10 cpy band. The individual periodograms were normalized so that the heights of the spectral peaks are comparable amongst data sets, but the levels of background noise are not. The *black vertical lines* indicate harmonics of the annual frequency. The *gray vertical lines* indicate harmonics of the GPS draconitic frequency.

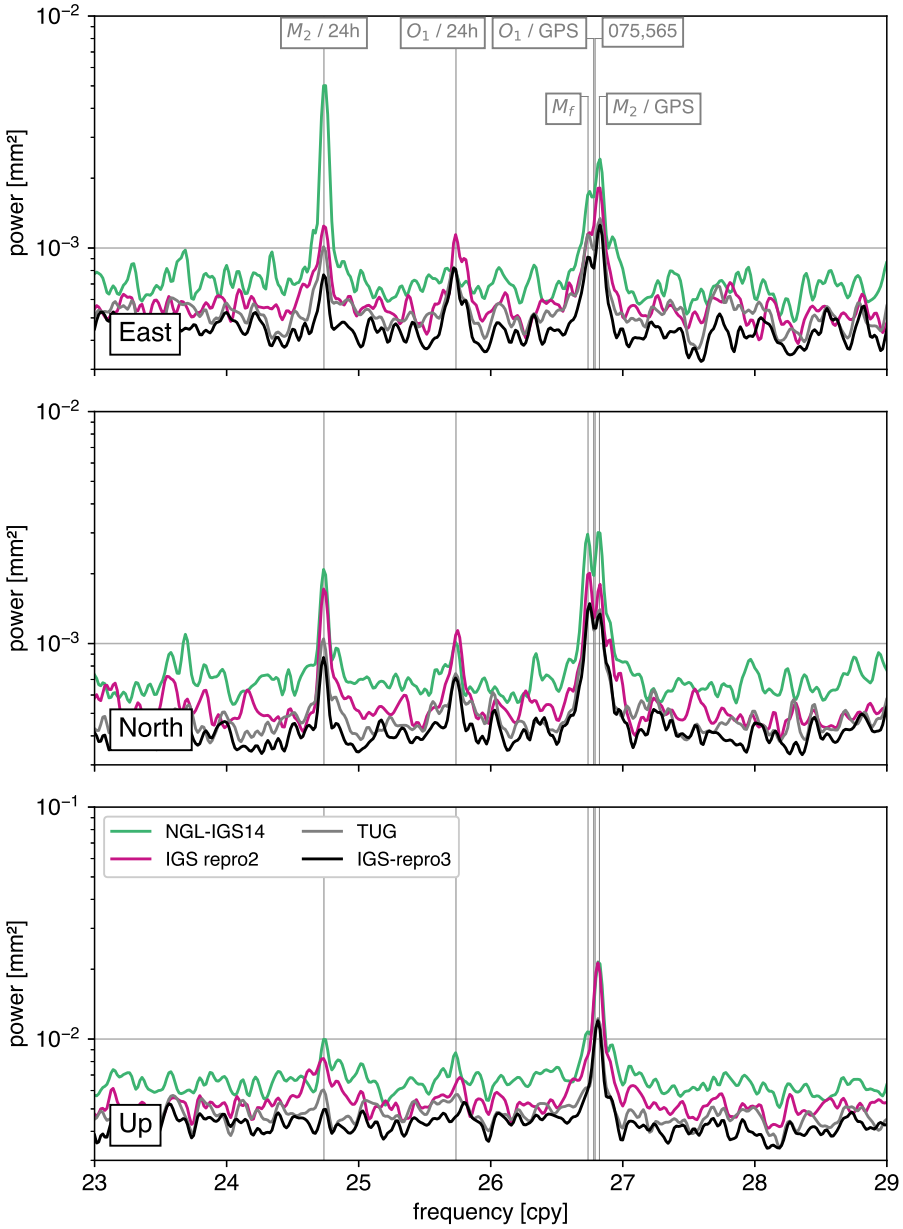

Fig. S71 Average periodograms of residuals from trajectory models adjusted to selected, loading-corrected, post-2005 station position time series: zoom on the fortnightly band. The individual periodograms were normalized so that the heights of the spectral peaks are comparable amongst ACs, but the levels of background noise are not. The *gray vertical lines* respectively indicate the alias period of the M_2 tide via daily sampling (24.74 cpy / 14.76 d), the alias period of the O_1 tide via daily sampling (25.74 cpy / 14.19 d), the M_f tide period (26.74 cpy / 13.66 d), the alias period of the O_1 tide via the GPS ground repeat period (26.78 cpy / 13.64 d), the 075, 565 tide period (26.79 cpy / 13.63 d) and the alias period of the M_2 tide via the GPS ground repeat period (26.82 cpy / 13.62 d).

References

Abbondanza C, Chin T, Gross R, Heflin M, Parker J (2023) An insight on scale definition in JTRF2020. EGU General Assembly 2023, Vienna, Austria, DOI https://doi.org/10.5194/egusphere-egu23-3212

Abraha KE, Teferle FN, Hunegnaw A, Dach R (2017) GNSS related periodic signals in coordinate time-series from Precise Point Positioning. Geophys J Int 208(3):1449–1464, DOI https://doi.org/10.1093/gji/ggw467

Abraha KE, Teferle FN, Hunegnaw A, Dach R (2018) Effects of unmodelled tidal displacements in GPS and GLONASS coordinate time-series. Geophys J Int 214(3):2195–2206, DOI https://doi.org/10.1093/gji/ggy254

Agnew DC, Larson KM (2007) Finding the repeat times of the GPS constellation. GPS Solut 11:71–76, DOI https://doi.org/10.1007/s10291-006-0038-4

Altamimi Z, Collilieux X (2009) IGS contribution to the ITRF. J Geodesy 83(3):375–383, DOI https://doi.org/10.1007/s00190-008-0294-x

Altamimi Z, Rebischung P, Métivier L, Collilieux X (2016) ITRF2014: A new release of the International Terrestrial Reference Frame modeling nonlinear station motions. J Geophys Res Solid Earth 121(8):6109–6131, DOI https://doi.org/10.1002/2016JB013098

Altamimi Z, Rebischung P, Collilieux X, Métivier L, Chanard K (2023) ITRF2020: an augmented reference frame refining the modeling of nonlinear station motions. J Geodesy 97(47), DOI https://doi.org/10.1007/s00190-023-01738-w

Amiri N, Desai S, Selle C, Sibois A (2016) The impact of time variable gravity field on GPS precise orbit determination. IGS Workshop 2016, Sydney, Australia, URL http://acc.igs.org/workshop2016/posters/Nikta_Amiri_Impact_Of_Time_Variable_Gravity_Field_on_GPS_Precise_Orbit_Determination_2016.pdf

Amiri-Simkooei AR (2007) Least-squares variance component estimation: theory and GPS applications. PhD thesis, Delft University of Technology, URL http://resolver.tudelft.nl/uuid:bc7f8919-1baf-4f02-b115-dc926c5ec090

Amiri-Simkooei AR (2013) On the nature of GPS draconitic year periodic pattern in multivariate position time series. J Geophys Res Solid Earth 118(5):2500–2511, DOI https://doi.org/10.1002/jgrb.50199

Amiri-Simkooei AR, Tiberius CCJM, Teunissen PJG (2007) Assessment of noise in GPS coordinate time series: Methodology and results. J Geophys Res Solid Earth 112(B7):B07413, DOI https://doi.org/10.1029/2006JB004913

Arnold D, Meindl M, Beutler G, Dach R, Schaer S, Lutz S, Prange L, Sośnica K, Mervart L, Jäggi A (2015) CODE's new solar radiation pressure model for GNSS orbit determination. J Geodesy 89:775–791, DOI https://doi.org/10.1007/s00190-015-0814-4

Bar-Sever Y, Kuang D (2004) New empirically derived solar radiation pressure model for Global Positioning System satellites. IPN Progress Report, URL https://ipnpr.jpl.nasa.gov/progress_report/42-159/159I.pdf

Bar-Sever YE, Russ KM (1997) New and improved solar radiation models for GPS satellites based on flight data. Tech. rep., Jet Propulsion Laboratory, California Institute of Technology, URL https://apps.dtic.mil/sti/pdfs/ADA485820.pdf

Bertiger W, Bar-Sever Y, Dorsey A, Haines B, Harvey N, Hemberger D, Heflin M, Lu W, Miller M, Moore A, Murphy D, Ries P, Romans L, Sibois A, Sibthorpe A, Szilagyi B, Vallisneri M, Willis P (2020) GipsyX/RTGx, a new tool set for space geodetic operations and research. Adv Space Res 66(3):4693–489, DOI https://doi.org/10.1016/j.asr.2020.04.015

Beutler G, Brockmann E, Gurtner W, Hugentobler U, Mervart L, Rothacher M, Verdun A (1994) Extended orbit modeling techniques at the CODE processing center of the International GPS Service for Geodynamics (IGS): theory and initial results. Manuscr Geodaet 19(6):367–386

Blewitt G, Hammond WC, Kreemer C (2018) Harnessing the GPS data explosion for interdisciplinary science. Eos 99, DOI https://doi.org/10.1029/2018EO104623

Bock Y, Melgar D (2016) Physical applications of GPS geodesy: a review. Rep Prog Phys 79(10):106801, DOI https://doi.org/10.1088/0034-4885/79/10/106801

Böhm J, Niell A, Tregoning P, Schuh H (2006a) Global Mapping Function (GMF): A new empirical mapping function based on numerical weather model data. Geophys Res Lett 33(7):L07304, DOI https://doi.org/10.1029/2005GL025546

Böhm J, Werl B, Schuh H (2006b) Troposphere mapping functions for GPS and very long baseline interferometry from European Centre for Medium-Range Weather Forecasts operational analysis data. J Geophys Res Solid Earth 111(B2):B02406, DOI https://doi.org/10.1029/2005JB003629

Böhm J, Möller G, Schindelegger M, Pain G, Weber R (2015) Development of an improved empirical model for slant delays in the troposphere (GPT2w). GPS Solut 19:433–441, DOI https://doi.org/10.1007/s10291-014-0403-7

Boy JP (2021) Contribution of GGFC to ITRF2020. Tech. rep., EOST/IPGS, Strasbourg, France, URL http://loading.u-strasbg.fr/ITRF2020/ggfc.pdf

Carrère L, Lyard F (2003) Modeling the barotropic response of the global ocean to atmospheric wind and pressure forcing - comparisons with observations. Geophys Res Lett 30(6):1275, DOI https:

//doi.org/10.1029/2002GL016473

Chanard K, Fleitout L, Calais E, Rebischung P, Avouac JP (2018) Toward a global horizontal and vertical elastic load deformation model derived from GRACE and GNSS station position time series. J Geophys Res Solid Earth 123(4):3225–3237, DOI https://doi.org/10.1002/2017JB015245

Chanard K, Métois M, Rebischung P, Avouac JP (2020) A warning against over-interpretation of seasonal signals measured by the Global Navigation Satellite System. Nat Commun 11(1375), DOI https://doi.org/10.1038/s41467-020-15100-7

Chen Q, van Dam T, Sneeuw N, Collilieux X, Weigelt M, Rebischung P (2013) Singular spectrum analysis for modeling seasonal signals from GPS time series. J Geodyn 72:25–35, DOI http://dx.doi.org/10.1016/j.jog.2013.05.005

Collilieux X, Schmid R (2013) Evaluation of the ITRF2008 GPS vertical velocities using satellite antenna z-offsets. GPS Solut 17:237–246, DOI https://doi.org/10.1007/s10291-012-0274-8

Collilieux X, van Dam T, Ray J, Coulot D, Métivier L, Altamimi Z (2012) Strategies to mitigate aliasing of loading signals while estimating GPS frame parameters. J Geodesy 86:1–14, DOI https://doi.org/10.1007/s00190-011-0487-6

Dach R, Selmke I, Villiger A, Arnold D, Prange L, Schaer S, Sidorov D, Stebler P, Jäggi A, Hugentobler U (2021) Review of recent GNSS modelling improvements based on CODEs Repro3 contribution. Adv Space Res 68(3):1263–1280, DOI https://doi.org/10.1016/j.asr.2021.04.046

Damiani T, Freeman W, Coloma F, Haw D, McFarland P, Saleh J, Sun L, Yoon S (2019) Strengthening the NOAA CORS network: foundation CORS, orbit analysis, and other initiatives. AGU Fall Meeting 2019, San Francisco, California, USA

Davis JL, Wernicke BP, Bisnath S, Niemi NA, Elósegui P (2006) Subcontinental-scale crustal velocity changes along the Pacific–North America plate boundary. Nature 441:1131–1134, DOI https://doi.org/10.1038/nature04781

Davis JL, Wernicke BP, Tamisiea ME (2012) On seasonal signals in geodetic time series. J Geophys Res Solid Earth 117(B1):B01403, DOI https://doi.org/10.1029/2011JB008690

Dee DP, Uppala SM, Simmons AJ, Berrisford P, Poli P, Kobayashi S, Andrae U, Balmaseda MA, Balsamo G, Bauer P, Bechtold P, Beljaars ACM, van de Berg L, Bidlot J, Bormann N, Delsol C, Dragani R, Fuentes M, Geer AJ, Haimberger L, Healy SB, Hersbach H, Hólm EV, Isaksen L, Kållberg P, Köhler M, Matricardi M, McNally AP, Monge-Sanz BM, Morcrette JJ, Park BK, Peubey C, de Rosnay P, Tavolato C, Thépaut JN, Vitart F (2011) The ERA-Interim reanalysis: configuration and performance of the data assimilation system. Q J Roy Meteor Soc 137(656):553–597, DOI https://doi.org/10.1002/qj.828

Degnan JJ, Pavlis EC (1994) Laser ranging to GPS satellites with centimeter accuracy. GPS World 5(9):62–70, DOI https://doi.org/10.1016/j.asr.2012.10.026

Desai SD, Sibois AE (2016) Evaluating predicted diurnal and semidiurnal tidal variations in polar motion with GPS-based observations. J Geophys Res Solid Earth 121(7):5237–5256, DOI https://doi.org/10.1002/2016JB013125

Dill R (2008) Hydrological model LSDM for operational Earth rotation and gravity field variations. Tech. rep., Deutsches GeoForschungsZentrum GFZ, Potsdam, Germany, DOI https://doi.org/10.2312/GFZ.b103-08095

Dill R, Dobslaw H (2013) Numerical simulations of global-scale high-resolution hydrological crustal deformations. J Geophys Res Solid Earth 118(9):5008–5017, DOI https://doi.org/10.1002/jgrb.50353

Dong D, Fang P, Bock Y, Cheng MK, Miyazaki S (2002) Anatomy of apparent seasonal variations from GPS-derived site position time series. J Geophys Res Solid Earth 107(B4):ETG 9–1–ETG 9–16, DOI https://doi.org/10.1029/2001JB000573

Dong D, Yunck T, Heflin M (2003) Origin of the International Terrestrial Reference Frame. J Geophys Res Solid Earth 108(B4):2200, DOI https://doi.org/10.1029/2002JB002035

Fernandes R, Bos M, Montillet JP, He X (2019) Study of the 5.5 day period in GPS time series. AGU Fall Meeting 2019, San Francisco, California, USA, URL https://www.researchgate.net/publication/337943222_Study_of_the_55_day_period_in_GPS_time_series

Glaser S, Rebischung P, Altamimi Z, Schuh H (2021) Rigorous propagation of Galileo-based terrestrial scale. Tour de l'IGS 1st Stop: repro3, URL https://files.igs.org/pub/resource/pubs/workshop/2021/07-Glaser.pdf

Gobron K, Rebischung P, Camp MV, Demoulin A, de Viron O (2021) Influence of aperiodic non-tidal atmospheric and oceanic loading deformations on the stochastic properties of global GNSS vertical land motion time series. J Geophys Res Solid Earth 126(9):e2021JB022370, DOI https://doi.org/10.1029/2021JB022370

Gobron K, Rebischung P, de Viron O, Demoulin A, Camp MV (2022) Impact of offsets on assessing the low-frequency stochastic properties of geodetic time series. J Geodesy 96(46), DOI https://doi.org/10.1007/s00190-022-01634-9

Gravelle M, Gobron K, Wöppelmann G (2022) The ULR-repro3 GPS data reanalysis solution. SONEL Data Assembly Centre, DOI https://doi.org/10.26166/sonel_ulr7a

Gravelle M, Wöppelmann G, Gobron K, Altamimi Z, Guichard M, Herring T, Rebischung P (2023) The ULR-repro3 GPS data reanalysis and its estimates of vertical land motion at tide gauges for sea level science. Earth Syst Sci Data 15(1):497–509, DOI https://doi.org/10.5194/essd-15-497-2023

Gross R, Abbondanza C, Chin T, Heflin M, Parker J (2023) JTRF2020: results and next steps. EGU General Assembly 2023, Vienna, Austria, DOI https://doi.org/10.5194/egusphere-egu23-2117

GSC (2023) Galileo satellite metadata. URL https://www.gsc-europa.eu/support-to-developers/galileo-satellite-metadata

Gualandi A, Avouac JP, Galetzka J, Genrich JF, Blewitt G, Adikhari LB, Koirala BP, Gupta R, Upreti BN, Pratt-Sitaula B, Liu-Zeng J (2017) Pre-and post-seismic deformation related to the 2015, Mw 7.8 Gorkha earthquake, Nepal. Tectonophysics 714–715:90–106, DOI https://doi.org/10.1016/j.tecto.2016.06.014

Harville DA (1977) Maximum likelihood approaches to variance component estimation and to related problems. J Am Stat Assoc 72(358):320–338, DOI https://doi.org/10.2307/2286796

Heflin M, Donnellan A, Parker J, Lyzenga G, Moore A, Ludwig LG, Rundle J, Wang J, Pierce M (2020) Automated estimation and tools to extract positions, velocities, breaks, and seasonal terms from daily GNSS measurements: Illuminating nonlinear Salton Trough deformation. Earth Space Sci 7(7):e2019EA00064, DOI https://doi.org/10.1029/2019EA000644

Herring T (2022) MIT Analysis Center Technical Report 2021. In: Villiger A, Dach R (eds) International GNSS Service Technical Report 2021, IGS Central Bureau and University of Bern, Bern Open Publishing, pp 91–102, DOI http://dx.doi.org/10.48350/169536

Hersbach H, Bell B, Berrisford P, Hirahara S, Horányi A, noz Sabater JM, Nicolas J, Peubey C, Radu R, Schepers D, Simmons A, Soci C, Abdalla S, Abellan X, Balsamo G, Bechtold P, Biavati G, Bidlot J, Bonavita M, Chiara GD, Dahlgren P, Dee D, Diamantakis M, Dragani R, Flemming J, Forbes R, Fuentes M, Geer A, Haimberger L, Healy S, Hogan RJ, Hólm E, Janisková M, Keeley S, Laloyaux P, Lopez P, Lupu C, Radnoti G, de Rosnay P, Rozum I, Vamborg F, Villaume S, Thépaut JN (2020) The ERA5 global reanalysis. Q J Roy Meteor Soc 146(730):1999–2049, DOI https://doi.org/10.1002/qj.3803

Huang W, Männel B, Brack A, Schuh H (2020) Two methods to determine scale-independent GPS PCOs and GNSS-based terrestrial scale: comparison and cross-check. GPS Solut 25(4), DOI https://doi.org/10.1007/s10291-020-01035-5

IAC (2023) About GLONASS. URL https://glonass-iac.ru/en/about_glonass

Johnston G, Riddell A, Hausler G (2017) The International GNSS Service. In: Teunissen PJG, Montenbruck O (eds) Springer handbook of global navigation satellite systems, Springer International Publishing, pp 967–982, DOI https://doi.org/10.1007/978-3-319-42928-1_33

Jungclaus JH, Fisher N, Haak H, Lohmann K, Marotzke J, Matei D, Mikolajewicz U, Notz D, von Storch JS (2013) Characteristics of the ocean simulations in the Max Planck Institute Ocean Model

(MPIOM) the ocean component of the MPI-Earth system model. J Adv Model Earth Sy 5(2):422–446, DOI https://doi.org/10.1002/jame.20023

King M, Watson CS (2014) Geodetic vertical velocities affected by recent rapid changes in polar motion. Geophys J Int 199(2):1161–1165, DOI https://doi.org/10.1093/gji/ggu325

King MA, Watson CS (2010) Long GPS coordinate time series: Multipath and geometry effects. J Geophys Res Solid Earth 115(B4):B04403, DOI https://doi.org/10.1029/2009JB006543

Klos A, Bos MS, Bogusz J (2018) Detecting time-varying seasonal signal in GPS position time series with different noise levels. GPS Solut 22(21), DOI https://doi.org/10.1007/s10291-017-0686-6

Kouba J (2003) Testing of the IERS2000 sub-daily Earth rotation parameter model. Stud Geophys Geod 47:725–739, DOI https://doi.org/10.1023/A:1026338601516

Kvas A, Brockmann JM, Krauss S, Schubert T, Gruber T, Meyer U, Mayer-Gürr T, Schuh WD, Jäggi A, Pail R (2021) GOCO06s – a satellite-only global gravity field model. Earth Syst Sci Data 13(1):99–118, DOI https://doi.org/10.5194/essd-13-99-2021

Lagler K, Schindelegger M, Böhm J, Krásná H, Nilsson T (2013) GPT2: Empirical slant delay model for radio space geodetic techniques. Geophys Res Lett 40(6):1069–1073, DOI https://doi.org/10.1002/grl.50288

Lambert A, Pagiatakis SD, Billyard AP, Dragert H (1998) Improved ocean tide loading corrections for gravity and displacement: Canada and northern United States. J Geophys Res Solid Earth 103(B12):30231–30244, DOI https://doi.org/10.1029/98JB02735

Landskron D, Böhm J (2017) VMF3/GPT3: refined discrete and empirical troposphere mapping functions. J Geodesy 92:349–360, DOI https://doi.org/10.1007/s00190-017-1066-2

Lavallée DA, van Dam T, Blewitt G (2006) Geocenter motions from GPS: A unified observation model. J Geophys Res Solid Earth 111(B5):B05405, DOI https://doi.org/10.1029/2005JB003784

Lockheed Martin (2021) Updated GPS-III Antenna Phase Center values for SVN-74 through SVN-78. URL https://www.navcen.uscg.gov/sites/default/files/pdf/gps/GPSIII_APCs_SVNs_74_78_ISC_SVN78_Dec2021.pdf

Lyard FH, Allain DJ, Cancet M, Carrère L, Picot N (2021) FES2014 global ocean tide atlas: design and performance. Ocean Sci 17(3):615–649, DOI https://doi.org/10.5194/os-17-615-2021

Ma Y, Rebischung P, Altamimi Z, Jiang W (2020) Assessment of geocenter motion estimates from the IGS second reprocessing. GPS Solut 54(55), DOI https://doi.org/10.1007/s10291-020-0968-2

Männel B, Rothacher M (2017) Geocenter variations derived from a combined processing of LEO- and ground-based GPS observations. J Geodesy 91:933–944, DOI https://doi.org/10.1007/s00190-017-0997-y

Männel B, Dobslaw H, Dill R, Glaser S, Balidakis K, Thomas M, Schuh H (2019) Correcting surface loading at the observation level: impact on global GNSS and VLBI station networks. J Geodesy 93:2003–2017, DOI https://doi.org/10.1007/s00190-019-01298-y

Männel B, Brandt A, Bradke M, Sakic P, Brack A, Nischan T (2020) Status of IGS reprocessing activities at GFZ. In: Freymueller J, Sánchez L (eds) Beyond 100: The Next Century in Geodesy. International Association of Geodesy Symposia, Springer, Cham, vol 152, DOI https://doi.org/10.1007/1345_2020_98

Männel B, Brandt A, Bradke M, Sakic P, Brack A, Nischan T (2021) GFZ repro3 product series for the International GNSS Service (IGS). GFZ Data Services, DOI https://doi.org/10.5880/GFZ.1.1.2021.001

Mao A, Harrison CGA, Dixon TH (1999) Noise in GPS coordinate time series. J Geophys Res Solid Earth 104(B2):2797–2816, DOI https://doi.org/10.1029/1998JB900033

Martens HR, Argus DF, Norberg C, Blewitt G, Herring TA, Moore AW, Hammond WC, Kreemer C (2020) Atmospheric pressure loading in GPS positions: dependency on GPS processing methods and effect on assessment of seasonal deformation in the contiguous USA and Alaska. J Geodesy 94(115), DOI https://doi.org/10.1007/s00190-020-01445-w

Masoumi S (2022) Switch of the IGS products to the IGS20.igs20.atx, repro3 standards and long filenames. IGSMAIL-8282, URL https://lists.igs.org/pipermail/igsmail/2022/008278.html

Mayer-Gürr T, Behzadpour S, Eicker A, Ellmer M, Koch B, Krauss S, Pock C, Rieser D, Strasser S, Süsser-Rechberger B, Zehentner N, Kvas A (2021) GROOPS: a software toolkit for gravity field recovery and GNSS processing. Comput Geosci 155(104864), DOI https://doi.org/10.1016/j.cageo.2021.104864

Meindl M, Beutler G, Thaller D, Dach R, Jäggi A (2013) Geocenter coordinates estimated from GNSS data as viewed by perturbation theory. Adv Space Res 51(7):1047–1064, DOI https://doi.org/10.1016/j.asr.2012.10.026

Mémin A, Boy J, Santamaría-Gómez A (2020) Correcting GPS measurements for non-tidal loading. GPS Solut 24(45), DOI https://doi.org/10.1007/s10291-020-0959-3

Métivier L, Collilieux X, Lercier D, Altamimi Z, Beauducel F (2014) Global coseismic deformations, GNSS time series analysis, and earthquake scaling laws. J Geophys Res Solid Earth 119(12):9095–9109, DOI https://doi.org/10.1002/2014JB011280

Montenbruck O, Steigenberger P, Villiger A, Rebischung P (2022) On the relation of GNSS phase center offsets and the terrestrial reference frame scale: a semi-analytical analysis. J Geodesy 96(90), DOI https://doi.org/10.1007/s00190-022-01678-x

Moritz H (1992) Geodetic Reference System 1980. B Geod 66:187–192, DOI https://doi.org/10.1007/BF00989270

Murphy D, Bertiger W, Hemberger D, Meyer R, Ries P, Sibois A, Sibthorpe A, Watson R (2021) JPL IGS Analysis Center Technical Report 2020. In: Villiger A, Dach R (eds) International GNSS Service Technical Report 2020, IGS Central Bureau and University of Bern, Bern Open Publishing, pp 93–98, DOI https://doi.org/10.7892/boris.144003

Niu Y, Wei N, Li M, Rebischung P, Shi C, Chen G (2022) Quantifying discrepancies in the three-dimensional seasonal variations between IGS station positions and load models. J Geodesy 96(31), DOI https://doi.org/10.1007/s00190-022-01618-9

Niu Y, Rebischung P, Li M, Wei N, Shi C, Altamimi Z (2023) Temporal spectrum of spatial correlations between GNSS station position time series. J Geodesy 97(12), DOI https://doi.org/10.1007/s00190-023-01703-7

Penna NT, Stewart MP (2003) Aliased tidal signatures in continuous GPS height time series. Geophys Res Lett 30(23):2184, DOI https://doi.org/10.1029/2003GL018828

Penna NT, King MA, Stewart MP (2007) GPS height time series: short-period origins of spurious long-period signals. J Geophys Res Solid Earth 112(B2):B02402, DOI https://doi.org/10.1029/2005JB004047

Perosanz F, Loyer S, Mercier F, Garcia AB, Mezerette A, Katsigianni G, Santamaría-Gómez A, Marty JC (2021) CNES-CLS Technical Report 2020. In: Villiger A, Dach R (eds) International GNSS Service Technical Report 2020, IGS Central Bureau and University of Bern, Bern Open Publishing, pp 87–92, DOI https://doi.org/10.7892/boris.144003

Petit G, Luzum B (2010) IERS conventions (2010). IERS Technical Note 36, Verlag des Bundesamts für Kartographie und Geodäsie, Frankfurt am Main

Ray J, Altamimi Z, Collilieux X, van Dam T (2008) Anomalous harmonics in the spectra of GPS position estimates. GPS Solut 12:55–64, DOI https://doi.org/10.1007/s10291-007-0067-7

Ray J, Collilieux X, Rebischung P, van Dam TM, Altamimi Z (2011) Consistency of crustal loading signals derived from models and GPS: Inferences for GPS positioning errors. AGU Fall Meeting 2011, San Francisco, California, USA, URL http://acc.igs.org/trf/pos-errs_agu-f11.ppt

Ray J, Griffiths J, Collilieux X, Rebischung P (2013) Subseasonal GNSS positioning errors. Geophys Res Lett 40(22):5854–5860, DOI https://doi.org/10.1002/2013GL058160

Ray J, Rebischung P, Griffiths J (2017) IGS polar motion measurement accuracy. Geod Geodyn 8(6):413–420, DOI https://doi.org/10.1016/j.geog.2017.01.008

Ray RD (2013) Precise comparisons of bottom-pressure and altimetric ocean tides. J Geophys Res Oceans 118(9):4570–4584, DOI https://doi.org/10.1002/jgrc.20336

Rebischung P (2016) Upcoming switch to IGS14/igs14.atx. IGSMAIL-7399, URL https://lists.igs.org/pipermail/igsmail/2016/001233.html

Rebischung P (2020) IGS Reference Frame Working Group Technical Report 2019. In: Villiger A, Dach R (eds) International GNSS Service Technical Report 2019, IGS Central Bureau and University of Bern, Bern Open Publishing, pp 237–246, DOI https://doi.org/10.7892/boris.144003

Rebischung P (2023a) IGS Reference Frame Working Group Coordinator Report 2022. In: Dach R, Brockmann E (eds) International GNSS Service Technical Report 2022, IGS Central Bureau and University of Bern, Bern Open Publishing, pp 217–226, DOI https://doi.org/10.48350/179297

Rebischung P (2023b) IGS repro3 SINEX solutions for 2021-2022. IGSMAIL-8329, URL https://lists.igs.org/pipermail/igsmail/2023/008325.html

Rebischung P, Altamimi Z, Springer T (2014) A collinearity diagnosis of the GNSS geocenter determination. J Geodesy 88(7):65–85, DOI https://doi.org/10.1007/s00190-013-0669-5

Rebischung P, Altamimi Z, Garayt B, Ray J (2016) The IGS contribution to ITRF2014. J Geodesy 90(7):611–630, DOI https://doi.org/10.1007/s00190-016-0897-6

Rebischung P, Garayt B, Altamimi Z (2017) IGS Reference Frame Working Group Technical Report 2016. In: Villiger A, Dach R (eds) International GNSS Service Technical Report 2016, IGS Central Bureau and University of Bern, Bern Open Publishing, pp 171–178, DOI https://doi.org/10.7892/boris.99278

Rebischung P, Collilieux X, Métivier L, Altamimi Z, Chanard K (2021) Analysis of IGS repro3 station position time series. AGU Fall Meeting 2021, New Orleans, Louisiana, USA, DOI https://doi.org/10.1002/essoar.10509008.1

Rebischung P, Villiger A, Masoumi S, Herring T (2022) Upcoming switch to IGS20/igs20.atx and repro3 standards. IGSMAIL-8238, URL https://lists.igs.org/pipermail/igsmail/2022/008234.html

Riddell AR, King MA, Watson CS, Sun Y, Riva REM, Rietbroek R (2017) Uncertainty in geocenter estimates in the context of ITRF2014. J Geophys Res Solid Earth 122(5):4020–4032, DOI https://doi.org/10.1002/2016JB013698

Sakumura C, Sibois A, Sibthorpe A, Murphy D (2017) Improved modeling of GPS Block IIF satellites for the GSPM13 solar radiation pressure model. IGS Workshop 2017, Paris, France, URL https://files.igs.org/pub/resource/pubs/workshop/2017/W2017-PY08-06%20-%20Sakumura.pdf

Santamaría-Gómez A, Ray J (2021) Chameleonic noise in GPS position time series. J Geophys Res Solid Earth 126(3):e2020JB019541, DOI https://doi.org/10.1029/2020JB019541

Santamaría-Gómez A, Bouin MN, Collilieux X, Wöppelmann G (2011) Correlated errors in GPS position time series: Implications for velocity estimates. J Geophys Res Solid Earth 116(B1):B01405, DOI https://doi.org/10.1029/2010JB007701

Santamaría-Gómez A, Rebischung P, Ray J (2016) Separating station-dependent from regionally-coherent GPS draconitics in station positions. AGU Fall Meeting 2016, San Francisco, California, USA, URL http://acc.igs.org/trf/pos-errs_agu-f11.ppt

Savcenko R, Bosch W (2012) EOT11a - Empirical ocean tide model from multi-mission satellite altimetry. Tech. rep., Deutsches Geodätisches Forschungsinstitut (DGFI), DOI https://doi.pangaea.de/10013/epic.43894.d001

Scargle JD (1982) Studies in astronomical time series analysis. II. Statistical aspects of spectral analysis of unevenly spaced data. Astrophys J 263:835–853, DOI https://doi.org/10.1086/160554

Schmid R (2017) Antenna Working Group Technical Report 2016. In: Villiger A, Dach R (eds) International GNSS Service Technical Report 2016, IGS Central Bureau and University of Bern, Bern Open Publishing, pp 139–144, DOI https://doi.org/10.7892/boris.99278

Schoenemann E, Dilssner F, Mayer V, Gini F, Otten M, Springer T, Bruni S, Enderle W, Zandbergen R (2021) ESA's efforts for more consistent geodetic products. EGU General Assembly 2021, Vienna, Austria, DOI https://doi.org/10.5194/egusphere-egu21-8899

Seitz M, Blossfeld M, Angermann D, Glomsda M, Rudenko S, Zeitlhöfler J, Seitz F (2023) DTRF2020 (Version v2). Zenodo, DOI https://doi.org/10.5281/zenodo.8369167

Selle C, Desai S, Fernandez MG, Sibois A (2014) Spectral analysis of GPS-based station positioning time series from PPP solutions. IGS Workshop 2014, Pasadena, California, USA, URL https://files.igs.org/pub/resource/pubs/workshop/2014/Workshop%202014%20-%20PS13%20-%20Selle%20-%202186%20-%20Spectral%20analysis%20of%20GPS-based%20station%20positioning%20time%20series%20from%20PPP%20solutions.pdf

Selmke I, Dach R, Arnold D, Prange L, Schaer S, Sidorov D, Stebler P, Villiger A, Jäggi A, Hugentobler U (2020) CODE repro3 product series for the IGS. Astronomical Institute, University of Bern, DOI http://dx.doi.org/10.7892/boris.135946

Shi C, Li M, Zhao Q, Geng J, Zhang Q (2023) Wuhan University Analysis Center Technical Report 2022. In: Dach R, Brockmann E (eds) International GNSS Service Technical Report 2022, IGS Central Bureau and University of Bern, Bern Open Publishing, pp 105–108, DOI http://dx.doi.org/10.48350/179297

Sibois A (2019) Analysis of high-frequency EOP (HFEOP) models and their impact on GPS data processing. IGS Analysis Centre Workshop 2019, Potsdam, Germany, URL https://s3-ap-southeast-2.

amazonaws.com/igs-acc-web/igs-acc-website/workshop2019/Sibois_IgsAcWorkshop_2019.pdf

Sibois A, Selle C, Desai S, Sibthorpe A, Weiss J (2014) GSPM13: an updated empirical model for solar radiation pressure forces acting on GPS satellites. IGS Workshop 2014, Pasadena, California, USA, URL https://www.researchgate.net/publication/283517257_GSPM13_An_Updated_Empirical_Model_for_Solar_Radiation_Pressure_Forces_Acting_on_GPS_Satellites

Steigenberger P, Montenbruck O (2023) Consistency of Galileo satellite antenna phase center offsets. J Geodesy 97(58), DOI https://doi.org/10.1007/s00190-023-01750-0

Steigenberger P, Boehm J, Tesmer V (2009) Comparison of GMF/GPT with VMF1/ECMWF and implications for atmospheric loading. J Geodesy 83:943–951, DOI https://doi.org/10.1007/s00190-009-0311-8

Stewart MP, Penna NT, Lichti DD (2005) Investigating the propagation mechanism of unmodelled systematic errors on coordinate time series estimated using least squares. J Geodesy 79:479–489, DOI https://doi.org/10.1007/s00190-005-0478-6

Strasser S (2022) Reprocessing multiple GNSS constellations and a global station network from 1994 to 2020 with the raw observation approach. PhD thesis, Technische Universität Graz, DOI https://doi.org/10.3217/978-3-85125-885-1

Strasser S, Mayer-Gürr T (2021) IGS repro3 products by Graz University of Technology (TUG). Graz University of Technology, DOI https://doi.org/10.3217/dataset-4528-0723-0867

Strasser S, Mayer-Gürr T, Zehentner N (2019) Processing of GNSS constellations and ground station networks using the raw observation approach. J Geodesy 93:1045–1057, DOI https://doi.org/10.1007/s00190-018-1223-2

Tregoning P, Herring TA (2006) Impact of a priori zenith hydrostatic delay errors on GPS estimates of station heights and zenith total delays. Geophys Res Lett 33(23):L23303, DOI https://doi.org/10.1029/2006GL027706

Tregoning P, Watson C (2009) Atmospheric effects and spurious signals in GPS analyses. J Geophys Res Solid Earth 114(B9):B09403, DOI https://doi.org/10.1029/2009JB006344

US Department of Defense (2020) Global Positioning System Standard Positioning Service performance standard. URL https://www.gps.gov/technical/ps/2020-SPS-performance-standard.pdf

Villiger A (2020) Antenna Working Group Technical Report 2019. In: Villiger A, Dach R (eds) International GNSS Service Technical Report 2019, IGS Central Bureau and University of Bern, Bern Open Publishing, pp 185–194, DOI https://doi.org/10.7892/boris.144003

Villiger A, Dach R, Prange L, Arnold D, Kalarus M, Schaer S, Stebler P, Jäggi A (2022) Compatibility between the preliminary ITRF2020 solution and GNSS antenna phase center offsets. EGU General

Assembly 2022, Vienna, Austria, DOI https://doi.org/10.5194/egusphere-egu22-5530

Vondrák J (1969) A contribution to the problem of smoothing observational data. B Astron I Czech 20(6):349–355

Vondrák J (1977) Problem of smoothing observational data II. B Astron I Czech 28(2):84–89

Williams SDP (2003) Offsets in Global Positioning System time series. J Geophys Res Solid Earth 108(B6):2310, DOI https://doi.org/10.1029/2002JB002156

Williams SDP, Bock Y, Fang P, Jamason P, Nikolaidis RM, Prawirodirdjo L, Miller M, Johnson DJ (2004) Error analysis of continuous GPS position time series. J Geophys Res Solid Earth 109(B3):B03412, DOI https://doi.org/10.1029/2003JB002741

Zajdel R, Masoumi S, Sośnica K, Gałdyn F, Strugarek D, Bury G (2023) Combination and SLR validation of IGS Repro3 orbits for ITRF2020. J Geodesy 97(87), DOI https://doi.org/10.1007/s00190-023-01777-3

Zhang J, Bock Y, Johnson H, Fang P, Williams S, Genrich J, Wdowinski S, Behr J (1997) Southern California permanent GPS geodetic array: Error analysis of daily position estimates and site velocities. J Geophys Res Solid Earth 102(B8):18035–18055, DOI https://doi.org/10.1029/97JB01380